Università degli Studi della Basilicata

Dottorato di Ricerca in

Ingegneria per l'innovazione e lo Sviluppo Sostenibile

EXPERIMENTAL AND NUMERICAL SEISMIC RESPONSE OF MULTI-STOREY POST-TENSIONED TIMBER FRAMED BUILDINGS WITH SUPPLEMENTAL DAMPING SYSTEMS

Settore Scientifico-Disciplinare

ICAR/09

Coordinatore del Dottorato
Prof. Carmine Serio

Dottoranda
Dott.ssa Nicla Lamarucciola

Tutor
Prof. Felice Carlo Ponzo

Co-tutor
Prof. Antonio Di Cesare

Ciclo XXXIII

"I know quite certainly that I myself have no special talent; curiosity, obsession and dogged endurance, combined with self-criticism have brought me to my ideas."

(Albert Einstein)

Abstract

This doctoral project aims to contribute to advancement of the research in the field of innovative and resilient timber buildings with high seismic performance and minimum environmental impact in a green and sustainable way.

Recent seismic events have raised questions about the adequacy of the current seismic design in code provisions. In modern seismic codes, the performance objectives are expressed in terms of life safety of the occupants and according to capacity design rules a certain damage level of structures is accepted under strong earthquakes. The resultant seismic damages are often difficult and financially prohibitive to repair. In order to significantly reduce structural and non-structural damage and avoid high economic loss, in the last decades research studies focused on the development of low damage design and technologies.

In this thesis, seismic design and performance of multi-storey post-tensioned timber framed buildings with different dissipative systems have been investigated in order to develop new low-damage construction systems for high seismic areas. An extensive experimental campaign was performed at the structural laboratory of the University of Basilicata (Italy), in collaboration with the University of Canterbury (New Zealand), considering a three-dimensional, two-third scale, three-storey, post-tensioned glulam timber frame building. Different testing configurations were considered: i) the bare timber frame with post-tensioning only at the beam-column connections (free rocking); ii) the post-tensioned timber frame with dissipative devices at the beam-column and column-foundation connections (dissipative rocking); and iii) the post-tensioned timber frame with dissipative bracing systems at all storey (dissipative bracing). The seismic response of test specimen was investigated through unidirectional shaking table tests under consecutive ground motions at increasing PGA intensities, while the cyclic behaviour of hysteretic dampers was characterized by means of quasi-static tests.

In particular, the testing configuration with dissipative bracing, which had not been previously implemented in post-tensioned glulam timber structures, has been deeply investigated in this research. The estimation of equivalent viscous damping has been proposed in order to optimize the displacement-based design procedure for sizing the hysteretic dissipative devices of the bracing systems. The experimental seismic response of the braced model is evaluated in terms of global and local behaviour and nonlinear numerical analysis have been carried out within two different FEM software (Sap 2000 and OpenSees). The comparison of the results obtained from all configurations demonstrated that the dissipative bracing system improved the seismic performance of post-tensioned timber buildings reducing inter-storey drift with full re-centring capability. During all seismic tests no damages were observed to structural elements, only localized breakage of external replaceable devices occurred during the test with strongest earthquake. More than one hundred inelastic cycles were experimentally recorded from dynamic tests before the failure of devices.

The reliability of quasi-static testing procedures proposed by current seismic and guidelines codes for type tests and factory production control tests was also investigated. The number of cycles estimated from shaking table tests and non-linear dynamic analyses shows a decreasing trend with the increase of ductility demand in line with American standards testing requirements.

Acknowledgements

Firstly, I would like to express my gratitude to my supervisors Prof. Felice Ponzo and Antonio Di Cesare for giving me the opportunity to participate in this important research project. They were patient mentors whose door was always open, without their guidance, technical discussion and support this work would not have been possible. A special thanks to Antonio Di Cesare for sharing his knowledge and for contribution to many helpful ideas in this research work.

I wish also to acknowledge Domenico Nigro for providing his precious advices and technician support during the experimental testing performed in this thesis.

I would like to acknowledge the financial support of ReLUIS (Rete dei Laboratori Universitari di Ingegneria Sismica) project 2016-18 and 2019-21 funded by the Italian Civil Protection Department.

Moreover, I wish to thank my new friends and colleagues of the School of Engineering at UNIBAS: Antonella Nigro, Alessio Telesca, Rocco Di Tommaso, Gianluca Auletta, Antonello Mossucca, for the conversations (not only technician) and for the lunch times and coffee breaks.

Thank you to my dear friend Isa for the uncountable chats, laughs and encouragement in difficult days, and to my friends Mariantonietta, Antonella, Monica, Rossella, Isabel for their support and nice evenings spent together.

Finally, I wish to extend my special thanks to my mum and dad, without their love and support I would not have reached this milestone, and to all my family, my grandparents Angela and Saverio, my aunts, uncles and cousins, who always believed in me.

TABLE OF CONTENTS

1 Introduction

1.1 Background

Structures designed in accordance with the current seismic codes around the world, (e.g., NTC 2018 [1], Eurocode (EC8) [2], in Italy ,Europe and ASCE-7 [3] in the U.S.A.) follow force-based design (FBD) approach, upon which buildings are expected to sustain damage during strong earthquakes while protecting the lives of the occupants. This damage requires often expensive repairs, significant business downtime and occasionally building demolition. The need to mitigate damage of buildings, even after strong earthquakes, has led to development of low-damage displacement-based design (DBD) approaches [4], and protective technologies that improve the seismic performance of buildings beyond the current code minimum requirements in order to obtain seismic resilient structures. The seismic resilience is defined as the capability of a structural system to maintain an appropriate level of functionality during and after a strong earthquake and the capability to restore its initial condition within a short time period. The need to satisfy high seismic performance of structures and to comply with the latest policies of environmental sustainability worldwide and reduction of greenhouse gas emissions is leading engineers and researchers to higher interest in timber buildings.

Historically, timber structures have performed well to the life safety in moderate earthquake risk areas, while these have sustained significant structural and non-structural damages under strong earthquakes. Recently, the application of the DBD procedure has been extended toward the design of timber buildings [5] and in order to improve the seismic performance a recent technology, named pre-stressed laminated (Pres-Lam) technology has been developed. This technique is based on the PREcast Seismic Structural System (PRESSS), originally developed at University of California (San Diego) by Priestley et al. [6] for precast concrete frame and wall constructions. The system, successfully applied to create timber jointed ductile

connections at the University of Canterbury (New Zealand) [7], consists in the use of high strength unbounded steel cables or bars to connect timber beams and columns, or columns and walls to their foundations, providing self-centering capability to the frame. In order to increase the seismic performance additional internal or external dampers are added, to provide additional strength and energy dissipation capability. The introduction of metallic yielding dampers represents an optimal low-cost solution requiring a little maintenance and easily replaceable in case of damage. This hybrid system allows to obtain damage-avoiding structures characterized by the typical flag-shaped response with the capability to absorb energy in a major earthquake while rocking back to an undamaged position after the shaking.

Several experimental studies have been performed considering the application of the Pres-Lam system, such as cross laminated timber (CLT) shear walls [8], coupled laminated veneer lumber (LVL) timber walls [9], and post-tensioned LVL timber frames without and with the addition of dissipative rocking systems [10],[11]. In recent years applications of the system to timber buildings are emerging in high seismic areas throughout the world, particularly widespread in New Zealand, while few applications are available in Europe. Further improvements in DBD procedure and in numerical modelling are still being investigated and new techniques aiming to minimize residual damage induced by earthquakes are developing.

An extensive program of shaking table tests has been performed at the University of Basilicata (Italy), in order to assess the effectiveness of different passive energy dissipating systems in controlling the seismic vibrations of post-tensioned timber framed buildings. The Pres-Lam Project was developed in collaboration with University of Canterbury (New Zealand) and consisted of two stages.

In Stage 1 of the Project the post-tensioning technology was successfully implemented to a full-scale beam-column joint made of glue-laminated timber [12], differently from previous application to LVL frames or walls. Quasi-static tests were performed with and without replaceable dissipative devices demonstrating the effectiveness of the

system to glulam timber joint. Moreover, a hidden steel tube was designed and tested to transfer vertical loads and to withstand the shear loads without interference with the rocking mechanism.

In the Stage 2 of the project the application of Pres-Lam technology was extended to a large-scale, three-dimensional glulam timber frame specimen, tested in three different configurations at increasing amounts of energy dissipation, considering the same set of spectra-compatible earthquake inputs. In the first and second configurations shaking table tests were performed on the timber frame with post-tensioning only and with the addition of dissipative steel angles at the beam-column and column-foundation joints [13]. The results demonstrated the effectiveness of the system to the glulam timber frame, providing self-centering capability, additional strength and energy dissipation when dissipative angles are introduced, creating a flag-shaped response of the system. The dissipative-rocking impacts on the seismic response by increasing the equivalent viscous damping and reducing maximum drift of approximately 30%. No damage was observed on the main structural elements up to large drift values of over than 3%. The effects of introduction of larger amount of energy dissipation in the post-tensioned timber frame are analysed in the present research study.

1.2 Motivation and scope of research

In order to limit the displacements of the post-tensioned frame building, improving the seismic resilient performances of the structure, a new configuration has been designed and tested within the last phase of the Pres-Lam Project by coupling the post-tensioned timber frame with dissipative bracing systems (not previously implemented in post-tensioned timber structures). The post-tensioning system provide the self-centering properties to the frame and the dissipative bracing systems equipped with hysteretic U-shaped Flexural Plate (UFP) dampers are designed to dissipate large amounts of energy during a strong seismic event, in order to significantly reduce the

inter-storey drifts respect to previous configurations, also regularizing the structure due to the additional stiffness and damping provided to the structural system. Moreover, the dissipative bracing system allows to regularize the structure and to obtain a more flexible architectural configuration e.g., respect to heavy-timber gravity-framing systems combined with CLT walls or post-tensioned rocking walls, showing comparable drifts. The experimental research study represents a fundamental step in understanding and validate the seismic behaviour of the braced post-tensioned timber frame (as well as of any new structural system). The experimental results are an essential support to calibrate and validate numerical simulations and optimize analytical parameters and design procedures.

The main objectives of this research study are listed in the following points:

1. *Investigation on the seismic response of the braced post-tensioned frames through the shaking table tests*, based on dynamic tests performed on a large-scale braced specimen with connection details similar to those necessary for implementation in practice at different damage levels, from a Service Level Earthquake (SLE) to a Design Base Earthquake (DBE). The experimental results of all the testing frame configurations were compared in terms of main global (e.g. displacement, drift, acceleration, base shear etc.) and local key parameters (e.g. hysteretic response, post-tensioning losses) with that of the bare post-tensioned frame with and without dissipative rocking in order to assess the performance of the bracing system.

2. *Numerical modelling of post-tensioned frame with different dissipative systems* capable of reliably simulate the experimental results of the post-tensioned timber building with dissipative rocking and with dissipative bracing systems in terms of global key parameters and local response.

3. *Displacement based design procedure for post-tensioned timber framed buildings with dissipative systems*, based on significant key parameters (target design displacement and typical flag-shape parameters related to the reliable amount of dissipation) under

a reference level of seismic intensity. The validation of the procedure is based on experimental and numerical results.

4. *Dynamic response of nonlinear dampers (NLDs)*, in terms of number of cycles at different ductility levels and cycles to failure, based on the experimental results of the U-shaped flexural steel dampers, used for dissipative bracing systems of this experimental campaign. The cyclic response estimated from the design earthquakes was compared with the current seismic codes in terms of cyclic testing procedure required for type tests (TT) and factory production control tests (FPCT) of nonlinear devices (NLD).

1.3 Content organization

Chapter 2 describes the state of the art of post-tensioned timber framed buildings. The main advantages of timber material, the origins and development of post-tensioned timber concept and the main experimental applications and successful building projects around the world are presented.

Chapter 3 presents an overview of displacement-based design philosophy, details the optimization of the procedure for dissipative rocking and dissipative bracing systems and describes the application of the step-by-step design procedure to the experimental models.

Chapter 4 presents the experimental testing campaign of the 3D post-tensioned timber frame model. The chapter describes preliminary quasi-static tests on U-shaped flexural Plate dampers comparing the experimental results and analytical design procedure and summarize the main characteristics of dissipative angles. Then experimental models, testing configurations, construction details are provided and the instrumentation of the braced frame, the input ground motions, shaking table testing program and table fidelity are described.

Chapter 5 presents the experimental response of the braced frame compared with that of post-tensioned frame with free and dissipative rocking, in terms of dynamic

identification, global key parameters response, local hysteretic response at the beam-column, column-foundation and bracing connection. Moreover, the post-tensioning losses over time and seismic post-tensioning losses due to a sequence of earthquakes are analyzed for each configuration.

Chapter 6 presents the numerical modelling of the rocking mechanism calibrated and validated on the post-tensioned timber frame with free and dissipative rocking mechanisms and the numerical simulations of the braced model, validated and calibrated against global and local experimental results of the post-tensioned frame with dissipative bracing.

Chapter 7 focuses on the validation of the design procedure (presented in Chapter 2). The experimental hysteretic energy dissipated in DF and BF configurations is compared and equivalent damping is estimated by experimental and numerical results. Then, the design procedure was validated based on the comparison between the design parameters and numerical and experimental results of the frame with dissipative rocking and dissipative bracing.

Chapter 8 presents the dynamic cyclic response of U-shaped flexural devices for the dissipative bracing systems of the post-tensioned timber frame of this experimental campaign. The number of cycles and cycles to failure estimation of the dampers is presented and finally compared with current testing code requirements in order to assess the reliability of testing procedures.

Finally, in *Chapter 9* the conclusions and future development of the research study presented in this thesis are discussed.

2 State of the art of post-tensioned timber buildings

2.1 Timber as building material

Timber is one of the most ancient materials, used for thousands of years to construct buildings and bridges in Europe (before 1800), then with the industrialization during the 19th and 20th century timber constructions were replaced by steel and concrete structures (Figure1a). Size limitations, strength capacity and costs restricted the use of timber in multi-storey buildings where large dimensions (long-spans and open space) were required. In recent years, Europe Union strategies and worldwide policies are moving towards the reduction of greenhouse gas emissions and there is an increased trend to consider again timber as construction material for multi-storey buildings optimizing the structural concept and the seismic design, with the dual purpose to obtain more sustainable and anti-seismic constructions [14][15].

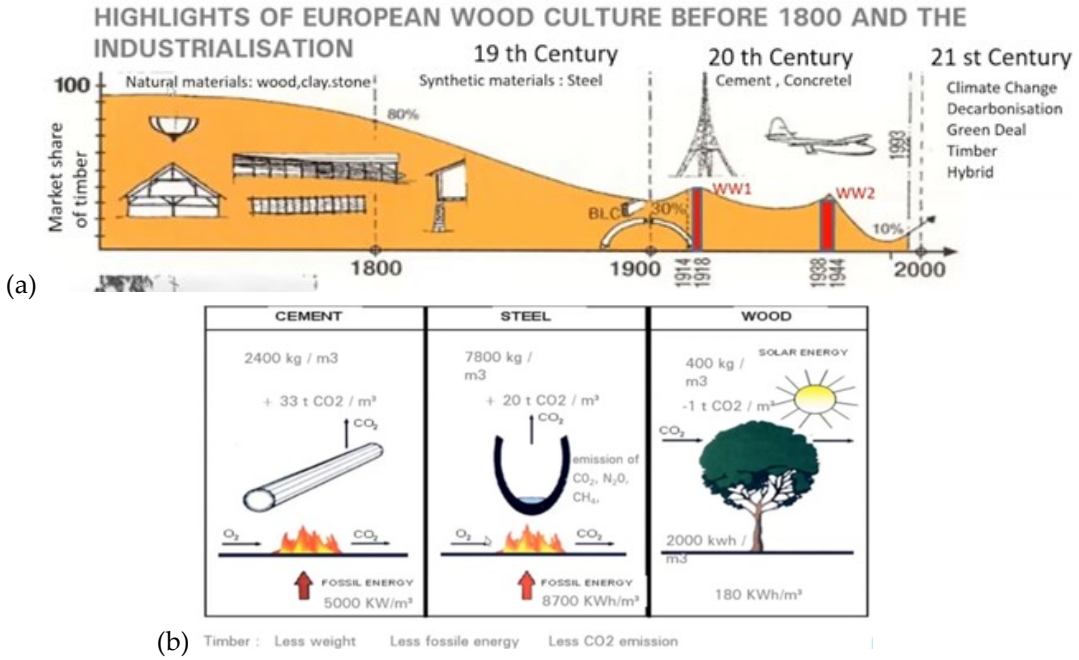

Figure 1 a) Development of timber as building material in Europe. b) Gas emissions and energy consumption of main construction materials (Images from Wolfgan Winter Richard Woschitz WCTE online talks)

Timber is the only natural, truly renewable and easily recyclable construction material. Timber due to the high strength-to-weight ratio allows to reduce the foundation costs of structures and it is advantageous for production, transportation and assembly,

allowing all major construction components to be prefabricated off-site for rapid construction [16]. The lower structural mass of timber constructions led to lower inertial forces but also less inherent resistance to overturning forces caused by lateral loads such as wind and seismic motions. For this reason the implementation of new low-damage technologies for timber structures is fundamental in order to increase the seismic performances allowing the timber buildings to be functional or recovered promptly even after strong earthquakes [17]. Moreover, timber has aesthetic qualities, with great possibilities also in architectural design, from traditional rustic to modern buildings.

Timber, unlike to other common materials, presents anisotropic behaviour due to the orientation of the wood fibers and the mechanical characteristics are different along the three perpendicular axes: parallel to the fibers, normal and tangential to the annual rings. When subjected to compression, timber behaves in a rather ductile manner, while in shear and tension the failure is brittle. The connection joints play a crucial role in bearing the design loads. In order to comply with the current seismic design approach of dissipative structures, the missing material ductility, in particular for joint connections, should be compensated with ductile joint solutions such as through plastic deformations of metallic connectors as an alternative to bolted connections [18] or adhesively bonded joints [19].

Some studies demonstrated [20] that by comparing costs of timber versus steel or concrete structures, including material and construction costs, timber solutions are less expensive than the other ones.

The fire resistance (calculated by subtracting the charred area and a thin layer of heat-affected wood from the original cross-section) showed an excellent behaviour of unprotected heavy timber, much better than other materials (e.g. steel) [21]. Recent reports on fire safety in timber structures[22][23] recommended protection of timber elements by full or partial encapsulation with non-combustible materials, in order to avoid rapid fire spread and to increase the fire resistance of the structural elements.

Moreover, the low thermal conductivity, acoustic absorption, versatility, environmental and economic benefits, are highly attractive and very competitive respect to other building materials, representing a valid alternative.

The development of timber buildings may be an important step for climate action, contributing to a sustainable development with minimum environmental impact providing that all timber buildings must be based on the requirement that the wood derives from sustainable forestry practices [24]. Various research regarding environmental aspects [25], compared timber buildings lifecycles with other mineral buildings with the same functions and demonstrated advantages for timber buildings, such as lower global warming potential and additional temporary carbon storage. The building sector plays a central role for reducing greenhouse gas emissions, accounting for about 40% of the total primary energy consumption in the European Union [26]. As a natural raw material requiring minimal energy input into the process of becoming construction material, timber shows indisputable environmental excellence with very low CO_2 emissions respect to other common materials (Figure 1b).

In order to improve structural properties as compared to traditional solid timber products, structural mass timber products were developed. The most common products are Laminated Veneer Lumber (LVL), Cross-Laminated Timber (CLT), Glued-laminated (Glulam) timber, nail-laminated timber (NLT), and dowel-laminated timber (DLT) [27].

LVL is a reconstituted dimensional timber that is commonly twice the strength of dimensional timber of the same species manufactured from rotary peeled veneers of spruce, pine or douglas fir of 3 mm thickness. Commonly the veneer grain is oriented in a single direction but cross-grained sections are also manufactured to offer tailored mechanical properties. Lengths of short veneer are jointed end-to-end with a scarf joint allowing limitless dimensional lengths.

Figure 2. Most common mass timber products.

CLT is made of timber panels with a minimum of three layers of boards cross tacked in alternate grain orientation and glued together to form a thickness in the range 50–500 mm suitable for floor, wall and roof elements of up to 13.5 m in length [28]. CLT was developed in Europe in the early 90's and it has been used extensively since then for housing and commercial building applications.

Glulam timber (GLT) is a structural engineered wood product composed by multiple pieces (at least two parallel lamination) of finger-joined dimension lumber, adhesively face-to face bonded to create the designed form. A typical GLT member ranges in depth from 114 to 2128 mm or more, in width from 80 to 365 mm, and in length of up to 40 m. A wide range of glulam grade is available [29]. GLT was first used in Europe in the early 1890s. Building systems based on structural engineered timber products have a great potential give great possibilities of applications, typically used to fabricate curved and long beams limited only by methods of transport.

Nail-laminated timber (NLT) is made by dimension lumber laminations stacked on edges and fastened together with nails, to create large-flat structural components. NLT systems were utilized as floor elements in the United States and diaphragm elements

of bridges and buildings for centuries. The maximum lengths of prefabricated NLT panels are typically 3–8 m [30]. The main problems of using NLT are its slow fabrication and after-fabrication process due to existence of nails.

Dowel-laminated timber (DLT) is composed by dimension lumber laminations fabricated without the use of metal fasteners or adhesives and connected together with hardwood dowels. It represents a more sustainable alternative to the other mass timber products. DLT applications include shear walls and floor diaphragms of buildings as alternatives to traditional materials [31]. However, very few research studies about development and characterization of DLT.

2.2 The Pres-Lam technology

Several researchers highlighted that the effects of rocking vibration can reduce seismic damage of structural systems subjected to strong motions [32]. Based on this knowledge, a rocking system based on post-tensioning of structural elements was proposed to obtain ductile moment resisting connections, achieving higher seismic performances of timber buildings.

The Pres-Lam technology is a method of mass engineered timber construction that uses post-tensioned unbonded steel tendons or bars passing through internal ducts (but can also be placed externally) to join beams to columns, or columns and walls to their foundations. It was firstly developed during the PREcast Seismic Structural Systems (PRESSS) research program at the University of California in San Diego during the 1990s under the leadership of Prof. Nigel Priestley [33], the system was conceived for application in concrete structures [6]. In 2002 the concept was extended to steel structures [34]. Later, the same concept was applied to timber constructions [7] [35] at the University of Canterbury (New Zealand), by a team lead by Professors Stefano Pampanin, Alessandro Palermo and Andy Buchanan in collaboration with Pre-Stressed Timber Limited (PTL). In post-tensioning moment-resisting frames, the

horizontal steel tendons in the beams passes through the columns, creating a moment connection. Post-tensioned timber structural walls or columns have vertical post-tensioned tendons in an internal cavity to anchor the walls to the foundation. The post-tensioning system gives to the structure the elastic re-centering capability avoiding cracking of the structural members by softening the structural response elastically through controlled rocking mechanisms. Due to the stress induced in timber members by post-tensioning, the technology finds its application within engineered wood materials, such as laminated veneer lumber (LVL), glue-laminated timber (glulam), and cross-laminated timber (CLT). The post-tensioning mass timber structural elements create stronger and more compact connections than traditional timber fastening systems. Generally, steel bars used for post-tensioning of timber members consist of either 7-wire strands or high-strength steel bars (Macalloy, Dywidag, or similar), already available from the concrete prestressing industry.

The Pres-Lam technology allows the design of timber frames with wide bay lengths (8–12m), large open spaces in floor plan (e.g. adequate for commercial use, office structures, etc.) and reduced cross-sections of structural elements.

In earthquake areas, the free rocking mechanism is coupled with supplemental energy dissipation dampers, creating a damage-avoiding structural system [36].

2.2.1 Rotation contributions of a post-tensioned timber frame

The moment - rotation capacity of a post-tensioned timber connection depends on various rotation contributions. The total rotation is immediately evaluable by the building drift (θ_T). It is composed by different rotation contributions: i) the elastic beam rotation (θ_b), ii) the elastic column rotation (θ_c), iii) the joint panel (θ_j), iv) the interface rotation (θ_{int}) and v) the gap rotation (θ_{gap}).

The beam and column rotations can be simply calculated based on the moment at the connection using common member deflection equations [37][38]. The post-tensioning induces large axial forces in the beams, due to the low shear modulus of timber, that

resulted in large elastic shear deformations in the joint panel which must be considered [39]. The joint panel contributions can be estimated based on equations proposed by Newcombe et al. [38].

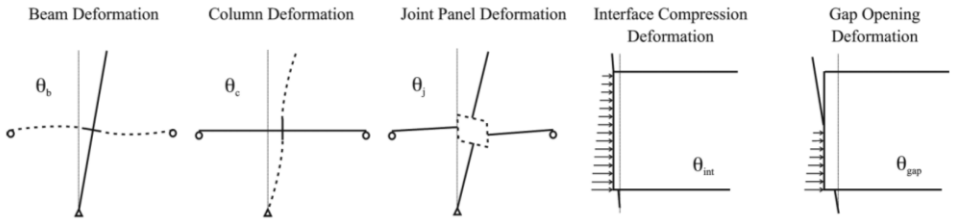

Figure 3. Rotation contributions [40].

The final two rotation contributions θ_{int} and θ_{gap} compose the contribution of rotation of the connection (θ_{con}). The gap opening between the elements occurs when the moment of the connection increases beyond the decompression moment:

$$M_{dec} = (F_{PT} + N) * \frac{Z}{A} \quad (1)$$

where F_{PT} is the post-tensioning force, N is the axial force, Z is the section modulus and A is the cross section area. Before decompression occur, an initial stiffness relating to the compression perpendicular to the grain on the column face is present. This initial stiffness is not captured by the design procedure used to calculate the post decompression behaviour and therefore must be evaluated separately. The θ_{int} contributions acts before the decompression point of the beam (i.e. before the gap opens) and the gap rotation θ_{gap} occurs after decompression. A multi-spring model was developed based on the compression stiffness of the timber [40] and used to calculate the moment rotation response of the connection before it decompresses.

After decompression a detailed procedure named "Modified Monolithic Beam Analogy" (MMBA) for the calculation of the moment capacity of a hybrid joint was developed [41]. The procedure is reported in the Zealand Code for the Design of Concrete Structures [42]. The MMBA procedure draws an analogy between the deformations and stresses in a hybrid joint and those occurring in a standard concrete connection and also applied to design of a timber hybrid connection providing few simple considerations. This procedure involves imposing a gap rotation (θ_{gap}) and the

initial estimation of a neutral axis distance *c*. Using the moment-rotation procedure, the forces in the post-tensioning tendon, compression in the timber, and the force in dissipative element are calculated (generally yielding steel device is used). Force equilibrium is then checked and if not satisfied a new value of *c* is selected.

2.2.2 Supplemental energy dissipation dampers

The implementation of seismic protection systems such as passive energy dissipation systems (e.g. seismic isolation and passive dampers) represents one of the most resilient solutions to mitigate the seismic risk of structures. Passive energy dissipation systems are considered one of the most efficient and cost-effective solutions to minimize the seismic energy dissipation demand on the structural members such as beams, columns, or walls and non-structural elements of new and existing structures. The installation of these systems allows to dissipate a large portion of earthquake input energy absorbing earthquake-induced energy and confining the eventual damage in structural replaceable anti-seismic devices, limiting cost and interruption of human occupancy and activities, with evident economic and social benefits. Passive dampers are based on the capability to dissipate energy either by conversion of kinetic energy to heat or by transfer of energy among different modes of vibration, enhancing damping, stiffness and strength. These systems include supplemental damping devices operating on frictional sliding (friction dampers), yield of metals (metallic dampers), deformation of viscoelastic solids (viscoelastic solid dampers), fluid orificing (viscoelastic or viscous fluid dampers), phase transformation in metals (shape memory alloys - SMA). Energy dissipation dampers are classified in two main categories due to a velocity dependent or a displacement dependent mechanism. In displacement dependent damping devices, the force response is primarily a function of the relative displacement between each end of the device. In velocity dependent devices the response is dependent by the relative velocity between each side of the device and the excitation frequency. Among all typologies of passive devices, non-

linear displacement dependent devices (NLDs) in which the hysteretic energy is dissipated through the yielding of steel material attracted more attention from civil engineers related to their cost-effectiveness and ease of fabrication, the symmetric and stable hysteretic behaviour, better low-cycle fatigue property, long-term reliability, and resistance to the environmental actions. Aging is of least concern because corrosion may only slightly reduce the section geometrical properties and an inspection and maintenance program should eliminate the problem. The development and testing of hysteretic steel dampers for the seismic protection of structures started in 1970s on mild steel devices of solid cross section characterized by high stability at high levels of plastic strain. A flexural metallic damper initially proposed and experimentally tested by Kelly et al. [43] (U-shaped Flexural Plate - UFP) was designed to provide energy dissipation between structural walls and adjacent floors. Thereafter, several metallic dampers such as torsional or flexural beam [44], single-axis dampers [45], U-strip [46], buckling-restrained brace (BRB) [47], were developed and tested. In the last decades the research and development of earthquake resilient performance of buildings equipped with dissipative systems achieved significant progress [48]-[59].

It has been proved that timber structures have the capacity to withstand strong earthquakes without collapsing due to the light weight of wood material, elastic deformation capacity, and ductility of connections [5]. Conventional timber buildings are usually regular and the seismic resisting structures are shear walls with ductile foundation anchorages designed against the base shear force. In these cases, the maximum seismic forces are limited by the activation of inelastic deformations that could cause serious damages at predefined locations in the structure. Among the recent research on the concept of low-damage structures, post-tensioned timber-framed buildings have been coupled with dissipative systems, generally internal expoied mild steel rods, external replaceable steel fuses (Figure 4), or other types of devices such as viscous dampers or friction dampers, introduced at joint connections or included into dissipative bracing. These devices can be designed to absorb energy

during strong earthquakes, confining the inelastic deformations in replaceable ductile fuses while the structure returns to the initial position allowing to remain operational even after severe earthquakes and increasing the seismic resilience of the building. Based on capacity design principles, the controlled rocking mechanisms of elastic post-tensioning provide self-centering action to eliminate residual drifts, while additional dissipative dampers, provide additional strength and damping and reducing lateral displacements of multi-storey buildings. This kind of connection is also known as hybrid connection. Internal or external mild steel bars, UFPs and steel angles devices represent the most widespread solutions used to realize various hybrid connections for post-tensioned timber frame buildings. Successful experimental and real applications widely demonstrated the effectiveness and reliability of these hysteretic steel dampers installed in various post-tensioned timber systems, such as connecting element between walls and frames, in coupled walls and at beam–column and column–foundation connections of frames.

During the rocking motion due to earthquake or other horizontal loads, a gap opening is produced at the beam-column (as shown in Figure 4), column- foundation or wall-foundation connection, activating the elongation of the unbounded PT ($F_{PT}+\Delta F_{PT}$) tendon or bar and the yielding of the hysteretic dissipation devices (F_y). The combination of the moment capacity due to post- tensioning M_{PT} (bilinear elastic response) and to yielding of steel devices M_s (hysteretic response), provide the total moment capacity $M_t = M_{PT} + M_s$ with the flag-shaped hysteretic behaviour, typical of hybrid systems. In case of failure of post-tensioning tendon due to an unexpected event, dissipative dampers can still provide capacity to the structural system. Without the addition of the dissipative devices, it is worth noting that the nonlinearity does not come from nonlinear material behaviour but from a sudden change in neutral axis when gap opening occurs (geometrical nonlinear behaviour without material damage).

The ratio between the elastic re-centering moment and the total moment capacity ($\beta=M_{PT}/M_t$) is the key parameter of the post-tensioned connection representative of the amount of energy dissipation provided to the system (Figure 5). It ranges from 1 to 0 for full free rocking condition (without dissipation) to full elasto-plastic (maximum hysteretic dissipation and no recentering properties) respectively and is the main aspect which affect the overall damping and non-linear stiffness of the dissipative post-tensioned timber frame.

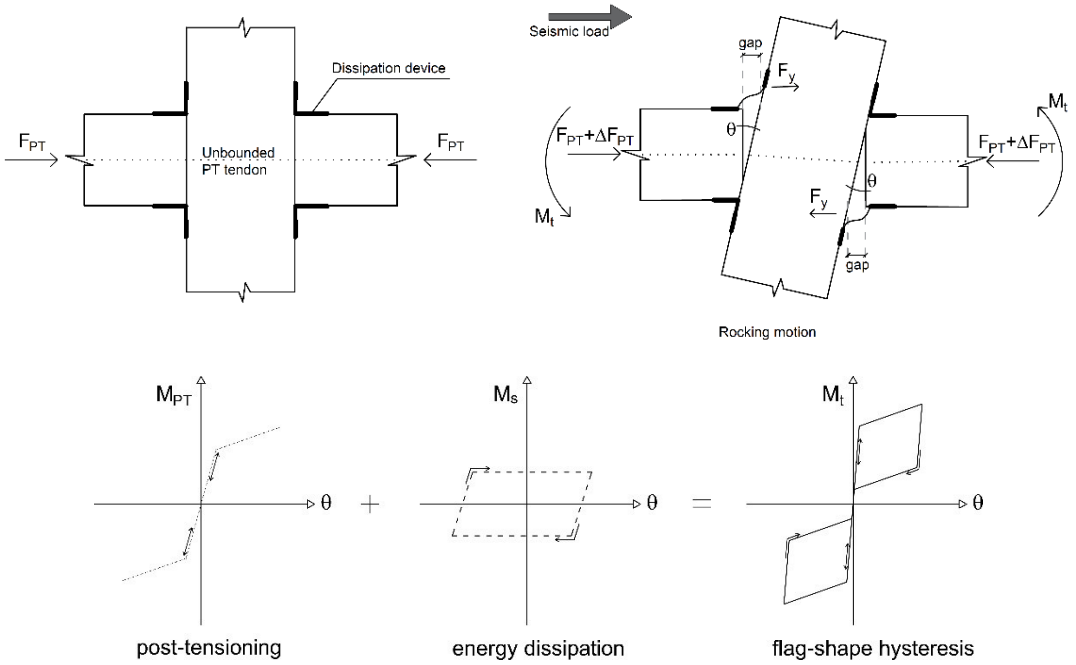

Figure 4. Example of post-tensioned beam-column connection with external hysteretic dissipative devices

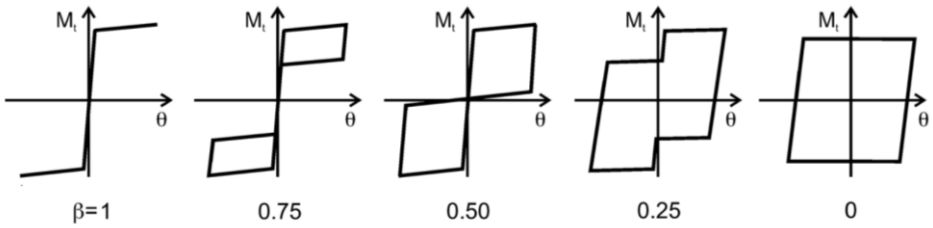

Figure 5. Moment response of a post-tensioned timber connection at various β ratio levels [12].

2.3 Experimental studies on post-tensioned timber systems

The main experimental tests performed on post-tensioned timber frame subassemblies, wall subassemblies and building tests are described. The first research campaign on the timber hybrid jointed ductile connections started in New Zealand in 2005. During the experimental campaign the first examples of post-tensioned structures using LVL timber elements were tested. Quasi-static tests on LVL post-tensioned beam-column subassembly at different levels of post-tensioning and both with and without internal mild steel bars were performed by Palermo et al. [7], obtaining a stable flag-shape response with full re-centering capability (Figure 6a).

The results proved the high seismic performance of the jointed ductile connection without and with dissipation, capable to sustain large drift demands, (over 2%) without significant damage to the structural frame elements. As expected, a very stable flag-shaped hysteretic behaviour was obtained for the hybrid solutions with fully re-centering capacity and adequate energy dissipation capacity. The first experimental investigation of Pres-Lam system with external dissipative devices was performed on a 2/3rd scale wall foundation with two fused type dissipative reinforcing with satisfactory results [60]. Then, a 2/3rd scale beam-column joint with external reinforcing was tested by Smith [61] providing excellent results in terms of both recentering and energy dissipation.

Following the system's success, various international research efforts were developed at ETH Zurich, the University of Basilicata, Washington State University and several other research institutions. In 2017 the NHERI Tallwood project was started with funding from the U.S. National Science Foundation focused on further validation of Pres-Lam in North America.

Iqbal et al. (2016) tested full-scale LVL beam–column subassemblies with and without fuse elastoplastic dissipaters [62] (Figure 6b). Steel armoring plates at the interface and long screws reinforcement were embedded into the column minimizing the joint shear panel deformations. The experimental results of the specimens showed full

recentering and significant energy damping when dissipative devices are added, with high levels of ductility and without significant residual deformations and structural damages.

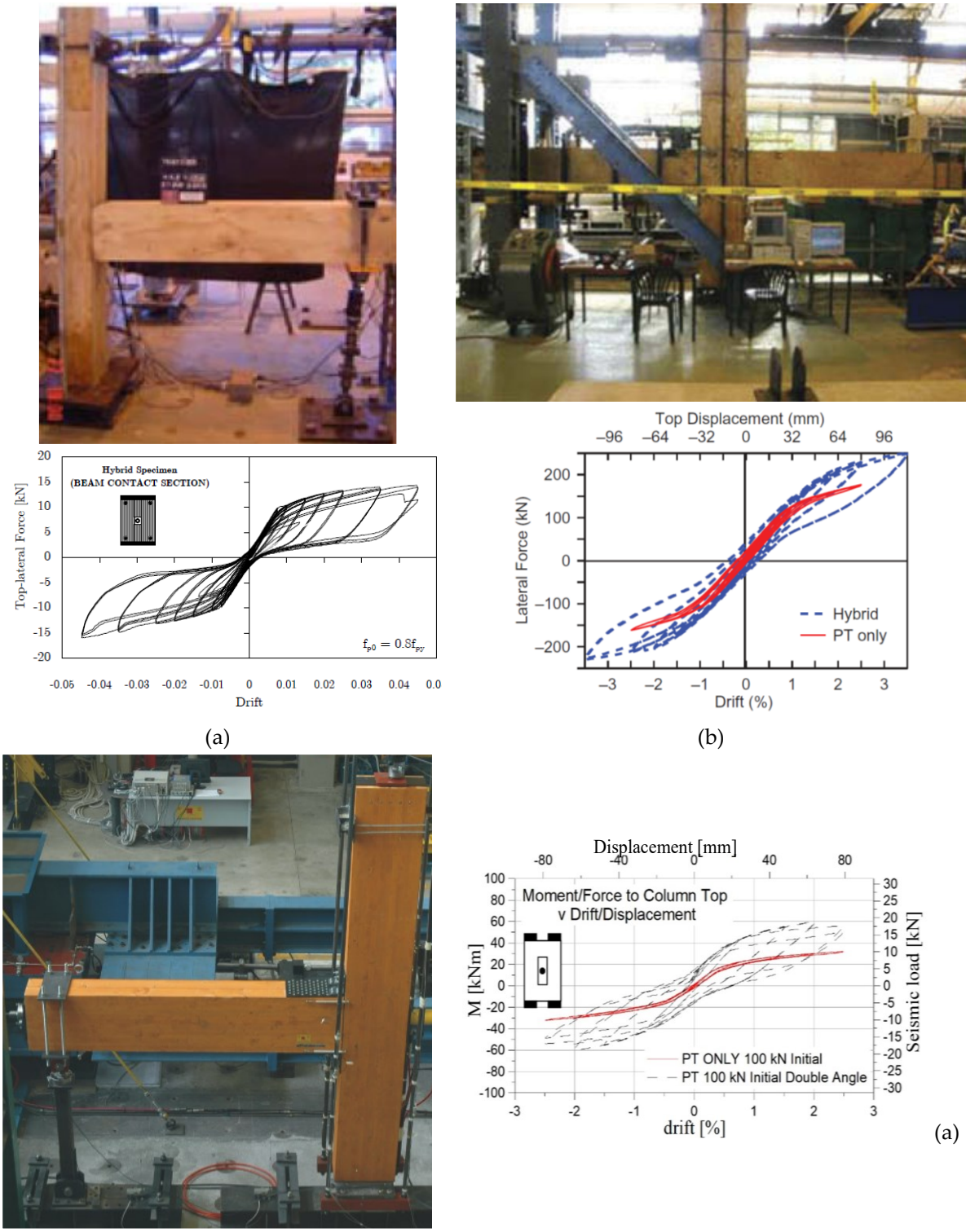

Figure 6. Quasi-static cyclic tests on: (a) LVL hybrid post-tensioned beam-column subassembly (Palermo et al. 2005) [7]; (b) beam-column subassembly (Iqbal et al. 2016) [62]; (c) post-tensioned beam-column joint with and without dissipative rocking tested at UNIBAS (Smith et al. 2014) [12].

A Pres-Lam project including collaborative experimental campaigns began between the University of Basilicata (UNIBAS), and the University of Canterbury. In the first stage, the post-tensioned timber concept was applied to a full-scale glulam beam-column joint subassembly with and without additional damping devices made of angular steel plates [12] (Figure 6c). It was designed, fabricated and tested in the structural laboratory of UNIBAS. A new shear key connection hidden within the beam and the column made of an embedded steel tube and not interfering with the rocking motion, was proposed. The column faces were reinforced with long screws to increase the strength of the timber perpendicular to the grain. The results showed excellent results increasing the moment capacity and the damping of the system (Figure 6c), demonstrating that the Pres-Lam technology can be applied to glulam timber elements with the same benefits of LVL members.

Quasi-static tests on hybrid post-tensioned glulam beam-column connections with energy dissipation devices (special steel cap or pair of steel angles), were performed by Li et al. (2018) [63], disc springs were also installed at the anchor of the steel strand to reduce the PT loss. The results showed that when dissipation was introduced on the specimens, the moment-resisting capacity and rotational stiffness of the specimen increased, but larger residual deformations were observed. Moreover, the disc springs failed to prevent pretension force loss under large deformation levels. Polocoșer et al. (2018) [64] tested a three-dimensional beam-to-column connection frictional dampers, then the connection was mounted in a three-level prototype frame and tested on a shake table showing good seismic performances.

Several quasi-static tests were performed on wall subassemblies. Sarti et al. (2016) [65] performed quasi static tests on post-tensioned LVL timber walls without (Figure 7a) and with internal mild steel bars and external fuse devices. Shear keys were installed at the wall–foundation. The specimens showed complete recentering without damages, observing that the walls exerted uplift forces on the floor plate. Then, in order to reduce uplift forces the post-tensioned wall was disconnected from the beams

and instead attached to the columns using a UFP. Iqbal et al. investigated both single and coupled post-tensioned LVL rocking walls connected by U-shaped flexural plates (UFPs) [66] (Figure 7b). The tests showed typical flag-shape response with good seismic performance without damages to the main structural elements. A stable behaviour of UFPs was recorded at different level tested coupled post-tensioned LVL. In 2017, Iqbal et al. [9] tested also walls connected by plywood shear panels (Figure 7c), providing dissipation by the nails connecting the shear plywood to the walls. A stiffness reduction was observed due to the nails yielding, however the system showed a stable performance without further degradation during tests.

Ho et al. (2016) [8] tested post-tensioned CLT walls without and with traditional shear panels (Figure 7d). The results showed no significant damage on the CLT panel and the configuration with traditional shear walls introduced additional dissipation to the system due to the yielding of the connecting nails.

Six specimens of CLT rocking wall tests in different design configurations, also including UFPs, were performed by Ganey et al. (2017) [67] as part of a large multiyear research project, the Natural Hazards Engineering Research Infrastructure (NHERI) Tallwood project, aimed at developing a resilience-based seismic design methodology for tall wood buildings. All specimens were pushed to very large lateral drifts in order to investigate on different damage states. The results showed that the walls were able to recenter with only limited damage under 5% lateral drift. The test results were used to validate the numerical modeling of CLT rocking walls and formed the basis for subsequent tests in the NHERI Tallwood project. Recently, Chen et al. (2020) [68] performed tests on post-tensioned CLT shear walls with energy dissipators in different configurations, with modified "plug and play" axial dissipators and with UFPs (Figure 7e). The results confirmed the high seismic performances of the system showing an increase of stiffness, strength and energy dissipation when fuses and UFPs are added.

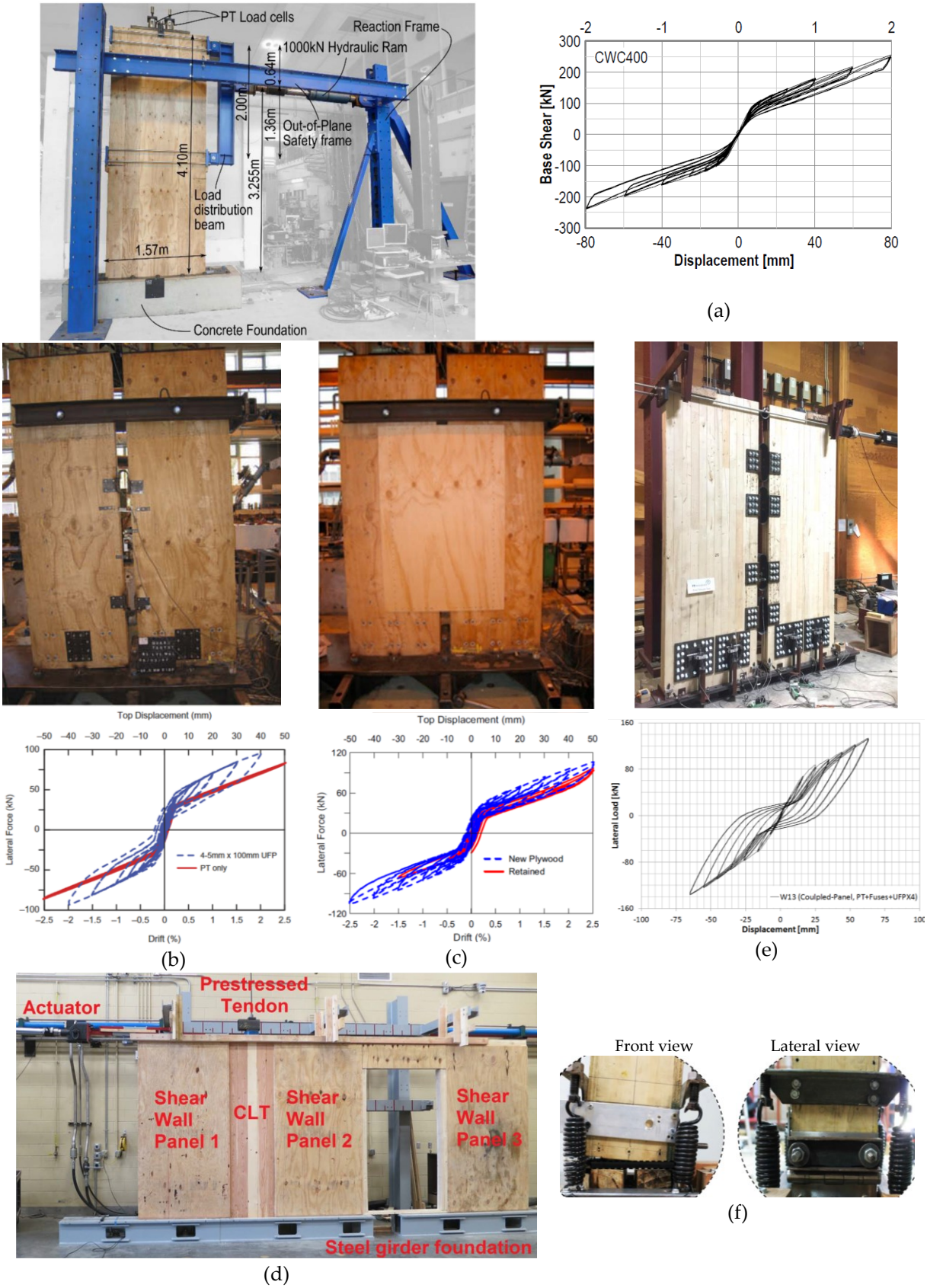

Figure 7. Experimental tests on: (a) LVL post-tensioned wall with internal mild steel bars (Sarti et al. 2016) [65]; (b) LVL post-tensioned walls with UFPs (Iqbal et al. 2015) [66]; (c) LVL plywood post-tensioned walls (Iqbal et al. 2017) [9]; (d)CLT walls with traditional shear panels (Ho et al. 2016) [8]; (e) CLT post-tensioned timber walls with modified plug and play dampers and UFPs (Chen et al. 2020) [68]; (f) self-centering semi-rigid connection (Padilla-Reyes et al. 2018)[70].

Hashemi et al. (2020) [69] compared mass timber wall systems with different types of seismic fuses, from conventional pinching connectors to self-centring friction connections. An alternative semi-rigid self-centering connection for the seismic protection of timber structures has been proposed by Padilla-Reyes et al. (2018) [70].The connection is composed by three fundamental components: the pivot system (made up of two stainless steel hinges), the post-tensioned elastic system (springs), and the friction dissipation system (Figure 7f).

In order to validate the effectiveness of the post-tensioned timber concept, it may be applied to building specimens. A few seismic tests on post-tensioned timber building specimens have been performed in New Zealand, United States and Italy [71].

Newcombe et al. (2010) [10] tested a 2/3-scale two-storey LVL building specimen made of PT frames in one direction and rocking walls equipped with UFP devices (Figure 8a) in the other by applying quasi-static loads. The experimental results showed fully re-centering and no significant damage up to 2% of drift.

Pei et al. (2019) [11] conducted a full-scale shake table test of a two-storey mass timber building with post-tensioned CLT rocking walls at the University of California San Diego (Figure 8b). The results showed the resilience of CLT rocking-wall system with a heavy-timber gravity system up to the MCE and validated the low-damage characteristics of different key connection details. Moreover, it was observed that the natural period of these buildings is relatively long for the given building height and post-tensioning losses of about 8% were observed for large earthquakes. Stiffness and deformation are likely to control the design for taller building implementations. In both cases, the systems were essentially damage free up to 2% of drift, while drift values higher than 3% caused fractures of the rocking wall corners [11] or cracking in columns and slabs due to high stress concentration around dissipative anchorages [71].

Bidimensional post-tensioned timber frame without dissipative dampers was tested in Switzerland at Eidgenössische Technische Hochschule (ETH) Zürich by Wanninger and Frangi (2016) [72]. The system, differently from New Zealand system, used

hardwood reinforcement (ash glulam) in the beam–column joints without steel fasteners. (Figure 8c) The influence of the post-tensioning force on the lateral stiffness of the frame was evaluated. The system showed good experimental results, with recentering and no structural damages.

Xiong et al. (2016) performed monotonic tests and cyclic tests on full-scale, post-tensioned timber (Figure 8d) specimens and braced specimens in various configurations (X-brace, K-brace, knee-brace) and a frame filled with light wood shear walls [73]. The results showed that the frame with a knee-brace system showed higher elastic stiffness than the simple frame system and provided higher ductility than the frames with the X-brace and the K-brace systems. The frame filled with the light wood shear walls system performed well in terms of elastic stiffness and ductility.

Pino et al. (2010) [74] tested a 1/4-scale, three and five-storey (Figure 8e) post-tensioned timber buildings without dissipation, estimating equivalent viscous damping ranging from 2% for low drifts to 8% for the larger ones. The tests proved the high capacity of the system at large lateral deformations with minimal damage.

Di Cesare et al. (2017) in a second stage of the Pres-Lam project at the structural laboratory of UNIBAS tested on the shaking table a 2/3rd, three-dimensional post-tensioned glulam timber frame without dissipation and with dissipative rocking [13] (Figure 8f) and dissipative bracing systems. The dissipative-rocking impacts on the seismic response by increasing the equivalent viscous damping and significantly reducing maximum drift. No damage was observed on the main structural elements up to drift values higher than the design ones.

In recent years, thanks to the increased knowledge and technology of timber engineering several experimental and numerical research studies on alternative seismic resistant timber multistorey buildings, are developing. An integrated low-damage timber-concrete building system was designed and pre-assembled in Italy and tested in Lisbona within the SERA project by Pampanin et al. (2020) [75]. It was

composed by timber-concrete seismic frames in one direction and post-tensioned dissipative rocking CLT walls in the other direction (Figure 8g).

Figure 8. Experimental testing on: (a) LVL frame with post-tensioning and post-tensioned rocking walls with UFPs (Newcombe et al. 2010) [10]; (b) mass timber building with post-tensioned CLT rocking walls (Pei et al. 2016) [11]; (c) bidimensional post tensioned frame (Wanninger and Frangi 2016) [72]; (d) post-tensioned portal frame (Xiong et al. 2016) [73]; (e) post-tensioned LVL timber framed building (Pino et al. 2010) [74]; (f) post-tensioned glulam timber framed building with dissipative rocking Pres-lam project UNIBAS (Di Cesare et al. 2017) [13]; (g) timber-concrete test building – SERA project (Pamapanin et al. 2020) [75].

The resilient seismic performance of post-tensioned timber buildings may be improved by coupling post-tensioned frame with dissipative bracing systems allowing a more flexible architectural configuration respect to heavy-timber gravity-framing

systems combined with cross-laminated timber (CLT) walls or post-tensioned rocking walls.

The seismic behaviour of moment-resisting timber frames with concentric or eccentric braced frames with fluid viscous dampers (FVD) in various configurations has been numerically investigated by Faggiano et al. (2020) [76]. However, further experimental and numerical studies on the seismic performance of dissipative braces for post-tensioned timber structures are required. The investigation of the experimental and numerical post-tensioned frame with dissipative bracing systems and the comparison with previous testing configurations is the object of this thesis.

2.4 Overview of existing post-tensioned timber buildings constructions

The first implementation of timber rocking systems was in an actual building in Nelson, NZ in 2011. The NMIT Arts and Media Building is a 3-storey LVL structure using PT rods and UFPs [77]. The structure was evaluated to be very cost competitive and represents the first commercial use of the post-tensioned dissipative timber system highlighting a fundamental change in timber design.

The Carterton Events Centre is an auditorium in Carterton (NZ), with 11 rocking walls of 6.7 m tall. Energy dissipation is provided by embedded mild steel rods. The Auditorium features use post-tensioned LVL shear walls for the lateral load resisting system and LVL roof trusses and a Library has been sympathetically strengthened with plywood sheathed shear walls [78]. The building was recognized of the NZ Timber Design Awards 2012 (Engineering Excellence Winner).

The College of Creative Arts building at Massey University in Wellington, New Zealand was built in 2014 using the post-tensioning at the beam-column joints and also at the column-foundation joints providing not only the connections and lateral load resisting system but also to resist gravity loading.

The Young Hunter House is the symbol of the rebuild after Christchurch earthquake of 2010. It is a three storey post-tensioned frame supporting a timber-concrete-composite floor with wide open spaces for commercial use.

The Trimble Navigation Offices [79] is a two-storey LVL building in Christchurch (New Zealand). The building is the first post-tensioned timber building which combine the use of LVL frames to resist lateral loads in one direction and LVL walls to resist lateral loads in the other direction. Post-tensioning and steel dissipaters were used at the beam column joints with a steel armor plates providing an anchoring point for the dissipation devices and reducing the stress in the columns. High strength connections were provided using of timber rivets and screws which fits perfectly into the building architecture. The new Trimble offices structure is currently the largest post-tensioned timber building in the world. Moreover, a monitoring system was installed on the structure.

ETH House of Natural Resources is a monitored office building for the laboratory of hydraulics, hydrology and glaciology of ETH Zurich (Switzerland). The structural system includes a post-tensioned glulam timber frames at the two upper stories, a composite beech laminated veneer lumber–concrete floor and a biaxial timber slab made of cross-laminated timber and beech laminated veneer lumber [80].

The fire laboratory at Tsukuba Science City, (Japan) was designed in collaboration between Tsukuba Research Institute of Sumitomo Forestry in Japan and PTL Structural Timber Consultants in Christchurch (NZ). The structure with an area of 390 mq combines the use of post-tensioned steel cables with large LVL timber members with eight walls providing lateral and vertical support to the structure. The technology allows for the large open spaces needed for the fire testing [81].

The Kaikoura Civic Centre in New Zealand, a three storey building architecturally designed to be a giant cray pot, was the first Pres-Lam building entirely made of timber and with post-tensioned CLT walls, which represent the lateral resisting system of the post-tensioned timber structure. The Kaikoura Civic Centre, opened in 2016, is a

tourist attraction with a museum at the first level, a library at the second level and council offices at the third level [81].

(a) Internal and external view of NMIT Arts and Media Building, Nelson, NZ [77].

(b) Construction phase and external view of auditorium in Carterton [78]

(c) internal and external view of College of Creative Arts Massey University, Wellington, New Zealand [81]

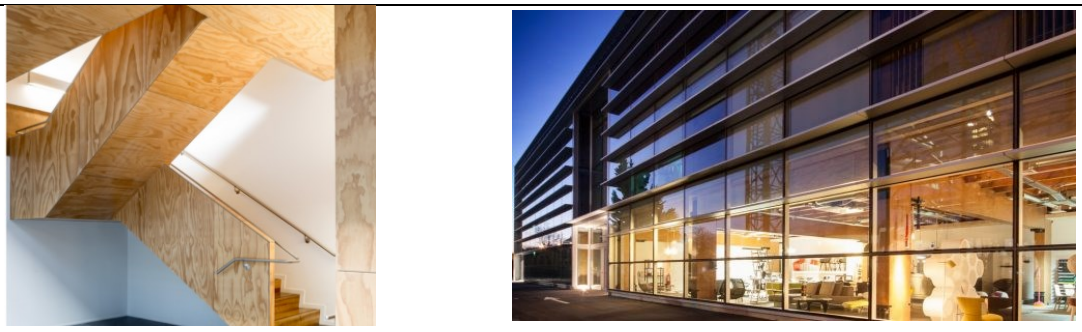

(d) Internal detail and external view of Young Hunter House, Christchurch (NZ) [81]


(e) construction and external view of Trimble navigation Office [79]


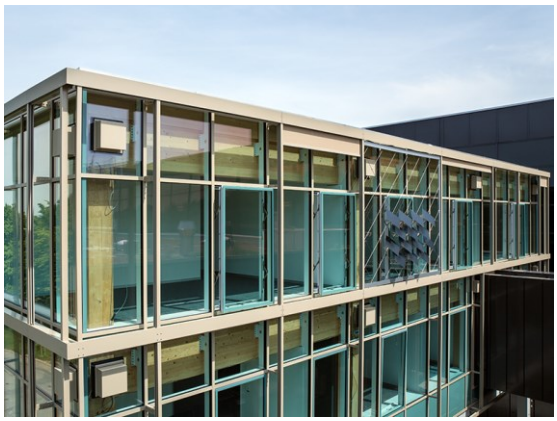

(f) beam-column detail and external view ETH House of Natural Resources Zurich [80]



(g) construction detail, internal and external view of the Tsukuba Science City Fire Laboratory, Japan Sumitomo [81]

(h) Construction and external view of Kaikoura Civic Centre in New Zealand [81]

Figure 9. Main post-tensioned timber construction in the world.

3 Design of post-tensioned timber frame with dissipative systems

With increasing interest in multistorey timber buildings worldwide, several research studies were devoted to the development of seismic design procedures. The seismic design of current codes, including Italian code (NTC 2018) [1] and European code (EC8) [2] follows the Force Based Design (FBD) approach. The essence of FBD is that structures may be designed to not exceed a specified limit state under a given seismic intensity. The procedure is based on 5% damped acceleration response spectra reduced by a behaviour factors correlated with potential ductility of the structure and a final displacement check is performed. Priestley [4] highlighted a fundamental problem with force-based design related to the selection of appropriate member stiffness assumptions (especially for concrete and masonry structures), made about member sizes before the design seismic forces are determined. Priestley demonstrated that stiffness assumption adopted in FBD for reinforced concrete structures can led to significant errors in period and displacement evaluations. Displacement-based design (DBD) procedure was firstly suggested by Priestley et al. [82] as alternative to full nonlinear time history analyses for concrete structures. The DBD method is based on the design displacement spectra and characterize the structure through an equivalent secant stiffness at maximum displacement and with appropriate level of equivalent viscous damping associated with the hysteretic energy dissipated during the inelastic response.

The design philosophy is based on determination of the optimum structural strength to achieve a given performance limit state, associated with a defined level of displacement (and related damage), under a specified level of seismic intensity. The fundamental concept of DBD consisted in the approximation of a multi-degree of freedom (MDOF) structure with a single degree of freedom (SDOF) system with effective mass (m_e), equivalent secant stiffness (K_e) and period (T_e), and equivalent

viscous damping (ξ_{eq}) at target design displacement (Δ_d) or drift (θ_d). The maximum displacement and base shear (F_u) of the SDOF system is approximately equal to the original MDOF structural response. The equivalent elastic properties of the SDOF system allowed the design of the MDOF structure through an elastic displacement response spectrum, reduced by ξ_{eq}. It allows to consider the energy dissipation due to the non-linear behaviour by reducing the linear response spectrum. In this way it is possible to solve a simple linear system instead of a non-linear system with reduced time and resource demanding.

Several design procedures for the seismic design and retrofitting of reinforced concrete (RC) frames [83], of moment resisting RC frames with viscous dampers [84] and various configurations of dissipative bracing systems incorporating replaceable metallic dampers have been developed for the seismic retrofitting of existing buildings and for the new buildings construction with different constitutive materials [58],[71],[85] -[93]. Traditional steel braces equipped with hysteretic dissipative devices were successfully used to reduce the seismic demand of existing reinforced concrete framed structures in [94]. Steel frames equipped with buckling-restrained axial dampers (BRAD) and externally connected to the façades of an existing building were considered in [95] in order to improve energy efficiency and earthquake-resistant performance. Crescent shaped braces (CSBs) were recently used for seismic retrofitting as hospital in order to connect the steel moment-resisting frames with two external reinforced-concrete cores [96],[97]. CSBs are characterized by a geometrical configuration which is “ad hoc” defined in order to provide the structure with prescribed multiple seismic performances, within the performance based seismic design framework. U-shaped hysteretic dampers included in a damping box located at the middle of a diagonal brace were proposed [98] to improve the performance of moment-resisting frames. The experimental behaviour of a self-centering timber brace that employs the resilient slip friction joint (RSFJ) for energy dissipation was investigated [99]. Steel frame braced with tension-only pseudo-elastic nickel-titanium

(NiTi) shape memory alloy (SMA) wires was developed in [100] for seismic retrofit applications.

Recently, the application of the DBD method has been extended toward the design of timber buildings [5] [101][102], such as CLT shear walls [103], coupled timber walls [104], and post-tensioned timber frames [105]. However, DBD applications to timber-framed buildings remain largely unexplored, and new techniques are still being investigated aiming to prevent or minimize damage induced by earthquakes to the frame elements and connections.

In this chapter the fundamentals of displacement-based seismic design are described along with the system parameters required for its application and optimized for post-tensioned timber framed buildings with dissipative systems, characterized by a flag-shaped hysteretic response. Moreover, the application of the proposed procedure for designing the prototype post-tensioned timber building in different configurations considered for shaking table testing is presented.

3.1 Proposed displacement based design procedure

The proposed method is based on DBD procedure, starting from a target displacement Δ_d (or drift) and assuming typical flag-shape parameters related to the reliable amount of dissipation of the dissipative frame system, under a reference level of seismic intensity. Starting from these parameters, the proposed method allows to evaluate the post-tensioning (PT) forces and to dimension the dissipative devices. In the step-by-step procedure, the equivalent SDOF systems of the bare post-tensioned frame (F) and of the hysteretic metallic yielding systems (dissipative devices at the beam-column and column-foundation connections or dissipative bracing systems) were considered as a bilinear and hysteretic system working in parallel, providing the equivalent flag-shape response of the dissipative rocking frame (DF) or of the braced post-tensioned frame (BF). The equivalent elastic properties of the SDOF system allowed the design of the

MDOF structure through an elastic displacement response spectrum, reduced by ξ_{eq}. Based on the flag-shape parameters, the equivalent contributions of the bare structure and of the dissipative systems can be evaluated and finally, the design assumption will be verified and the design completed. Figure 10 summarizes the proposed design procedure valid for both DF and BF systems.

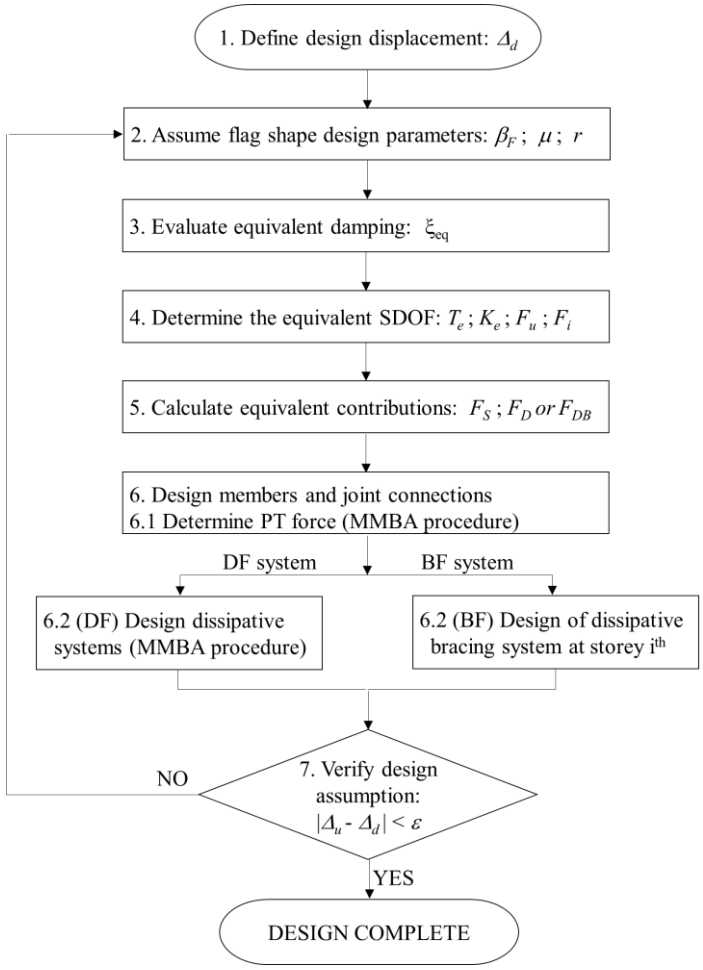

Figure 10. Design procedure for post-tensioned timber frames with dissipative rocking (DF) and dissipative bracing (BF) systems.

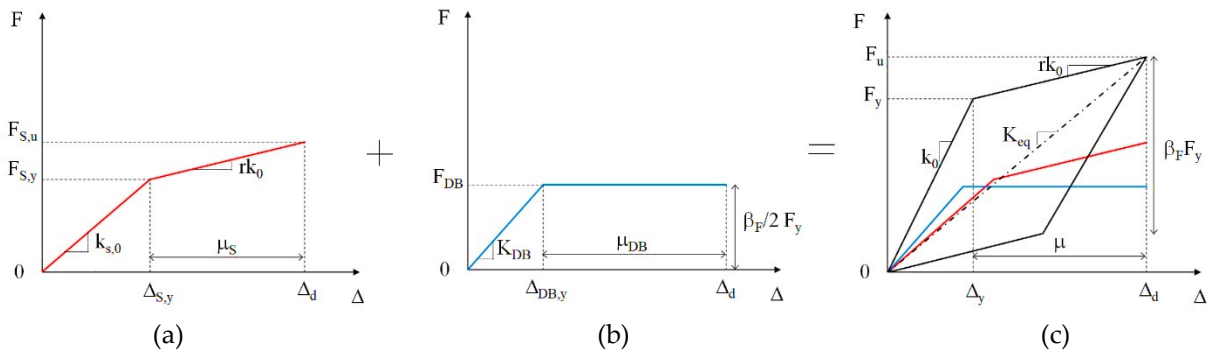

Figure 11. Equivalent SDOF system of: (a) bilinear elastic model of the bare post-tensioned timber structure; (b) hysteretic model of dissipative bracing system (DB); (c) Flag-shape of the braced post-tensioned frame (BF).

Step 1. Define design drift. The procedure starts defining a target displacement or drift at the design limit state. The range of target drift for post-tensioned timber buildings varies between θ_d = 1.5 ÷ 2.5% based on nonstructural elements and their connections and anchorages Usually, design values are suggested within the design code or governed by allowable material strain limits.

Step 2. Assume flag shape design parameters. The force-displacement of the DF or the BF system (Figure 11c) consisted in the flag-shaped hysteretic behaviour, which combined the equivalent bare post-tensioned frame (Figure 11a) with the equivalent dissipative devices (D) of the dissipative rocking system or of the dissipative bracing (DB) system (Figure 11b). The design parameters of the flag-shape of the equivalent SDOF system are the post-yield stiffness ratio r, the displacement ductility μ, and the amount of dissipation of the global system β_F (flag loop parameter). Suggested values are $1.5< \mu \leq 3$; $0.1< r \leq 0.3$ and $0<\beta_F \leq 0.6$ for the DF and $0.6<\beta_F \leq 1$ for the BF.

Step 3. Evaluate equivalent damping. When supplemental hysteretic dissipation devices are added to the structural system, the equivalent damping ξ_{eq} of the substitute SDOF structure is modelled as sum of energy dissipation resulting from viscous damping $\xi_{eq,v}$ and inelastic hysteresis $\xi_{eq,h,v}$. In order to account for the random nature of seismic inputs values of hysteretic damping should be corrected by a reduction factor k [106]. For post-tensioned timber structures suggested range of values is k = 0.6 ÷ 1 [107]. The total equivalent damping is calculated as follows (Equation 1):

$$\xi_{eq} = \xi_{eq,v} + k \cdot \xi_{eq,h,v} \quad (1)$$

Although the design drift θ_d is mainly related to the structural system whereby typical values can be easily considered the estimation of the equivalent damping ξ_{eq} depends strongly on the energy dissipation mechanism. A value of elastic viscous damping $\xi_{eq,v}$ = 2 ÷ 5% was considered acceptable [107] for concrete structures. Based on previous studies ([108]) suggested value of elastic damping for timber buildings is $\xi_{eq,v}$=2%.

The hysteretic damping $\xi_{eq,h,v}$ includes the effects of the dissipation devices on the base of their force-displacement relationship. The equivalent viscous damping of the flag

model $\xi_{eq,h,v}$ can be estimated through the following Equation 2, proposed by Priestley and Grant for flag-shaped systems [109]:

$$\xi_{eq,h,v} = \frac{\beta_F(\mu - 1)}{\mu\pi[1 + r(\mu - 1)]} \quad (2)$$

where μ is the displacement ductility, r is the post-yield stiffness ratio, and β_F is the re-centering ratio of the global system, which controls the global amount of dissipation (Figure 11c).

Step 4. Determine the equivalent SDOF. The equivalent parameters of the SDOF system, in terms of design displacement Δ_d and equivalent mass me at the effective height H_e, are determined according to the fundamental mode, assuming a linear displacement profile of the i^{th}-storey of the structure Δ_i, as Equation 3, where m_i and H_i are the storey masses and storey height [106].

$$\Delta_d = \frac{\sum_{i=1}^{n}(m_i\Delta_i^2)}{\sum_{i=1}^{n}(m_i\Delta_i)};\ m_e = \frac{\sum_{i=1}^{n}(m_i\Delta_i)}{\Delta_d};\ H_e = \frac{\sum_{i=1}^{n}(m_i\Delta_i H_i)}{\sum_{i=1}^{n}(m_i\Delta_i)} \quad (3)$$

From the target displacement Δ_d, the equivalent period T_e and stiffness K_e of the SDOF system shall be calculated by direct transformation of the design acceleration response spectrum $S_d(T_e)$, as defined by Equations (4) [2]. The design displacement spectrum is reduced to account for the ductility/damping of the system using the damping correction factor $\eta = \sqrt{10/(5 + \xi_{eq})}$ [1].

$$S_D(T_e) = S_d(T_e) \cdot \left(\frac{T_e}{2\pi}\right)^2; \qquad K_e = m_e \cdot \left(\frac{2\pi}{T_e}\right)^2 \quad (4)$$

The base shear F_u or ultimate force capacity can be calculated at the target displacement, and then the yield force F_y of substitute structure can be determined as a function of the parameters μ and r (Equations 5).

$$F_u = K_e \cdot \Delta_d; \qquad F_y = \frac{F_u}{1 + r(\mu - 1)} \quad (5)$$

The base shear F_u is distributed in proportion to the floor mass and displacement as:

$$F_i = F_u \frac{m_i \Delta_i}{\sum_{i=1}^{n}(m_i \Delta_i)} \tag{6}$$

Step 5. Calculate equivalent contributions. The post-tensioning and the dissipative bracing system can be determined on the base of the flag-shape model (Figure 11c). The hysteretic contribution of the dissipative angles (D) or the dissipative bracing system (DB) is idealized as an elasto-plastic system (Figure 11b). Assuming the design ductility μ_{DB} of the equivalent SDOF of the dissipative bracing system, the yield force F_{DB}, the yield displacement $\Delta_{DB,y}$ and the elastic stiffness k_{DB} are defined as Equations (7). The same Equation 7 is valid for the dissipative devices at the joint connections, with yield force, yield displacement and elastic stiffness named as F_D, $\Delta_{D,y}$ and k_D, respectively.

$$F_{DB} = \frac{\beta_F}{2} \cdot F_y; \qquad \Delta_{DB,y} = \frac{\Delta_d}{\mu_{DB}}; \qquad k_{DB} = \frac{F_{DB}}{\Delta_{DB,y}} \tag{7}$$

Then, the ultimate force $F_{S,u}$ and the yielding force $F_{S,y}$ and the yield displacement $\Delta_{S,y}$ on the bare post-tensioned structure can be calculated as Equations (8), where k_S is the initial stiffness of the equivalent bare structure, evaluated as $k_0 = k_S + k_{DB}$ (Figure 11a) in case of BF or $k_0 = k_S + k_D$ in case of DF.

$$F_{S,u} = F_u - F_{DB}; \qquad F_{S,y} = k_S \cdot \Delta_{S,y}; \qquad \Delta_{y,S} = \frac{F_{S,u} - r k_0 \Delta_d}{k_{S,0} - r k_0} \tag{8}$$

Step 6. Design members.

6.1. Determine PT force (MMBA procedure). The seismic design of post-tensioning force is performed through the Modified Monolithic Beam Analogy (MMBA) procedure [110]. This procedure is reported in detail in previous works [111]. The beam-column connections are designed considering the moment demand related to the ultimate force $F_{S,u}$ and ductility μ_S on the bare post-tensioned frame.

6.2 (DF). Design dissipative devices at joint connections. Key to the hybrid connection defined for a post-tensioned timber system is the ratio β [112] between the moment resistance provided by the post-tensioning (M_{PT}) and the total moment resistance of

the frame ($M_{dis} = M_{PT} + M_s$, where M_s is the moment resistance provided to the system by the dissipative devices). This local factor β could be related to the re-centering ratio of the global system β_F, defined in step 2, as reported in the following equation:

$$\beta = \frac{M_{PT}}{M_{dis}} = \frac{M_{PT}}{(M_{PT} + M_{s)}} = 1 - \frac{\beta_F}{2} \quad (9)$$

For the dissipative elements, the sum of the ultimate force of the structure and of the yielding force ($F_{S,u} + F_D$) is distributed to each floor and the resultant moment demand is then used to define the characteristics of the hysteretic devices, in terms of stiffness, yielding force and ductility. Different hysteretic dampers could be considered by varying the base material and/or the way to dissipate energy.

6.2 (BF). Design of dissipative bracing system at storey i^{th}. The characteristics of the equivalent SDOF dissipating system (F_{DB}, $\Delta_{DB,y}$, k_{DB}), determined in Step 5, are distributed along the height of the building following the design procedure proposed by Di Cesare et al. [85]. The stiffness $k_{DB,i}$ of the equivalent bracing of the storey i^{th} is determined hypothesizing that the ratio between the stiffness at the i^{th} storey of the relative bracing $k_{DB,i}$ and that of the bare structure $k_{S,i}$ is proportional to the ratio r_k between the elastic stiffness of the bracing systems k_{DB} and the elastic stiffness of the the equivalent bare structure $k_{S,0}$, as shown by (Equations 10). The stiffness of the storey i^{th} of the bare structure $k_{S,i}$ can be calculated from the inter-storey displacement $\Delta s_{,i}$ generated by linear static analysis (LSA) applying to each storey the distribution of horizontal seismic forces F_i.

$$k_{DB,i} = r_k k_{S,i}; \quad r_k = \frac{k_{DB}}{k_{S,0}}; \quad k_{S,i} = \frac{1}{\Delta s_i} \sum_i F_i ; \quad F_i = F_u \cdot \frac{m_i \Delta_i}{\sum_{i=1}^{n} (m_i \Delta_i)} \quad (10)$$

In the same way, the yield force $F_{DB,}$ of the equivalent bracing at the i^{th} storey is determined in the hypothesis that the ratio between the yield force at each floor of the bare structure $F_{Sy,i}$ and that of relative bracing $F_{DB,i}$ is distributed proportionally to the ratio r_F between the strength of equivalent bracing F_{DB} systems and the strength of equivalent bare structure $F_{s,y}$ (Equations 11). The yield force of the bare structure $F_{S,y,i}$

at i^{th} storey can be calculated in a simplified manner starting from the displacements at the elastic limits $\Delta_{s,y,i}$. This is determined by redistributing the displacement at elastic limit of the bare structure $\Delta_{s,y}$ as a function of the ratio between the inter-storey displacement Δs_i and the total elastic displacement s_{TOT} calculated by means of Linear static analysis.

$$F_{DB,i} = r_F F_{S,y,i}; \qquad r_F = \frac{F_{DB}}{F_{S,y}}; \qquad F_{S,y,i} = k_{S,i}\Delta_{S,y,i}; \qquad \Delta_{S,y,i} = \frac{\Delta s_i}{s_{TOT}}\,\Delta_{S,y} \tag{11}$$

The elastic stiffness $k_{DBi,j}$ and the yield force $F_{DB,i,j}$ of the single j^{th} dissipating brace at i^{th} storey are finally defined starting from the equivalent dissipative bracing system, as function of the number of dissipative braces at the i-th storey $n_{DB,i}$, as in the following Equations 12.

$$k_{DB,i,j} = \frac{k_{DB,i}}{n_{DB,i}}; \qquad F_{DB,i,j} = \frac{F_{DB,i}}{n_{DB,i}} \tag{12}$$

At this point, it is possible to evaluate damper (D) and brace (B) mechanical properties, depending on the dissipative bracing system adopted. The stiffness $k_{D,i,j}$ and the yield force $F_{Di,j}$ of the single hysteretic damper at the i^{th} storey are related to the stiffness $k_{B,i,j}$ of the elastic bracing rods and to the yield force $F_{DB,i,j}$ of the dissipative brace. Generally, the dissipative brace stiffness $k_{DB,i,j}$ can be determined as a series composition of rigid brace and damper (Equations 13).

$$k_{DB,i,j} = \frac{k_{D,i,j} \cdot k_{B,i,j}}{k_{D,i,j} + k_{B,i,j}}; \qquad F_{D,i,j} = F_{DB,i,j} \tag{13}$$

Step 7. Verify design assumption. After the design is complete, the analysis of the MDOF structure can be performed and the resultant ultimate drift θ_u is compared with the design value θ_d (assumed in the Step 1). The ultimate displacement can be evaluated through (static or dynamic) non-linear analysis, considering a suitable modelling of the post-tensioned structure with dissipative rocking or dissipative bracing systems (described in the following Chapter 7), assuming a tolerance value ε. If $|\theta_u - \theta_d| < \varepsilon$, the

design procedure is complete, on the contrary repeat the procedure from Step 2 assuming different values of design parameters.

3.2 Design of experimental model

The proposed procedure was applied for the design of a three-storey post-tensioned timber frame model tested within the Pres-Lam project in collaboration with University of Canterbury (New Zealand) at the structural laboratory of the University of Basilicata with different amount of energy dissipation. In particular, the three following configurations have been considered:

i) bare post-tensioned frame (F), representing the free rocking condition with post-tensioning only without energy dissipation ($\beta_F = 0$, see Figure 12a), designed for a target drift of about 3%;

ii) dissipative frame (DF), representing the bare frame (F) with additional dissipative rocking at the beam-column joints and at the column-foundation connections ($\beta_F = 0.47$, see Figure 12b), designed for a target drift of about 2 % [113];

iii) braced frame (BF), representing the bare frame (F) with dissipative braces ($\beta_F = 0.8$, see Figure 12c), designed for a target drift of 1.25% [93].

Figure 12 shows a schematization of the frame configurations under gravity and seismic loads, with corresponding moment contribution at the ground floor and the beam-column joint connection moments. The prototype model was a 3D, three-storey frame, characterized by single bays in both directions and post-tensioned in both directions. It was designed according to European code [2] for office use at first and second floors (live load of Q = 3 kPa) and considering a rooftop garden load (Q = 2 kPa). The seismic demand was characterized by a peak ground acceleration (PGA) of 0.44 g and a medium soil class for high seismic zone. The geometry of the test specimen was determined based on several aspects including the limitation of shake table available at the structural laboratory of the University of Basilicata [114]. A scale factor of 2/3 was applied to the prototype building obtaining an inter-storey height of 2 m

and a scaled footprint of 4 m x 3 m (Figure 13a and Figure 16a). Suitable scale factors were used observing mass similitude related to the Cauchy-Froude similitude laws [115]. The additional masses due to scaling of dead load and live load were made up of concrete blocks and steel hold downs. Table 1 summarizes the loads of the DF and BF models.

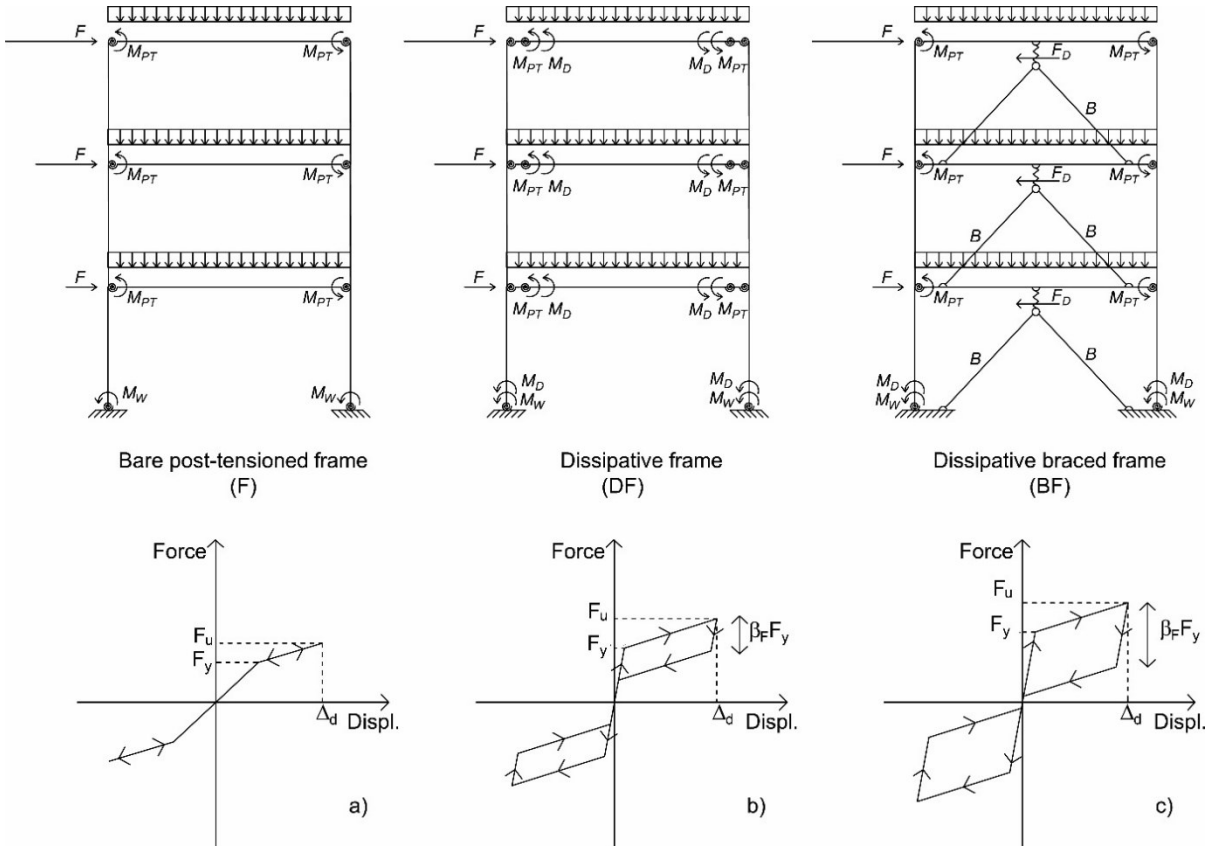

Figure 12. Force-displacement behaviour of three different configurations of the experimental model: (a) bare post-tensioned frame (F); (b) dissipative frame (DF); (c) dissipative braced frame (BF)

Table 1. Loads of the DF and BF prototype frames.

Level	DF model (kN)	BF model (kN)	Additional masses (kN)	Total weight DF (kN)	Total weight BF (kN)
1 and 2	10.7	11.2	44.1	54.8	55.8
3	9.9	10.4	44.1	54.0	54.5

3.3.1 Dissipative rocking

The application of the step by step design procedure to the DF prototype model (Figure 13a) is reported in the following.

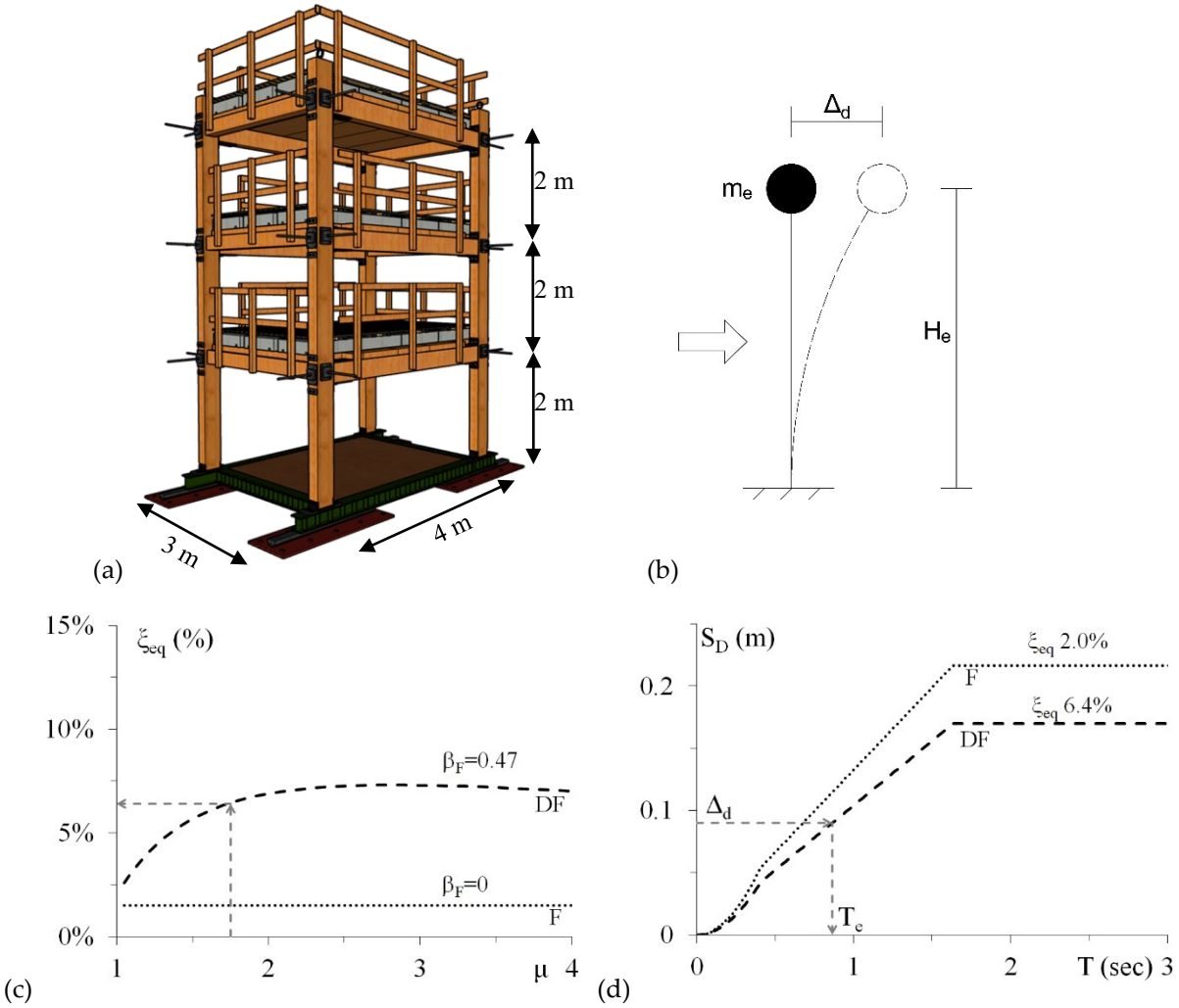

Figure 13. Basics of design approach: (a) Sketch of the MDOF of prototype model with dissipative rocking (DF); (b) equivalent SDOF representation; (c) equivalent viscous damping versus ductility; (d) design displacement spectra of the equivalent DF.

Table 2. *Characteristics of the MDOF and SDOF systems of the DF model.*

MDOF

Storey	M_i (t)	h_i (m)	Δ_i (mm)	F_i (kN)
1	5.58	2	38	6
2	5.58	4	77	12
3	5.50	6	115	18

SDOF

m_e	14.3 (t)
H_e	4.66 (m)
Δ_d	0.09 (m)

Step 1. The design procedure at the design basis earthquake (DBE) starts from the assumption of the design drift θ_d = 1.9% or equivalent roof displacement Δ_u = 0.09 m.

Step 2. The post-yield stiffness ratio r = 0.3, the displacement ductility μ = 1.75 and the re-centering ratio of the dissipative rocking system β_F = 0.47 have been assumed in order to define the basic flag-shape system.

Step 3. The equivalent viscous damping ξ_{eq} was evaluated based on previous Equation 1 and Equation 2, considering an elastic viscous damping $\xi_{eq,v}$ = 2% and a correction of the hysteretic contribution by a reduction factor k = 0.85. The damping versus displacement ductility (μ) response is plotted in Figure 13c.

Step 4. The equivalent period T_e of the equivalent SDOF of the dissipative frame (Figure 13b) can be derived from the design displacement response spectrum (Figure 13d) reduced to account for the ductility/damping of the systems, using the damping correction factor η. As highlighted, when equivalent viscous damping increased from the post-tensioned frame to the braced frame, the design displacement substantially reduced. The equivalent stiffness K_e, the yield force F_y and ultimate force F_u of the structure have been evaluated by Equation 5. Table 2 summarizes the main characteristics of the MDOF and SDOF systems of the DF model.

Step 5. From the flag-shape behaviour, the characteristics of the equivalent bare frame ($F_{s,y}$, $F_{s,u}$, μ_s) and of the equivalent dissipative rocking system ($F_{D,y}$, μ_D) have been calculated using Equation 7 and Equation 8. The main design results from step 1 to step 5 are summarized in Figure 14 in terms of force-displacement of the equivalent SDOF systems compared with the seismic design demand.

Step 6. The equivalent force and stiffness of the bare frame (F) and of dissipative system (D) were distributed up to the stories and the post-tensioning resistant moments M_{PT} and yielding moment of dissipative devices M_D were evaluated through MMBA method [26] and structural members were dimensioned. For the experimental model the design of post-tensioning force was 100 kN and 50 kN for the primary and secondary direction, respectively. Based on the DIS-CAM concept [116], steel angle

devices were designed for DF configuration. Two different types of external replaceable steel angle devices placed at the beam-column and column-foundation connections were selected as dissipative dampers of the frame, identified with ID5A and ID8A, respectively (Figure 15). They were created by milling down a certain section of the angles to provide a region in which yielding is concentrated and hysteretic energy is dissipated through the inelastic behaviour of steel. The parameters used to control the angle's performance are the thickness of the worked area (t), the height of the worked area (d) and the width of the angle (b). The angles were designed to remain elastic up until the serviceability limit state demand following which yielding would occur. The main characteristics of ID5A and ID8A are summarized in Table 3.

Step	*Design Parameter*	
1	Δ_d	0.09 m
	θ_d	1.9 %
2	β_F	0.47
	μ	1.75
	r	0.3
3	$\xi_{eq,v}$	2.0%
	ξ_{eq}	6.4%
4	T_{eq}	0.86 s
	K_e	770 kN/m
	F_u	70 kN
5	$F_{S,y}$	39 kN
	$F_{S,u}$	56 kN
	μ_S	2.5
	$F_{D,y}$	13 kN
	μ_D	7.5

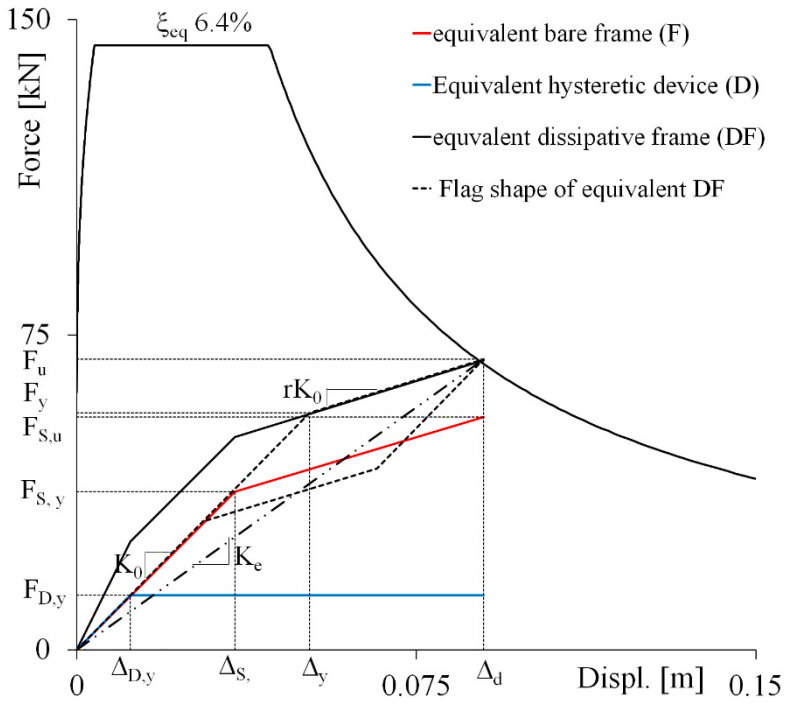

Figure 14. Results of the design procedure applied to the post-tensioned timber experimental model with dissipative rocking.

Table 3 Characteristics of the dissipative steel angle devices.

Hysteretic damper	Location	Device ID	t_A (mm)	b (mm)	t_A (mm)	d (mm)	l (mm)	Steel grade
Dissipative angle	Beam-Column joint	2L 100x10x80	10	2*80	6	40	100	S275
	Column-foundation joint	L 100x8.5x160	8.5	160				

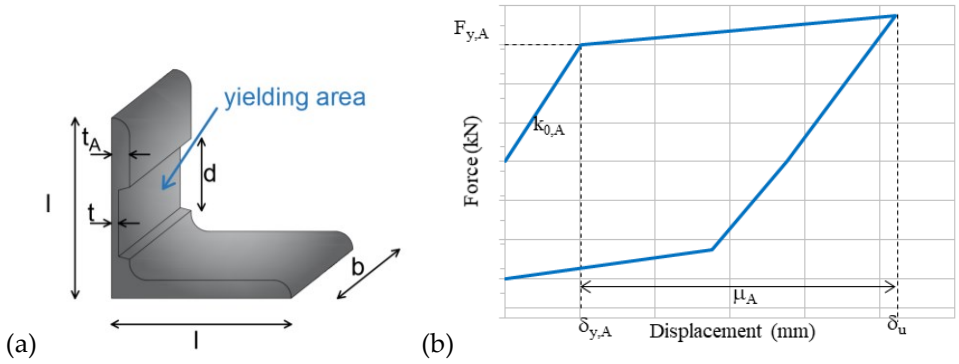

Figure 15. (a) Steel angle design characteristics; (b) Force-displacement behaviour of steel angle.

Details about the application of MMBA procedure to the prototype frame with dissipative rocking systems can be found in previous research works [111].

The validation of the proposed design procedure, through experimental and numerical results will be presented in Chapter 7.

3.3.2 Dissipative bracing systems

The same step by step design procedure applied to the design of the experimental post-tensioned braced model (Figure 16a), is described in this paragraph.

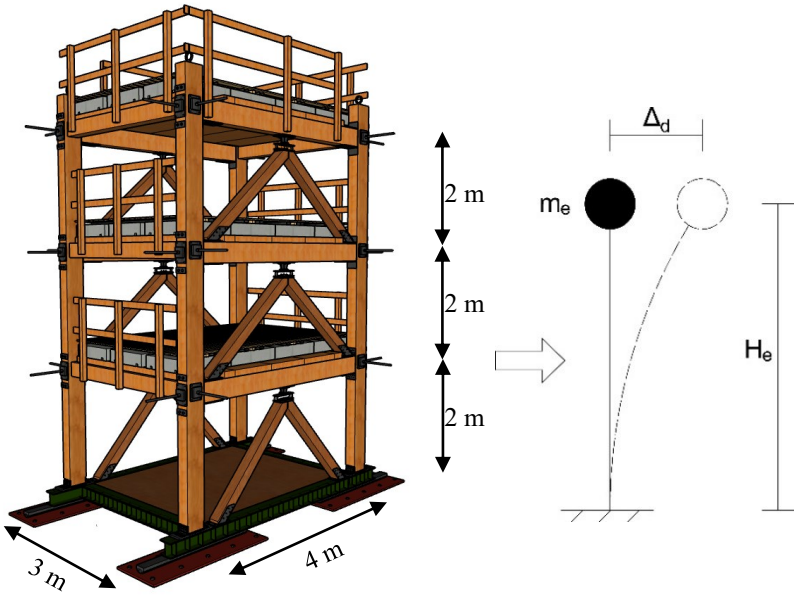

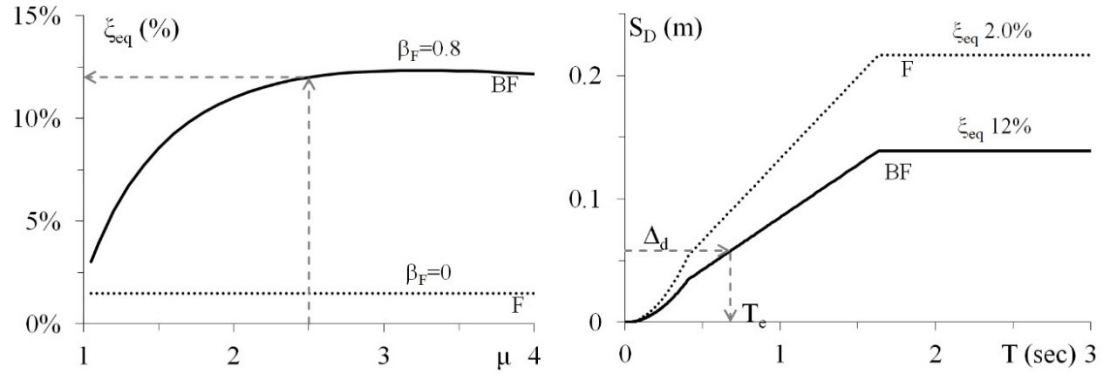

(c) (d)

Figure 16. Basics of design approach: (a) Sketch of the MDOF of prototype model with dissipative bracing systems (BF); (b) equivalent SDOF representation; (c) equivalent viscous damping versus ductility; (d) design displacement spectra of the equivalent BF.

Table 4. Characteristics of the MDOF and SDOF systems of the BF model.

MDOF

Storey	M_i (t)	h_i (m)	Δ_i (mm)	F_i (kN)
1	5.64	2	25	12
2	5.64	4	50	24
3	5.56	6	75	36

SDOF

m_e	14.4 (t)
H_e	4.66 (m)
Δ_d	0.058 (m)

Step 1. The design procedure at the design basis earthquake (DBE) starts from the assumption of the design drift $\theta_d = 1.25\%$ or roof displacement $\Delta_u = 0.058$ m.

Step 2. The post-yield stiffness ratio r = 0.2, the displacement ductility $\mu = 2.5$ and the re-centering ratio of the braced system $\beta_F = 0.8$ have been assumed in order to define the basic flag-shape system.

Step 3. The equivalent viscous damping ξ_{eq} versus displacement ductility μ is plotted in Figure 16c considering an elastic viscous damping $\xi_{eq,v} = 2\%$ and a correction of the hysteretic contribution by a reduction factor k = 0.85.

Step 4. The equivalent period T_e of the SDOF braced frame can be derived from the design displacement response spectrum (Figure 16d) reduced to account for the ductility/damping of the systems, using the damping correction factor [106]. As highlighted, when equivalent viscous damping increased from the post-tensioned frame to the braced frame, the design displacement substantially reduced. The

equivalent stiffness K_e, the yield force F_y and ultimate force $F_{S,u}$ of the structure have been evaluated by Equation (5).

Step 5. From the flag-shape behaviour, the characteristics of the equivalent bare frame and of the equivalent dissipative bracing system have been calculated using Equation 6 and Equation 7. The main design results from step 1 to step 5 are summarized in Figure 8 in terms of force-displacement of the equivalent SDOF systems compared with the seismic design demand.

Step 6.1. The equivalent force and stiffness of the bare frame (F) have been distributed up to the stories ($k_{S,i}$, $F_{S,y,i}$) and the post-tensioning resistant moments M_{PT} were evaluated through MMBA method [110], as reported in detail in previous works [111].

Step 6.2. Two V-inverted chevron braces for each storey ($n_{DB,i}$ = 2) both compounded by two linear elastic timber braces (B) in series with the elasto-plastic damper (D) composed the DB system (Figure 16a). The force and stiffness of the equivalent DB system were distributed up to the stories ($k_{DB,i}$, $F_{DB,i}$) and in plan, then the characteristics of the single dissipating brace $k_{DB,i,j}$, $F_{DB,i,j}$ were defined. The main results of the design are summarized in Table 5.

Step	*Design Parameter*	
1	Δ_d	0.058 m
	θ_d	1.25 %
2	β_F	0.8
	μ	2.5
	r	0.2
3	$\xi_{eq,v}$	2.0%
	ξ_{eq}	12%
4	T_{eq}	0.68s
	K_e	1228 kN/m
	F_u	71 kN
5	$F_{S,y}$	39 kN
	$F_{S,u}$	49 kN
	μ_S	1.6
	$F_{D,y}$	22 kN
	μ_D	3.5

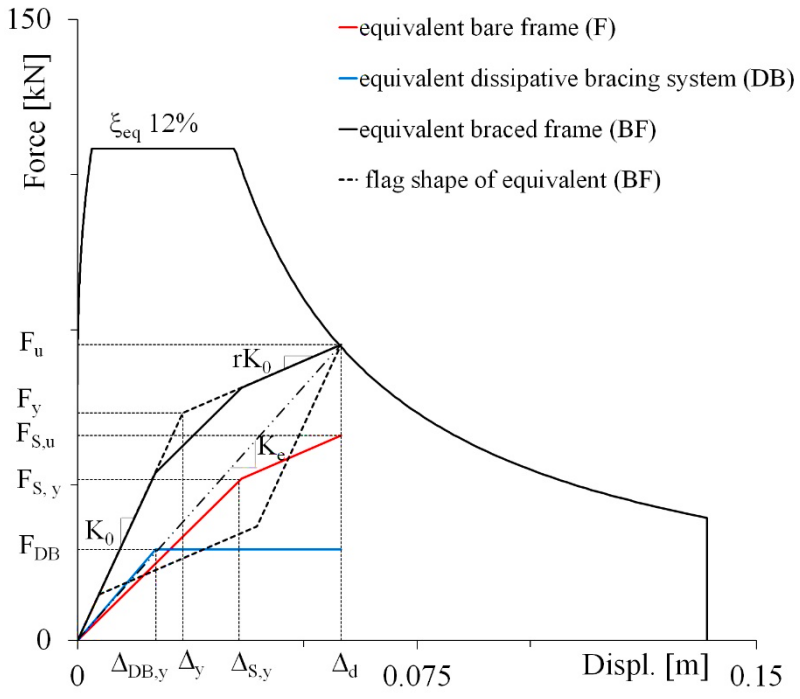

Figure 17 Results of the design procedure applied to the post-tensioned timber experimental model with dissipative bracing systems.

Table 5. Main design characteristics of the braced post-tensioned frame.

Storey	Δs_i (mm)	$F_{s,y,i}$ (kN)	$k_{s,i}$ (kN/mm)	$F_{DB,i}$ (kN)	$k_{DB,i}$ (kN/mm)	$F_{DB,i,j}$ (kN)	$k_{DB,i,j}$ (kN/mm)
1	15.3	53	4.7	30	5.5	15.0	2.8
2	33.2	44	3.3	25	3.9	12.5	2.0
3	48.7	26	2.3	15	2.7	7.5	1.4

In the hypothesis of rigid bracing truss and flexural UFPs damper ($k_{B,i,j} >> k_{D,i,j}$), the stiffness $k_{Di,j}$ of the damper corresponded to the stiffness $k_{DB,i,j}$ of the j^{th} dissipative brace at the i^{th} storey ($k_{D,i,j} \cong k_{DB,i,j}$).

U-shaped flexural steel plates (UFPs) were selected as dissipative dampers (D), placed between the bottom surface of the principal beam and the supporting timber rods (B), in order to comply with the force requirement at each storey without changing the gravity loads distribution on beams and columns and reducing the influence on the post-tensioned beam-column joints.

The design assumptions (*Step 7*) are validated through experimental results and nonlinear time history analyses, as reported in the following Chapter 7.

Design of rigid brace support

The supporting timber rods were designed with a stiffness of at least one magnitude order higher than that of the dampers:

$$k_{B,i,j} = \frac{E_t A_B}{L_B} \gg k_{D,i,j} \cong k_{DB,i,j} \quad (14)$$

Where E_t represent the elastic values (parallel to the grain) of glulam timber grade GL24h, equal to 9600 MPa, A_B represent the area of the supporting timber brace, equal to 180 x 160 mm (to comply with nature of the attachment system at the frames), and L_B is the length of the brace about equal to 2600 mm at each storey.

Design of U-shaped Flexural Plate dampers

U-shaped Flexural plates were initially proposed and experimentally tested by Kelly et al. [43] to provide energy dissipation between structural walls and adjacent floors,

and then applied for several structural applications, such as for seismic isolation systems with auxiliary dissipation devices [117], coupled CLT walls [46], included in superelastic SMA system [118], and recently also for dissipative bracing systems [93] [119].

The dampers designed for the dissipative bracing system of the case study consisted of two UFPs in series with two V-inverted timber rods.

UFPs can be designed for a large range of possible displacements and force levels by varying the plate thickness t, the plate width b and curvature diameter D, as shown in Figure 18a. The force provided by a single UFP was derived analytically [43] by relating the coupling shear of the UFP to the plastic moment. The plastic moment M_P (Equation 15) is defined when the entire region of a rectangular section yields. The yielding force $F_{y,UFP}$ can be determined by Equation 16. Coupling shear and plastic moment of UFP is shown in Figure 18b. The yield displacement $\delta_{y,UFP}$ (Equation 17) of a UFP can be determined using energy methods [120].

$$M_p = \frac{f_y b t^2}{4} \tag{15}$$

$$F_{y,UFP} = \frac{f_y b t^2}{2D} \tag{16}$$

$$\delta_{y,UFP} = \frac{27\pi F_y D^3}{16Ebt^3} \tag{17}$$

Where f_y is the steel yield stress and E is the steel elastic section modulus. The initial stiffness $k_{0,UFP}$ of single UFP can thus be defined as follows:

$$k_{0,UFP} = \frac{16Eb}{27\pi}\left(\frac{t}{D}\right)^3 \tag{18}$$

The typical force-displacement behaviour of UFP is shown in Figure 18c. The factors used to define the cyclic hysteretic performance of UFP are: i) the initial stiffness $k_{0,UFP}$, ii) the yield strength $F_{y,UFP}$ or the yield displacement $\delta_{y,UFP}$, and iii) the ductility μ_{UFP} or the ultimate displacement $\delta_{u,UFP}$. The capability of UFPs to dissipate energy is due to the behaviour when stressed beyond elastic limit. When one side of UFP is subjected to a displacement relative to the opposite side, the semi-circular section rolls along the

plate and work is done at two points where the radius of curvature is changed from straight to curved and vice-versa.

In order to obtain approximately the "ideal" design values of $F_{DBi,j}$ and $k_{DB,i,j}$ of the dissipative bracing system (Table 5), UFPs have been dimensioned using the previous Equations 15-17. A small ratio between the plate thickness and diameter was desired in order to minimize strain and accommodate large displacements. For reasons connected with the installation and bolting of UFPs the geometrical diameter and thickness of were fixed (D=60 mm and t= 6 mm) and based on previous design value, the UFPs made of C60 stainless steel was performed varying the width b at each floor, as reported in Table 6.

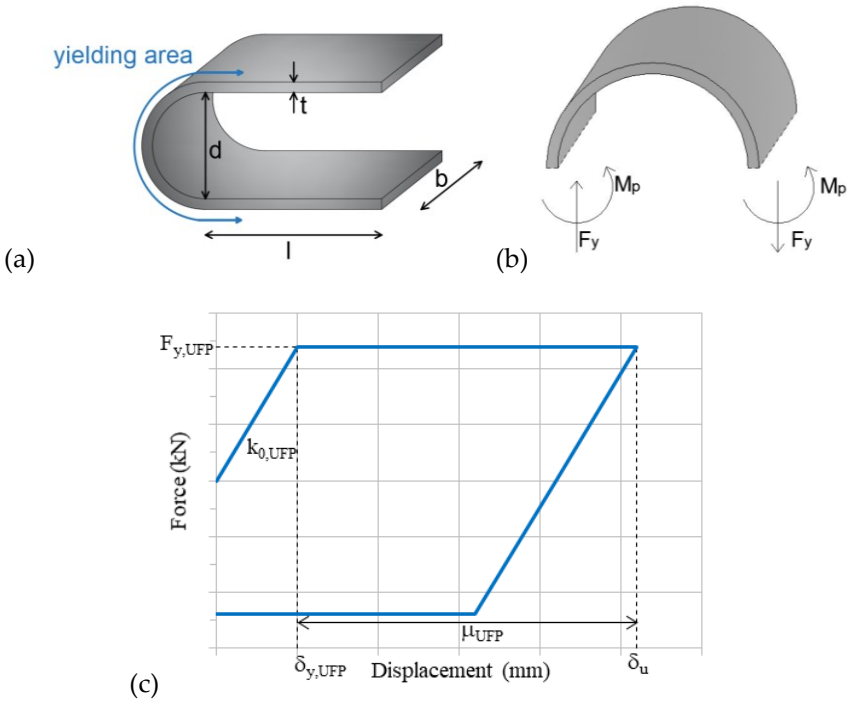

Figure 18(a) UFP design characteristics; (b) Coupling shear and plastic moment of UFP;(c) Force-displacement behaviour of UFP dissipator.

Table 6. Characteristics of the UFPs by design

Hysteretic damper	Location	Device ID	b (mm)	t (mm)	d (mm)	l (mm)	Steel grade
U-shaped dissipative plate	1st floor brace	UFP1	60	6	60	100	C60
	2nd floor brace	UFP2	40				
	3rd floor brace	UFP3	30				

4 Experimental testing of post-tensioned timber frame with dissipative systems

In this chapter the experimental testing campaign performed within the Pres-lam Project at the University of Basilicata. Controlled displacement tests performed on the dissipative steel angles and U-shaped Flexural Plates devices are presented. Then, the shaking table testing campaign of a 3D post-tensioned timber frame building in different configurations has been described, particularly focusing on the last testing phase with dissipative bracing systems. The construction details of the specimen are provided, the instrumentation apparatus, ground motions inputs and testing program are also described.

4.1 Quasi-static tests on hysteretic devices

4.1.1 Dissipative angles

Different angle types with two different methods of providing an area of concentrated yielding (milled angle and holed angle) and considering different stainless steel have been tested at the structural laboratory of University of Basilicata. In case of milled angle (Figure 19a), which were considered for dissipative rocking connections of DF model, the concentrated yield area was created by milling down a certain section of the angles, taken from equal angle sections. In case of holed angle (Figure 19b), the yield area was created using holes drilled into the angle face.

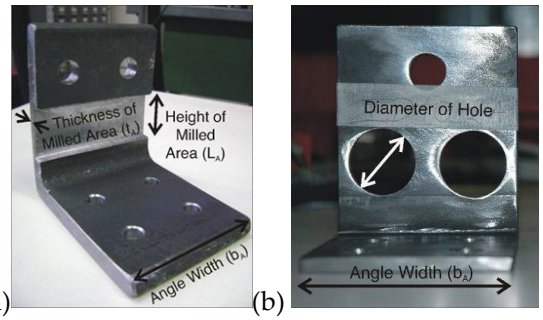

Figure 19. (a) Milled steel angle and (b) holed steel angle tested at University of Basilicata (Di Cesare et al.) [121].

Figure 20 shows the scheme adopted for quasi-static testing and testing setup of steel angles devices of S275 steel grade and the force-displacement response behaviour for two different geometrical configurations relevant to beam-column joints (2 L 100x10x80) and to column-foundation connections (L 100x8.5x160), respectively.

Controlled displacement testing was performed using a hydraulic jack. The steel angle was bolted to the test equipment and the central plate was moved up or down only in the positive direction corresponding with its expected performance when installed at the joint connections of the frame. The angle was loaded at a rate of 0.5mm/sec and the test sequence was performed applying two cycles at increasing amplitudes up to the 100% of the design displacement. Displacement and applied load were recorded by potentiometer and load cell. As can be observed a stable hysteretic behaviour of devices was recorded. For more information about characteristics and testing of steel angles devices please refer to Di Cesare et al. [121].

(a)

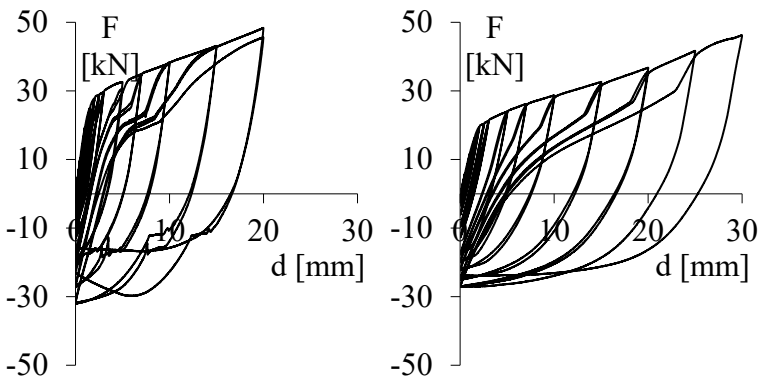

(b) (c)

Figure 20 a) Testing set-up for quasi-static testing of dissipating angle. Force-displacement behaviour of: b) 2L 100x10x80 for beam-column joints and c) L 100x8.5x160 for column-shake table connections.

Table 7. Main experimental characteristics of selected steel angles tested.

Steel Angle ID	Dimension	$F_{y,A}$ (kN)	$k_{0,A}$ (kN/mm)	μ_A	post-yield ratio
ID 5A	L 100x10x80	15	9.4	12.5	0.5
ID 8A	L100x8.5x160	24.5	13.6	16.7	0.9

4.1.1 U-shaped Flexural Plates

During the experimental campaign, preliminary quasi-static tests were performed to characterize the force-displacement behaviour of UFP steel dampers [122].

UFPs were formed from bending a mild steel plate section around a fixed radius to form a "U" shape (Figure 3a). The values of nominal yield strength of steel (f_y) were evaluated by means of tensile testing specifically performed on tensile specimen (Figure 3b).

(a)

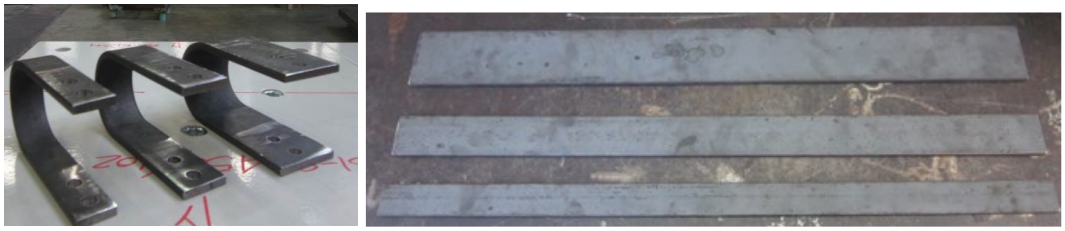

(b)

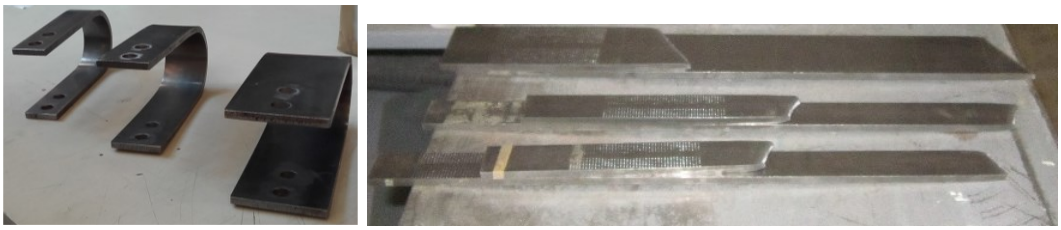

Figure 21(a) UFPs and tensile specimen selected for testing of UFP1 UFP2 and UFP3 of (a) S275 and (b) C60 stainless steel.

Table 8 Main characteristics of UFPs tested

Steel	UFP	N° UFPs	D (mm)	t (mm)	b (mm)	f_y (N/mm^2)
S275	UFP 1	4	60	6	60	325
	UFP2	4	60	6	40	325
	UFP 3	4	60	6	30	350
C60	UFP 1	4	60	6	60	540
	UFP2	4	60	6	40	590
	UFP 3	4+2	60	6	30	610

Quasi-static tests were performed on two series of UFPs, with the geometrical characteristics (D, t, and b), as representative of the devices installed at each storey of the braced post-tensioned timber frame model and by two different stainless steel, C60 (design value) and S275 were considered, as summarized in Table 8.

The testing setup consisted of a pair (Figure 4a) or a single UFP bolted between the external and the central platform. The central platform was attached to the loading actuator and driven up and down between the UFPs in order to impose displacement demand upon the UFPs. The displacement-controlled loading protocol consisting of two cycles at increasing amplitudes was used to undertake the quasi-static cyclic loading. The UFPs were loaded at a rate of 0.5 mm/s up to a maximum displacement of 25 or 30 mm (Figure 4c). A load cell of 250 kN attached to the loading actuator and a linear potentiometer were used to record the load and the vertical displacements.

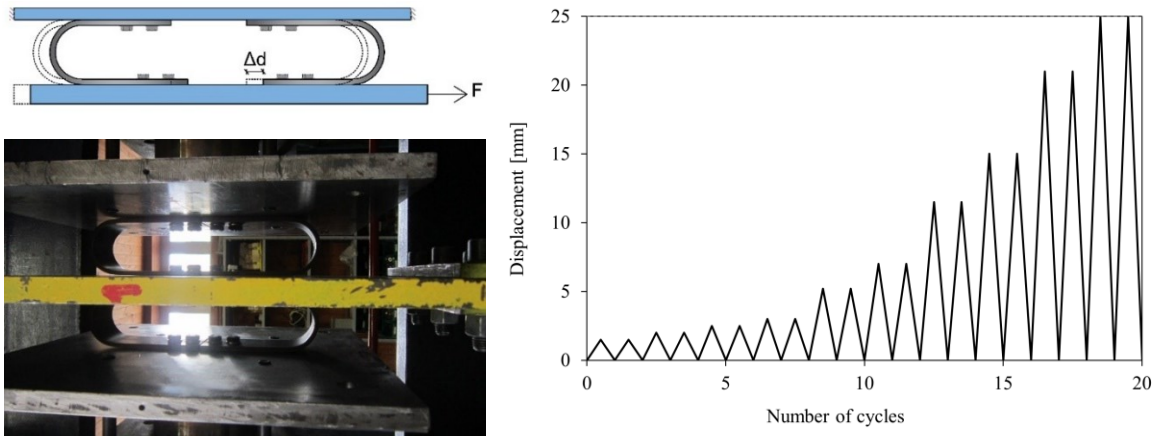

(a) (b)

Figure 22. (a) Testing setup: four UFPs in parallel; (b) loading protocol for UFPs

Figure 23a and Figure 23b show the experimental results of quasi-static tests in terms of force-displacement for UFPs of S275 and C60 stainless steel, respectively. As can be observed, all UFPs showed a stable hysteretic behaviour, with a large damping capacity, without any sign of failure.

Experimental results of quasi-static tests were compared with analytical outcomes (red line of Figure 23) referred to a couple of UFPs, in terms of yield strength $F_{y,UFP}$ (Equation 2) and initial stiffness k_0. As can be observed in Table 9, analytical results in

terms of yield strength well approximate the corresponding experimental values. A discrepancy has been observed between analytical and experimental values of initial stiffness. In all cases of both testing sessions, the ratio between analytical (Equation 4) and experimental values of initial stiffness k_0^*/k_0, is always approximatively to a constant value of 0.5.

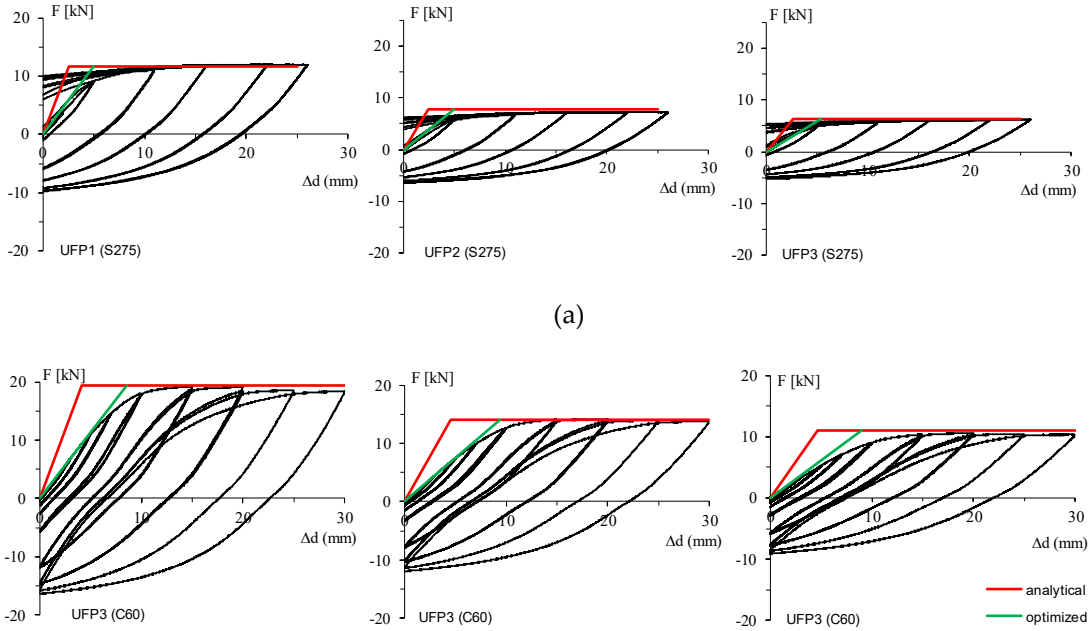

Figure 23 Force-displacement response obtained by quasi-static tests of a couple of UFP1, UFP2and 2UFP3 of (a) S275 and (b) C60 stainless steel.

Based on these experimental evidences, a corrective factor (0.5) of initial stiffness (k_0^*) was proposed in order to optimize the design of UFP (Equation 1). The optimized value, indicated with green line in Figure 23, show a best fit with the experimental behaviour.

$$k_0^* = 0.5 \cdot k_0 = \frac{8Eb}{27\pi}\left(\frac{t}{D}\right)^3 \quad (1)$$

Figure 24 shows the quasi-static tests of the UFPs (C60) representative of the dampers designed and installed at each storey of the braced frame compared with the results of the design procedure described in Chapter 3 (blue lines). The experimental results

show that the design assumptions [93] are consistent with the actual UFPs dampers behaviour.

Table 9. Experimental vs analytical characteristics of UFPs

		Experimental		Analytical		
UFP	N°	$F_{y,UFP}^*$ (kN)	$k_{0,UFP}^*$ (kN/mm)	$F_{y,UFP}$ (kN)	$k_{0,UFP}$ (kN/mm)	$k_{0,UFP}^*/k_{0,UFP}$
UFP1 (S275)	2	12	2.3	12	4.6	0.5
UFP2 (S275)	2	8	1.5	8	3.1	0.5
UFP3 (S275)	2	6	1.2	6	2.3	0.5
UFP1 (C60)	2	19	2.3	20	4.6	0.5
UFP2 (C60)	2	14	1.5	14	3.1	0.5
UFP3 (C60)	2	11	1.2	11	2.3	0.5

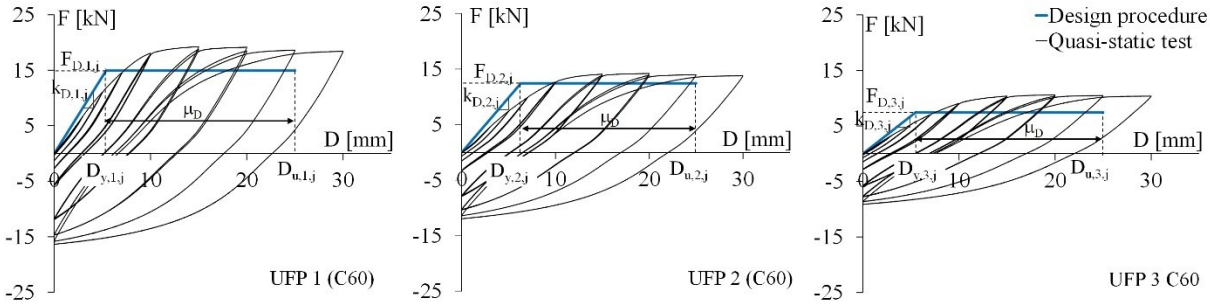

Figure 24. Comparison between quasi-static tests of UFP to be installed into the braced frame and design procedure.

4.2 Shaking table testing of experimental model

4.2.1 Construction details

A photographic view of the 3D 2/3 scaled experimental specimens tested at the structural laboratory of the University of Basilicata with post-tensioning only (F)[122] and with dissipative bracing systems (BF) [123], are shown in Figure 25 and in Figure 25b, respectively. The additional masses were made up of a combination of concrete blocks and steel hold downs with 12 blocks being spread out across each floor (Figure 26a). Each block had a total weight of 3.3 kN with an additional 0.28 kN provided by each hold down (UPN100 steel section, 0.1 kN/m). The post-tensioned frame was

realized using glulam grade GL32h (CNR-DT 206 2018)[124]. The section sizes of columns (continuous through the floor diaphragms) were 200 x 320 mm while primary and secondary beams were 200 x 305 mm and 200 x 240 mm, respectively and the flooring consisted of 150 mm thick solid timber panels (Figure 26b) [13].

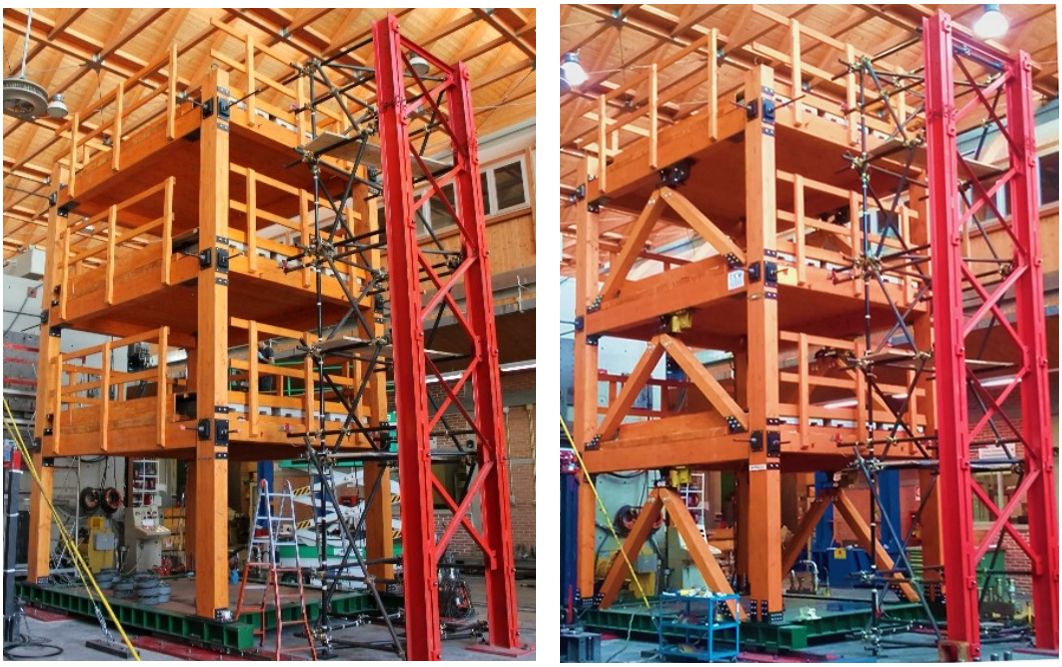

(a) (b)

Figure 25. General views of experimental model at the structural laboratory of University of Basilicata: (a) post-tensioned timber bare frame (F configuration); (b)post-tensioned model with dissipative bracing systems (BF configuration)

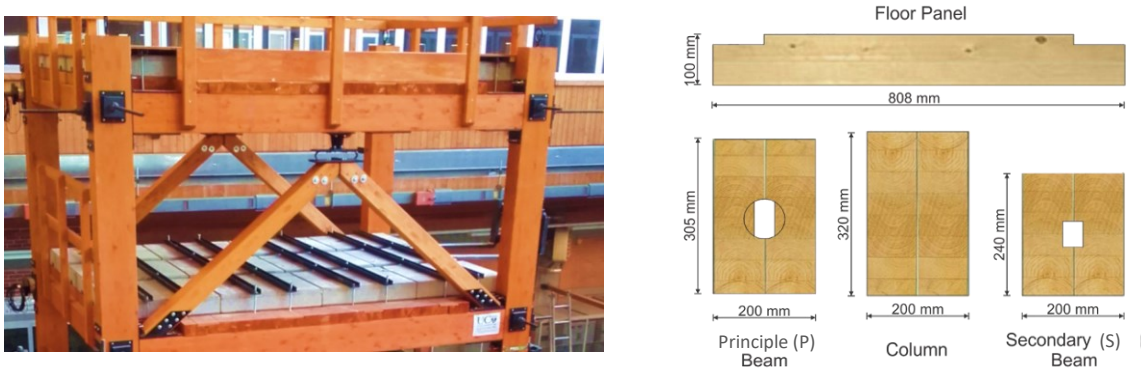

(a) (b)

Figure 26. (a) Additional masses on the test frame and (b) section sizes of elements used in the frame.

Figure 27 shows the construction details of the beam to column joints and of the column to shake table connections. The beam-column joints (Figure 27a) were composed by a single 26.5 mm diameter steel bar crossing the beam, with f_y = 1050 N/mm^2 yield strength and 170 kN/mm^2 Young's modulus, post-tensioned at 100 kN

and 50 kN for the longitudinal and transversal direction, respectively. In order to protect the column face, thirty-six ϕ 8 mm screws, 80 mm long screws were installed in the column face adjacent to the beam and 30 screws were installed in contact with the post-tensioning backing plate. Vertical loads were transferred through a ϕ 76.1 mm steel tube which extends 66 mm from the beam and sits inside to the column. Twenty-two ϕ 8 mm 80 mm long screws were used to reinforce where the beam and the post-tensioning backing plate meet the column. The post-tensioning forces in both directions were recorded by 2 load cells located in a monitored joint for each storey. The column base connection (Figure 27b) was fitted with a steel shoe which was epoxied into the base of the column and was left free to rock on a base plate using four ϕ 20 mm bars of 300 mm length. Shear transfer was achieved using a ϕ 76.1 mm steel tube which extended 15 mm from the steel shoe and slotted into a cavity in the base plate. The steel angles dampers were attached to the structural elements by M16 bolts fixed to backing plates. Moreover, a reinforcement with ten ϕ 80 mm long screws was introduced in the contact zone between the plate and the column. In order to facilitate the attachment of steel angles devices, holes were drilled and tapped in the steel shoe.

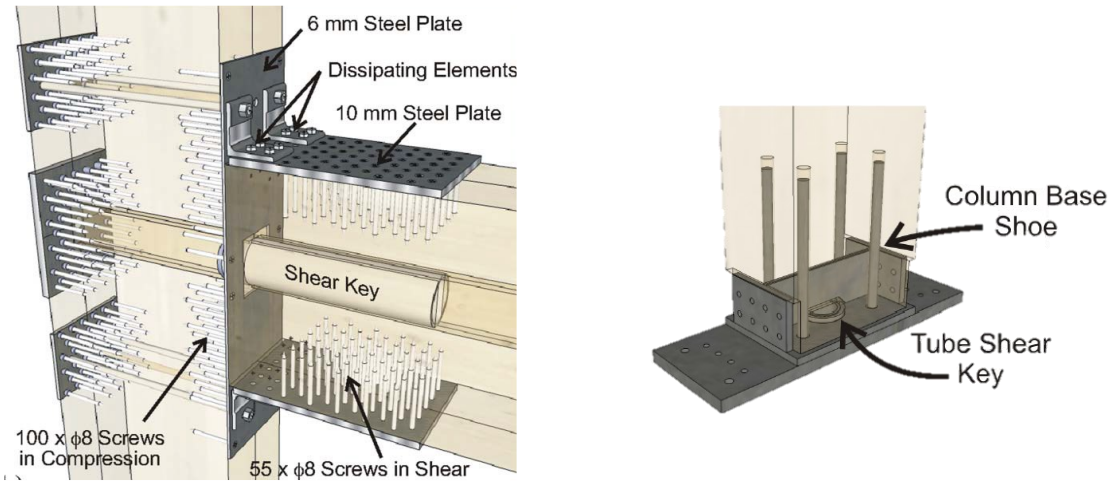

(a)

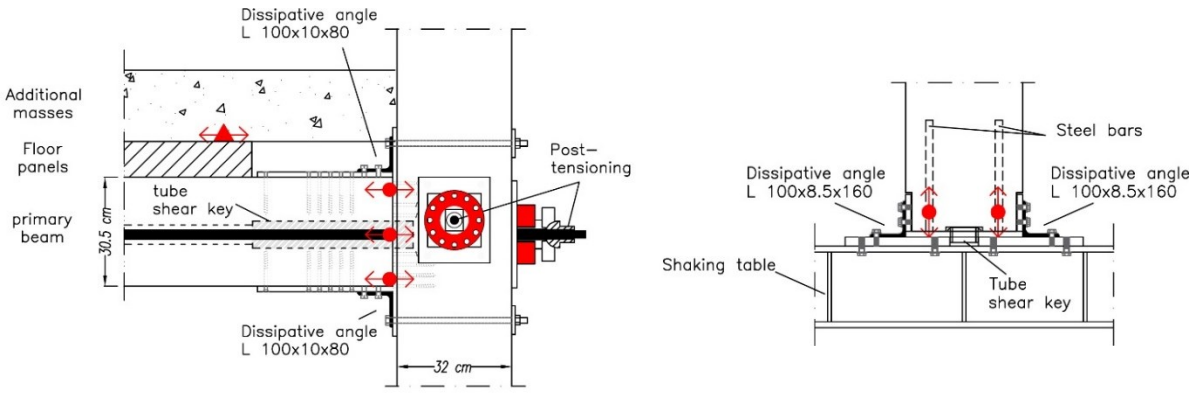

(b)

(c)

Figure 27. (a) Construction details [13], (b) instrumentation and (c) photographic view of beam to column joints and column to shake table connections.

Figure 28 shows the construction details of bracing connection to UFP and beam. Each dissipative brace was composed by two 160 mm x 180 mm V-inverted timber rods, realized using glulam grade GL24h [124], and hysteretic dampers consisting of two C60 steel grade U-shaped flexural plates (UFP) dampers working in parallel. UFP devices were selected as dampers in order to provide steady restraint in horizontal direction, to accommodate rotations and vertical displacements, i.e. do not transmit bending moments and vertical loads (UNI EN 15129 2018) [125]. In order to easily install and replace the devices on the bracing system, bolted connections were chosen. Then, two bolting holes were drilled into the straight region of the plates. The bending is performed on pre-heated plates in order to prevent stress concentrations. The timber rods were designed to behave elastically for an axial force greater than the yielding force of the UFPs fixed to the top and bottom flanges through four M10 bolts. The two timber rods were compacted through two steel plates connected to a central steel plate

with thickness of 10 mm. The two internal plates were bolted with the rods through 6 M10 for each rod. The bottom flange was held to the top of rods through height ϕ 8 mm 120 mm long screws and twelve ϕ 16 dowels. In order to acquire the shear force of the braces, the top flange was connected under the beam through a load cell with a pinned connection. In order to avoid possible out-of-plane displacements of braces, safety stoppers were installed, by using steel rigid elements with slotted holes which accommodate free relative displacement (without friction) between the UFPs and the rigid support of about 2 mm along out-of-plane direction and 20 mm along in-plan direction.

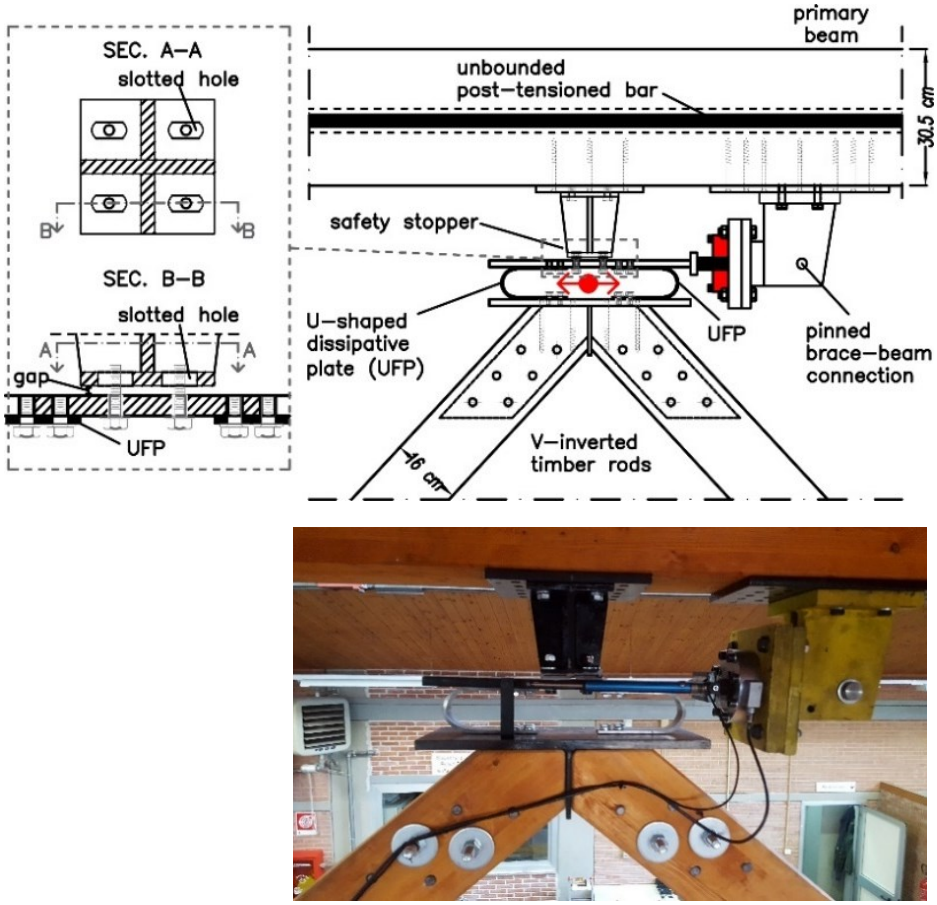

Figure 28. Details and photographic view of dissipative bracing and UFP devices connections

4.2.2 Instrumentation and data acquisition

A plan and elevation view of the testing apparatus and the sensor location is shown in Figure 29. The testing apparatus consisted of a single degree of freedom (in longitudinal direction) shaking table driven by an MTS dynamic actuator characterized by ±500 kN maximum load capacity of and ±250 mm stroke. The actuator has two cylindrical hinges and was fixed at the base of the shake table and pushed against a reaction wall. Three hydraulic pumps, each capable of a flow rate of 600 l/min, operated the actuator controlled by an inner load cell and temposonic linear displacement transducer. The shaking table consisted of a four-profile rail guides located under the columns, each composed by two carriages with a friction factor of less than 1%.

The seismic response of the frame was recorded by more than 50 acquisition channels, reported in detail in Appendix A. Different types of sensors were installed on the test frame, providing measurements of acceleration, displacement force and strain. A longitudinal, transversal and plan view of the instrumentation installed on the frame are shown in Figure 29. Fourteen horizontal and two vertical accelerometers were placed on different storey. The absolute horizontal displacements and rotations were measured directly by 7 displacement transducers connected from shake table to an external reference structure. The tension loading of the post-tensioned bars in both directions was measured by 6 load cells, the gap opening due to the rocking motion was recorded by 3 potentiometers placed across 3 beam-column joints and 2 potentiometers at the base of 2 columns (see details in Figure 27). Local force-displacement of the dissipative bracing systems were measured using a load cell and a potentiometer displacement transducer placed on all hysteretic dampers (see details in Figure 28).

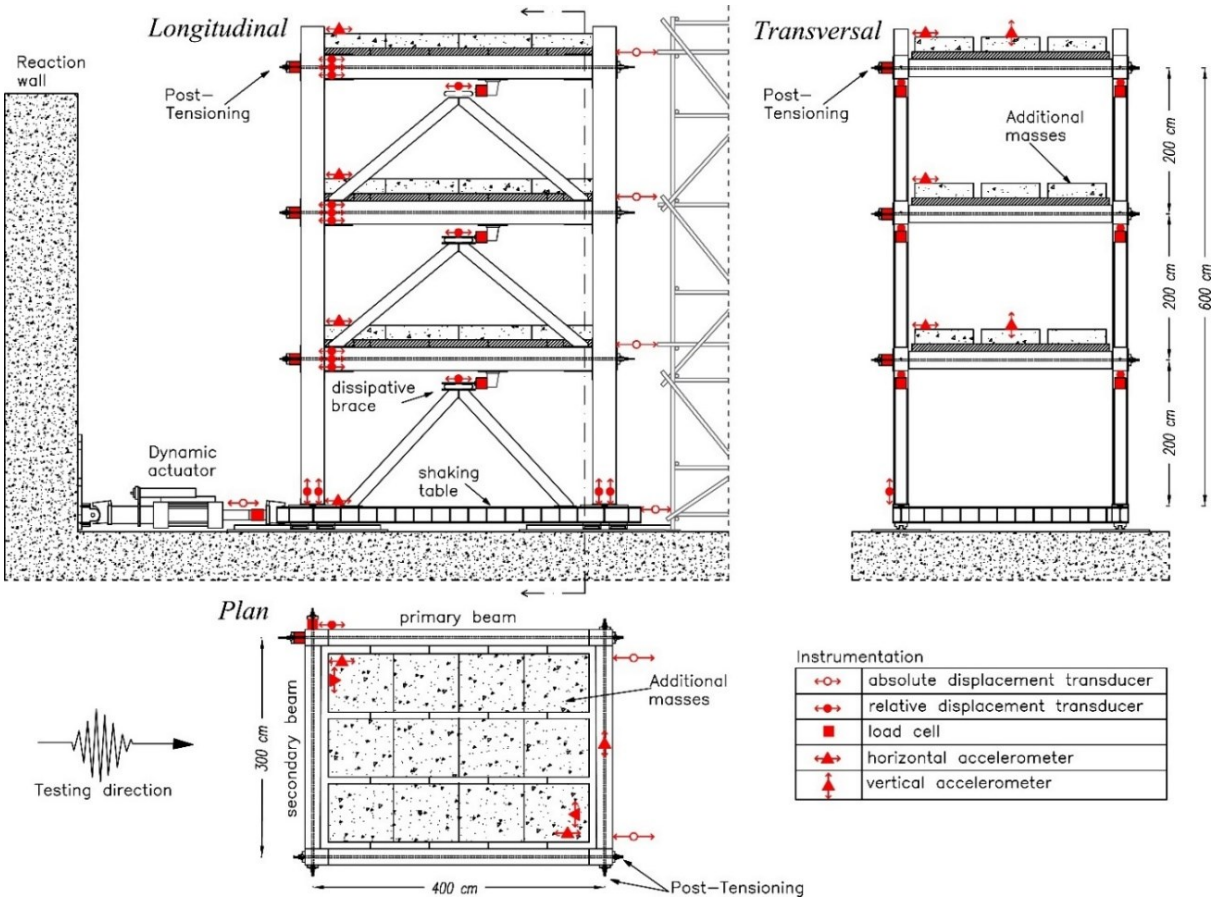

Figure 29. Testing apparatus of the dissipative braced frame (BF configuration).

4.2.3 Input ground motions and testing program

The experimental campaign was performed using a set of seven natural earthquake records, selected from the European strong motion database. These spectra-compatible records were defined according to the current Eurocode [2] considering a peak ground acceleration PGA of 0.44 g and medium soil class (type B) in high seismic zone (Figure 30). To ensure consistency with the scale of the experimental model, all input accelerations were scaled down in duration by a factor of $1/\sqrt{(3/2)}$. In order to match the real acceleration inputs to the Eurocode response spectrum it was necessary to scale four of the earthquakes by means of an appropriate scale factor. Main information regarding each record is reported in Table 10 (i.e.: station; identification number of the registration; magnitude (M_W); peak ground acceleration (PGA) in the horizontal direction; and scale factor, etc.).

Table 10. Earthquakes main characteristics

ID Code	Location	Station	Date	M_W	PGA (g)	PGV (ms^{-1})	Epic.Dist. (km)	Scale Factor
001228xa	Izmit, Turkey	Gezbe-Tubitak	17/08/1999	7.6	0.357	0.332	47	1.5
00196xa	Montenegro Serbia	Petrovac Hotel Oliva	15/04/1979	6.9	0.454	0.388	25	1
00535ya	Erzican Turkey	Erzican-Mudurlugu	13/03/1992	6.6	0.769	1.077	13	1.5
00187xa	Tabas, Iran	Tabas	16/09/1978	7.3	0.926	0.844	57	1
00291ya	Campano Lucano, IT	Calitri	23/11/1980	6.9	0.264	0.413	16	1.5
004673ya	South Iceland	Hella	17/06/2000	6.5	0.716	0.720	15	1.5
004677ya	South Iceland	Selsund	17/06/2000	6.5	0.227	0.208	21	1

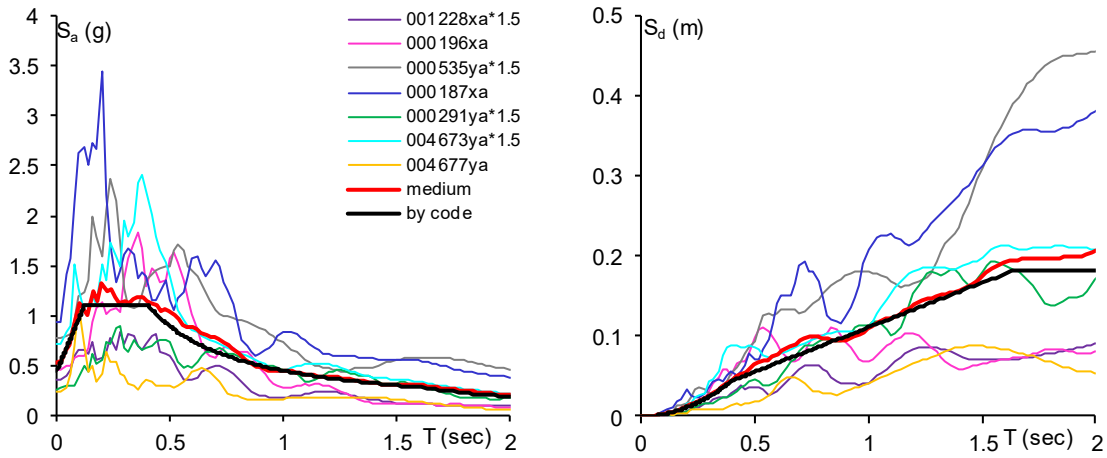

Figure 30. Selected earthquake inputs for shaking table testing and design spectra.

The shake table testing program of all experimental configurations (bare frame F, dissipative frame DF and braced frame BF) for the seven selected seismic inputs is summarized in Table 11. The intensity of the ground motion was progressively increased in acceleration for earthquake cases 1228, 196, 535 from 10% to 100% of average PGA for DF and BF configurations, in order to provide additional information regarding the frame response at varying damage levels. In case of bare frame (F) the PGA level was increased up to 75% because an imposed interlock of 3.5% of maximum inter-storey drift was reached, except for the weaker earthquake (ID code 1228).

Table 11. Testing program for F, DF and BF model configurations.

PGA (%)	*Seismic Inputs*						
	1228	*196*	*535*	*187*	*291*	*4673*	*4677*
10	F, DF, BF	F, DF, BF	F, DF, BF	-	-	-	-
25	F, DF, BF	F, DF, BF	F, DF, BF	-	-	-	-
50	F, DF, BF	F, DF, BF	F, DF, BF	F, BF	F, BF	F, BF	F, BF
75	F, DF, BF	F, DF, BF	F, DF, BF	-	-	-	-
100	F, DF, BF	DF, BF	DF, BF	DF, BF	DF	DF	DF

During any dynamic campaign it is important to control the input acceleration. The control performance of shaking tables is greatly affected by the interaction between the table and the test specimen, because the dynamic characteristics of large specimens can give significant force disturbances to the table. For this reason, during dynamic campaigns it is important to control the input acceleration and compare them with the acceleration recorded on the shaking table with the specimen if good control is desired. As mentioned in Section 4.2.1 the shaking table was displacement controlled. During dynamic testing of the model the frequency content of the seismic input, measured by the accelerometers placed on the shaking table, was compared with the desired input for each ground motion. Figure 31a shows the comparison for three seismic inputs 1228, 196 and 535 at all PGA levels. It was observed that the recorded response spectra earthquake motions at the shake table with the BF model matched well with the desired spectra of the original seismic input at all intensities around the fundamental frequency of the BF model. It ranged over the desired spectra at high frequency range at lower intensities (10% and 25% of PGA), which may have a slight impact on the seismic response of the model at higher modes. Moreover, the desired and the actual pseudo-velocity spectra response have been considered to evaluate the seismic input energy for all earthquakes at all PGA levels based on the Housner Spectrum Intensity (S_I) [126]. Figure 31b compares the desired and actual integral function S_I (area under the pseudo-velocity response spectra) computed in the period range T = 0-4 sec. As can be observed a good agreement was obtained at all PGA levels for all earthquakes.

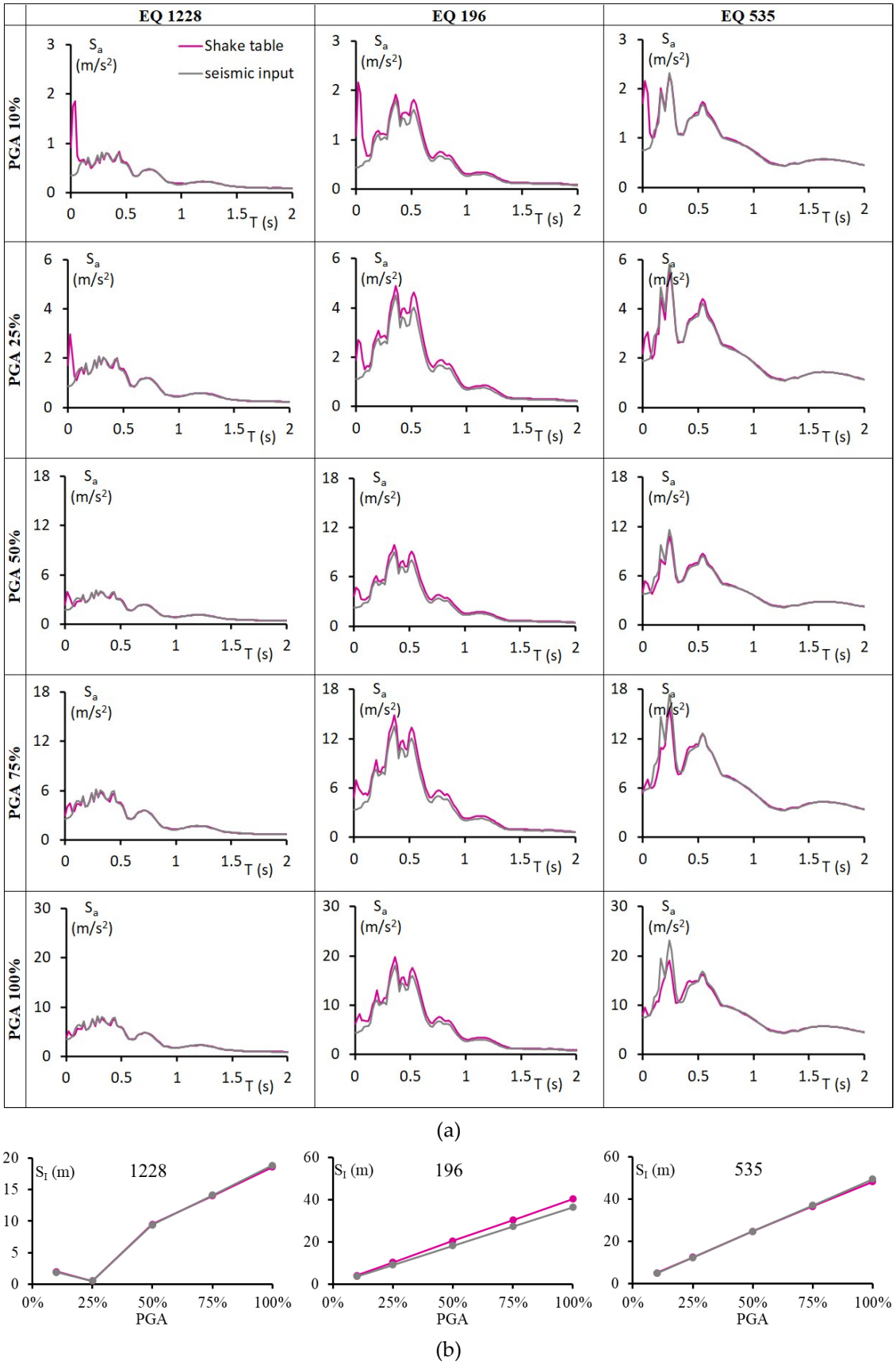

Figure 31. (a) Comparison between: (a) desired and actual frequency content and (b) Housner intensity by desired and actual velocity spectra of BF model for earthquake inputs 1228, 196 and 535 at all PGA levels.

At the end of the experimental campaign the post-tensioned timber frame model was disassembled in two days by two workers, no damages were observed on the structural elements. The possibility of reuse and recycling the structural elements is an important characteristic and advantage of timber constructions to extend the service life of building materials and elements, potentially reducing future resource consumption, waste generation and environmental impacts of future constructions.

5 Experimental results

This chapter describes the experimental study performed on the 3-storey post-tensioned timber framed (Pres-Lam) building model equipped with different supplemental damping systems. The shaking table tests of the post-tensioned timber frame with dissipative bracing systems (BF model) performed during this doctoral research project has been investigated and compared with the previous two configurations of the of the experimental campaign considering the bare frame with post-tensioning only (F model) and with dissipative rocking mechanisms (DF model) [13],[125]. The dynamic properties and the main global and local seismic parameters have been investigated.

5.1 Dynamic characteristics of the prototype models

The dynamic properties of the experimental model for the three considered configurations have been identified by dynamic characterization tests. Hammer impact and pink noise excitation sources have been performed for the Welch's Power Spectral Density (PSD) estimation [127]. Figure 32 show the experimental results in terms of frequencies corresponding to the first and second vibration mode in the main direction for the braced frame BF (blue line), dissipative frame DF (red line) and bare frame F (black line).

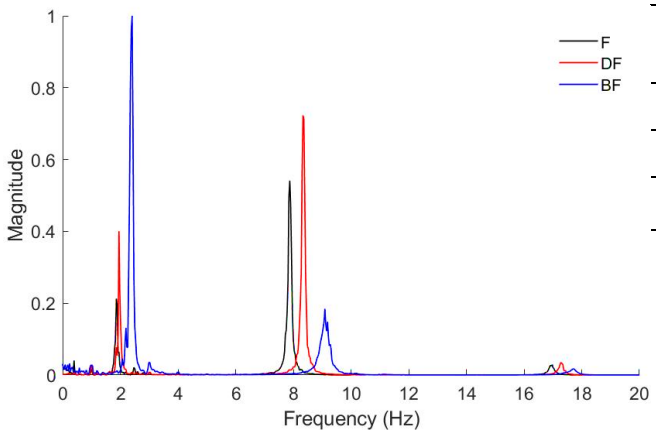

Model Configuration	Frequency (Hz)		
	Mode 1	Mode 2	Mode 3
F	1.9	7.9	17.0
DF	2.0	8.4	17.3
BF	2.4	9.1	17.7

Figure 32. Frequencies of first three modes of vibration before testing for: bare frame (F), dissipative frame (DF), braced frame (BF).

As the mass remained almost the same, this result highlight, as expected, a greater stiffness of the BF model respect to the DF and F ones, more evident for the second mode.

All detected frequencies and the relevant modes were used to calibrate the numerical models. More details about numerical modelling and comparison between numerical analysis and experimental results are reported in Chapter 6.

5.2 Global seismic response

The global seismic response of shaking table tests performed on the three model configurations has been presented for three selected seismic inputs (1228, 196 and 535) at all PGA levels. In Figure 33 the spectra of selected ground motions and their average spectra are compared with the elastic design (DBE) spectrum and the experimental fundamental periods of the three configurations have been also indicated.

The global seismic response of F, DF and BF model configurations has been investigated in terms of distribution along the building height of the maximum and mean values maximum of the experimental maximum values of key parameters for all tests, time histories of drift and acceleration and global hysteresis.

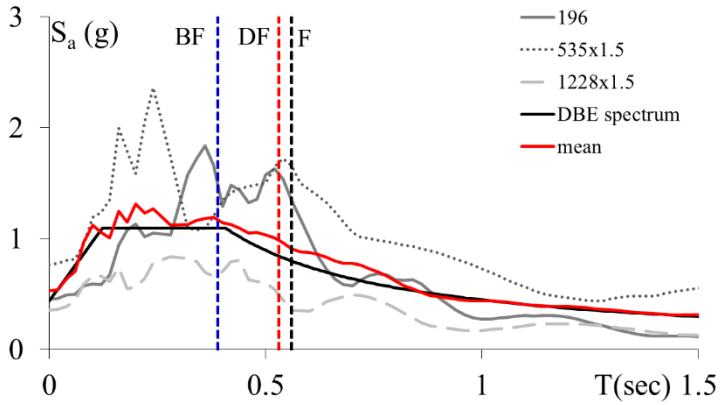

Figure 33. Seismic inputs selected for experimental results comparison.

5.2.1 Maximum key parameters

Figure 34 shows the distribution along the building height of the maximum and mean values maximum inter-storey drift (MID), maximum storey displacement (MD) and acceleration (MA) and maximum columns shear force (MCF). As can be observed, the effect of the dissipating braces is clearly evidenced from the reduction of MID and MD values. Comparing the MID of the three configurations no significant variations of the mean values were observed up to 25% of PGA. It is worth noting that the dissipative devices become effective in reducing the drift respect to the bare frame F when the earthquake intensity exceeded a threshold value of 25% of PGA as a function of the yield strength of the dampers. In particular, for the BF model at 75% of PGA the values of MID and MD reduced of about 20% than DF model and of about 45% than F model, while MA values were similar for all configurations due to the additional damping of the dissipative bracing system. It is interesting to note that for the BF configuration the values of the MIDs at all stories were comparable (this means an optimal activation of the dampers) and the mean value of MID was about 1.5% at 100% of PGA, coherently with experimental results of post-tensioned timber structures with rocking walls at the DBE level [10][11]. This result further proved the reliability and robustness of the design procedure (design drift 1.25%) meeting the criteria for regularity in elevation required by code for buildings categorised as regular in elevation.

The MCF profiles highlighted that the introduction of dissipative bracing systems was effective in reducing the columns shear respect to DF and F configurations. The bare frame F and the dissipative rocking frame DF exhibited the highest values of MID and MA when subjected to the earthquake 535, characterized by high spectral values in comparison with those of the elastic design spectrum in the range of vibration periods of interest for the examined cases ($T1 > 0.5$ s). The earthquake 196 provided the highest response for the braced frame BF, this behaviour can be explained comparing the spectral acceleration corresponding to the fundamental vibration periods of the structure with damped braces (see Figure 33).

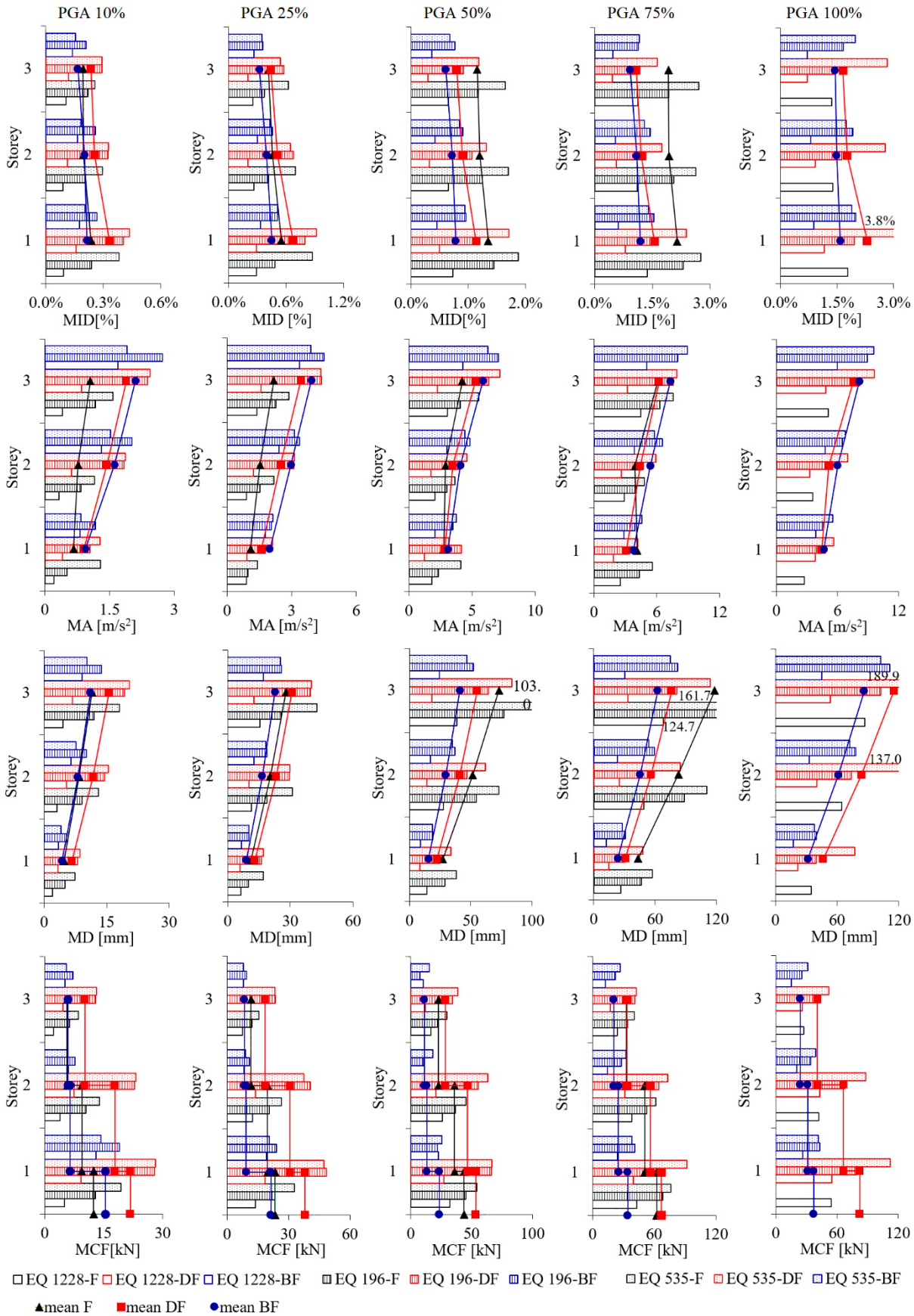

Figure 34. Distribution along the building height of the experimental maximum values of key parameters for all tests.

The results of BF model under the seismic action having a larger probability of occurrence than the design seismic action (50% of PGA), showed that the "damage limitation requirement" was satisfied (UNI EN 1998-1 2013), limiting the average values of maximum inter-storey drift to MID < 0.75% (see mean BF of Figure 34), in accordance with buildings having ductile non-structural elements.

The maximum global base shear and corresponding mean values are shown in Figure 35 for all configurations of selected seismic inputs at increasing PGA levels. The base shear is obtained by subtracting from the actuator force the contribution of the shake table due to its inertial mass (5kN) and frictional forces (friction coefficient less than 1%). As expected, the global base shear reached by the BF, evaluated as the sum of shear columns and braces, was greater than ones relevant to DF and F configurations.

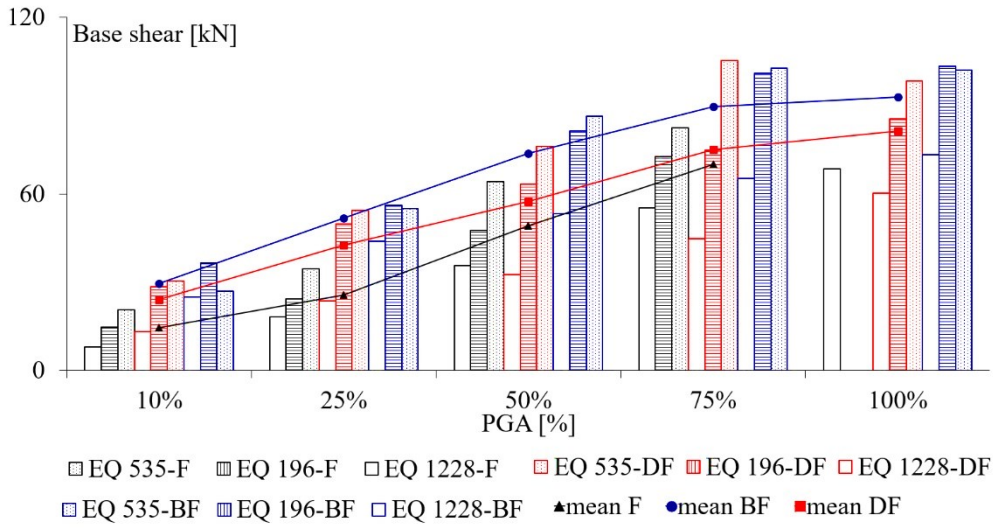

Figure 35. Base shear profile at increasing PGA levels for selected seismic inputs.

5.2.2 Drift and base shear time hystories

The time histories of first storey drifts and of base shear are reported in Figure 36 Figure 37, respectively, for all testing configurations considering the seismic inputs at 25% and 75% of PGA levels. The comparison confirmed a drift increasing of about 2 times of the maximum peak values for F and DF models respect the BF model. The recorded time histories highlighted that all configurations of the building frame were able to recentre with negligible residual drift even for large ground motion events.

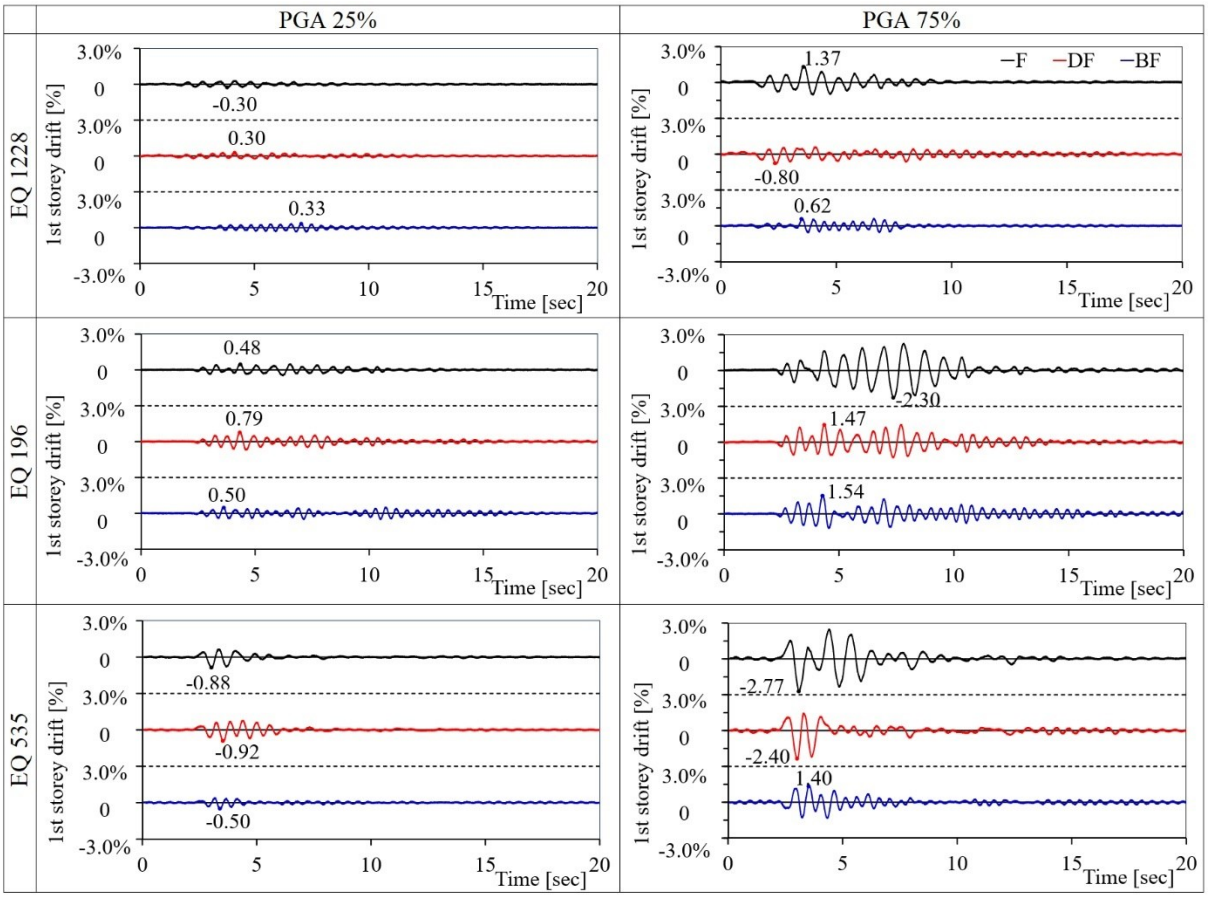

Figure 36. Inter-storey drift time history for selected seismic inputs at 25% and 75% of PGA levels for all test configurations.

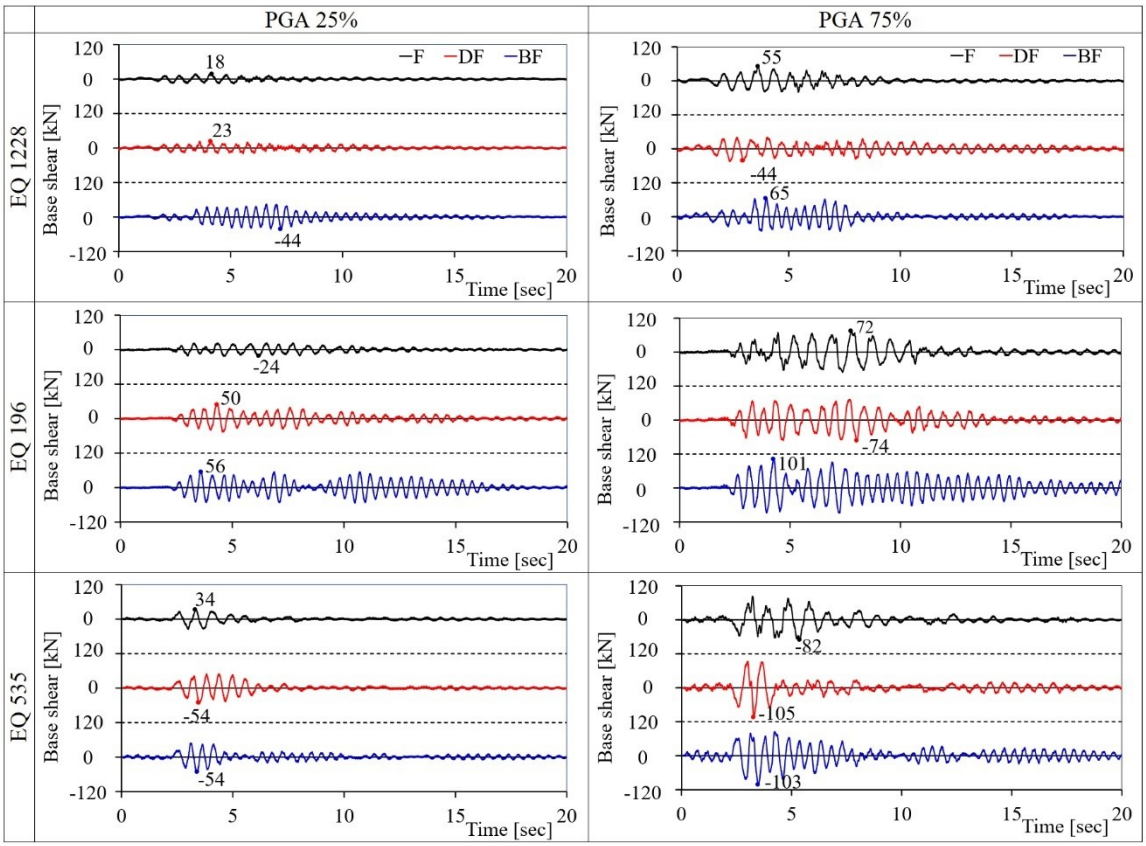

Figure 37. Base shear time history for selected seismic inputs at 25% and 75% of PGA levels for all test configurations.

5.2.3 Global hysteresis

The global building hysteresis in terms of base shear vs inter-storey drift for all testing configurations are shown in Figure 38, Figure 39, Figure 40, considering all selected seismic inputs at 25%, 75% and 100% of PGA levels, respectively.

The hysteresis curves at low-level ground motions (PGA level of 25%, see Figure 38) show that the frame responses of all configurations are nearly elastic. In case of strong earthquakes (Figure 39 and Figure 40) the global flag shape hysteretic loop was more evident.

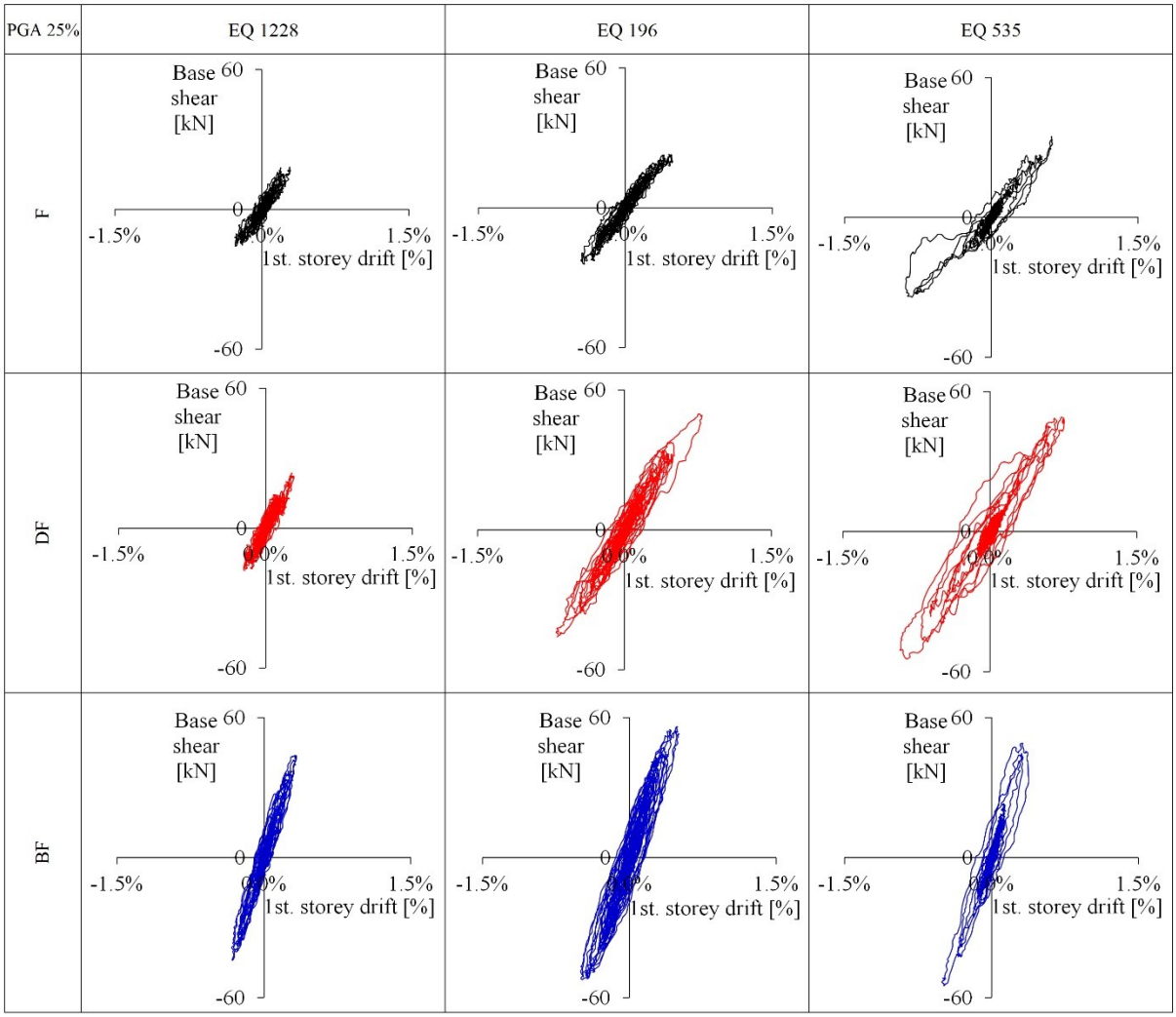

Figure 38. Base shear vs inter-storey drift for selected seismic inputs of all testing configurations at 25% of PGA.

As can be observed, the braced frame BF configuration was able to dissipate higher amount of energy through hysteretic damping for the strongest earthquake inputs (EQ 196 and EQ 535). In case of tests with earthquake EQ535, from Figure 39 and Figure 40 is evident that the seismic response of the structure was drastically reduced in terms of drift amplitude with a slight increase of base shear when the dissipative bracing systems were used.

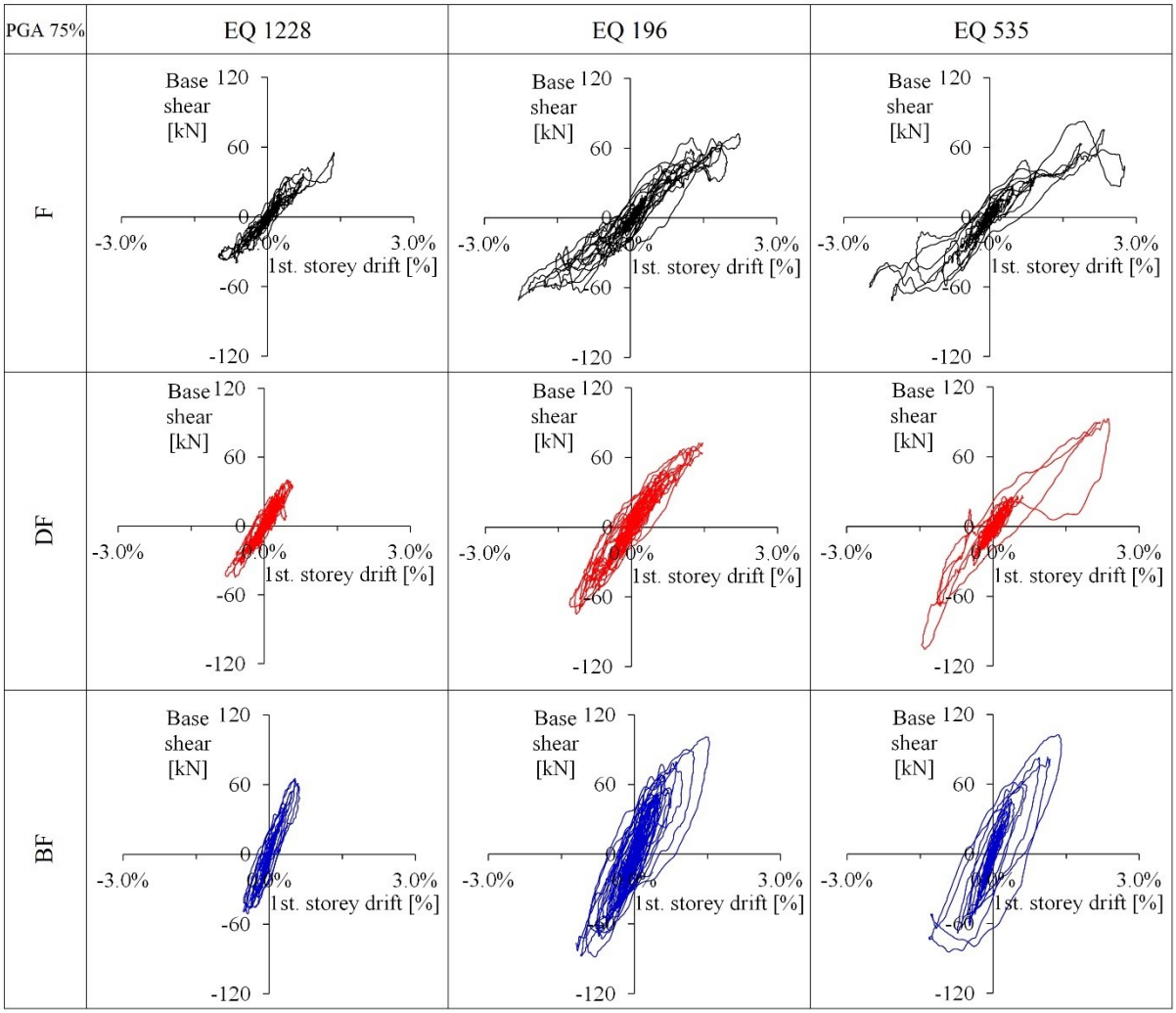

Figure 39. Base shear vs inter-storey drift for selected seismic inputs of all testing configurations at 75% of PGA.

The braced model configuration BF permitted the highest value of PGA to be reached, without visible structural damage. The overall hysteretic energy dissipation is a reflection of many contributors, mainly including the yielding of hysteretic dampers and nonlinear geometric behaviour of rocking mechanisms of beam-column joints and of column-foundation connections.

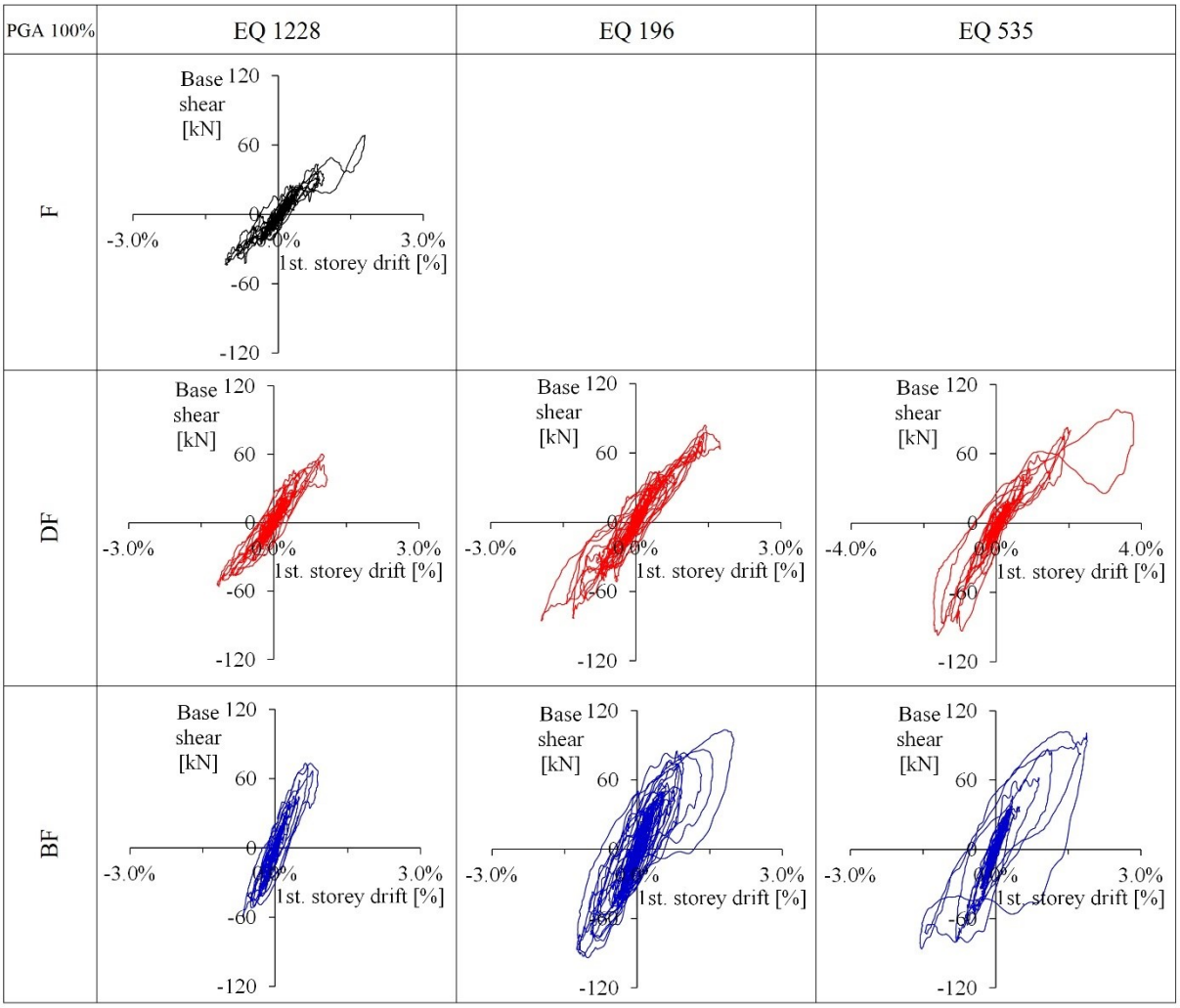

Figure 40. Base shear vs inter-storey drift for selected seismic inputs of all testing configurations at 100% of PGA.

5.3 Local response

The local response of the post-tensioned timber model has been investigated in terms of hysteretic beam-column and column-foundation response of the frame with and without dissipative rocking mechanisms (F and DF configurations) and the local hysteretic force-displacement response of the UFP dampers installed into the dissipative bracing systems. Moreover, the maximum variation of post-tensioning and seismic post-tensioning losses in the three different configurations has been analysed. Finally, the hysteretic energy dissipated at the design level (100% of PGA) by the angle

devices at the beam column joint in DF configuration and by the U-shaped Flexural plates installed into the bracing system have been compared.

5.3.1 Beam-column joints

The local response of the beam column joints is a fundamental aspect in the post-tensioned frame buildings. During dissipative rocking mechanisms at the beam-column connection of DF, the initial post-tensioning force F_{PT}, plus increases due to gap opening ΔF_{PT} and yielding force F_y of the dissipative element, generate the whole moment capacity M, computed about the centroid of the resultant timber compression force. The rocking mechanisms both without (F model configuration) and with dissipative dampers (DF model configuration) have been investigated in terms of gap opening and amount of post-tensioning force, recorded by the three potentiometers placed across the beam-column connection by the load cells placed in each post-tensioned bar at all storey of the model (see Figure 27a).

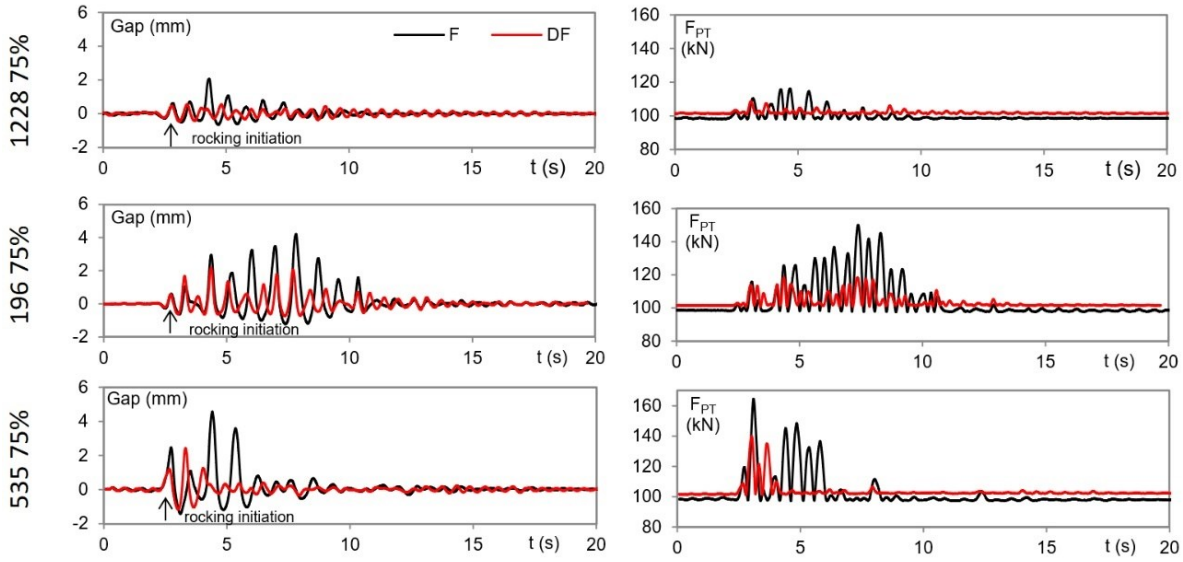

Figure 41. Time histories of gap opening, post-tensioning force of beam-column connection and moment-rotation response at the first storey for earthquake inputs 1228, 196 and 535 at 75% of PGA.

Figure 41 shows an example of the local time histories of post-tensioning force and gap opening (measured by top potentiometer) of the beam-column connection at the first storey for the earthquake inputs 1228, 196 and 535 at 75% of PGA level. The figure

shows that when gap opening occurs, rocking mechanism starts and the post-tensioning force begins to increase. A reduction of peak values of gap opening and post-tensioning force can be observed due to the additional energy dissipation capacity of dissipative-rocking systems in DF configuration.

In order to calculate the hysteretic contribution of steel angles the support of a simple numerical model was necessary. The dissipative hysteretic mechanism of steel angles (Figure 42) was simulated using nonlinear Bouc-Wen [128][129] link element with hysteretic force-displacement behaviour. The mechanical characteristics of the steel angles were evaluated by characterization tests (presented in Section 4.1). Nonlinear time history analyses based on gap opening recorded by displacement potentiometers were carried out for each seismic input.

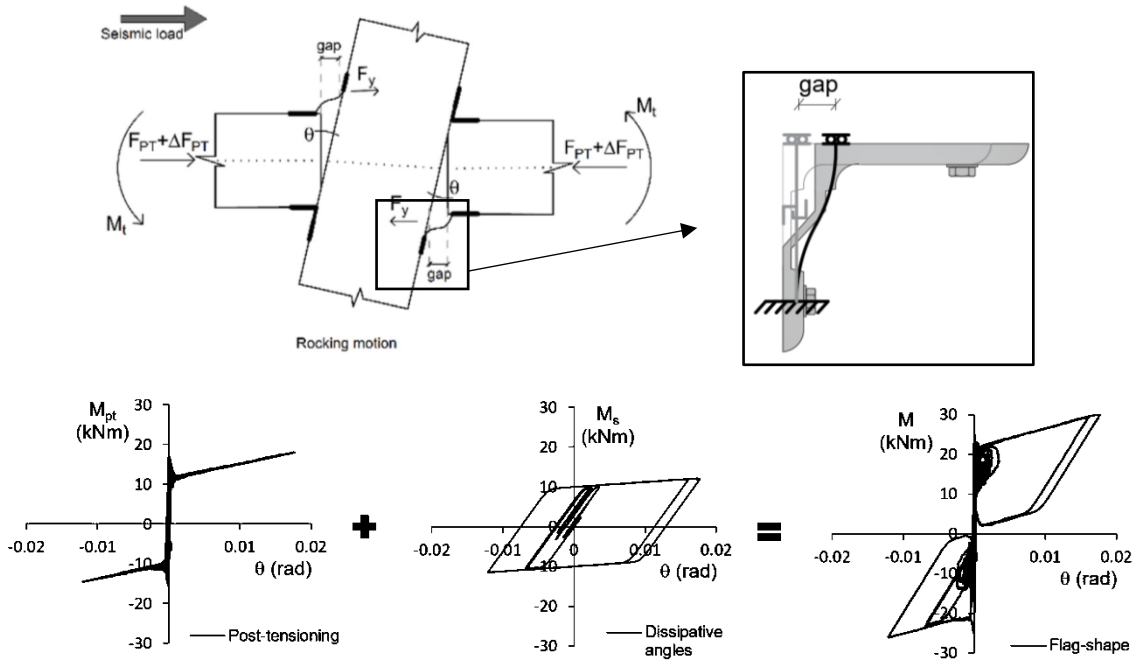

Figure 42. Sketch of dissipative rocking mechanism at the beam column connection and moment-rotation response.

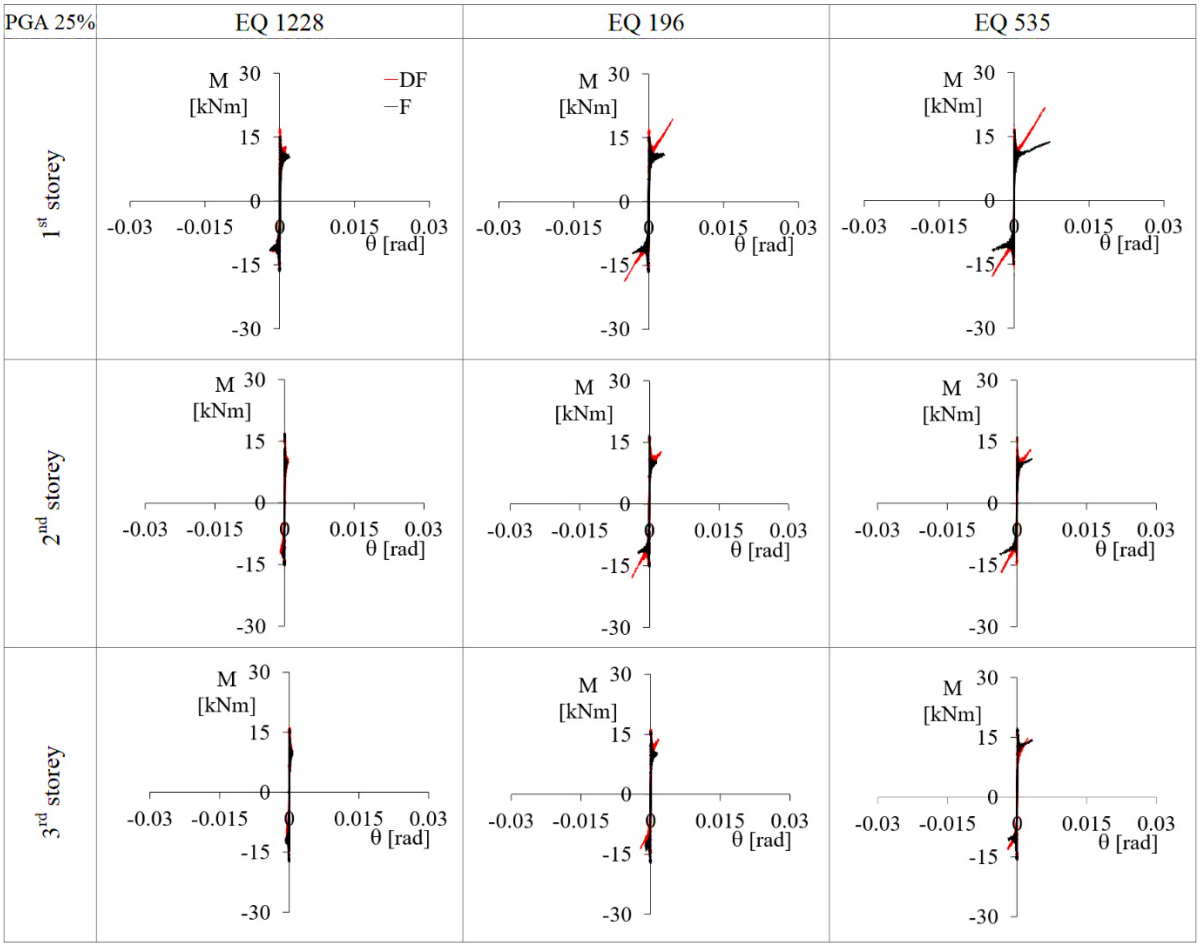

Figure 43. Moment- rotation of the beam-column connection at the three storey in F and DF configurations for seismic inputs 1228, 196 and 535 at 25% of PGA level.

Figure 43, Figure 44 and Figure 45 show the local response of the beam-column joint for all the three storey of the prototype frame without and with dissipative steel angles (F and DF configurations respectively) in terms of moment - rotation of the connection for 1228, 196 and 535 seismic inputs at 25%, 75% and 100% of PGA levels. As depicted, the post-tensioned connection of the bare frame (F) created an elastic bilinear system with self-centering of the post-tensioned beam-column joint in F configuration, and the typical flag-shaped hysteretic response in DF model for all ground motion intensities at each level. High dissipative capacity of steel angles was evident for highest seismic inputs 196 and 535.

In case of DF configuration, the steel angles of the post-tensioned connection remained in elastic range at 25% of PGA level with reduced rotations. The dissipative capacity was clearly observed at 75% and 100% of PGA level with the typical flag-shaped

behaviour of the connection and a complete re-centering capability. All tests sowed stable hysteretic behaviour. As expected by design, the dissipative angles were activated at all levels with an increase of the overall moment capacity and a reduction of the rotations. The graphs of the post-tension moment contribution versus rotation present a peak of the experimental moment due to dynamic effects at the beginning of the interface opening.

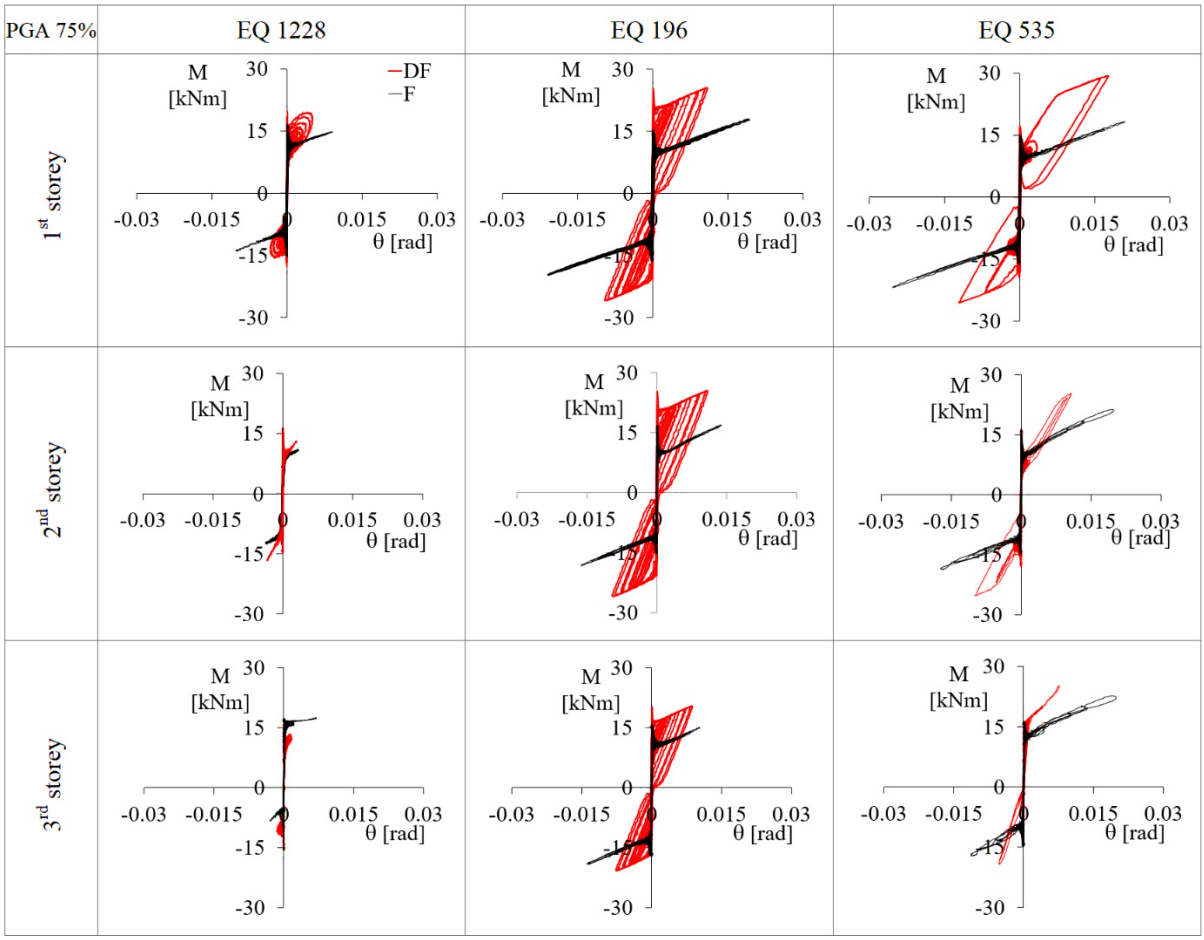

Figure 44. Moment- rotation of the beam-column connection at the three storey in F and DF configurations for seismic inputs 1228, 196 and 535 at 75% of PGA level.

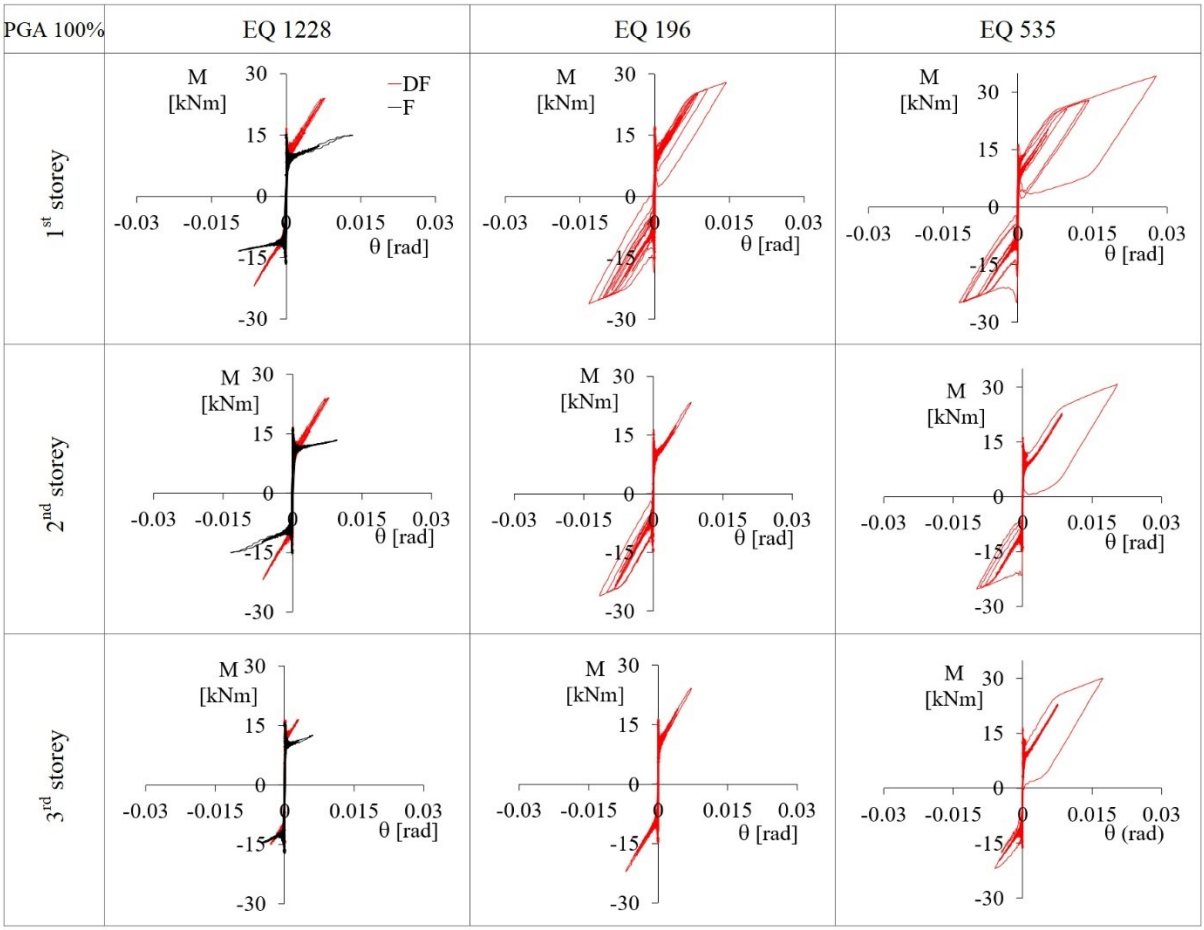

Figure 45. Moment- rotation of the beam-column connection at the three storey in F and DF configurations for seismic inputs 1228, 196 and 535 at 100% of PGA level

5.3.2 Column-foundation joints

Figure 46 shows an example of the local response of the south west column-foundation connection in F and DF configurations in terms of gap opening recorded at the column foundation connection by local potentiometers and in terms of column axial load N as gravity G plus seismic N_E contributions, for 1228, 196 and 535 seismic inputs at 75% of PGA. The analytical procedure used to determine distribution of internal actions and the various contributions of local moment-rotation response is based on the equilibrium approach [130] and discussed in the following Chapter 6 about numerical modelling.

It can be observed that when rocking motion starts the seismic contribution N_E of column axial load N changes as the column create a tension compression couple to resist overturning. When dissipative devices are present at the column-foundation interface the yield due to the column uplift during the frame displacement enables to increase the dissipation potential of the frame. As shown in Figure 46, when dissipative devices are introduced, a reduction of peak values of gap opening has been observed, preserving almost the same column axial load N for both configurations.

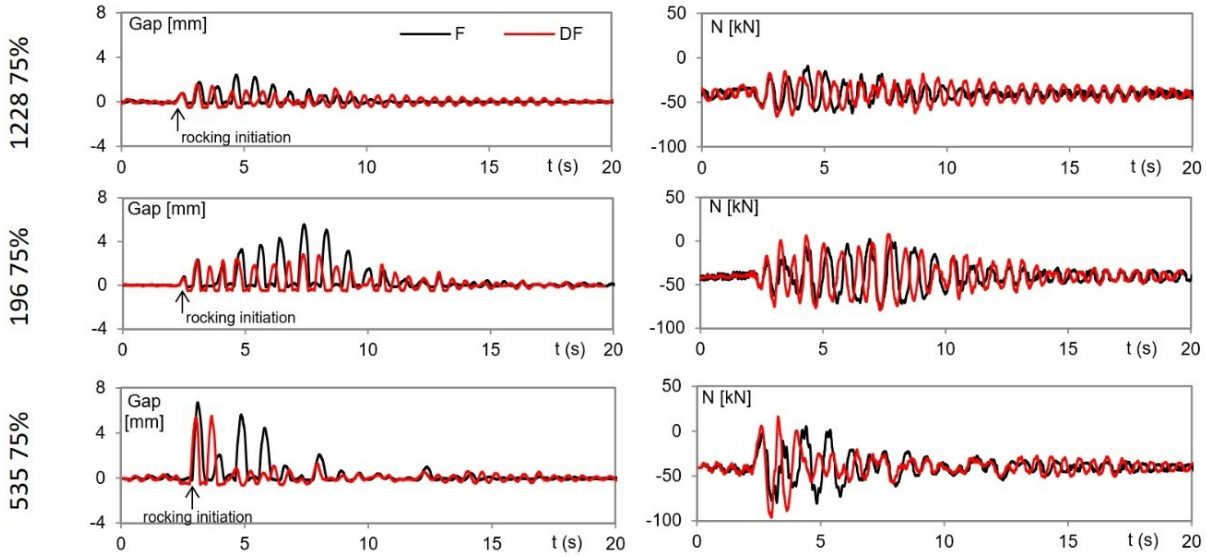

Figure 46. Time histories of gap opening, axial force of column - foundation connection for earthquake inputs 1228, 196 and 535 at 75% of PGA.

The test results display effectiveness in the design purpose of additional dissipative devices in reducing horizontal displacements, PT force demand and gap opening. The comparison between the free and dissipative-rocking configurations highlights the improved ultimate seismic performance of the structure due to the additional energy dissipation capacity and total moment resistance provided by the steel angles.

5.3.3 Dissipative bracing connection

The local hysteresis of the UFP dampers at the three storey of the braced frame BF are displayed in Figure 47 Figure 48 and Figure 49 in terms of force-displacement behaviour for the selected ground motions at 25%, 75% and 100% of PGA levels, respectively.

As mentioned above, figures show that the UFP dampers were not fully activated at lower intensities (25% of PGA, Figure 47) for all seismic inputs and were mobilized exhibiting an excellent dissipative capacity at higher PGA levels (75% of PGA, Figure 48, and 100% of PGA, Figure 49).

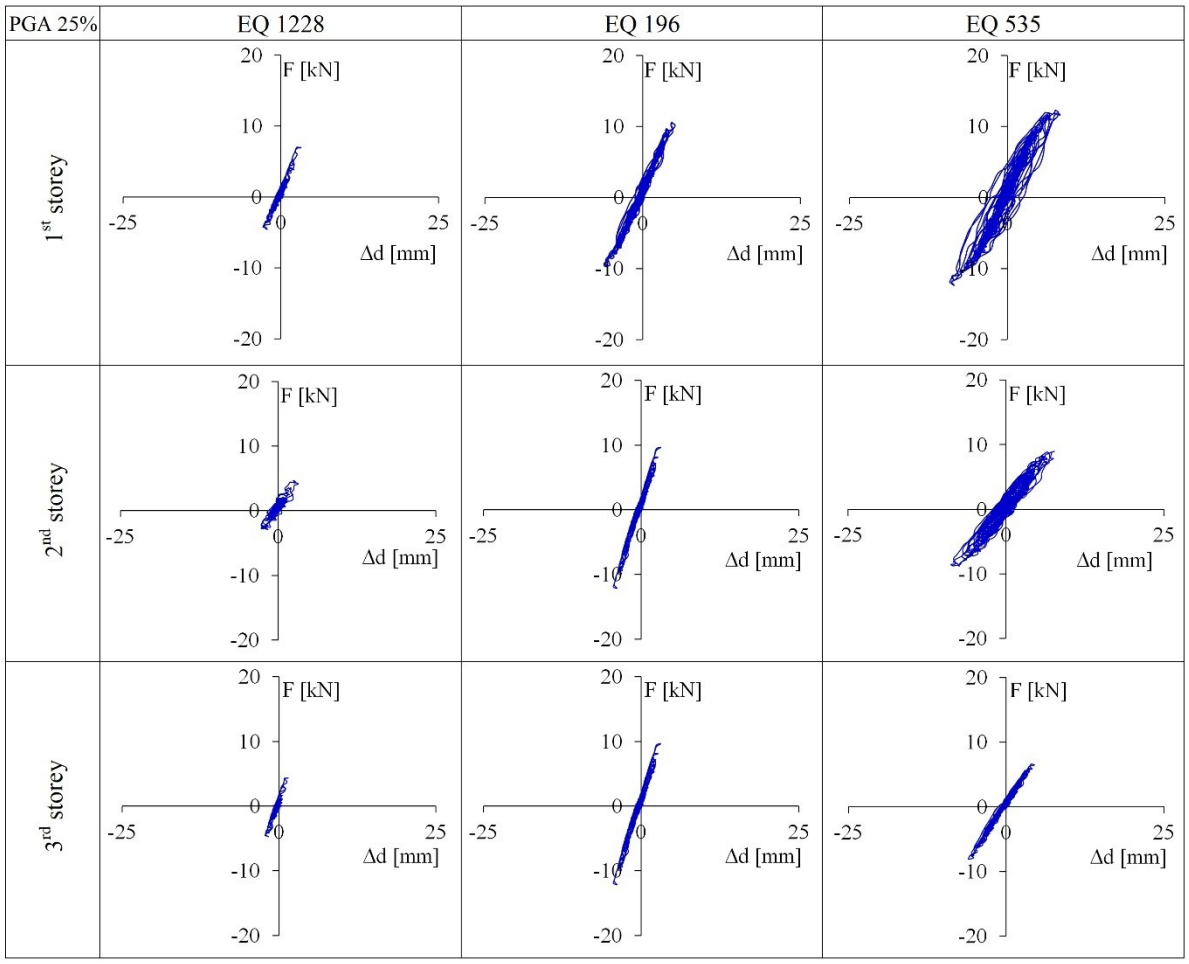

Figure 47. Force-displacement of UFPs of each storey of the BF model for selected seismic inputs at 25% of PGA.

The UFPs at all stories (UFP1, UFP2 and UFP3) showed a stable hysteretic behaviour without degradation in strength and stiffness with similar maximum displacements.

This response confirmed the uniform distribution of the maximum inter-storey drift (MID) along the building height (see Figure 34), thus minimizing the possibility of concentration of excessive inelastic deformation and damage in a single storey or in localized regions. It is pointed out that the characteristics of hysteretic behaviour of UFPs obtained from the dynamic tests are consistent with the results obtained by the quasi-static cyclic tests performed on the mock-up devices (see section 4.1).

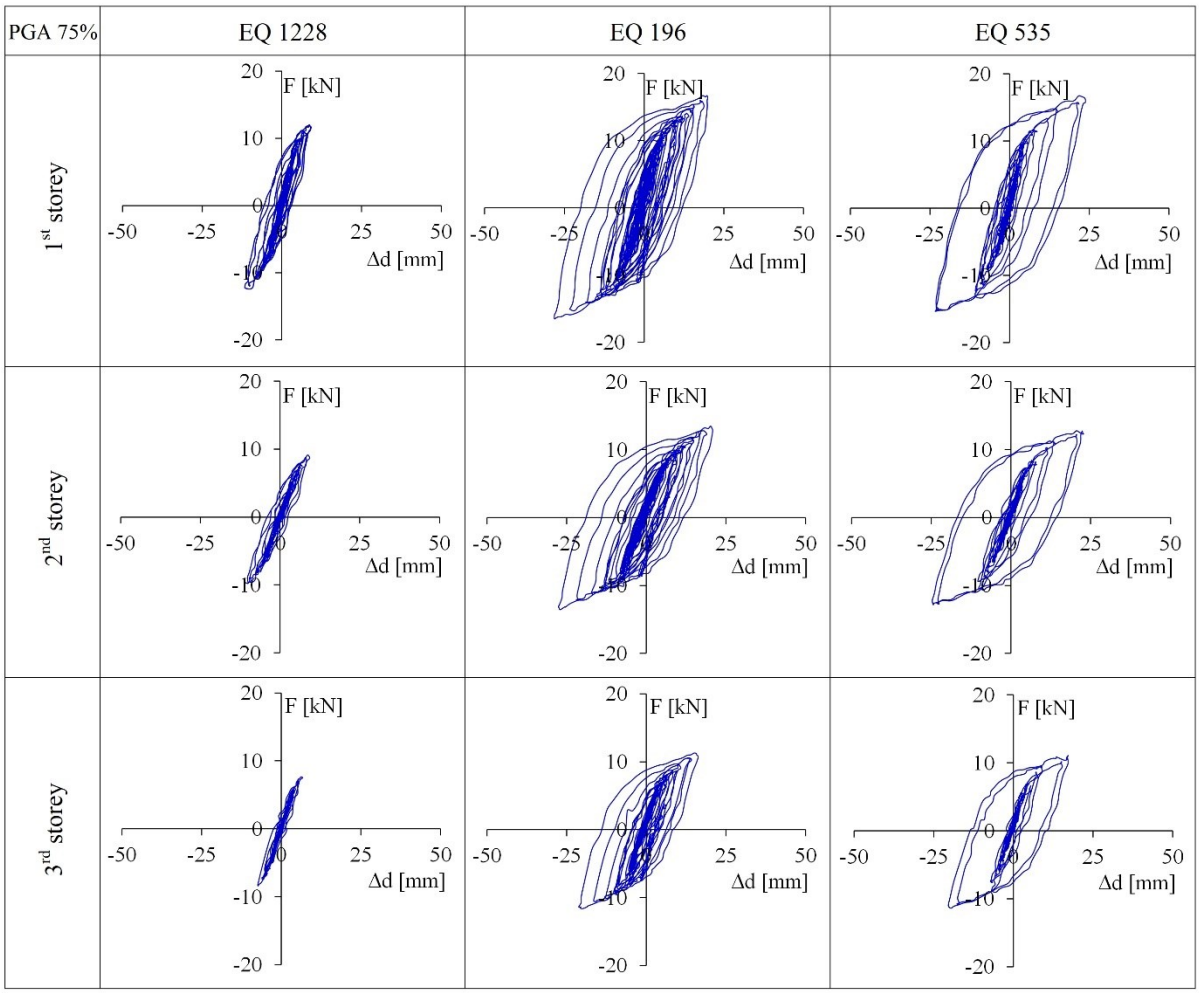

Figure 48. Force-displacement of UFPs of each storey of the BF model for selected seismic inputs at 75% of PGA.

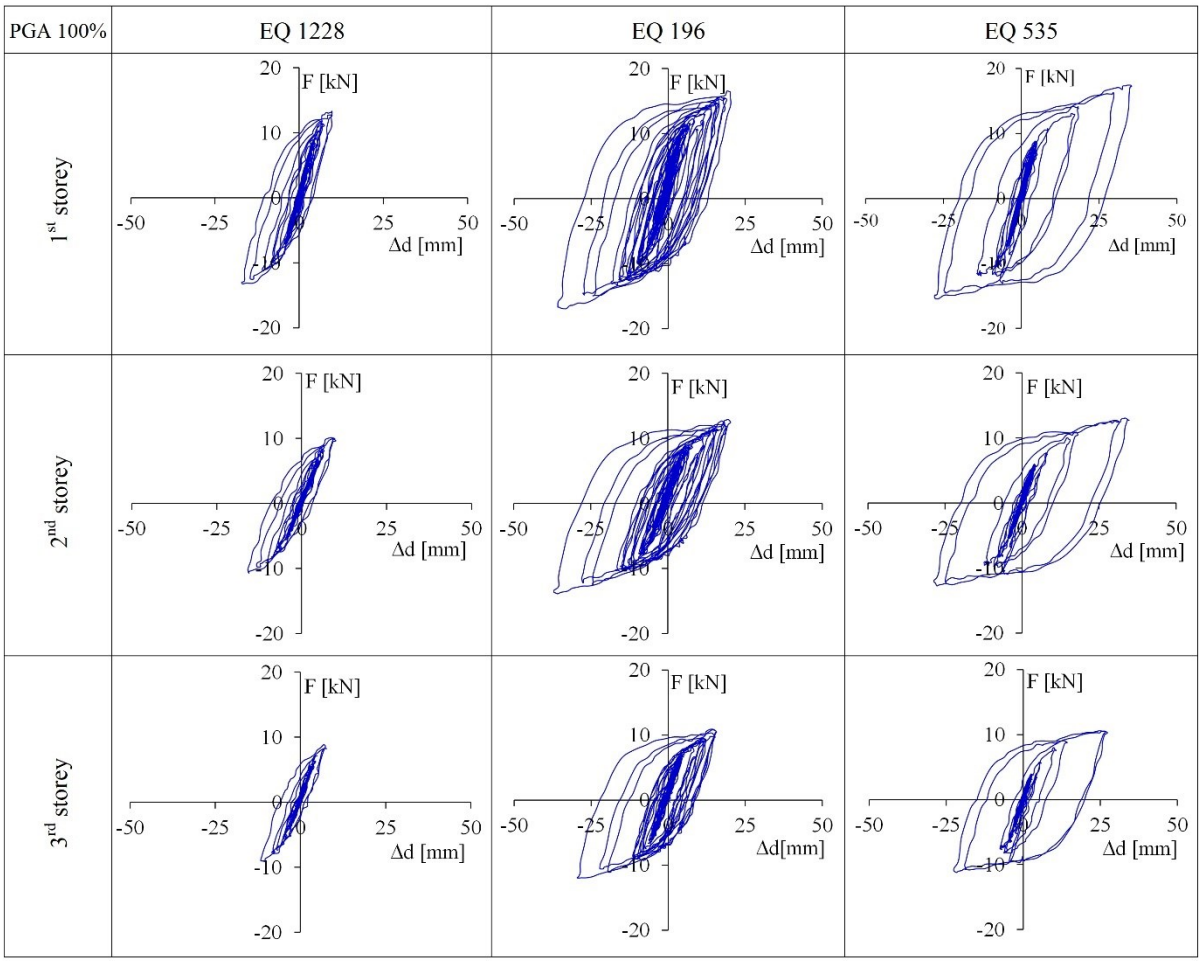

Figure 49 Force-displacement of UFPs of each storey of the BF model for selected seismic inputs at 100% of PGA.

5.3.4 Post-tensioning losses

Post-tensioning (PT) loss in post-tensioned timber framed buildings represents a crucial aspect which can led to reduction of the moment capacity of the connection, affecting the global seismic performance of the frame. Recent experimental and analytical studies [131],[132],[133] on post-tensioning loss deriving from creep phenomena in compressed timber elements showed expected losses in the range of 6-50% in 50 years. During the experimental campaign the long-term post-tensioning losses among the various configurations and seismic post-tensioning losses during shaking table tests have been recorded. The long-term post-tensioning losses at all levels both in longitudinal and transversal direction of F and DF configurations are

shown in Figure 50 in terms of post-tensioning force (F_{PT}) recording over time and in Table 12 in terms of post-tensioning losses percentages. The post-tensioning losses were recorded over a time period of about one year after testing of F configuration and over about three years after testing of DF configuration. As expected, a decreasing trend was observed in both configurations. Highest post-tensioning losses were recorded for both F and DF in the transversal direction, in which the initial post-tensioning was half than that in the longitudinal direction. It can be pointed out that by comparing the trend of post-tensioning force recorded for F and DF specimens both in the longitudinal and transversal direction, higher post-tensioning losses can be observed in the frame with free rocking mechanism at the beam-column connections. This result highlight that post-tensioning losses can be significant when the PT connection is left to transfer the post-tensioning load.

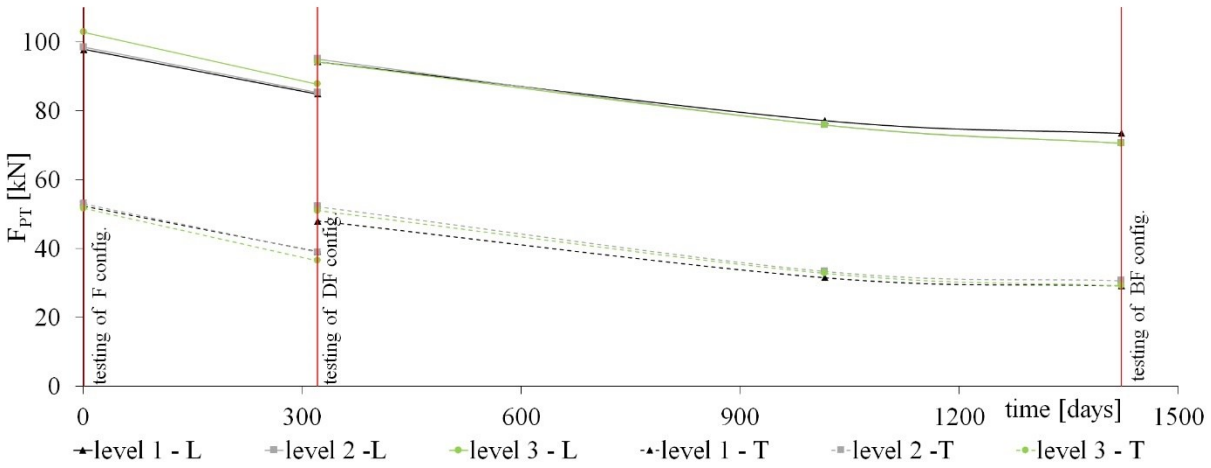

Figure 50. Post-tensioning losses over time after testing of F and DF configurations at all storey in longitudinal and transversal directions.

Table 12. Post-tensioning losses recorded over time at all storey for the F and DF configurations.

		Post tensioning losses [%]					
		Longitudinal			Transversal		
Model Config.	Δt [days]	1st storey	2nd storey	3rd storey	1st storey	2nd storey	3rd storey
F	321	15%	13%	13%	29%	27%	25%
DF	1101	25%	26%	22%	43%	41%	39%

During shaking table tests the post-tensioning variation $\Delta F_{PT} = (F_{PT,max} - F_{PT,initial})$ for the three testing configurations (F, DF and BF) have been compared both in terms of time history and ΔF_{PT} versus drift at the first storey of the testing frames. Figure 51 shows the post-tensioning variation time histories of the first storey beam column connection. Post-tensioning variation versus drift of the F, DF and BF for the three selected inputs at 25% and 75% of PGA level are shown in Figure 52 and Figure 53.

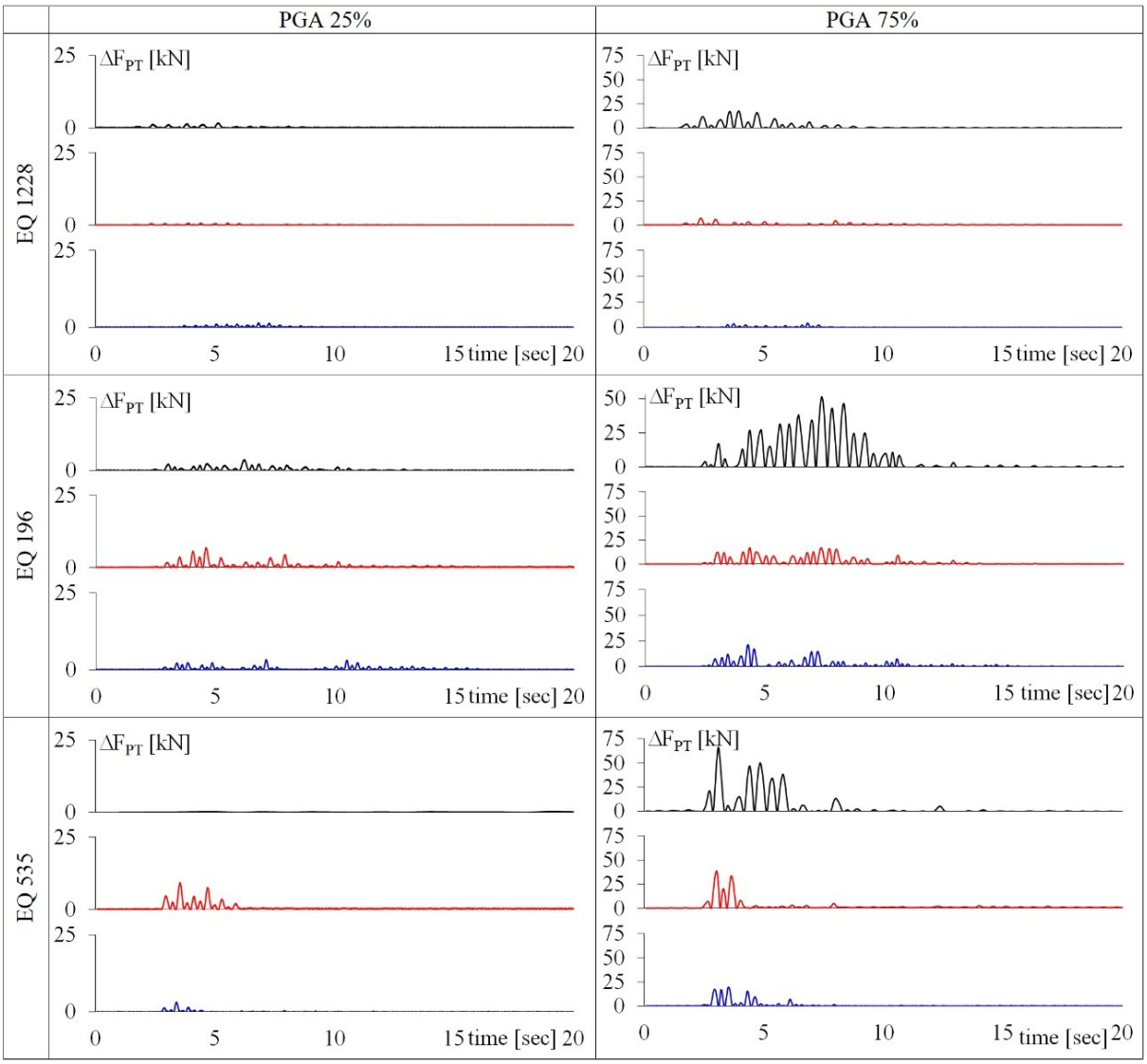

Figure 51. Post-tensioning variation time histories at the first storey beam-column connection for seismic inputs 1228, 196 and 535 at 25% and 75% of PGA levels.

As can be observed at low PGA level due to the elastic response of the frame the PT bar was slightly activated for all seismic inputs with a maximum PT variation of 12 kN in F configuration. At PGA 75% the re-centering effect due to the post-tensioning is

more evident in all configurations. It can be observed that increasing amount of energy dissipation introduced in the frame (passing from F to DF to BF configurations) led to a significant reduction of drift and of post-tensioning force variation demonstrating the effectiveness of the design procedure. In all cases a complete re-centering of the connection is observed without damages on the structural elements in all configurations tested. The maximum and mean variation of post-tensioning force ΔPT are shown in Figure 59 for all configurations at increasing PGA levels. The maximum percentage of variation of PT force, calculated as $\Delta PT = (PT_{max} - PT_{initial}) /100$, was highest for the case of bare frame F model, with a mean value of ΔPT of about 50% at PGA of 75%. In case of BF model the mean value of ΔPT was almost 25% at PGA of 100%.

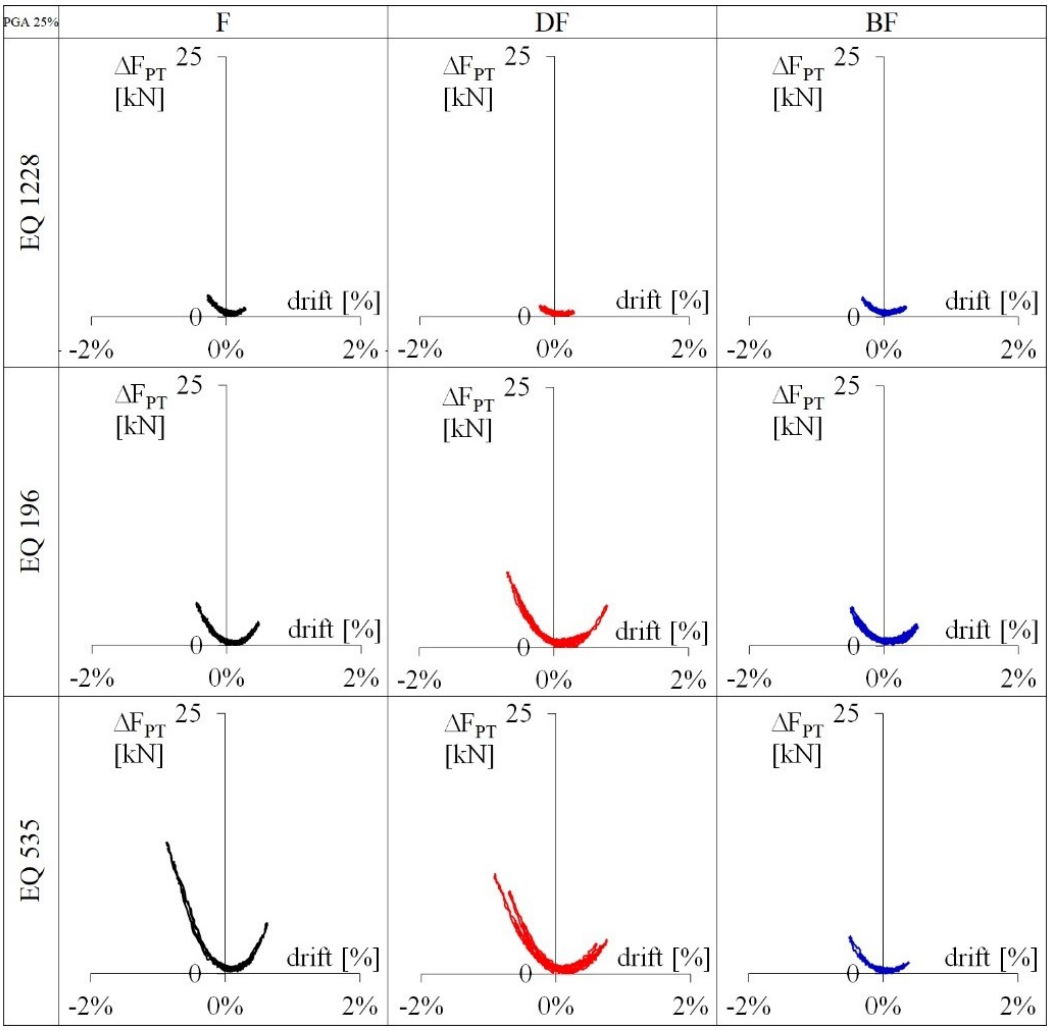

Figure 52. Post-tensioning variation versus drift for the three selected seismic inputs at 25% of PGA.

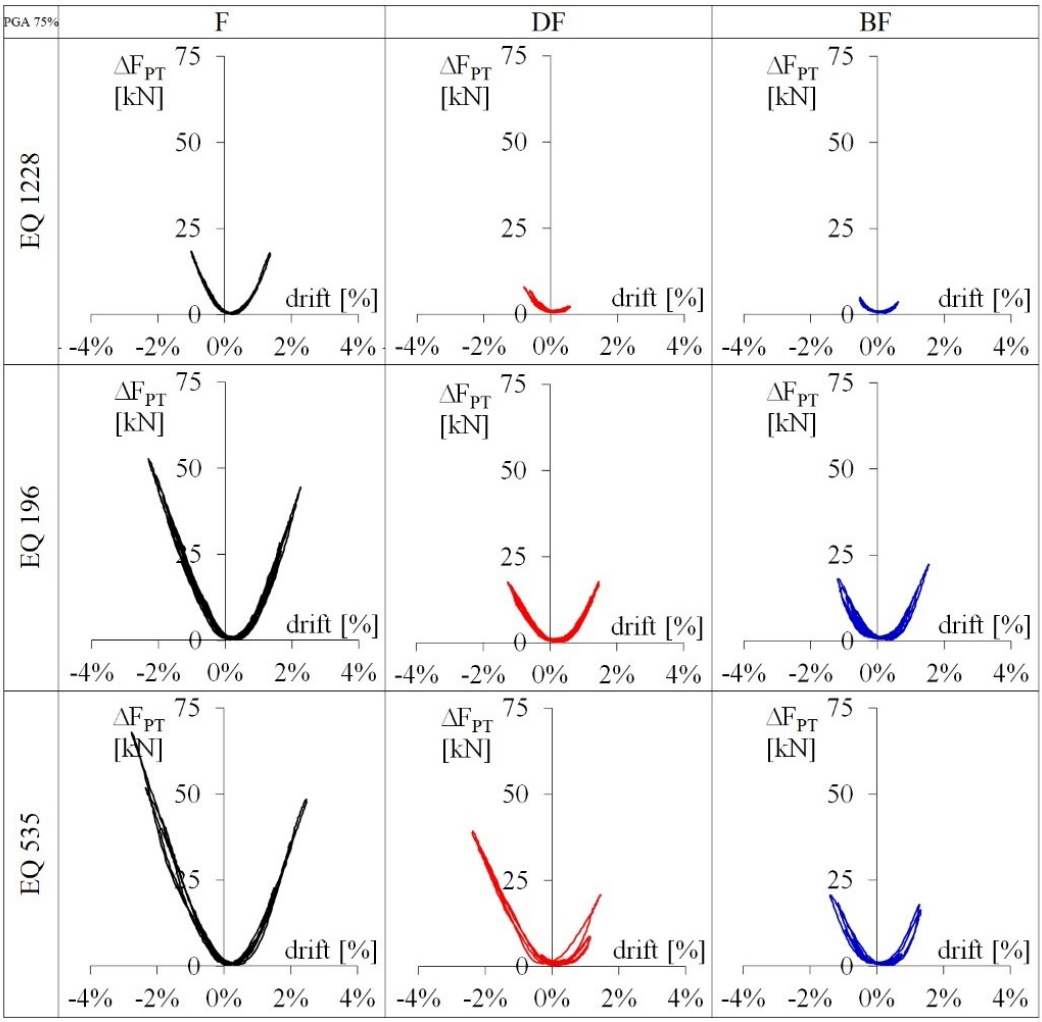

Figure 53. Post-tensioning variation versus drift for the three selected seismic inputs at 75% of PGA.

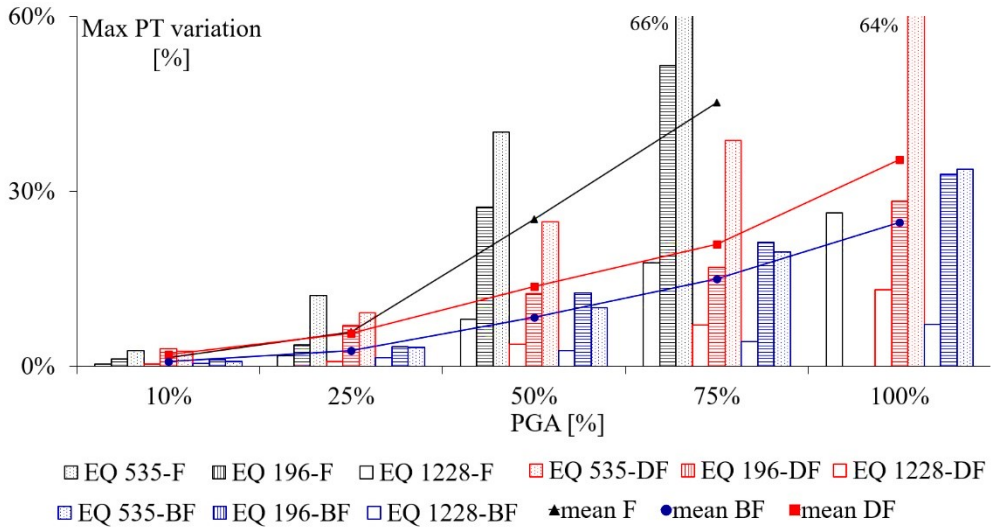

Figure 54. Maximum post-tensioning force variation profiles at increasing PGA levels for the three selected seismic inputs.

Seismic post-tensioning losses due to subsequent earthquakes have been also investigated, considering the complete sequence of seven spectra-compatible seismic inputs at all PGA levels for each shaking table testing configuration of F, DF and BF model. During shaking table tests of the complete set of ground motions for each model configuration increasing PGA levels (from 10% to 100%), the post-tensioned bars were not re-tensioned, highlighting the capability of the building to withstand multiple consecutive strong earthquakes. Figure 55 shows the post-tensioning loss due to seismic action, defined as the variation between the initial and the final value of the post-tensioning force recorded within the complete set of ground motion for each testing configuration at all levels both in longitudinal and transversal direction. It is negligible for the cases of bare post-tensioned frame F model and of braced frame BF model. It is slightly higher than 2% at all storey for the DF model configuration in the longitudinal direction due to the strengthening effect of dissipative angles of the post-tensioned beam-column joints.

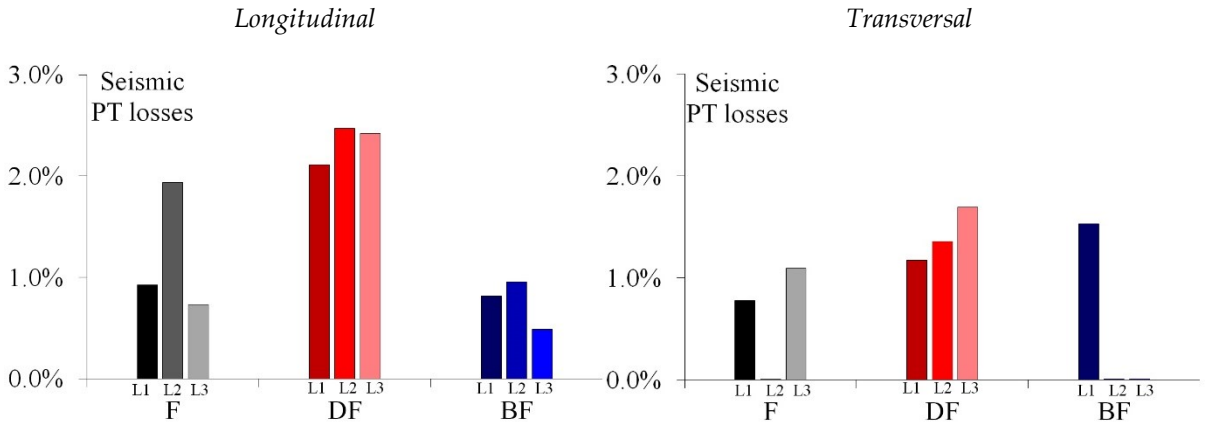

Figure 55. Seismic post-tensioning losses recorded for the three testing configurations at the three levels in longitudinal and transversal direction.

6 Numerical modelling of post-tensioned timber frame with dissipative systems

In structural design, it is crucial that simple models exist providing sufficiently accurate building response without requiring a large amount of time in processing or programming. From the beginning of the post-tensioned jointed ductile concept, it has been clear that the nature of the controlled rocking mechanism leant itself well to the use of a lumped plasticity approach which combines the use of elastic elements with springs representing plastic rotations in the system.

In this chapter an alternative numerical modelling of the post-tensioned timber frame with free (F) and dissipative rocking (DF) has been proposed and compared with previous available models. The analytical procedure for modelling the rocking mechanisms at the column-foundation connection has been presented. Then, a numerical model of the post-tensioned timber frame with dissipative bracing systems (BF) has been developed with two different software (SAP2000 and OpenSees). The numerical simulations of F, DF and BF models have been calibrated against experimental results.

The main objective of this study is the validation of the seismic performance of the experimental predicting accurately the global and local seismic behaviour through non-linear time history analyses (NTHA) without requiring a large amount of computational time is an important task for an adequate modelling.

Based on the effectiveness of the numerical models, the design procedures presented in chapter 3 have been validated through the comparison with numerical and experimental results. Finally, the experimental equivalent viscous damping has been estimated and compared with numerical outcomes and analytical procedures.

6.1 Modelling of post-tensioned timber frame with dissipative rocking

Two different numerical models have been developed to represent the timber frame both free and dissipative rocking mechanisms in F and DF configurations, as reported in previous studies [134], [12],[135]. A new modelling of f and DF model have been proposed in this study, introducing rotational springs at the base column connection (Figure 56). Elastic elements were used to represent the structural elements (beams and columns) and the plasticity was concentrated in rotational springs [12],[135]. The specimen at the beam-column joints (Figure 57) was modelled considering a combination of rotational springs to represent the contribution of the post-tensioning and of dissipative devices. The flexibility of the joint panel was accounted for introducing an additional linear rotational spring, with stiffness value opportunely calibrated for each model. Post-tensioning response was represented using tri-linear elastic moment rotation springs [136] and a Bouc-Wen [128][129] rotational spring model was used to represent the hysteretic steel elements (Fig. 3b).

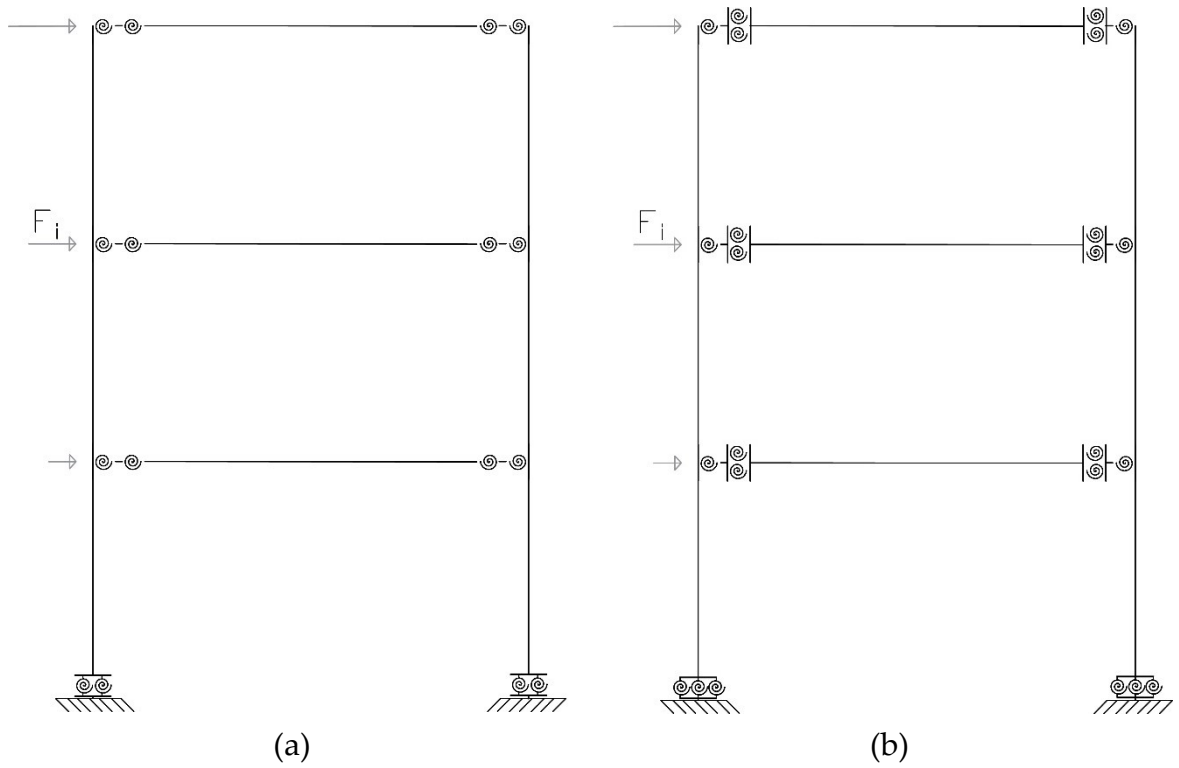

Figure 56. Numerical modelling (Model 2) developed for the post-tensioned frame in (a) F configuration and (b) DF configuration.

Previous studies modelled the base connection by using a pinned base connection or multi-spring link (Model 1) [12],[135]. In this study alternative modelling (Figure 56) of the free and dissipative rocking mechanism at the column-foundation connection (Model 2) has been proposed and compared with previous modelling.

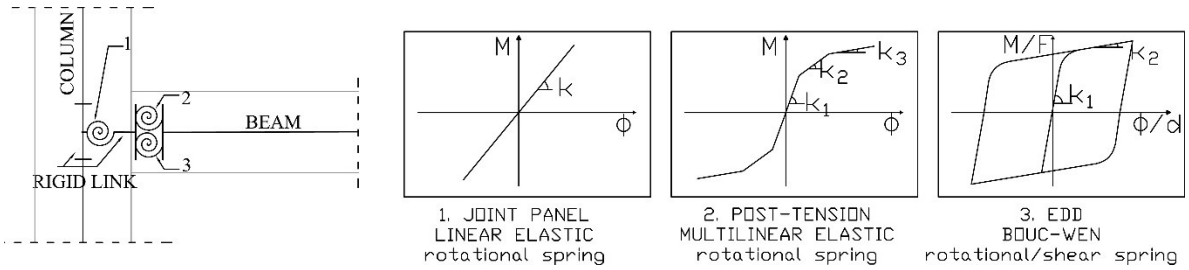

Figure 57. Numerical modelling of the beam-column joint of post-tensioned timber frame with dissipative angles (DF model configuration).

The varying column axial load complicates the modelling of the column base performance during seismic loading. When dissipative devices are not activated at the column base (F configuration), the column axial load, given by the contribution of gravity plus seismic axial load, provides the moment resistance. A simplified modelling was used to represent the free rocking at the column-foundation connection is given by the introduction of a perfectly pinned base (PB) constraint, (Model 1, free rocking - Figure 58a) however, this assumption cannot always provide an accurate representation of global seismic response. In order to improve the reliability of numerical F model, accounting for the base moment contributions, non-linear action of the critical rocking interface has been modelled (Model 2, free rocking - Figure 58c) by using two rotational springs (2RS) representing re-centering springs corresponding to the moment contribution of gravity and seismic axial load. Re-centering rotational springs have been calculated by applying an analytical model based on an equilibrium approach to determine varying of axial load caused by seismic action [130].

When dissipative devices are applied to the column base (DF model), an additional moment contribution must be accounted. In the Model 1, dissipative rocking has been modelled with a combination of axial springs [13], or multi-spring model (MS), which accounts for the sudden loss of stiffness due to gap opening but also allows for the change in capacity due to changing axial load (Model 1, dissipative rocking - Figure

58b). The multi-spring elements were modelled assigning a restraint to horizontal translation and using two axial gap links and Bouc-Wen linear springs placed in parallel 160 mm from the column centreline.

A different modelling of dissipative rocking was proposed [137] (Model 2, dissipative rocking - Figure 58d) introducing three rotational springs (3RS) representing re-centering springs corresponding to the moment contribution of gravity and seismic axial load and the hysteretic contribution of dampers with a Bouc-Wen model.

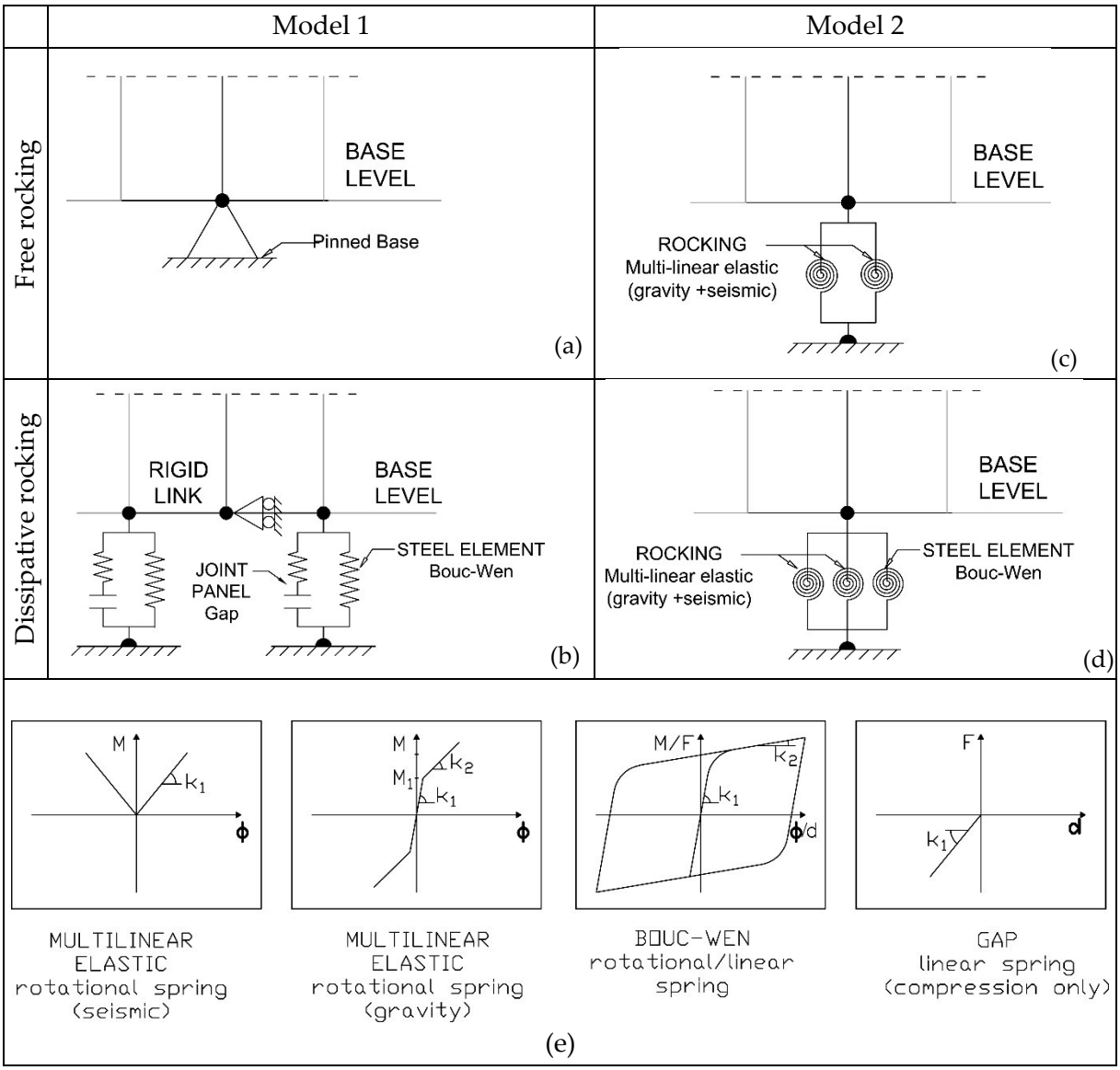

Figure 58. Numerical models of base column connection: (a) Model 1 with Pinned Base (PB) for free rocking and (b) Multi-Spring model (MS) for dissipative rocking; (c) Model 2 with 2 Rotational Springs (2RS) for free rocking and (d) 3 Rotational Springs (3RS) for dissipative rocking. (e) link laws.

6.1.1 Rocking mechanism at the column- foundation

The moment capacity of the columns depends on the reinforcement within the section as well as the axial load demand acting on the section. In earthquake conditions, when the rocking mechanism and gap opening occurs, at the column-foundation, the axial load due to the gravity loads (G) and the variation of the seismic axial load N_E, in addition to the yielding force F_y of the dissipative element, generate the whole moment capacity M_t, computed about the centroid of the resultant timber compression force. Analytical procedure was used to determine distribution of internal action based on the equilibrium approach [130].

In order to calculate the moment rotation contributions at the ground floor, the column axial load (gravity plus seismic) may be determined. The gravity induced axial loads acting each column is determined from tributary areas, as follows:

$$N_{G+Q} = \frac{1}{4}\sum W_i \qquad (1)$$

The earthquake induced axial load is determined from the building overturing moment (OTM) demand and the geometry of the building.

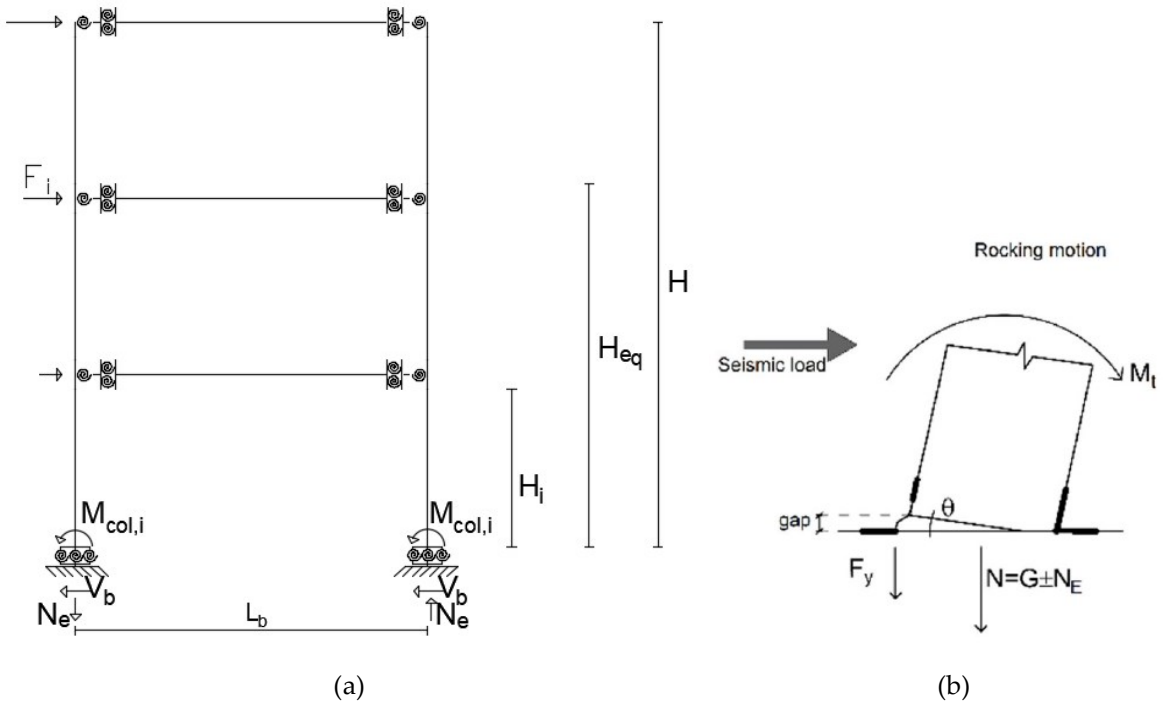

Figure 59. (a) Seismic demand at the base of the frame and (b) distribution of internal action of the column.

With reference to Figure 59 the OTM is given by the following expression:

$$OTM = \sum_{i=1}^{n} F_i H_i = \sum_{i=1}^{n} M_{col,i} + N_{E,i} L_b \qquad (2)$$

In order to calculate moment at the base of the column, it needs calculation of earthquake axial load N_E, this objective can be achieved with following steps.

1) Calculation of lateral forces F_i:

$$F_i = m a_i \qquad (3)$$

Where a_i is the acceleration registered by accelerometers at each floor and appropriately filtered and m is the mass of structure at each storey reported in previous chapter 4. When the lateral force F_i is applied, the column behaves like a conventional column until the rocking mechanism starts and initial gap uplift occurs at one side of the base. After uplift, even though the column has elastic properties, the lateral behaviour is highly non-linear, because the boundary condition varies continuously [138].

2) Verification of translation equilibrium, given by the following expression:

$$\sum_{i=1}^{n} F_i = V_B \qquad (4)$$

Where V_B is base shear of structure, registered by load cell of the experimental model.

3) Verification of rotation equilibrium. If inelastic deformed shape of the frame structure well approximates the first mode of vibration, it is possible to write rotation equilibrium by the following expression:

$$\sum_{i=1}^{n} F_i H_i = V_B H_e = \frac{2}{3} V_B H \qquad (5)$$

A reliable hypothesis on the effective heigh was made, imposing that is H_e =2/3H.

4) Writing different contribution of base moment capacity, in order to calculate N_E. Column base moment capacity ($M_{col,i}$) is given by the contributions of axial load ($M_{N,i}$), hysteretic steel devices ($M_{s,i}$) and the post-tensioned moment contribution ($M_{PT,i}$=0) which is zero in this case.

$$M_{col,i} = M_{N,i} + M_{s,i} \quad (6)$$

The axial load moment contribution ($M_{N,i}$) presented in Equation 8 is the sum of two contributions: the earthquake contribution ($M_{E,i}$) specified in Equation 9 plus gravity contribution ($M_{W,i}$) specified in Equation 10. These two contributions are related to the seismic and gravity column axial load demand ($N_{col,i}=N_{E,i}+N_{Gi+Q,i}$).

$$M_{N,i} = M_{E,i} + M_{W,i} \quad (7)$$

$$M_{E,i} = N_{E,i} e_i \quad (8)$$

$$M_{W,i} = N_{G,i+Q,i} e_i \quad (9)$$

Moment contribution provided by hysteretic energy dissipation devices ($M_{s,i}$) is calculated as a function of tension steel force $T_{s,i}$ of angle device and the distance $d_{s,i}$ from centroid of the timber compression fiber to centroid of steel angle reinforcement, as reported in Equation 11:

$$M_{s,i} = T_{s,i} d_{s,i} \quad (10)$$

Equations (9), (10), (11), can be substituted in (8), obtaining the total moment of the column *i*:

$$M_{col,i} = N_{E,i} e_i + N_{G,i+Q,i} e_i + F_{y,s,i} d_{s,i} \quad (11)$$

5) Equations (5) and (11) can be substituted in equation (2) to calculate earthquake axial contribution $N_{E,i}$.

In particular it can be calculated as follows, in function of base connection rocking system.

Free rocking configuration (F)

In F configuration gravity and seismic loads contribute to the total moment capacity. In order to calculate the moment contributions has been calculated on the centroid of timber compression force (based on neutral axis calculation), as schematized in Figure 60.

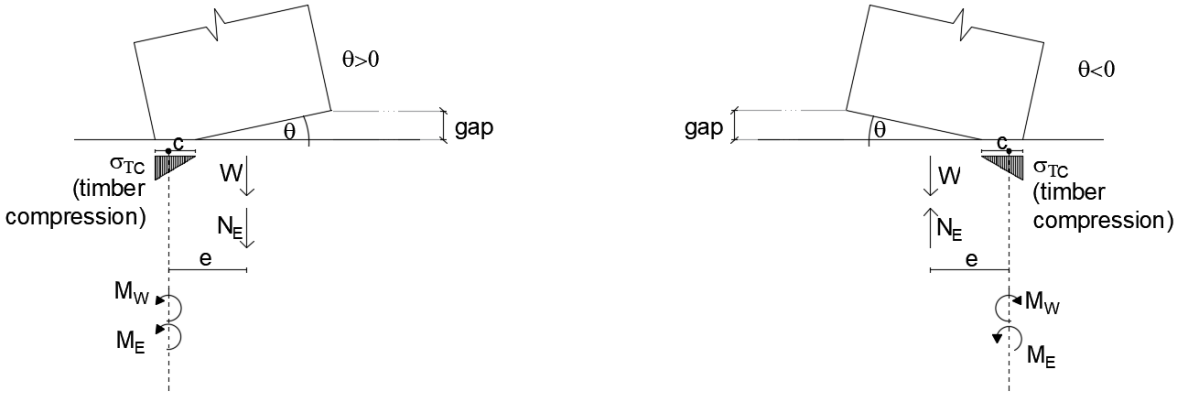

Figure 60. Sketch of the base column rocking mechanism without dissipative angles (positive and negative rotations).

$$\vartheta > 0 \qquad \vartheta < 0$$

$$M_{col,i} = M_{W,i} + M_{E,i} = N_{G+Q}e_i + N_E e_i \qquad M_{col,i} = M_{W,i} - M_{E,i} = N_{G+Q}e_i - N_E e_i$$

$$V_B \frac{2}{3} H = N_{G+Q}e_{SW} + N_E e_{SW} + N_{G+Q}e_{NW} + N_E e_{NW} + N_E L_b \rightarrow$$

$$N_E = \frac{V_B \frac{2}{3} H - N_{G+Q}(e_{SW} + e_{NW})}{L_b + e_{SW} + e_{NW}} \tag{12}$$

Where e_{SW} and e_{NW} represent the distance between the centroid of timber compression force and the axial loads of north and south columns of the frame.

Dissipative rocking configuration (DF)

In DF configuration gravity, seismic loads and hysteresis of dampers contribute to the total moment capacity. The moment contributions have been calculated on the centroid of timber compression force (based on neutral axis calculation), as schematized in Figure 61.

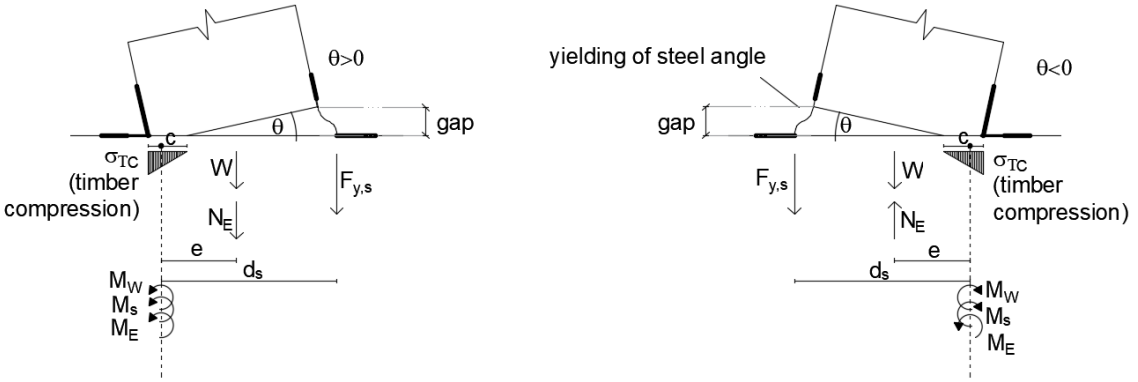

Figure 61. Sketch of the base column rocking mechanism with dissipative angles (positive and negative rotations).

$$\vartheta > 0 \qquad\qquad \vartheta < 0$$

$$M_{col,i} = M_{W,i} + M_{E,i} + M_{s,i} \qquad M_{col,i} = M_{W,i} - M_{E,i} + M_{s,i}$$
$$= N_{G+Q}e_i + N_{E,i}e_i \qquad = N_{G+Q}e_i - N_{E,i}e_i$$
$$+ F_{y,s,i}d_{s,i} \qquad + F_{y,s,i}d_{s,i}$$

$$V_B\frac{2}{3}H = N_{G+Q}e_{SW} + N_E e_{SW} + T_{s,SW}d_{s,SW} + N_{G+Q}e_{NW} + N_E e_{NW} + T_{s,NW}d_{s,SW} + N_E L_b \rightarrow$$
$$N_E = \frac{V_B\frac{2}{3}H - N_{G+Q}(e_{SW} + e_{NW}) - T_{s,SW}d_{s,SW} - T_{s,NW}d_{s,NW}}{L_b + e_{SW} + e_{NW}} \qquad (13)$$

Based on the knowledge of N_E it is possible to calculate base connection moment by substituting N_E calculated (equations 12 and 13) in equation 11.

6.1.2 Experimental vs numerical results

The natural frequencies of vibration of the experimental model after earthquakes were evaluated and compared with numerical results of the model developed in SAP2000 [139]. The power spectral density (PSD) estimation [18] of the earthquake signal 196 at PGA level of 50% was carried out. Table 13 shows the experimental and numerical results of fundamental vibration modes of the frame with free (F model) and

dissipative rocking mechanisms (DF model). As can be observed the experimental and numerical results are in good agreement.

Table 13. Comparison between numerical and experimental results of the fundamental vibration modes of F and DF model

	F		DF	
Mode	$T_{i,exp}$ (sec)	$T_{i,num}$ SAP2000 (sec)	$T_{i,exp}$ (sec)	$T_{i,num}$ SAP2000 (sec)
1	0.54	0.58	0.51	0.54
2	0.12	0.13	0.12	0.13
3	0.06	0.06	0.06	0.06

Dissipative rotational springs have been calibrated against the experimental results. The calibration of the local response of the base column is shown in Figure 62a,b for F and DF configurations, respectively. Similarly to the beam-column connection, in order to obtain the hysteretic moment-rotation contribution of steel angles at the base, nonlinear time history analyses based on experimental gap opening, recorded at the base of columns by displacement potentiometers, were carried out for each seismic input using a simple numerical model based on the same hysteretic link described in Section 5.3.1.

As can be observed a good agreement was found for all the moment-rotation contributions. A reduction of 50% of the angles stiffness respect to mechanical characteristics obtained by quasi-static testing results of the steel angles was considered. It is to account the lower stiffness of dissipative devices placed at the base column connection than the behaviour of the single steel device tested. The characteristics of the numerical models 1 and 2 are reported in Table 14.

Table 14. Characteristics of the link elements considered for numerical modelling.

Beam-column joint (Model 1 and 2)			K_1	M_1	K_2	M_2	K_3
Description	Link type	Behaviour	*kN·m/rad*	*kN·m*	*kN·m/rad*	*kN·m*	*kN·m/rad*
Post tension	Rotational Spring	Multilinear Elastic	7500	7000	1670	11000	450
Steel element	Rotational Spring	Bouc-Wen	1960	10000	210	-	-
Joint panel (Model 1)	Rotational Spring	Linear Elastic	30000	-	-	-	-
Joint panel (Model 2)	Rotational Spring	Linear Elastic	3500	-	-	-	-
Column-foundation connection (Model 1)			K_1	F_1	K_2	-	-
Description	Link type	Behaviour	*kN/m*	kN	*kN/m*	-	-
Base steel element	Linear Spring	Bouc-Wen	13600	24.5	900	-	-
Rocking at the base	Linear Spring	Gap	2000	-	-	-	-
Column-foundation connection (Model 2)			K_1	M_1	K_2	-	-
Description	Link type	Behaviour	*kN·m/rad*	kN·m	*kN·m/rad*	-	-
Base steel element	Rotational Spring	Bouc-Wen	800	8.00	130	-	-
Rocking at the base (seismic)	Rotational Spring	Linear Elastic	400	8.00	-	-	-
Rocking at the base (gravity)	Rotational Spring	Multilinear Elastic	7000	7.00	0.00	-	-

Figure 63 shows the numerical outcomes of Model 1 and Model 2 for testing Session 1, subjected to seismic input 535, developed using finite element software SAP 2000. The comparisons between numerical and experimental results show that Model 1 and Model 2 provide an efficient representation of the seismic response of the testing frame with few discrepancies in terms of peak values of base shear. In F configuration some discrepancies of drift peak values have been observed for Model 1, while a best fit was provided by Model 2. In DF configuration both Model 1 and Model 2 present an adequate representation of experimental results. For both F and DF testing configurations, the base shear versus drift response shows that all numerical models reliable approximate the stiffness of the test frames [137].

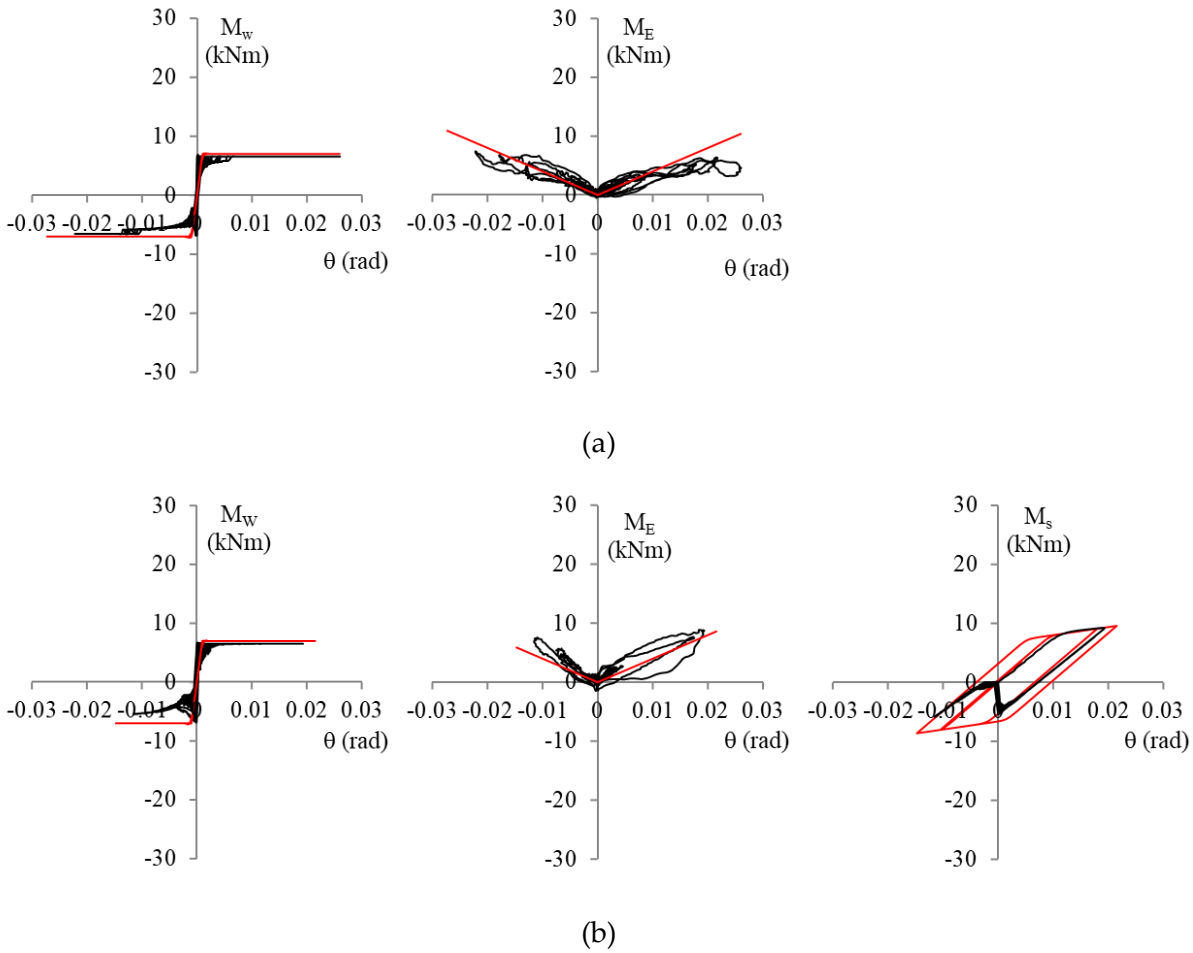

Figure 62. Calibration of rotational link at the base (south column): comparison between experimental and numerical results of the moment-rotation contributions for seismic input 535 at 75% of PGA in (a) F and (b) DF configuration.

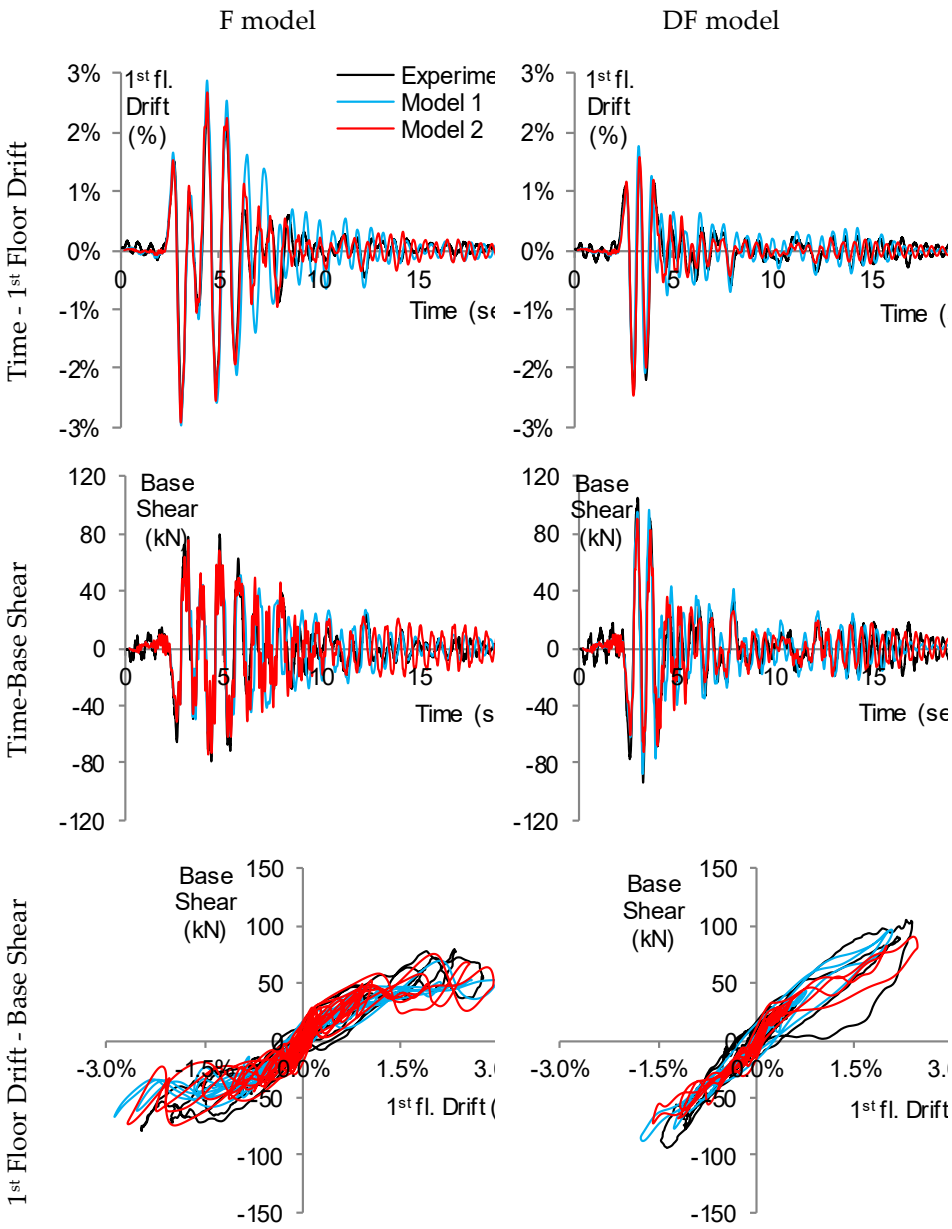

Figure 63. Comparison between experimental and numerical results of the two different numerical models (model 1 and model 2) for seismic input 535 at 75% of PGA level of the (a) F and (b) DF model configurations.

In order to further analyse the experimental results at the design level, non-linear dynamic analyses of Model 2 in DF configuration were performed considering the complete set of the seismic inputs at 100% of PGA level. The experimental results obtained have been used to validate the design procedure, as explained in detail in the following section 6.9. The time-histories of total drift and total drift versus base shear from numerical analysis and experimental tests are compared in Figure 64 for all inputs. As can be observed, the numerical simulations are in good agreement with experimental tests.

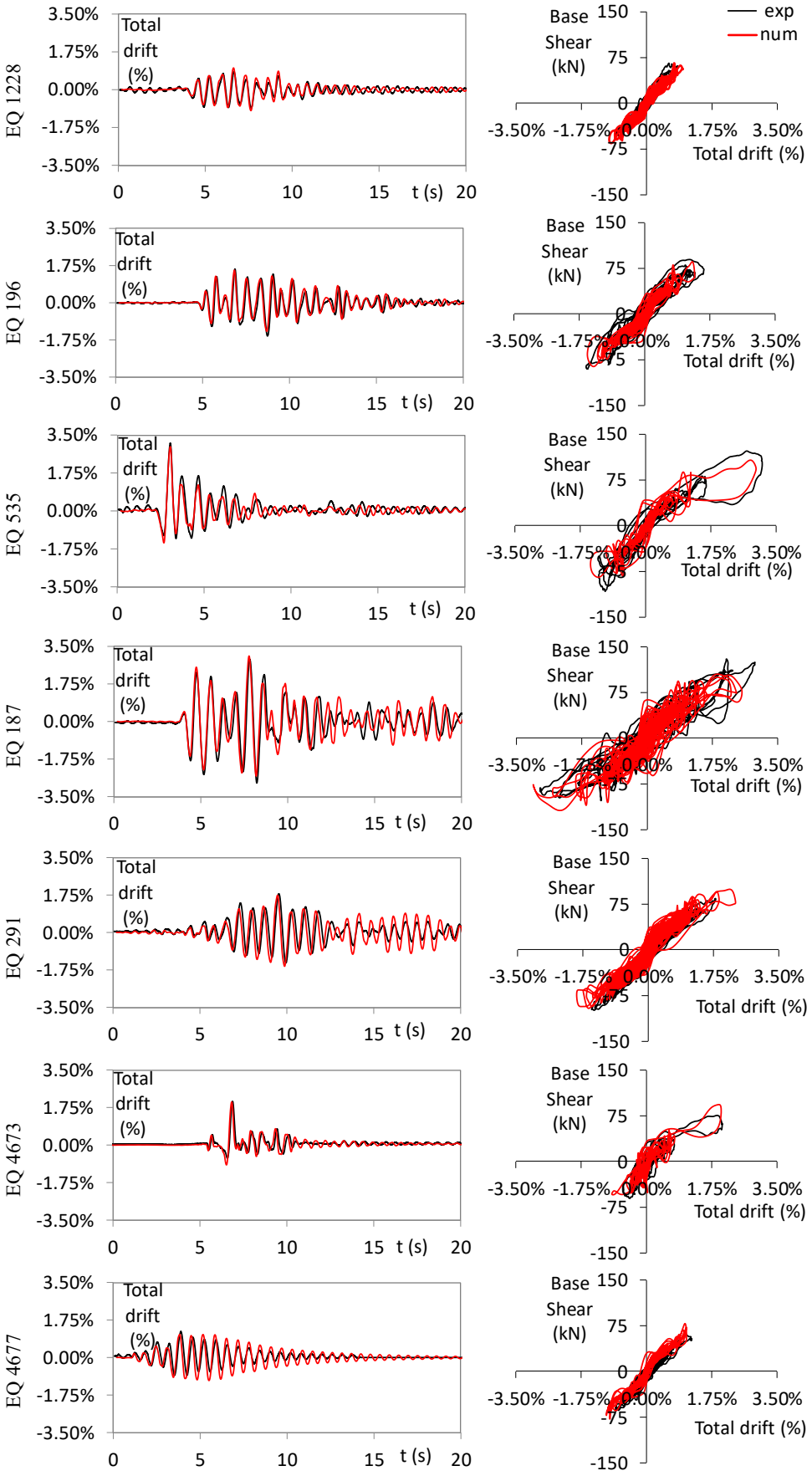

Figure 64. Comparison between numerical and experimental results of DF model at 100% of PGA level.

Moreover, as expected from the design assumption, the flag-shape behaviour is evident for the stronger earthquakes (535-187).

The comparison between numerical and experimental results obtained for the dissipative-rocking configuration are summarized in Table 15 in terms of maximum total drift and corresponding base shear. As can be observed, the mean values of numerical and experimental results are in good agreement and confirmed the results obtained from the design procedure reported in Table 2 (θ_d =1.9% and F_u=70 kN).

Table 15 Comparison between experimental (Exp.) and numerical (Num.) results of the model with dissipative rocking (D) at the 100% of PGA level.

Seismic Input		*1228*	*196*	*535*	*187*	*291*	*4673*	*4677*	*Mean*
Maximum Total Drift (%)	Num.	1.0	1.5	3.0	3.1	2.3	2.0	1.1	2.0
	Exp.	0.9	1.6	3.1	2.9	1.8	2.0	1.2	1.9
Corresponding Base Shear (kN)	Num.	59	67	94	76	79	84	56	73
	Exp.	53	73	103	125	83	62	52	79

6.2 Modelling of post-tensioned timber frame with dissipative bracing

The numerical modelling of the test frame with dissipative rocking mechanism at the column-foundation connections and with dissipative bracing systems was developed based on the lumped plasticity approach which combines the use of elastic elements with springs representing plastic deformations in the system (figure 3a). The model was developed with two different finite element software to simulate the seismic non-linear dynamic response: SAP2000 [139] and Opensees [140]. The structural elements (beams, columns and braces) were modelled as elastic elements with anisotropic glulam timber material in SAP2000 and uniaxial material elastic in OpenSees. The specimen at the beam-column joints (Figure 65a) was modelled considering a combination of rotational springs to represent the contribution of the post-tensioning (tri-linear-elastic moment–rotation spring) and the flexibility of the joint panel (linear spring), with stiffness values opportunely arranged for each model. The flexibility of the joint panel influenced the response of SAP2000 and OpenSees models, for this

reason different amounts of stiffness of the rotational spring were tested to check the sensitivity of both models. The column base connection (Figure 65c) was modelled with 3 rotational springs in parallel, based on the previous Model 2 see previous (see Figure 58b,c), which considered the moment resistance given by the contribution of the gravity plus seismic axial load and the additional moment contribution of hysteretic steel elements [137].

When dissipative bracing systems were introduced to the bare structure, the hysteretic contribution of UFP dampers was modelled by considering a linear spring with hysteretic behaviour in series with V-inverted elastic elements (Figure 65b). In order to represent the hysteretic steel elements (steel angles and UFPs) the Bouc-Wen spring model [128],[129] and the Giuffrè Menegotto-Pinto hysteresis rule ("uniaxialMaterial Steel02") were adopted respectively, in SAP2000 and OpenSees models [141]. Inherent damping was provided using Raleigh damping of 2% in modes 1 and 3 for both models.

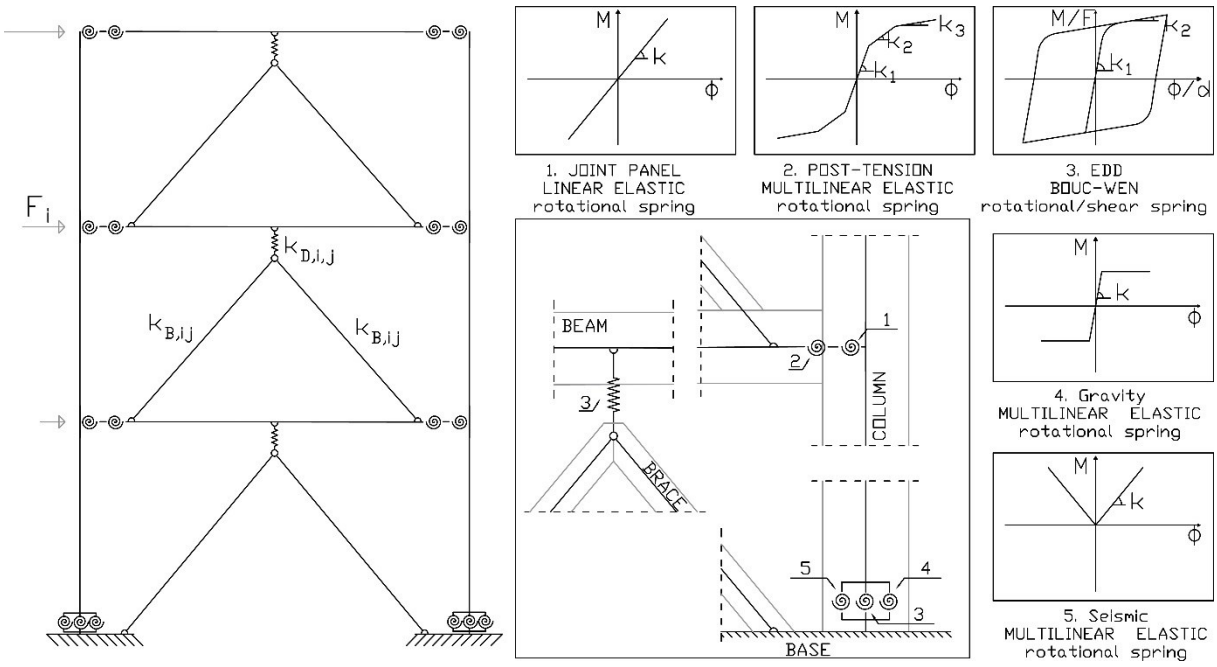

Figure 65 Numerical modelling of the frame with dissipative bracing systems and details of: (a)dissipative bracing connection; (b) beam-column joints and (c) column-foundation joints.

6.2.1 Experimental vs numerical results

Preliminary shaking table tests on the post-tensioned timber frame model with dissipative bracing systems were performed on a smaller set of two ground motions 196 and 291 earthquakes (Figure 66) which provide a good representation of the design spectra. These results were used to calibrate the numerical model.

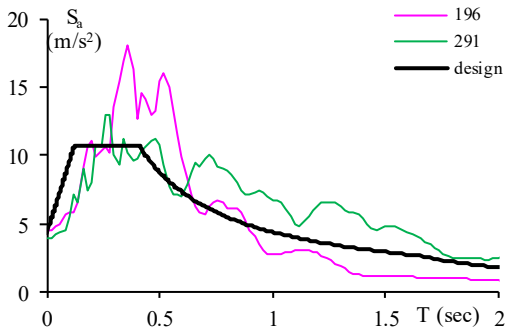

Figure 66. Selected seismic inputs for preliminary shaking table tests of the BF model.

The natural frequencies of vibration of the experimental model after earthquakes were evaluated and compared with numerical results. The power spectral density (PSD) estimation [127] of the frame with dissipative bracing systems (BF model) was compared with experimental and numerical results in terms of fundamental periods of vibration. As highlighted from the Figure 67, the numerical predictions of the first three periods of the frame compared with the 2-D OpenSees and SAP2000 numerical predictions ($T_{i,num}$) for both models matched well with experimental results $T_{i,exp}$.

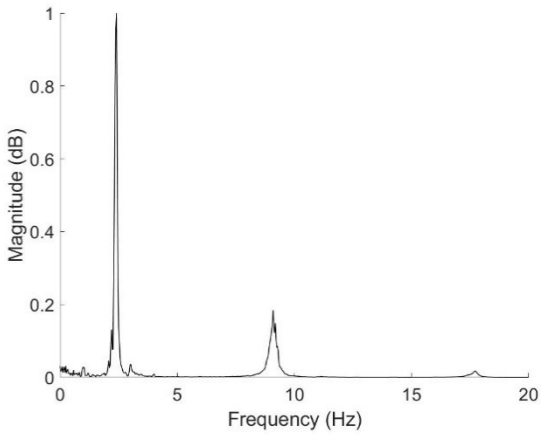

Mode	BF model		
	$T_{i,exp}$ (sec)	$T_{i,num}$ OpenSees (sec)	$T_{i,num}$ SAP2000 (sec)
1	0.43	0.45	0.41
2	0.11	0.11	0.12
3	0.06	0.04	0.05

Figure 67. Experimental Welch's Power Spectral Density estimation of BF model and comparison between numerical and experimental periods of vibration.

In order to calibrate the numerical model preliminary shaking table test results of the post-tensioned timber specimen with dissipative bracing systems were compared with non-linear dynamic analysis results of the proposed models developed in OpenSees and SAP2000. The key indicators used in order to describe the frames seismic global behaviour are first floor drift and base shear.

The key parameters of the OpenSees and SAP2000 link modelling of the connection between the bracing systems and the beam at each level, estimated by the characterization tests of dampers, are listed in Table 16, in terms of the yielding force F_1, the initial stiffness K_1 and the post-yielding stiffness ratio K_2/K_1. The characteristics of the link elements considered for the beam-column, joint panel and column-foundation are the same reported in Table 14 (Model 2).

Table 16 Characteristics of the link elements considered for numerical modelling of each braced frame.

Storey	Weight (kN)	Hysteretic damper	F_1 (kN)	K_1 (kN/mm)	K_2/K_1
1st	27.6	UFP 1	13.5	1.70	0.3
2nd	27.6	UFP 2	10.0	1.15	0.3
3rd	27.2	UFP 3	6.0	0.63	0.3

The local behaviour of hysteretic dissipation of the bracing system was described in terms of force-displacement of the U-shaped Flexural Plates at first level of the structure. The outcomes reported refers to the earthquake inputs Montenegro (ID 196) at PGA level of 50% and Campano-Lucano (ID 291) at PGA level of 75% [141].

Figure 68 and Figure 69 show the numerical predictions of OpenSees and SAP2000 models for the seismic inputs 196 at 50% of PGA level and 291 at 75% of PGA level. As can be observed for both earthquake cases analyzed (196 and 291), the comparisons between numerical predictions and preliminary experimental results showed that models constructed with OpenSees and SAP2000 software provided an efficient representation of the seismic response of the braced testing frame.

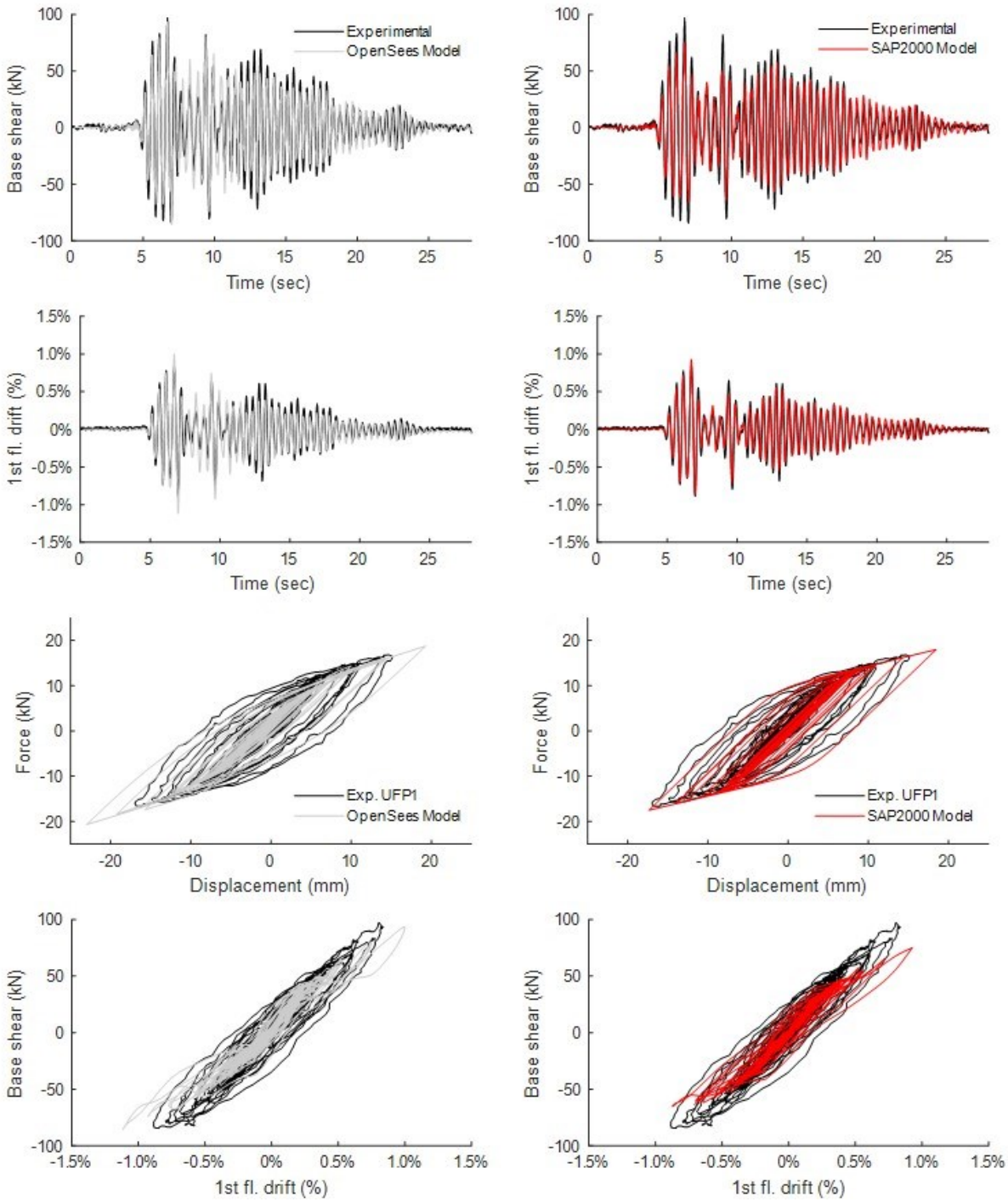

Figure 68 BF model configuration: comparisons between experimental and numerical results of OpenSees and SAP2000 models with dissipative bracing systems for 196 seismic input at 50% of PGA intensity.

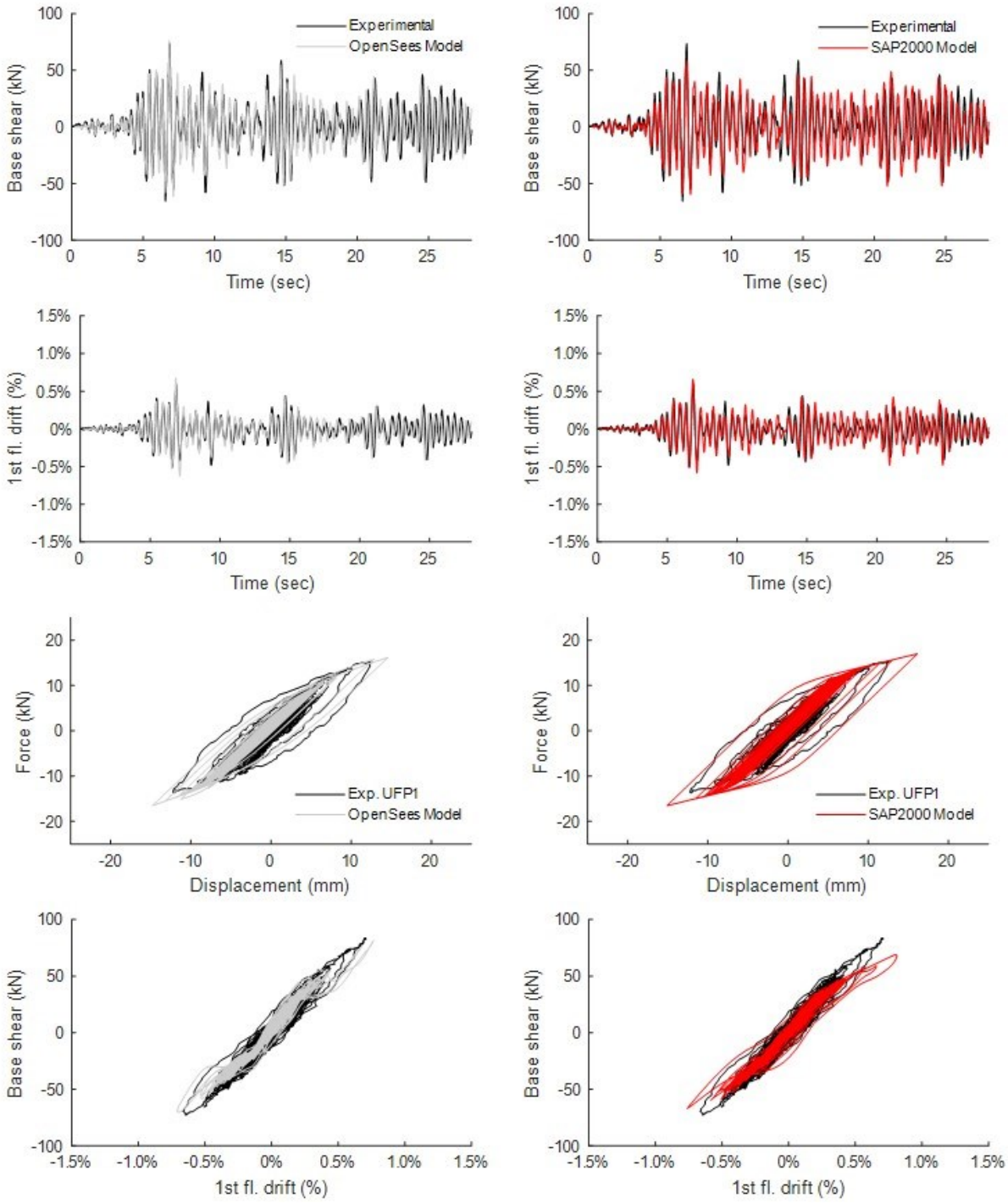

Figure 69 BF model configuration: comparisons between experimental and numerical results of OpenSees and SAP2000 models with dissipative bracing systems for 291 seismic input at 75% of PGA intensity.

It can be observed that the Opensees model well represented maximum peak values of the base shear, while slightly over predict maximum force and displacement of hysteretic steel dampers. For all numerical simulations, the study of the base shear versus drift response showed that numerical models reliable approximated the

stiffness of the test frame with dissipative bracing systems. The flag-shaped hysteretic behaviour of the frame was not very prominent because low PGA levels of earthquake input were performed in preliminary shaking table tests.

The numerical model calibrated against preliminary experimental results was further refined [93] and nonlinear time history analyses (NLTHA) were compared with the results of the whole shaking table testing performed on the post-tensioned timber frame with dissipative bracing systems. The numerical and experimental time histories of the key design variables (displacement and base shear) are displayed in Figure 70 for 1228, 196 and 535 seismic inputs at the Design Base Earthquake (DBE) level corresponding to 100% of PGA.

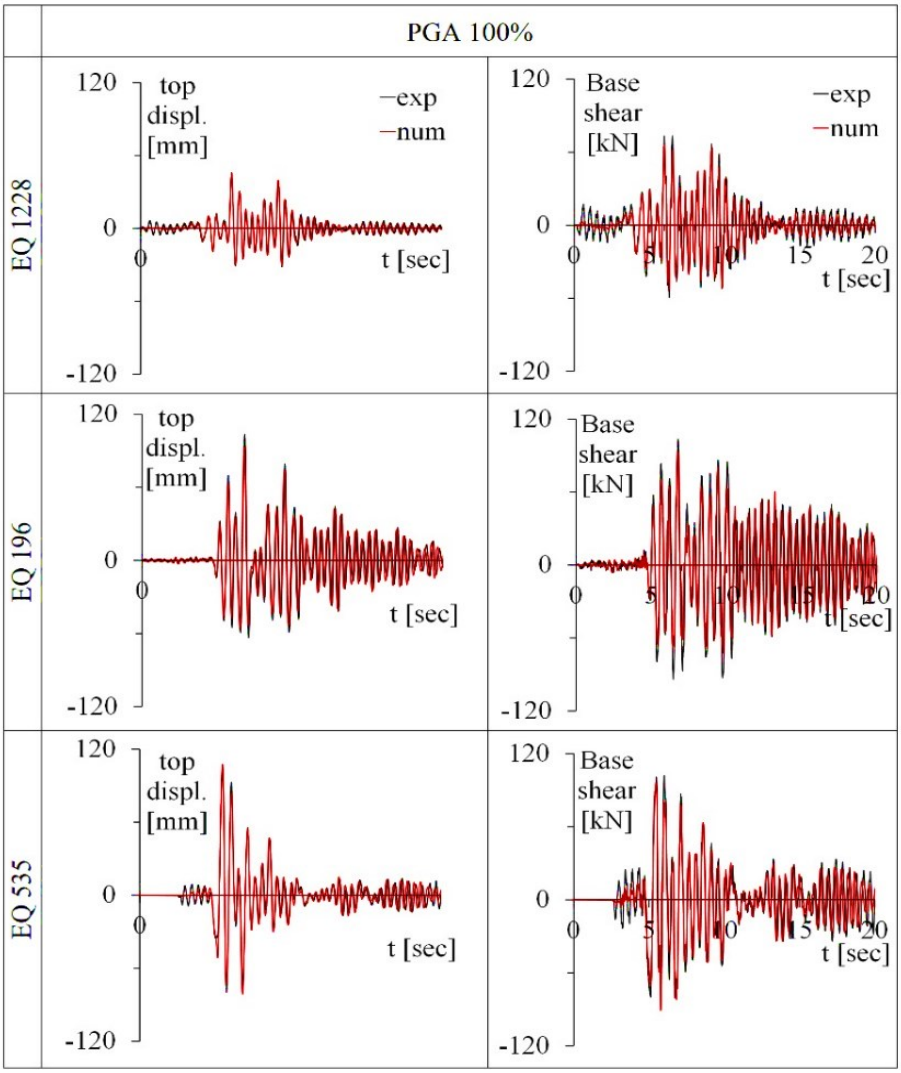

Figure 70. Top displacement and base shear time histories of BF model for 1228, 196 and 535 seismic inputs at 100% of PGA level.

Computational and experimental results are also compared in terms of global force-displacement behaviour of BF model (Figure 71) and local hysteretic response of UFP dampers at the first storey (Figure 72) for the three selected seismic inputs at 25%, 75% and 100% of PGA levels, in order to analyze the performance of the system at various damage states, from Service Level Earthquake (SLE), intermediate, and ultimate damage (DBE) states. The results show that the numerical simulations are in good agreement with experimental results, both in terms of global time histories and force-displacement, simulating the flag-shaped response of the frame, only few discrepancies can be observed on the peak values of base shear. The local response in terms of UFP cyclic behaviours weas reliably predicted.

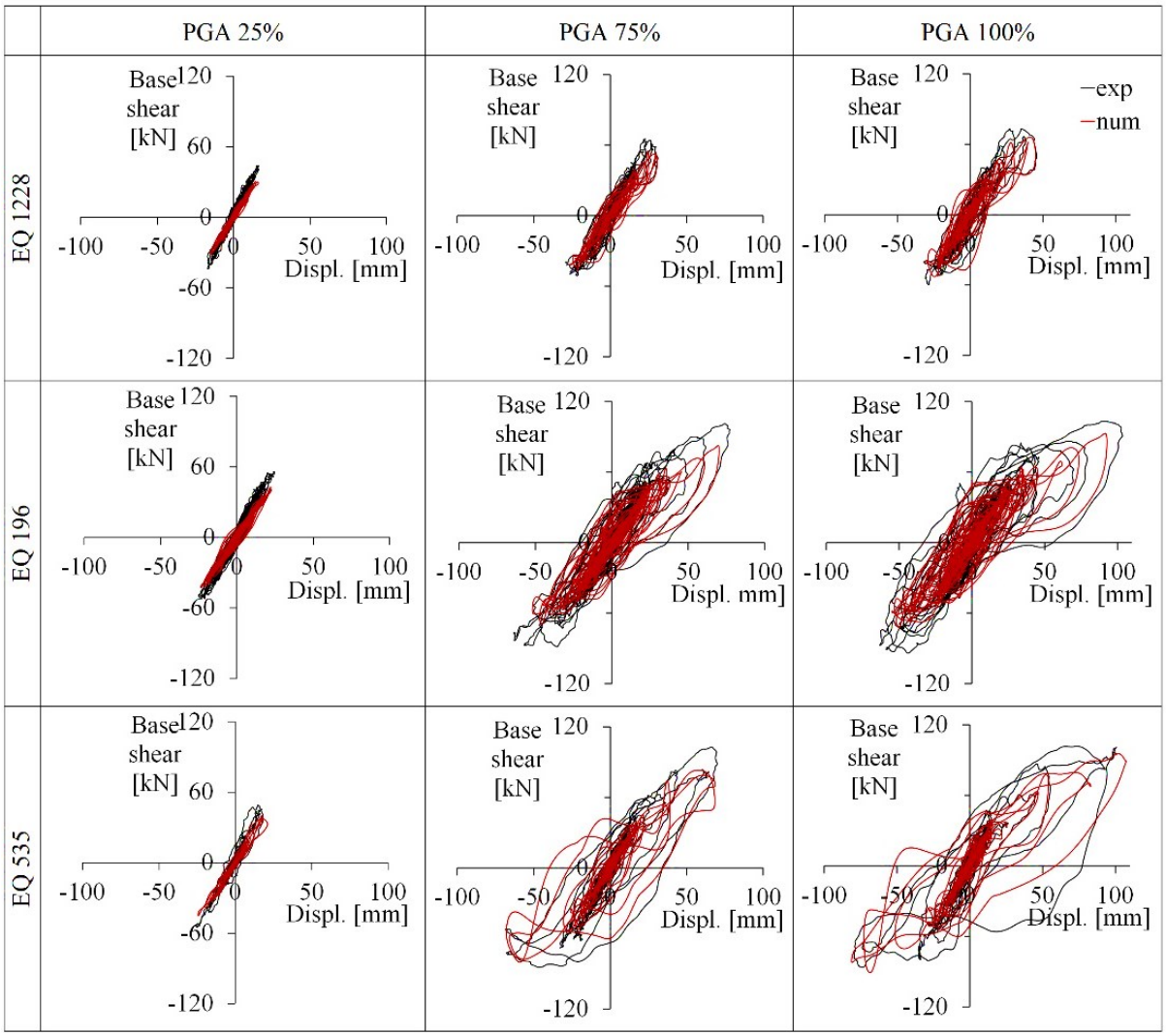

Figure 71. Global displacement vs base shear of BF model for the three selected seismic inputs at 25%, 75% and 100% of PGA level.

The comparison between experimental and numerical results of the braced frame tested at 100% of PGA has been summarized in Table 17.

Table 17 Main numerical and experimental results of braced frame at 100% of PGA level.

	Total drift (%)		Base shear (kN)	
	Num.	Exp.	Num.	Exp.
1228 PGA 100%	0.74	0.72	66	62
196 PGA 100%	1.54	1.60	93	98
535 PGA 100%	1.76	1.63	98	114

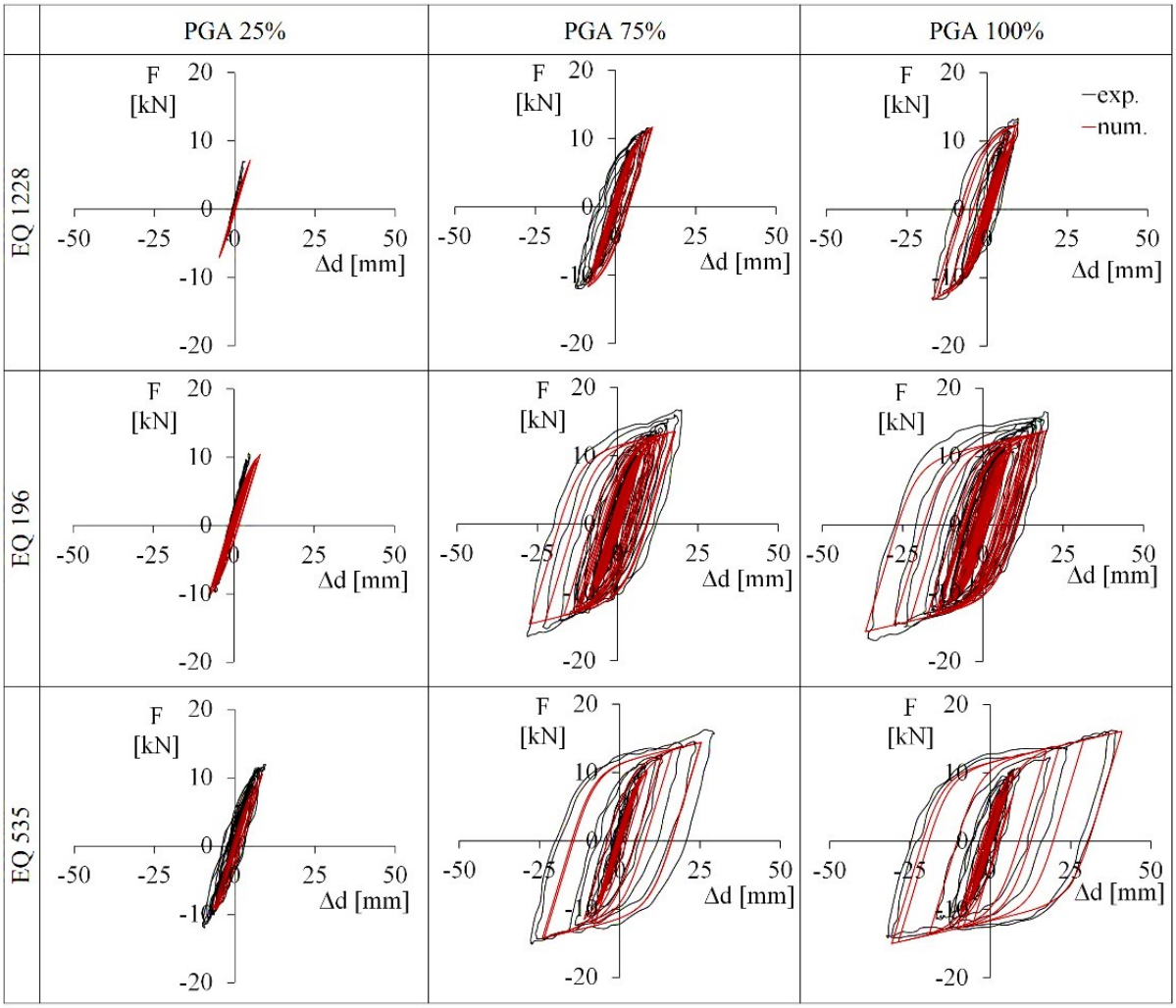

Figure 72 Local hysteretic response of UFP 1 of BF model for the three selected seismic inputs at 25%, 75% and 100% of PGA level.

Moreover, Figure 73 summarized the maximum numerical and experimental maximum peak values and corresponding mean in terms of the total drift of the BF model and ductility of the UFP at the first storey at all PGA levels for the three seismic

inputs. The reference yield displacement considered is equal to 6.25 mm (derived by the experimental characterization tests of dampers). As can be observed numerical and experimental results are in good agreement, few discrepancies were highlighted for the case of seismic input 196.

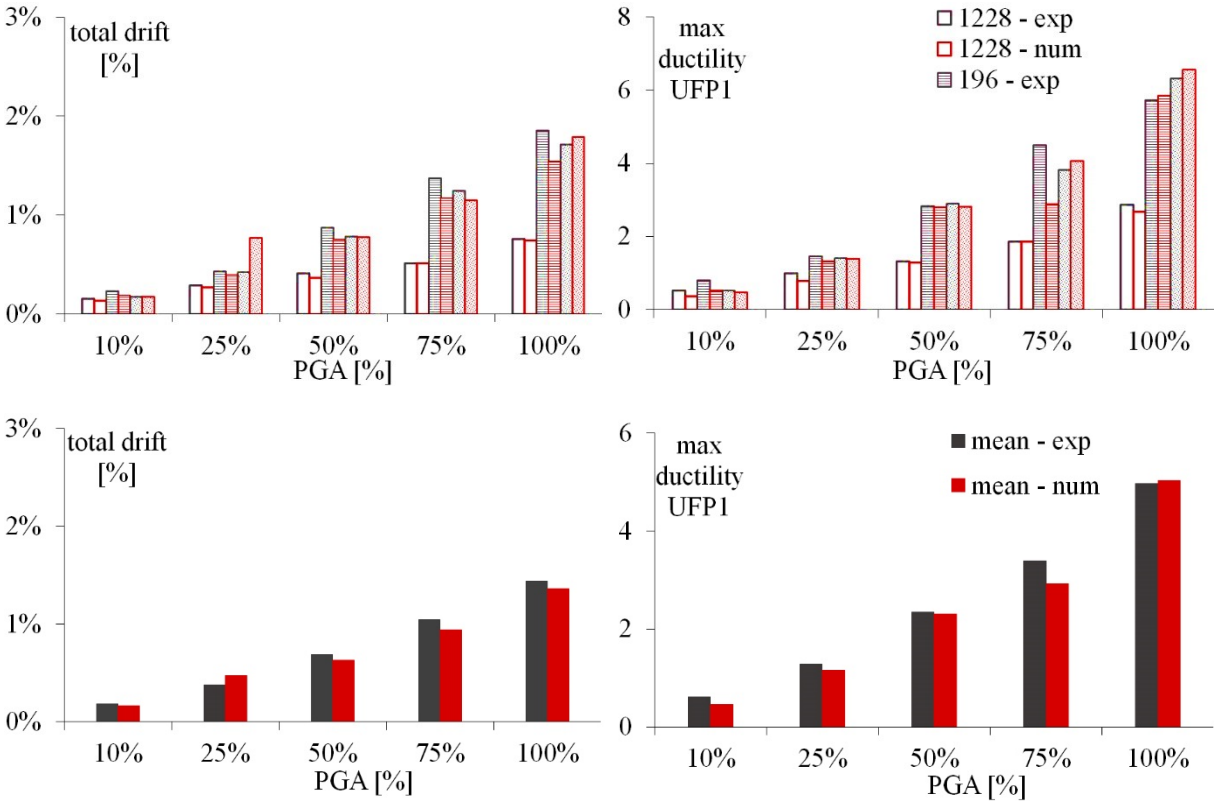

Figure 73. Comparison between numerical and experimental peak values of total drift and ductility of UFP1 for the three selected seismic inputs and mean values at all PGA levels.

Figure 74 shows the results of nonlinear static analysis (NLSA) performed applying two horizontal distributions of lateral loads, "modal" and "uniform" patterns [2], in order to predict the variation in strength and post-elastic stiffness of the BF configuration. Figure 74 compares the pushover curves with the experimental results of the complete set of earthquakes performed at different PGA levels in terms of maximum total drift and corresponding base shear of the braced frame. The shaking table testing results are included between the two curves, the results confirmed that the numerical model provides an efficient representation of the real dynamic response of the testing frame. NLSA are capable of simulating adequately the observed experimental behaviour, representing a reliable tool for predicting the nonlinear dynamic seismic response.

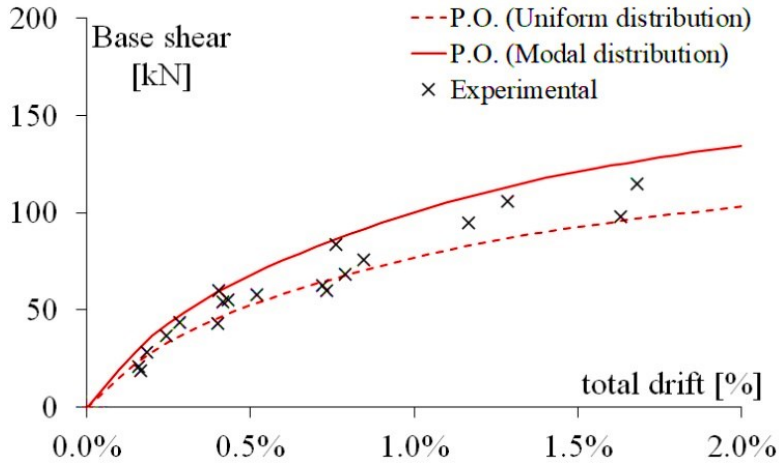

Figure 74. Comparisons between peak values by dynamic testing results against pushover curves for the complete set of seismic inputs at all PGA levels.

7 Validation of the design procedure

A reliable estimation of the equivalent damping ξ_{eq} (elastic and hysteretic contributions) of the idealized SDOF system plays a fundamental role in DBD procedure for a correct design of the structural system. It is a reliable tool to evaluate the reduction of the design spectrum for this type of structures, based on the dissipation mechanism adopted.

The concept of viscous damping is generally used to represent various mechanisms of energy dissipation of the structure (such as cracking, nonlinearity in the elastic phase of response, interaction with non-structural elements, soil-structure interaction, etc.). There is no direct relationship of such damping with the real physical phenomena, however the adoption of the viscous damping concept facilitates the solution of the differential equation of motion.

In order to validate the proposed displacement-based design procedure the total equivalent viscous damping ξ_{eq}, (hysteretic ξ_{hyst} and elastic ξ_0 contributions) of the braced frame has been estimated and the drift compatibility of the proposed design method was verified based on the experimental and numerical results obtained in dissipative rocking and dissipative bracing configurations.

7.1 Energy dissipation

The overall hysteretic energy dissipation is a reflection of many contributors, mainly including the yielding of hysteretic dampers and nonlinear geometric behaviour of rocking mechanisms of beam-column joints and of column-foundation connections. The hysteretic energy dissipated by the devices has been estimated for UFP installed into dissipative braces (two UFPs for each side) at each storey of the BF model shown in Figure 75. As can be observed, different amounts of hysteretic energy have been dissipated by UFPs, that reduced by passing from 1st to 3rd storey.

Figure 76 shows the comparison between cumulated hysteretic energy dissipated by the dampers (two UFPs) installed into the V-inverted bracing at the 1st storey of the BF model configuration and the dissipative angles installed at the single beam column connection (two ID5A) at the 1st storey of the DF model configuration for the three selected seismic inputs at 100% of PGA. As can be observed the amount of hysteretic energy dissipated significantly increase when UFP dampers are introduced into the model, as expected by design.

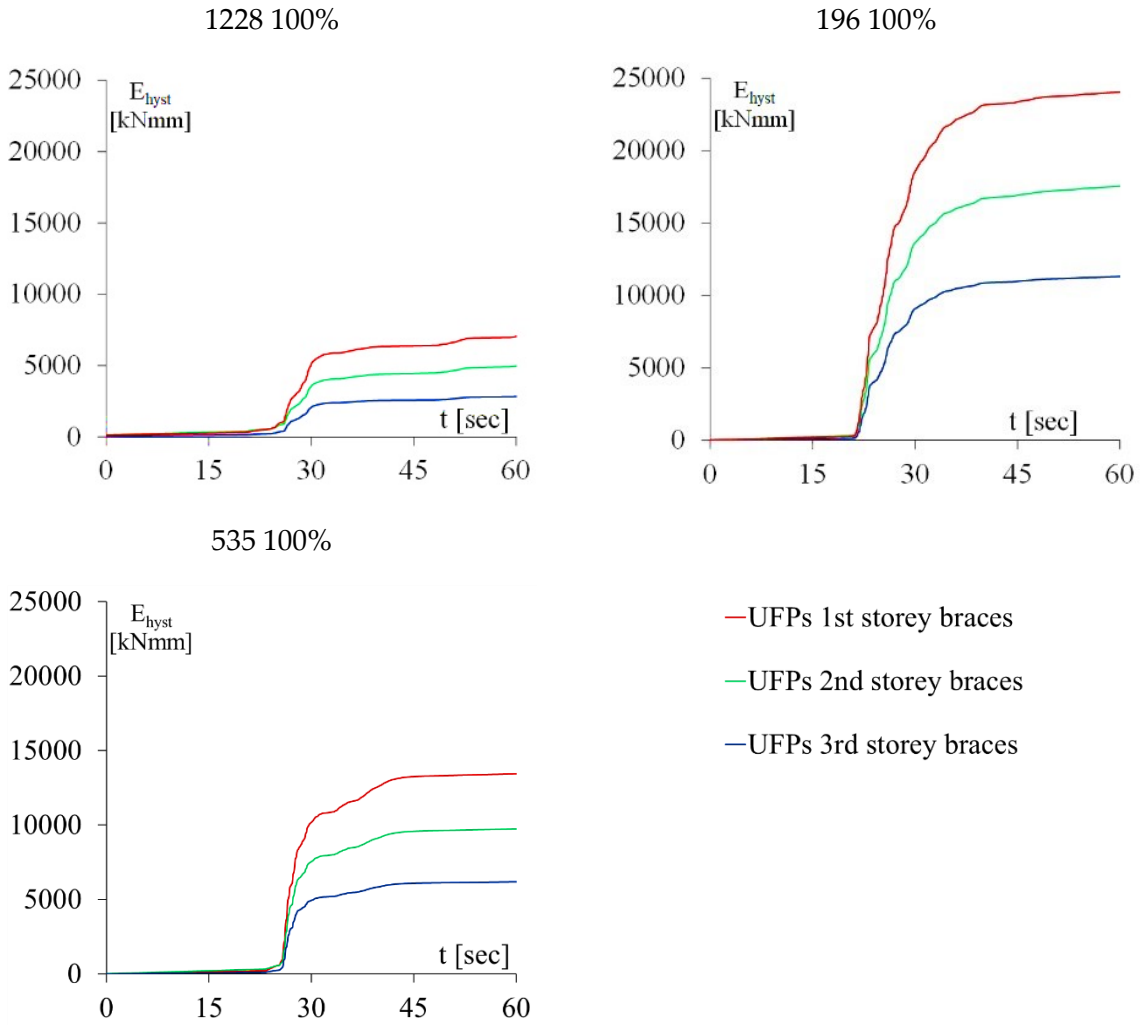

Figure 75. Comparison between cumulated hysteretic energy dissipated by UFP devices installed into dissipative braces at the three storey of the post-tensioned timber BF model for the selected seismic inputs at 100% of PGA.

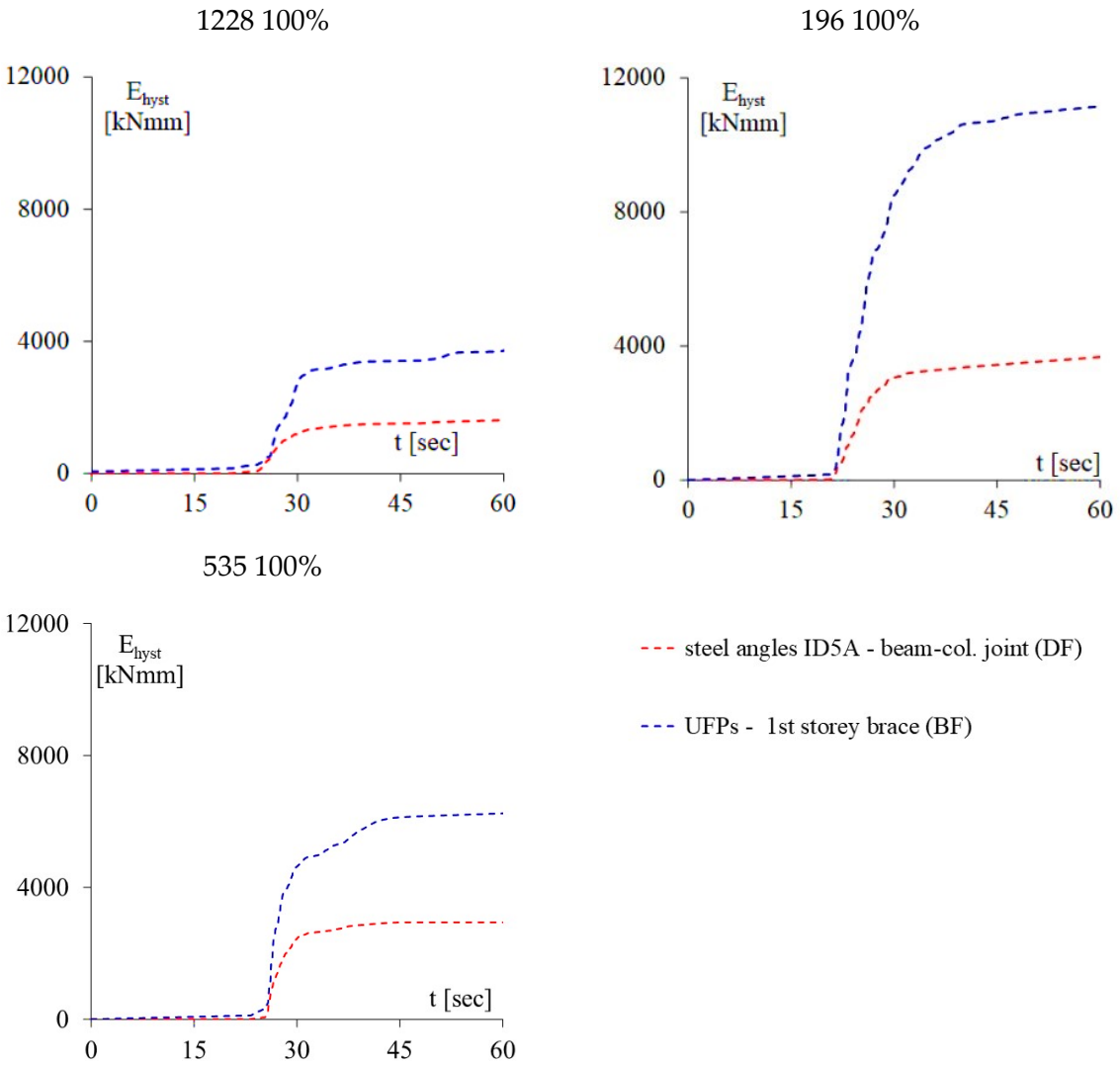

Figure 76. Comparison between cumulated hysteretic energy of the couple UFP devices installed into the single dissipative brace at the first storey of the BF model configuration and the couple of dissipative angles installed at the single beam column connection at the first storey of the DF model configuration for the selected seismic inputs at 100% of PGA.

Figure 77 show the global energy dissipated, estimated by the global hysteretic flag-shape response of DF and BF models, for 1228, 196 and 535 seismic inputs at 100% of PGA level. As can be observed the global amount of dissipated energy reflects the same response of the local hysteretic energy dissipated by steel angles and UFPs, with higher amount of energy dissipated by the BF model, perfectly in line with the design purpose.

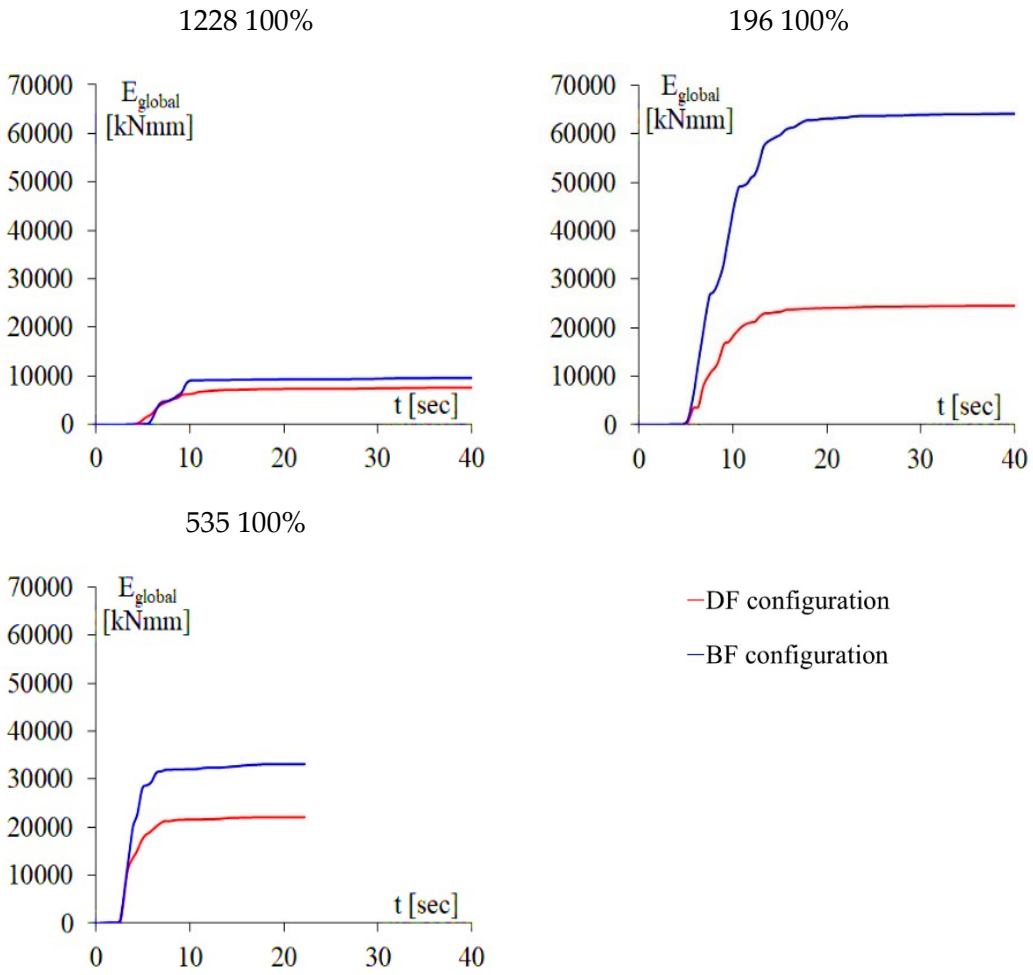

Figure 77. Comparison between global energy dissipated by the DF and BF models for 1228, 196 and 535 earthquakes at 100% of PGA level.

Figure 78 shows maximum values of the global energy dissipated for DF and BF configurations averaged on the three selected seismic input at each PGA level performed (from 10% to 100% of PGA). It can be observed that up to SLE (< 25% of PGA level) the maximum energy dissipated is almost similar between DF and BF model configurations because the dampers are not yet activated, while at higher PGA levels (>50% of PGA) the effect of dissipative bracing (BF model) is evident with higher amount of energy dissipated respect to DF model.

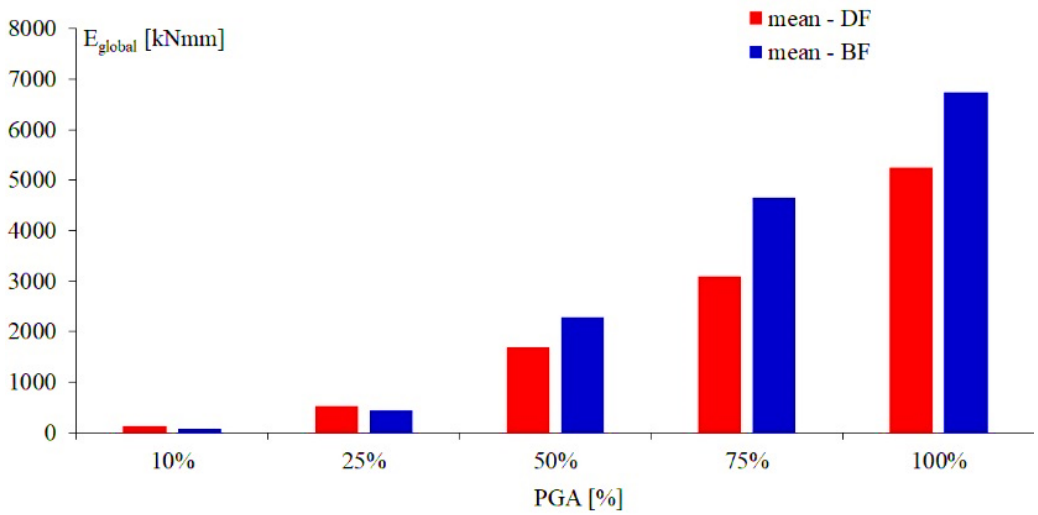

Figure 78. Maximum global energy dissipated by DF and BF models at all PGA levels averaged on the three selected seismic inputs.

7.2 Equivalent viscous damping

The equivalent damping approach was first proposed by Jacobsen in 1930 [142], suggesting an approximate solution of the steady-state response of a nonlinear oscillator by defining an equivalent linear oscillator with the same natural frequency and dissipating equal energy per cycle of sinusoidal response. In 1960 Jacobsen [143] proposed the estimation of the hysteretic equivalent viscous damping of building structures producing large deflections beyond its elastic limit, by equating the energy absorbed by hysteretic cyclic response at a given displacement amplitude to the equivalent viscous damping of the SDOF system, considering a sinusoidal response to ensure complete loops. Experimental hysteretic responses and idealized construction were used to estimate the damping of composite structures based on the concept of dissipated (E_{Diss}) and stored (E_{sto}) energy as shown in Figure 79.

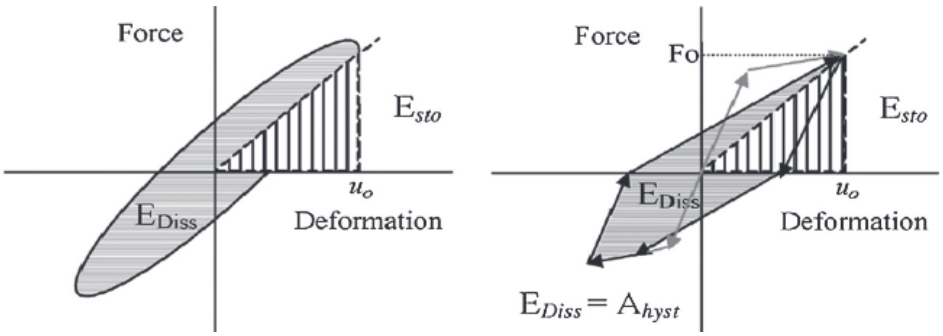

Figure 79: Dissipated and stored force for viscous damping and hysteretic cycles (Jacobsen's formulation)

The following Equation (14) was proposed, where A_{hyst} represents the area of dissipated energy, F_0 and u_0 are the maximum force and displacement for the given hysteretic loop.

$$\xi_{hyst} = \frac{1}{4\pi}\frac{E_{diss}}{E_{sto}} = \frac{1}{2\pi}\frac{A_{hyst}}{F_0 u_0} \qquad (14)$$

It is worth noting that there are many difficulties in the prediction of effective damping of building during a strong motion earthquake, due to the random excitation and to the observation that the complete loops are not formed in each cycle.

Chopra (1995) [107] estimated the elastic viscous damping measuring the amplitude decay from experimental tests in laboratories or real buildings. In practice, for r.c buildings the value of the coefficient ranges between 2% and 5%. Other studies demonstrated that post-tensioned timber systems typically display low levels of elastic damping taken as 2-3% [144][145].

Based on this initial formulation of equivalent hysteretic damping, the equivalent damping was investigated by several authors. Rosenblueth and Herrera (1964) [146] developed the equivalent damping expression as a function of ductility (μ) and post-yielding stiffness ratio (r), based on secant stiffness, at the maximum displacement by considering the period shift between the original and equivalent systems. Extending the work of Jacobsen (1960), Gulkan and Sozen (1974) [147] applied the concept of substitute damping to approximate the inelastic behaviour of a SDOF reinforced concrete (RC) frames utilizing energy balance to obtain equivalent damping values for Takeda model. Iwan (1980) [148] proposed an expression of equivalent viscous damping for elastic coulomb and slip elements. The study by Dwairi et al. (2007) [149] used a large number of real accelerograms to calibrate the equivalent viscous damping, providing a relationship for a given rule, ductility and period. Dwairi proposed a hyperbolic damping ductility law based on nonlinear ductility at peak displacement for unbounded post-tensioned concrete systems, RC beams, RC columns and steel members. Filialtraut (2003) [145] estimated the equivalent damping variation of wood

framed buildings with displacement amplitude. Blandon and Priestley (2005) [150] compared the EVD based on Jacobsen's approach and EVD from the iterative time history analyses for six different hysteretic models. They concluded that Jacobsen's approach overestimated EVD values; thus, they proposed corrected equations for the DBD method. Priestley and Grant (2005) [109] proposed the equivalent damping for different hysteretic model as a function of the ductility (μ), the post-yield stiffness ratio (r), and the re-centering ratio of the global system (β_F), for the flag-shape model. Pennucci et al. (2009) [151] proposed an equivalent viscous damping equation for flag-shaped hybrid systems as a function of λ (related to the flag loop parameter as the ratio between the amount of post-tensioning and the amount of dissipation). A revised relationship of the equivalent viscous damping based on Jacobsen's approach was proposed for the hysteretic damped brace used for retrofitting framed buildings, by introducing corrective factors, as a function of the design parameters of the damper (K, d and r) [152]. An equivalent viscous damping-ductility law for various post-yield stiffness ratios, valid for steel members, was defined by Bezabeh et al. (2016) [153] considering a series of non-linear time histories analyses. The results of some of these studies are summarized in

Table *18*.

Equation (15) shows the total equivalent damping ξ_{eq} of the SDOF system as reported in Priestley et al. [130]:

$$\xi_{eq} = \xi_0 + \xi_{hyst} \qquad (15)$$

where ξ_0 is the elastic viscous damping and ξ_{hyst} is related to the inelastic hysteresis. Priestley et al. [109] suggested that the hysteretic damping value should be corrected by a dynamic reduction factor k to obtain hysteretic damping that is consistent with the results of inelastic time history analysis Equation (16), in order to account for the random nature of seismic inputs.

$$\xi_{eq} = \xi_0 + k\xi_{hyst} \qquad (16)$$

Table 18: Existing equivalent viscous damping equations.

Structural system	*Researcher*	*Equation*
Bilinear elasto-plastic systems	Rosenblueth and Herrera (1964) [146]	$\xi_{eq} = \xi_0 + \frac{2}{\pi}\left[\frac{(1-r)(\mu-1)}{\mu - r\pi + r\mu^2}\right]$
Takeda model	Gulak and Sozen (1974) [147]	$\xi_{eq} = \xi_0 + 0.2\left(1 - \frac{1}{\sqrt{\mu}}\right)$
Elastic and Coulomb slip elements	Iwan (1980) [148]	$\xi_{eq} = \xi_0 + 0.0587(\mu-1)^{0.371}$
Wood framed buildings	Filialtraut (2003) [145]	$\xi_{eq} = \begin{cases} 0.5\Delta_b + 0.02 & 0 \le \Delta_b \le 0.36\% \\ 0.2 & \Delta_b > 0.36\% \end{cases}$
RC flag-shaped hysteretic systems	Priestley and Grant (2005) [109]	$\xi_{eq} = \xi_0 + k\frac{\beta_F(\mu-1)}{\mu\pi[1+r(\mu-1)]}$
	Dwairi (2007) [149]	$\xi_{eq} = \xi_0 + C\left(\frac{\mu-1}{\mu\pi}\right)$ $C = 30 + 35(1-T_e) \quad T_e < 1sec$ $C = 30 \quad T_e > 1sec$
	Pennucci et al. (2009) [151]	$\xi_{eq} = \xi_0 + k\frac{2}{(\lambda+1)}\left(\frac{\mu-1}{\mu\pi}\right)$

In design procedure applied to the post-tensioned timber frame model the equivalent damping equation proposed by Priestley and Grant [109] for unbounded post-tensioned systems (flag-shape model) was used. In order to validate the reliability of the equivalent damping considered in the design procedure of post-tensioned timber framed buildings with dissipative bracing systems, the results of the shaking table tests were compared with the corresponding design values and with the results of non-linear dynamic analyses of BF model.

7.2.1. Experimental and analytical estimation of equivalent viscous damping

The equivalent viscous damping has been experimentally estimated as sum of the elastic and hysteretic damping contributions [130] and numerically verified as reported in the following Equation (17):

$$\xi_{eq} = \frac{\delta}{\sqrt{\delta^2 + 4\pi^2}} + k\,\frac{1}{2\pi}\frac{A_{hyst}}{F_0 u_0} \qquad (17)$$

The first contribution of Equation 17 represents the elastic damping of the structural system. It was estimated from experimental and numerical time-domain free vibration response of displacement of the bare post-tensioned frame. Figure 80 shows the reference earthquake input 1228 at the design level (100% of PGA) and the time history of the recorded top displacement compared with the numerical outcome. As can be observed, experimental and numerical results were in good agreement. The free vibration response highlighted in the graph was shown in detail in Figure 81 and based on the measured peak.

displacement amplitudes of successive cycles, the logarithmic decrement δ [154] was used to find the experimental and numerical elastic damping. It was estimated by averaging many cases of elastic damping (first member of Equation 17) for all successive peaks of the free vibration time history.

As shown in Figure 81 the time-displacement free vibration response was in line with the exponentially narrowing curve (dashed line), related to a value of elastic damping ξ_0 = 2.5%. The same value was estimated by using free vibrations of displacement time histories of the post-tensioned model with dissipative bracing systems. This result highlighted that during free oscillations the dissipative dampers are not activated and the frame responded elastically.

The second contribution of Equation 17 represents the hysteretic damping of the braced frame based on the Jacobsen's formulation [143], multiplied by the dynamic reduction factor assumed in the design procedure k=0.85 [93]. Starting from the global flag-shape hysteretic experimental and numerical responses of the braced model (Figure 71), the hysteretic area A_{hyst} and related maximum force F_0 and displacement u_0 were evaluated for the three seismic input at all PGA levels and the hysteretic equivalent damping was estimated.

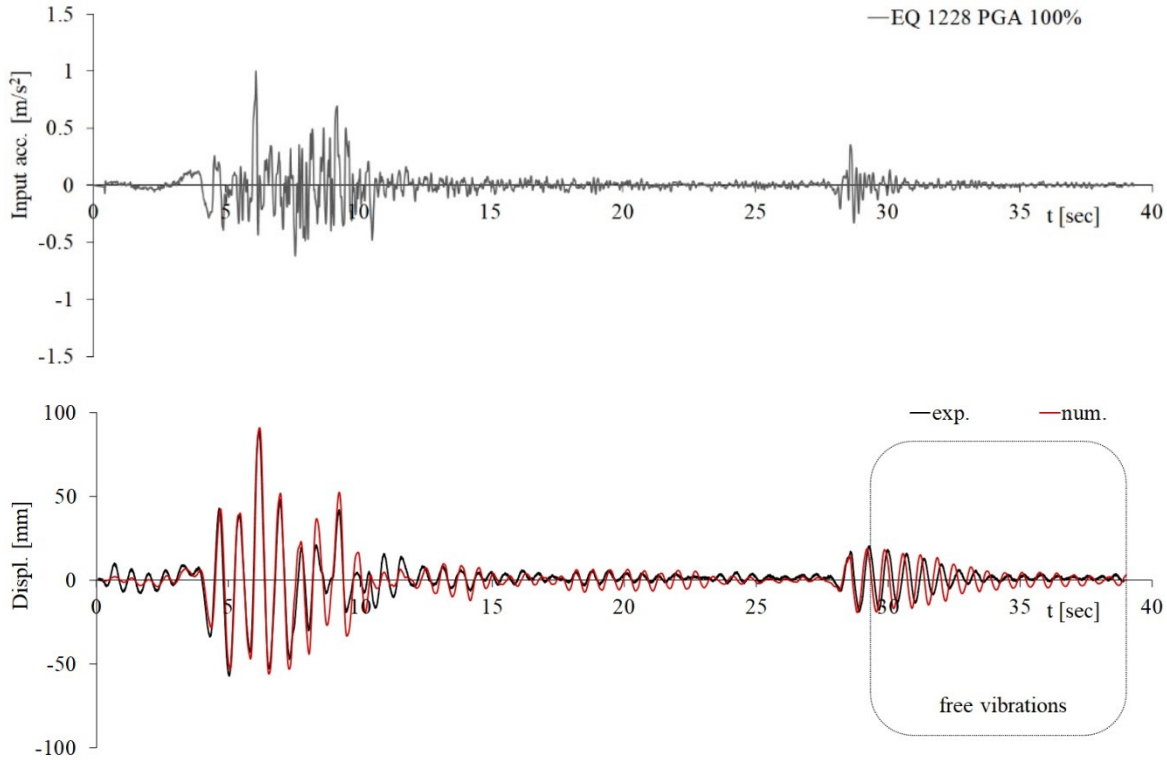

Figure 80: Input acceleration and recorded top displacement of the bare post-tensioned frame model for earthquake 1228 at 100% of PGA.

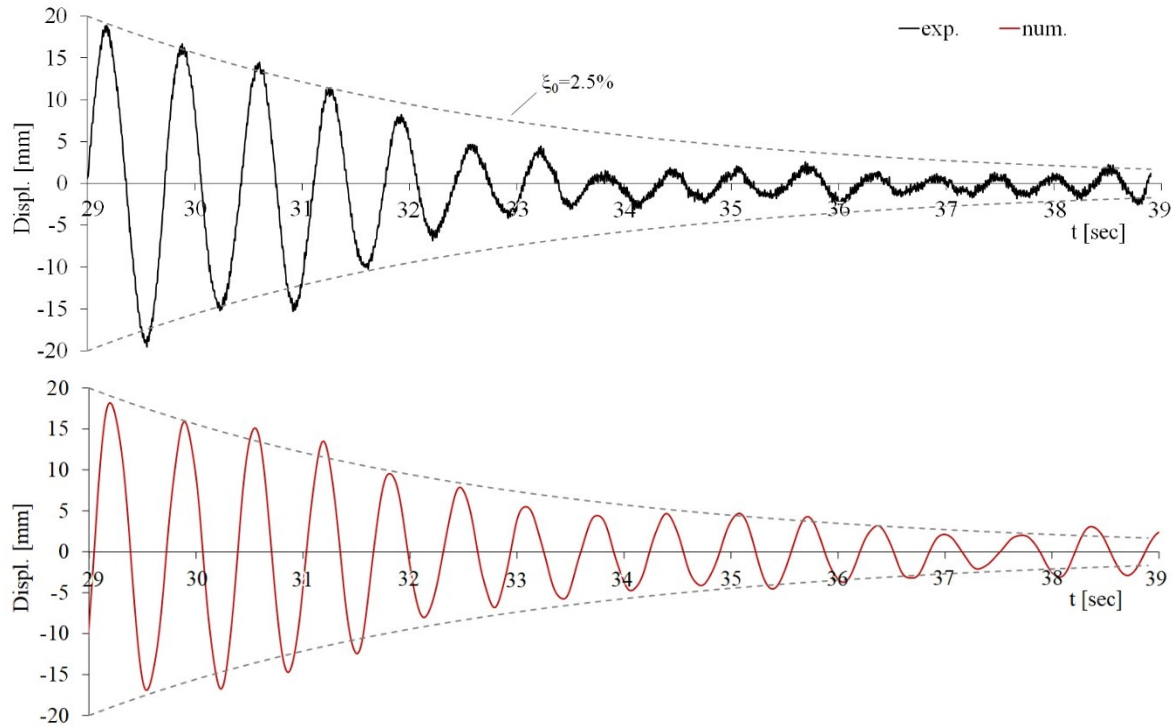

Figure 81: Estimation of elastic damping from free vibration displacements versus time response for the bare post-tensioned frame model.

In order to demonstrate the effectiveness of the damping system the equivalent hysteretic damping contribution estimated for BF model has been compared with that of DF model in Figure 82. As can be observed, the mean value of the hysteretic experimental damping grows for increasing PGA levels for both DF and BF. At 10% of PGA the hysteretic dampers were not yet activated and the experimental equivalent hysteretic damping was almost the same for both configurations ($\xi_{hyst,exp} \cong 2.5\%$). At higher PGA levels (>50% of PGA) the hysteretic experimental equivalent damping of BF was significantly higher than DF configuration confirming the effectiveness of the bracing system. It was stable in the range of 13%-14% in BF configuration and 5%-6% in DF configuration.

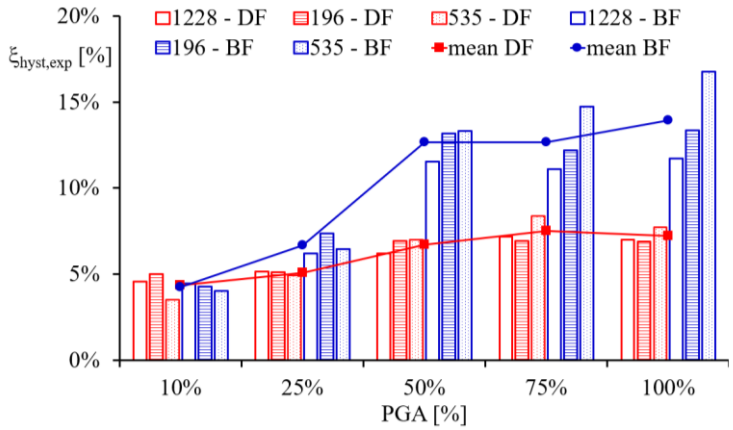

Figure 82: Experimental hysteretic damping estimation at increasing PGA values for DF and BF model configurations.

Figure 83a shows the comparison between experimental and numerical estimation of equivalent damping (ξ_{eq}) in terms of mean value obtained for the three seismic inputs at increasing PGA levels. As can be observed, a good agreement between numerical and experimental results was observed. At PGA values higher than 50%, when dissipative dampers were activated, the experimental estimated damping was stable around 14% and around 13% for the numerical model. The design value of equivalent damping ξ_{eq}=12% was in line with the experimental and numerical results.

Figure 83b shows the equivalent damping versus ductility formulations available in literature proposed by some notable authors ([109],[147],[148],[149],[151]) for different structural systems compared with the experimental estimations of equivalent

damping and corresponding ductility obtained for the three seismic inputs considered in this study at all PGA levels. Ductility of experimental models was calculated from global hysteresis responses as the ratio between the ultimate displacement and the displacement corresponding to the yield point on the idealized response curve. In the current study a maximum value of equivalent damping in the range of 11–16% for ductility values in the range of 3-5 at 100% of PGA was obtained.

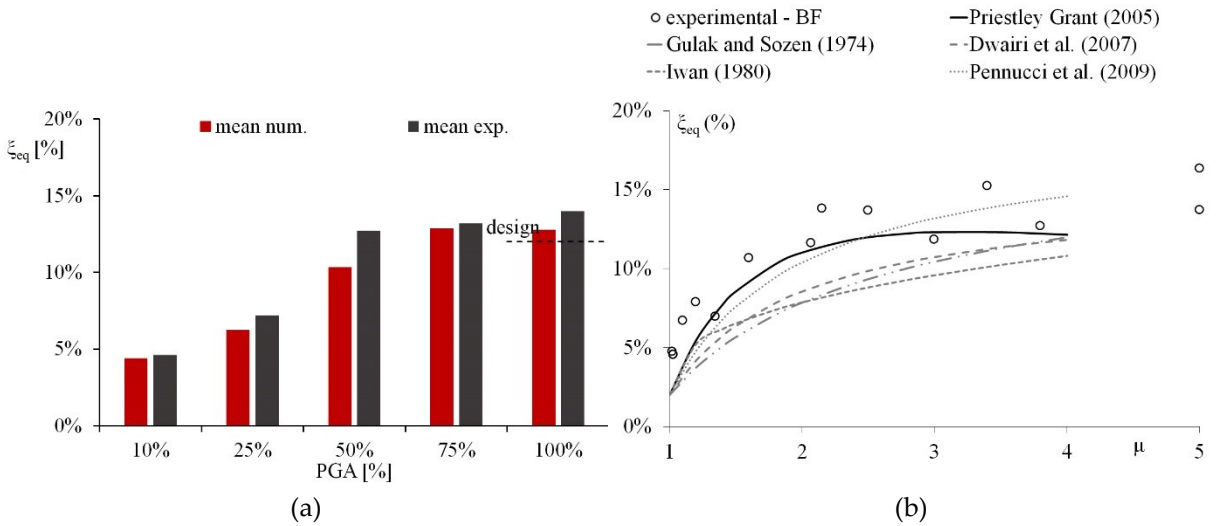

Figure 83: Comparison between experimental estimation of equivalent damping and some of the existing equivalent damping formulations.

As can be observed the experimental results are in line with the formulation of Pennucci et al. (2009) applied to the design flag-shape system (λ=2.23) and with that used in the design procedure due to Priestley and Grant (2005) introducing the reduction factor k=0.85. The formulations proposed by Gulak and Sozen for Takeda model, Iwan for Elastic and Coulomb slip elements and Dwairi for RC flag-shaped hysteretic systems are similar, and the experimental results slightly overestimate the damping-ductility curves.

7.3 Experimental and numerical validation of design procedure

The design procedure applied to DF (section 3.3.1), and BF (section 3.3.2) model configurations has been validated based on the experimental shaking table test results and numerical outcomes of NLTHA [93], [113].

The structural capacity curves of the SDOF system obtained by the design procedure and the demand spectrum of DF configuration (Figure 84b) and that of F configuration (Figure 84b) are plotted in the acceleration-drift response spectrum format. The experimental maximum top displacement (divided by the effective height of the structure) and the corresponding base shear (divided by the equivalent mass of the structure) recorded in free (F) and dissipative (DF) configurations of the post-tensioned frame at different PGA levels have been also reported in the figure.

In Figure 84b the mean value of the experimental total displacements normalized by height ϑ recorded in case of dissipative (DF) configuration at 100% of PGA level (Figure 64 and Table 15), corresponding to the design earthquake is compared with the target drift ϑ_d assumed in Step 1 of design procedure (dashed vertical line) and with the mean numerical value. As can be seen, the mean experimental drift (averaged on 7 tests) is accurately predicted by the design target drift ϑ_d = 1.9%. Therefore, the drift compatibility (Step 7 of design method) of the experimental and numerical models in dissipative rocking configuration is verified.

At a PGA level of 100%, it can be pointed out that the dissipative rocking configuration allows an improvement of seismic behaviour when compared to the free-rocking (F) condition. In fact, a reduction of the inter-storey drift ϑ_d from 3% to 1.9% and an increase of the equivalent damping ξ_{eq} from 2% to 6.4% and of the equivalent stiffness K_e from 513 kN/m to 770 kN/m are shown.

Furthermore, Figure 84 displays the experimental maximum values of tests performed at various PGA levels, and the equivalent SDOF system of dissipative (DF) and free (F) rocking conditions. The drift increases with increasing level of seismic input and

the design curves provide a good representation of the experimental results in both the F and DF configurations.

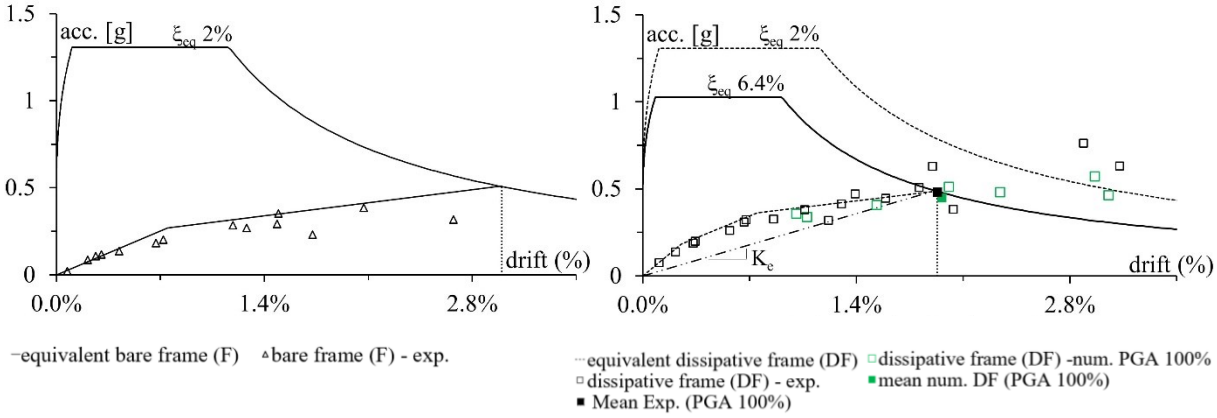

Figure 84. Comparison between design results and experimental peak values in: (a) F configuration and (b) DF configuration of experimental post-tensioned timber model.

The design assumptions used for the BF model (Figure 85a) have been validated through comparison with the experimental and numerical outcomes. The equivalent SDOF system obtained from design procedure of F and BF models compared with the acceleration-drift response spectrum format are plotted in Figure 85. The experimental total drift (i.e., maximum top displacement normalized by height of the structure) vs. corresponding accelerations (i.e., base shear divided by the equivalent mass) recorded at different PGA levels are reported in Figure 85a for the F model and in Figure 85b for the BF model.

The numerical results of non-linear dynamic analyses carried out on the BF model for all seismic inputs at 100% of PGA level have been compared with the target displacement Δ_d or drift θ_d assumed in the design procedure (dashed vertical line at 1.25%) in Figure 85b. As can be observed, the mean value of numerical drift (averaged on seven earthquakes) was accurately predicted by the design target drift θ_d, as a verification of the design procedure (Step 7 of design method). From Figure 85 it can be pointed out that the seismic response of the BF model at the DBE (100% of PGA) reduces the inter-story drift "d more than twice if compared with the response of model F from 3 to 1.25%. This effect is mainly due to the increase of the equivalent

damping ξ_{eq} from 2 to 12%, perfectly in line with equivalent damping estimations, and of the equivalent stiffness K_e from 513 to 1228 kN/m.

Moreover, the drift increases with an increasing PGA level of seismic inputs and the equivalent SDOF systems provides a reliable representation of the experimental results in both configurations (F and BF models).

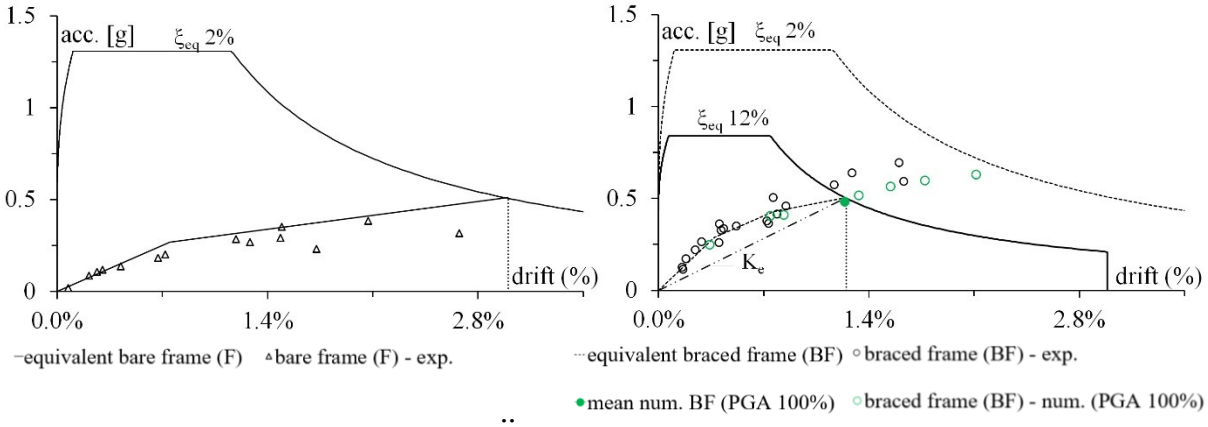

Figure 85. Comparison between design results and experimental peak values in: (a) F configuration and (b) BF configuration of experimental post-tensioned timber model.

The experimental peak values of all earthquakes at all PGA levels of the three model configurations and corresponding design spectra are shown in Figure 86. As can be observed, the trend was in line with the equivalent damping obtained by the design for each model configuration, confirming the increase of strength and stiffness passing from bare frame F to dissipative frame DF and braced frame BF configurations.

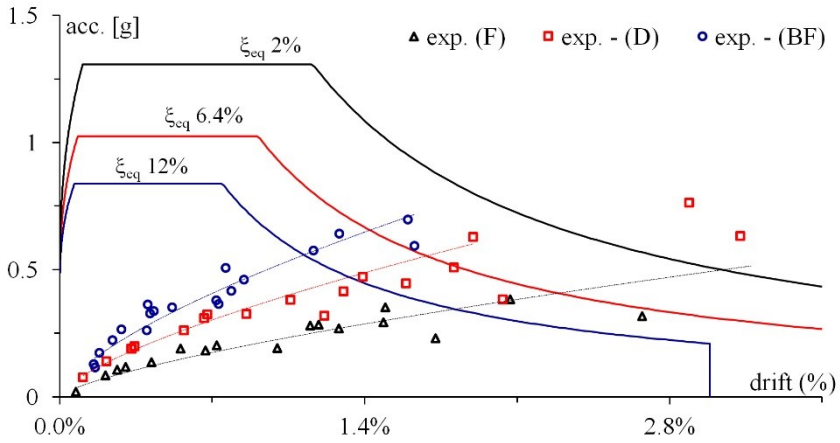

Figure 86 Design spectra and experimental peak values of all model configurations.

8 Dynamic response of nonlinear displacement dependent devices

The performance characteristics of nonlinear displacement dependent devices (NLD) shall be defined by the force-displacement cyclic behaviour, as well as the expected number of cycles related to both the duration of the earthquake and to the fundamental frequency of the structural systems. One of the fundamental parameters investigated to demonstrate the efficacy of metallic dampers is the number of cycles, which can be related to the capacity to dissipate energy for a given displacement and to the fatigue and eventual failure of the devices, leading to different level of damage to the structural system [155]-[157].

Specific codes are adopted worldwide to regulate the use of these seismic-resilient devices. AASHTO Guide Specification for Seismic Isolation Design [158] was the first code which established rules for the dimensioning and the use of anti-seismic devices. This document was firstly focused on isolation systems, then recommendations to energy dissipating devices were also extended. Nowadays the regulation of anti-seismic devices has been included in national standards, as example the Italian seismic code NTC 2018 [1], the European Standards EN 15129 [125] and the American Standards ASCE/SEI 7-10 [3] and guidelines such as the American FEMA 461 [159]. These codes specify the performance requirements of nonlinear displacement dependent device (NLD) in order to reproduce the actual working conditions of the devices, covering all the stages of the life cycles. In general, in case of metallic dampers the velocity has negligible influence and quasi-static tests can be carried out to establish their performance capability. The test procedure shall include the steps listed in the codes unless otherwise prescribed in the design specifications.

As described above, NLDs have been widely used and consolidated as dampers of dissipative bracing systems for anti-seismic steel buildings, but less used for braces of timber buildings, which have the similarity with steel constructions for the assemblage

of members through appropriate joints, even though they are different materials for mechanical characteristics and origins.

Based on the results of the experimental campaign performed at the structural laboratory of University of Basilicata (Italy), in the present chapter the attention is focused on cyclic performance of flexural steel NLD dampers installed in V-inverted dissipative bracing systems of the post-tensioned timber frame extensively described above (Pres-Lam project) [93], [125]. The main objective of this chapter is to assess the reliability of current seismic codes in terms of cyclic testing required for type tests and factory production control tests of NLD.

8.1 Testing code requirements

Steel devices typically show a stable hysteretic behaviour characterized by yield capacity that is well known as function of the steel type considered and that can be determined with simple material tests. The conformity of mechanical characteristics of NLDs with the performance requirements shall be verified by specific tests representing the working conditions and constraints of the device. The Italian and European seismic codes NTC 2018 [1], EN 15129 [125], and American Standards ASCE 7-10 [3] use different empirical approaches for determining the testing protocols for quasi-static tests of the devices. Moreover, several guidelines suggest different loading histories for eventual incorporation in existing standards for the seismic design. FEMA 461 [159] suggests quasi-static testing protocols as an interim basis for testing of building components, it is not intended for seismic performance qualification testing to satisfy the requirements of building codes.

The displacement at the collapse prevention limit state d_2 by NTC 2018 [1], corresponding to the design displacement d_{bd} including the reliability factor $\gamma_x \times d_{bd}$ by EN 15129 [125], or the displacement at the maximum credible earthquake d_{MCE} by ASCE 7-10 [3] shall be considered for the design and analysis of structures with energy dissipative systems. The mechanical tests of the devices shall be carried out by imposing cyclic deformations according to the schedule and the procedures indicated

as type tests (TT) and factory production control tests (FPCT) of devices. All devices shall be qualified under the responsibility of the manufacturer, according to TT procedure provided by codes. Test specimens shall not be used for construction, unless they are approved by the responsible for design of the structure and meet the required qualification documentation, the geometric verification, and dimensional tolerances as well as the FPCT tests for all types of devices. Testing on devices must be performed and certified by a laboratory equipped with adequate competence, equipment, and organization.

Type tests (TT) shall be carried out on at least one specimen in order to reproduce the actual working conditions of the devices given in the design specifications. The specimens shall be loaded so as to produce the same stresses and strains as those experienced during the response of the structure to the design earthquake up to a maximum displacement, at least equal to $\pm d_{bd}$ [125]. For type tests the NTC 2018 [1] refers to EN 15129 [125] (series TT [EN 15129] of Figure 87a). Increasing amplitude cycles shall be imposed at 25%, 50% and 100% of d_{bd} applying five cycles for each intermediate amplitude and at least ten cycles for the maximum amplitude. Moreover, a ramp test shall be performed for the static evaluation of the failure displacement up to a displacement not less than the maximum displacement taking into account the partial factors $\gamma_b \times \gamma_x \times d_{bd}$. The reliability factor γ_x, equal or greater than 1, depends on the role that the devices play in the stability of the construction after the earthquake. The partial factor γ_b, not less than 1.1, is related to action effects other than seismic which can affect the initial configuration of the device. According to NTC 2018 factory production control tests (FPCT) of devices shall be always carried out on the devices prior to their installation on at least 20% of the supply, and however not less than 4 devices [1]. Quasi-static test shall be performed imposing five cycles at the maximum displacement $\pm d_2$ [1] (series FPCT [NTC 2018] of Figure 87b). Differently, Eurocode [125] reduces the devices number to tests to at least 2% with a minimum number of one device with the same increasing amplitude cycles applied for TT (series FPCT [EN 15129] of Figure 87b).

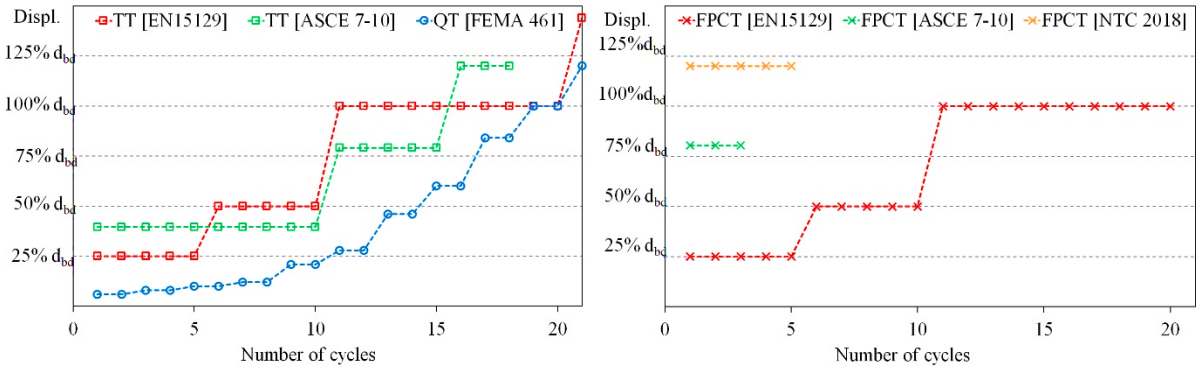

Figure 87. Sketch of deformation-controlled loading history proposed by main codes and guidelines for (a) type tests (TT) and (b) factory production control tests (FPCT).

ASCE 7-10 [3] requires prototype tests (TT) on at least two prototype devices at 33%, 67%, and 100% of the displacement d_{MCE} applying ten, five, and three cycles, respectively (series TT [ASCE 7–10] of Figure 87a). Production tests (FPCT) shall validate the nominal properties by testing 100% of the devices for three cycles at 67% of the d_{MCE} at a frequency equal to $1/(1.5 \times T_1)$ (series FPCT [ASCE 7–10] of Figure 87b). On the other hand, FEMA [159] describes a recommended loading history appropriate for hysteretic testing if a single specimen will be used to quantify all damage states. The loading history consists of repeated cycles of 10 step-wise increasing deformation amplitudes until the targeted deformation amplitude (d_{db}) is reached. Two cycles at each amplitude shall be completed. It highly recommends performing an additional monotonic test to provide a baseline for estimating the cumulative damage effect at each damage state (series QT [FEMA 461] of Figure 87a).

Figure 87a,b compare conceptual diagrams of the loading history required for type tests by the European codes (TT [EN 15129]), by American Standards (TT [ASCE 7-10]) and that recommended for quasi-static Tests (QT) by American guidelines (QT (FEMA 461)) and for factory production control tests by the European code (FPCT (EN 15129)), by American Standards (FPCT [ASCE 7-10]) and by the Italian code (FPCT [NTC 2018]).

8.2 Seismic cycles of NLDs and comparison with testing code requirements

As extensively described in Section 4.1, before shaking table testing, quasi static tests were performed on different types of UFPs. Figure 88 reports the testing setup and an example of the experimental force-displacement responses obtained by controlled displacement tests of two UFPs (C60 stainless steel) in parallel as representative of the devices installed into the bracing system, normalized considering the experimental yielding force (F_y) and displacement (d_y) obtained from experimental tests of each single device (see Table 9). The reference design ductility value was $\mu_d = 4$. The quasi-static testing procedure used for UFPs (Figure 88b) followed the interim protocol for quasi-static cyclic testing proposed by FEMA 461 [159] (see Figure 87). In this case the loading protocol was composed by two cycles at increasing amplitudes with five steps in the elastic range and five steps at ductility values of $\mu = 1$, $\mu = 1.8$, $\mu = 2.5$, $\mu = 3.5$, and $\mu = 4$. A monotonic ramp test up the amplitude of $\mu > 4$ was applied. As can be observed in Figure 88b, the force-displacement results obtained by quasi-static tests, exhibited a stable hysteretic cyclic behaviour without failure over the design ductility.

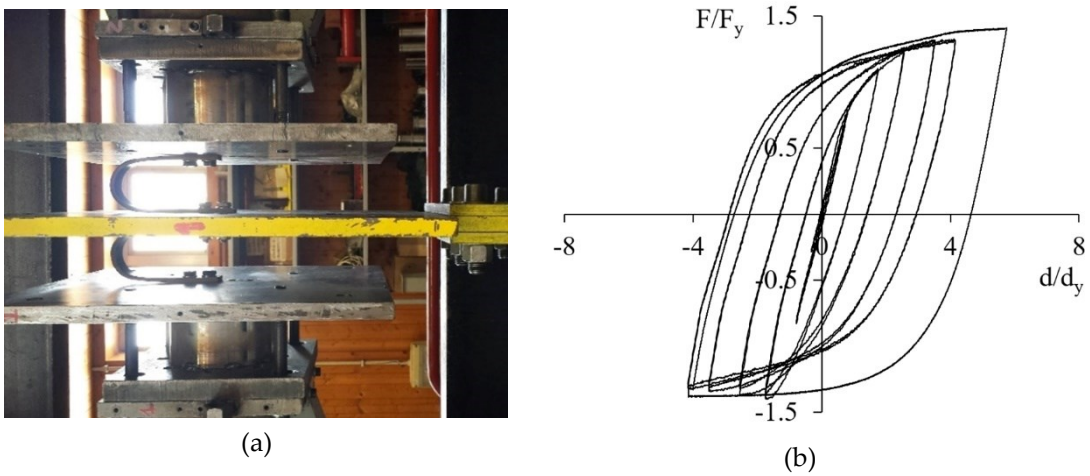

Figure 88. (a)Quasi-static testing set-up and (b)normalized force-displacement response of U-shaped flexural plates (UFPs).

The complete seismic sequence of the BF model with duration of about one thousand seconds is composed by 20 consecutive seismic inputs, collected from the set of seven

natural spectra-compatible earthquakes presented in Chapter 4, at increasing intensities from 10% to 100% of PGA.

The time-history of global drift of BF model is shown in Figure 89 and Figure 90 shows the time-history of demand ductility up to the UFPs devices breakage occurred during the test with earthquake input 187 at 100% of PGA level at the first storey.

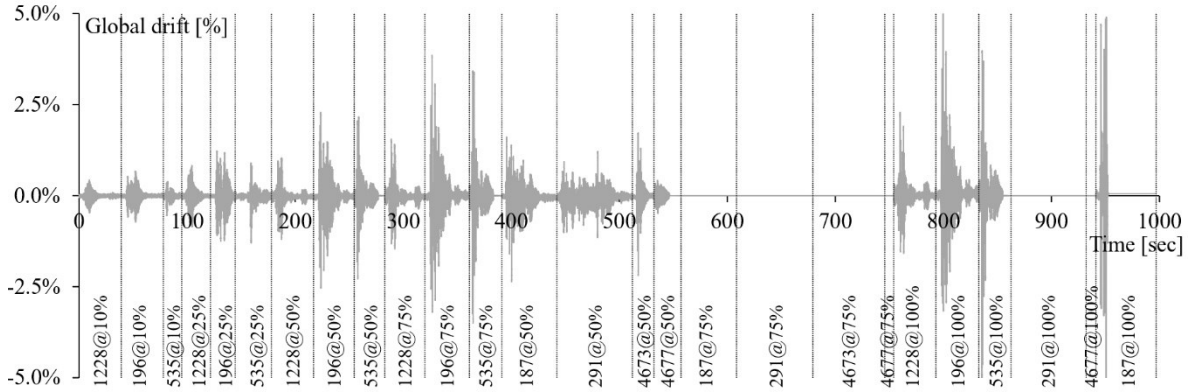

Figure 89. Time history of global drifts of the post-tensioned timber braced frame (BF model).

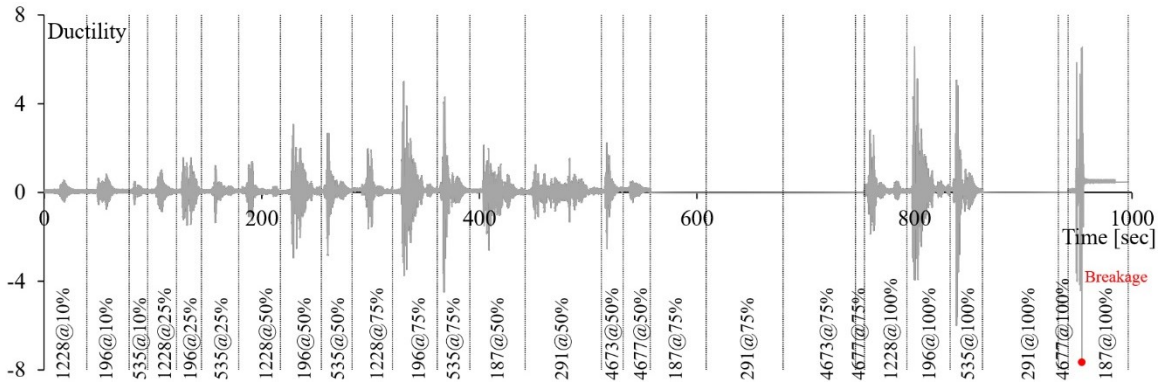

Figure 90. Time history of the ductility of dampers of UFPs at the first story of the BF model.

As can be observed the braced frame exhibited a complete re-centering capability, with negligible residual inter-story drift and displacements of dampers accumulated during the complete seismic sequence. Up to 50% of PGA level the global drift reached the design drift of 1.25%, for most severe earthquakes and the ductility of UFPs slightly exceeds the design value.

The displacement time history and the force-displacement behaviour of devices of the last test of the seismic sequence (187 at 100% of PGA), during which the failure condition for fatigue was reached by UFP at the first storey, are shown in Figure 91.

As shown by photo of Figure 91, the rupture occurred through fracture of the yielding section at ductility values higher than the design ones.

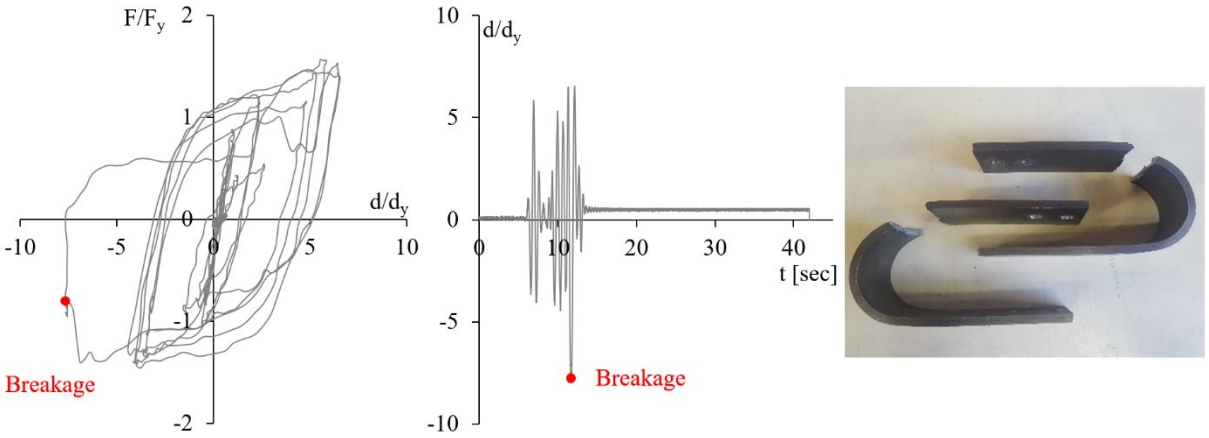

Figure 91. Time-history of displacement and force-displacement cycles for seismic input 187 at 100% of PGA level and photos of the rupture of UFP at the first story.

The estimation of the total number of cycles at different ductility levels obtained for first story UFP dampers from the experimental testing sequence has been summarized in Table 19. The mean values of number of cycles considering all earthquakes and the value of the standard deviation, representing the measure of the dispersion of the data, are also reported. The estimation highlighted a high number of cycles at low ductility values (up to $\mu = 2$) spread out over a wide range, while at higher ductility values ($\mu > 2$) a reduced number of cycles was recorded with low dispersion. The number of cycles estimated at the design ductility and at higher values ($\mu \geq 4$) resulted significantly lower than the minimum number of testing cycles required by codes both for TT and FPCT. The failure of UFP devices occurred during the stronger earthquake input considered, after more than 100 cycles sustained over the elastic range.

Table 19 Number of cycles of UFP dampers at the first story from all seismic sequence.

Ductility	UFPs from Dynamic Tests of TBF		
	Total n. Cycles	Mean	St. Dev.
$\mu \leq 1$	986	49.3	32.7
$1 < \mu \leq 2$	83	4.2	4.2
$2 < \mu \leq 3$	26	1.3	1.8
$3 < \mu \leq 4$	5	0.25	0.6
$\mu > 4$	9	0.45	0.9

Figure 92 shows the estimation of the number of cycles of the first story UFP devices of the BF model under the design earthquakes (100% of PGA) as a function of different

ductility demands. In order to consider the complete set of ground motions the number of cycles estimation of UFPs was evaluated considering the available dynamic experimental results (grey bars) and nonlinear numerical analysis (blue bars) as shown in Figure 92a,b. As can be observed the number of cycles at each ductility level varies between the earthquakes, depending on the characteristics of each ground motion. Figure 92c shows the average value of the mean number of dynamic cycles from experimental and from numerical results (mean dynamic num-exp). As can be observed, a good agreement was found between the mean experimental and numerical number of cycles estimated for UFP devices. In both cases the number of cycles considerably decrease at increasing level of required ductility.

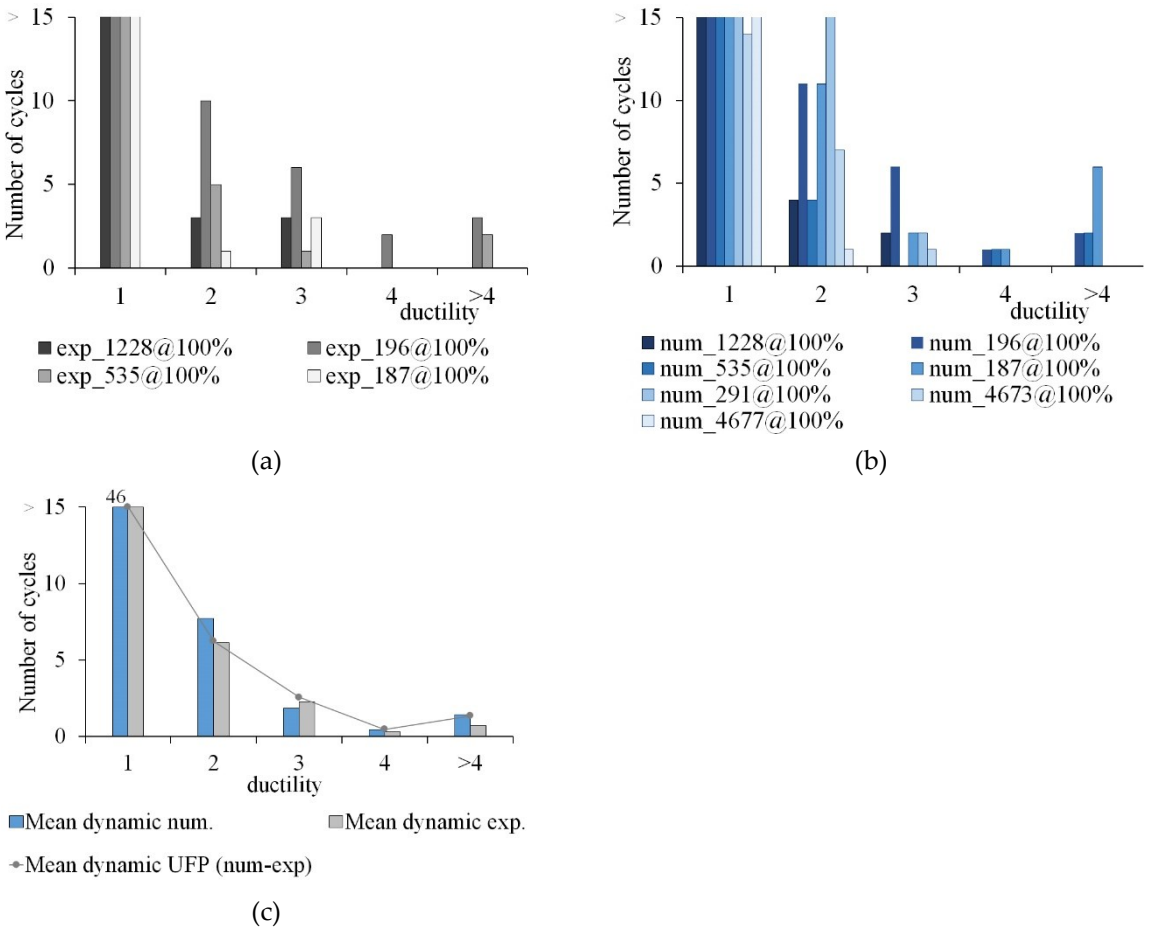

Figure 92. Number of cycles vs. ductility demand of UFPs during the design earthquakes (PGA 100%) obtained by(a) experimental dynamic tests (b) nonlinear numerical analyses and (c) corresponding mean values.

The mean values of number of cycles estimated from the design earthquakes compared with the main code requirements for TT and FPCT testing of NLD devices standards [1],[3],[125] and guidelines [159] is shown in Figure 93 as function of the ductility demand. The mean number of cycles confirms the trend proposed by American standards and guidelines (TT [ASCE 7-10]) and QT [FEMA 461]) for quasi-static characterization tests, in accordance with characterization tests performed on UFPs (see Figure 88b). On the contrary the loading protocol required by European code EN 15129, also assumed by Italian code NTC 2018, seems to penalize devices excessively being not in good agreement with both experimental dynamic results. The minimum testing requirement for TT by European code (TT [EN 15129]) overestimated the number of cycles at the design displacement (corresponding to $\mu = 4$).

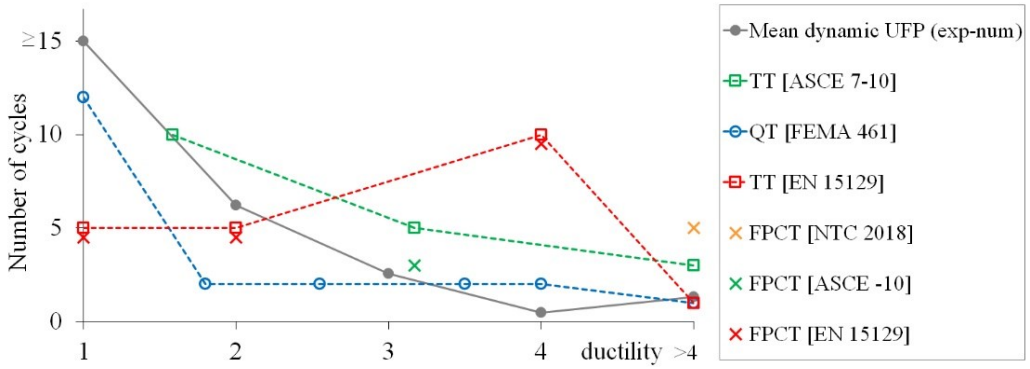

Figure 93. Number of cycles estimated for UFPs of the timber braced frame from dynamic tests compared with various code requirements.

The minimum required for FPCT by Italian code (FPCT [NTC 2018]) at the maximum displacement ductility is much higher than the corresponding average values observed for dynamic tests. Moreover, FPCT by Italian code is required for a minimum of four NLD dampers of the same type and size. A high number of device testing should be unnecessary due to the typically stable hysteretic behaviour of yielding steel dampers. Moreover, stronger performance requirements than the actual seismic working condition of the devices could mean that the devices become unusable after testing besides higher costs required for testing procedures.

9 Conclusions

The experimental campaign performed at University of Basilicata on the post-tensioned glulam timber frame with supplemental damping systems has provided an opportunity to study various parameters that influence the seismic response of these systems and to provide a research contribution in the field of seismic resilient timber frame structures. The key objective of this thesis was the experimental investigation and numerical prediction of seismic response of post-tensioned timber frame buildings with dissipative bracing systems. The research focused on shaking table tests performed at the structural laboratory of University of Basilicata on a 3D, 2/3rd scaled, post-tensioned timber frame with V-inverted dissipative bracing including U-shaped Flexural Plate dampers (UFPs). The testing of braced frame (BF) was part of an extensive shake table testing campaign in collaboration with University of Canterbury (New Zealand), in which the bare post-tensioned frame without (F) and with (DF) steel angles placed at the beam-column and column foundation joints, were also tested. In order to validate the effectiveness of the bracing system, the experimental data of the three configurations (over than 100 tests performed) were compared and used to calibrate analytical procedure for design of dampers and numerical models of F, DF and BF specimen. All experimental results performed at increasing PGA levels (from 10% to 100% of PGA) pointed out the fundamental role of the dissipative bracing system in controlling the seismic vibrations improving the performance of the glulam post-tensioned timber frame building.

The main findings and conclusions drawn from this research work are summarized below, based on the main research objectives reported in Section 1.2.

1. Investigation on the seismic response of the braced post-tensioned frames through the shaking table tests.

The bracing system including external replaceable UFP dampers allowed of developing a resilient and more flexible architectural system for post-tensioned timber (Pres-Lam) buildings without changing the gravitational load distribution on beams and columns and reducing the influence on the post-tensioned beam-column joints. The introduction of the dissipative bracing systems resulted in significant benefits on the overall seismic behaviour, reducing the maximum inter-storey drift of about 20% than DF model and of about 45% than F model at 75% of PGA level. UFPs remained in the elastic range at input levels lower than 25% of PGA (SLE) and exhibited a stable hysteretic behaviour for all seismic inputs under a large number of deformation cycles with an excellent dissipative capacity at higher PGA levels up to 100%. The global response of the braced model showed a flag-shaped hysteretic behaviour with a complete re-centering capability. A larger amount of energy was dissipated by BF model respect to the DF model, in line with the design purpose. The combination of post-tensioned timber timber frame and dissipative bracing system has permitted to achieve a resilient seismic performance without observing structural damages and negligible seismic post-tensioning losses under repeated earthquakes.

2. Numerical modelling of post-tensioned frame with different dissipative systems.

Numerical models of F, DF and BF were developed in SAP 2000 and OpenSees software. Dynamic characteristics, in terms of the first three natural periods of vibration of the test frames were well approximated by numerical simulations. Non-linear time history analyses of the F, DF and BF were performed considering the set of seven spectra compatible earthquakes, providing a reliable response of the seismic global response and local behaviour of hysteretic UFP dampers. Nonlinear static analyses provided a well approximation of the maximum values recorded by experimental dynamic tests.

3. Displacement based design procedure for post-tensioned timber framed buildings with dissipative systems.

Numerical and experimental dynamic results were used for the validation of the optimized displacement-based design procedure proposed for post-tensioned timber frame with dissipative rocking and with dissipative bracing systems. The equivalent viscous damping was experimentally estimated and resulted in line with the design values of 2% for F model, 6.4% for DF model and 12% for BF model configuration. The target design drift of 1.9% for DF model and of 1.25% for BF model provided an accurate approximation of the averaged numerical and experimental value of the maximum drift at the design level (PGA of 100%), showing the reliability of the design procedure.

4. *Dynamic response of nonlinear dampers (NLDs).*

The dynamic hysteretic behaviour of U-shaped flexural steel dampers of the dissipative bracing systems was investigated in terms of number of cycles at different ductility levels. The UFPs provided ductile and stable performances with excellent dissipative capacity also when the displacement exceeded the design value. More than one hundred inelastic cycles were experimentally recorded from the complete seismic sequence of about 20 earthquakes at increasing PGA levels before the device failure, without damages to the structural elements. The number of cycles under the design earthquakes (PGA 100%) considerably decreased with increasing of ductility demand of UFP devices. This trend was in line with American standards testing requirements ASCE 7-10 [3] for prototype tests (TT) and in good agreement with the loading history suggested by American guidelines FEMA 461 [159]. The procedure imposed for type tests (TT) and for factory production control tests (FPCT) by European (EN 15129) [125] and Italian (NTC 2018) [1] seismic codes significantly overestimated the number of cycles at the design ductility for both experimental case studies. Finally, it can be pointed out that the number of devices required for FPCT by the NTC 2018 appear

redundant compared with EN 15129, this becomes uneconomical especially in case of supply of few steel-based dampers unusable after testing.

The promising numerical and experimental results highlighted in this work represents the basis for further studies aiming to derivate the seismic fragility curves and hazard level for each limit state and determine the mean annual frequency of exceeding a threshold level of damage associated with global or local engineering demand parameters (e.g. global drift and local hysteretic response of dampers or post-tensioning losses) for the proposed high performance timber buildings with different energy dissipation systems.

References

[1] NTC 2018, Norme Tecniche per le Costruzioni, Decreto Ministeriale del 17 Gennaio 2018; Ministero delle Infrastrutture e dei Trasporti: Rome, Italy, 2018.

[2] UNI EN 1998-1 (2013) EUROCODE 8: design of structures for earthquake resistance—part 1: general rules, seismic actions and rules for buildings. European Committee for Standardization, Brussels, Belgium.

[3] ASCE/SEI 7-16 Minimum Design Loads for Buildings and Other Structures; American Society of Civil Engineers: Reston, VA, USA, 2016.

[4] Priestley, M. J. N. (1999). Displacement-based approaches to rational limit states design of new structures. *Proc. 11 ECEE*, *2*, 317-335.

[5] Ugalde D., Almazán J. L., Santa María H., and Guindos P. (2019). Seismic protection technologies for timber structures: a review. *Eur. J. Wood Wood Prod. 77*, 173–194. doi: 10.1007/s00107-019-01389-9.

[6] Priestley M.J.N., Sritharan S., Conley J.R., Pampanin S. (1999). Preliminary Results and Conclusions from the PRESSS Five-Story Precast Concrete Test Building. *PCI Journal*, 44.

[7] Palermo A., Pampanin S., Buchanan A. and Newcombe M.P., (2005) Seismic Design of Multi-Storey Buildings using Laminated Veneer Lumber (LVL), *NZSEE Conference*, Taupo, New Zealand.

[8] Ho T.X., Dao T.N., Aaleti S., van de Lindt J.W., Rammer D.R. (2016) Hybrid system of unbonded post-tensioned CLT panels and light-frame wood shear walls. *J Struct Eng 143*(2),040

[9] Iqbal A., Fragiacomo M., Pampanin S., Buchanan A. (2017) Seismic resilience of plywood-coupled LVL wall panels. *Eng Struct 167*(1), 750–759. https ://doi.org/10.1016/j.engst ruct.2017.09.053

[10] Newcombe M.P., Pampanin S., Buchanan A.H. (2010) Global response of a two-storey Pres-Lam building. In: Proceedings of New Zealand society for earthquake engineering conference Wellington, New Zealand: New Zealand Society for

Earthquake Engineering 16171. https ://doi.org/10.1061/ (ASCE)ST.1943-541X.00016 65.

[11] Pei S., van de Lindt J.W., Barbosa A.R., Berman J.W., McDonnell E., Dolan J.D., Blomgren H.E., Zimmerman R.B., Huang D., Wichman S. (2019) Experimental seismic response of a resilient 2-story mass-timber building with post-tensioned rocking walls. *J Struct Eng 145*(11), 04019120.

[12] Smith T., Ponzo F.C., Di Cesare A., Pampanin S., Carradine D., Buchanan A.H., Nigro D. (2014) Post-tensioned Glulam Beam-column joints with advanced damping systems: testing and numerical analysis. *J Earthq Eng 18*(1), 147–167.

[13] Di Cesare A., Ponzo F.C., Nigro D., Pampanin S., Smith T. (2017) Shaking table testing of post-tensioned timber frame building with passive energy dissipation systems. *Bull Earthq Eng 15*(10), 4475–4498.

[14] Saunders, W. S. A., & Becker, J. S. (2015). A discussion of resilience and sustainability: Land use planning recovery from the Canterbury earthquake sequence, New Zealand. *International journal of disaster risk reduction*, *14*, 73-81.

[15] Pei, S., Van De Lindt, J. W., Popovski, M., Berman, J. W., Dolan, J. D., Ricles, J., ... & Rammer, D. R. (2016). Cross-laminated timber for seismic regions: Progress and challenges for research and implementation. *Journal of Structural Engineering*, *142*(4), E2514001.

[16] Thelandersson, S., & Larsen, H. J. (Eds.). (2003). *Timber engineering*. John Wiley & Sons.

[17] Uma, S. R., Dhakal, R. P., & MacRae, G. A. (2013). Implementation of low damage construction: What are the challenges? In: Proceedings of New Zealand society for earthquake engineering conference Wellington, New Zealand: New Zealand Society for Earthquake Engineering

[18] Fairweather, R. H. (1992). Beam column connections for multi-storey timber buildings. PhD dissertation, University of Canterbury (NZ).

[19] Angelidi, M., Vassilopoulos, A. P., & Keller, T. (2018). Ductility of adhesively bonded timber joints. *Timber Structures and Engineering*, 125.

[20] Dunn, A. (2015). Final report for commercial building costing cases studies: traditional design versus timber project. Melbourne, Australia: Forest and Wood Products Australia. [Report No. PNA308-1213].

[21] Buchanan AH (2001) Structural design for fire safety. Wiley, West Sussex: 421pp

[22] Buchanan AH, Ostman B, Frangi A (2014) Fire resistance of timber structures. NIST white paper. National Institute of Standards and Technology, Washington, DC

[23] Östman B et al (2010) Fire safety in timber buildings – technical guideline for Europe. SP Report 2010:19. SP Technical Research Institute of Sweden, Stockholm

[24] Falk, R. H. (2009). Wood as a sustainable building material. *Forest products journal, 59* (9), 6-12.

[25] Hart, J., & Pomponi, F. (2020). More Timber in Construction: Unanswered Questions and Future Challenges. *Sustainability, 12*(8), 3473.

[26] Rhodes, C. J. (2016). The 2015 Paris climate change conference: COP21. *Science progress, 99*(1), 97-104.

[27] Gong, M. (2019). Lumber-Based Mass Timber Products in Construction. In Timber Buildings and Sustainability. IntechOpen

[28] Mohammad M, Gagnon S, Douglas BK, Podesto L. (2012). Introduction to cross laminated timber. *Wood Design Focus.; 22*(2), 3-12.

[29] European Standard EN 14080:2013 Timber structures – Glued laminated timber and glued solid timber - Requirements. Bruxelles, Belgium, June 2013.

[30] Binational Softwood Lumber Council (BSLC). Nail-Laminated Timber: US Design & Construction Guide. Ver. 1.0. Minneapolis, MN, USA: StructureCraft; 2017. 142.

[31] Rombach, (2018). Rombach Nur Holz. Available at: http://www.nur-holz.com/startseite/6/de/home.html, 20th November 2018.

[32] Chopra, A.K. and Yim, S.C., (1985). Simplified analysis of structure with foundation uplift. *Journal of Structural Engineering*, 111(4), pp. 906-930.

[33] Priestley, M.J.N. 1991. Overview of PRESSS research program. *PCI Journal* 36(4): 50-57.

[34] Christopoulos, C., Filiatrault, A., Uang, C., and Folz, B. (2002). Post-tensioned energy dissipating connections for moment resisting steel frames. *Journal of Structural Engineering, 128*(9),1111–1120.

[35] Buchanan, A., Deam, B., Fragiacomo, M., Pampanin, S. and Palermo, A., (2008) Multi-Storey Prestressed Timber Buildings in New Zealand. *Journal of the International Association for Bridge and Structural Engineering, 18*(2), pp. 166-173.

[36] Palermo, A., Pampanin, S. and Carradine A., (2005) Efficiency of Simplified Alternative Modelling Approaches to Predict the Seismic Response of Precast Concrete Hybrid Systems. *FIB symposium "Keep Concrete Attractive"*, Budapest, Hungary.

[37] Buchanan, A. H. and Fairweather, R. H. (1993) Seismic design of Glulam structures, *Bulletin of the New Zealand Society for Earthquake Engineering* 26(4),415–436

[38] Newcombe, M., Cusiel, M., Pampanin, S., Palermo, A., and Buchanan, A. H. (2010) Simplified design of post-tensioned timber frames, CIB W18 Workshop on Timber Structures, Nelson, New Zealand.

[39] Cusiel,M. R., Newcombe,M. P., Pampanin, S., Buchanan, A. H., and Palermo, A. 2010. The effect of joint flexibility on the seismic response of post-tensioned LVL frames, 14*th European Conference on Earthquake Engineering*, Ohrid, Republic of Macedonia.

[40] Van Beerschoten, W., Smith, T., Palermo, A., Pampanin, S., and Ponzo, F. C. (2011). The stiffness of beam to column connection in post-tensioned timber frames, *CIB W18 Workshop on Timber Structures*, Alghero, Italy.

[41] Pampanin, S., Priestley, N., and Sritharan, S. (2001) Analytical modelling of the seismic behaviour of precast concrete frames designed with ductile connections, *Journal of Earthquake Engineering* 5(3), 329–367.

[42] NZS 3101:1995 [2006] *Concrete Structures Part 1. The Design of Concrete Structures. Secondary Concrete Structures Part 1. The Design of Concrete Structures*, Standards New Zealand, New Zealand.

[43] Kelly, J.M.; Skinner, R.I.; Heine, A.J. (1972). Mechanisms of energy absorption in special devices for use in earthquake resistant structures. *Bull. NZ Soc. Earthq. Eng.*, 5, 63–88.

[44] Montuori, R.; Nastri, E.; Piluso, V. (2015). Advances in theory of plastic mechanism control: Closed form solution for MR-Frames. *Earthq. Eng. Struct. Dyn.*, *44,* 1035–1054.

[45] Skinner, R.I.; Kelly, J.M.; Heine, A.J. (1974). Hysteretic dampers for earthquake-resistant structures. *Earthq. Eng. Struct. Dyn., 3*, 287–296, doi:10.1002/eqe.42900 30307.

[46] Baird, A.; Smith, T.; Palermo, A.; Pampanin, S. (2014). Experimental and numerical study of U-shape flexural plate (UFP) dissipators. In New Zealand Society for Earthquake Engineering Conference; University of Canterbury: Christchurch, New Zealand.

[47] Watanabe, A.; Hitomi, Y.; Saeki, E.; Wada, A.; Fujimoto, M. (1988). Properties of brace encased in buckling-restraining concrete and steel tube. In Proceedings of the Ninth World Conference on Earthquake Engineering, 2–9August, Tokyo, Japan; Volume 4, pp. 719–724.

[48] Javanmardi, A.; Ibrahim, Z.; Ghaedi, K.; Ghadim, H.B.; Hanif, M.U. (2020). State-of-the-art review of metallic dampers: Testing, development and implementation. *Arch. Comp. Methods Eng., 27*, 455–478.

[49] Nuzzo, I., Losanno, D., Cilento, F., & Caterino, N. (2020). Analytical and numerical modelling of shear-link device for seismic energy dissipation in frame structures. *Engineering Structures, 214,* 110630.

[50] Mazza, F., & Mazza, M. (2019). Seismic retrofitting of gravity-loads designed rc framed buildings combining CFRP and hysteretic damped braces. Bulletin of *Earthquake Engineering, 17*(6), 3423-3445.

[51] Bertero, R.D.; Bertero, V.V. (2002). Performance-based seismic engineering: The need for a reliable conceptual comprehensive approach. *Earthq. Eng. Struct. Dyn., 31,* 627–652.

[52] Symans, M.D.; Charney, F.A.; Whittaker, A.S.; Constantinou, M.C.; Kircher, C.A.; Johnson, M.W.; McNamara, R.J. (2008). Energy dissipation systems for seismic applications: Current practice and recent developments. *J. Struct. Eng., 134*, 3–21.

[53] Wang, J.; Zhao, H. (2018). High performance damage-resistant seismic resistant structural systems for sustainable and resilient city: A review. *Shock Vib.*, 1–32, doi:10.1155/2018/8703697.

[54] Tirca, L.; Serban, O.; Lin, L.; Wang, M.; Lin, N. (2016). Improving the seismic resilience of existing braced-frame office buildings. *J. Struct. Eng., 142,* C4015003, doi:10.1061/(asce)st.1943-541x.0001302.

[55] Christopoulos, C.; Filiatrault, A. (2006). Principles of Passive Supplemental Damping and Seismic Isolation; IUSS Press: Pavia, Italy,p. 480.

[56] Jahangir, H.; Bagheri, M.; Delavari, S.M.J. (2020). Cyclic Behavior Assessment of Steel Bar Hysteretic Dampers Using Multiple Nonlinear Regression Approach. *Iran J. Sci. Technol. Trans. Civ. Eng.*, 1–25, doi:10.1007/s40996-020-00497-4.

[57] Wijaya, H.; Rajeev, P.; Gad, E.; Amirsardari, A. (2019). Effect of hysteretic steel damper uncertainty on seismic performance of steel buildings. *J. Constr. Steel Res., 157*, 46–58.

[58] Di Cesare, A.; Ponzo, F.C.; Nigro, D. (2014). Assessment of the performance of hysteretic energy dissipation bracing systems. *Bullettin Earthq. Eng., 12,* 2777–2796.

[59] Vargas, R.; Bruneau, M. (2009). Experimental response of buildings designed with metallic structural fuses. II. *J. Struct. Eng., 135*, 394–403, doi:10.1061/(ASCE)0733-9445(2009)135:4(394).

[60] Loock, P. (2005). LVL Wall with Varied External Dissipation Options. University of Canterbury, Christchurch, New Zealand.

[61] Smith T. (2006). LVL Rocking Shear Walls: with External Dissipater Attachment, University of Canterbury, Christchurch, New Zealand. 3rd Professional Year Project.

[62] Iqbal, A., Pampanin, S., & Buchanan, A. H. (2016). Seismic performance of full-scale post-tensioned timber beam-column connections. *Journal of earthquake engineering*, *20*(3), 383-405.

[63] Li, Z., M. He, and K. Wang. 2018. Hysteretic performance of selfcentering glulam beam-to-column connections. *J. Struct. Eng. 144 (5),* 04018031. https://doi.org/10.1061/(ASCE)ST.1943-541X.0002012.

[64] Polocoșer, T., Leimcke, J., & Kasal, B. (2018). Report on the seismic performance of three-dimensional moment-resisting timber frames with frictional damping in beam-to-column connections. *Advances in structural engineering*, *21*(11), 1652-1663.

[65] Sarti, F., Palermo, A., & Pampanin, S. (2016). Development and testing of an alternative dissipative posttensioned rocking timber wall with boundary columns. *Journal of Structural Engineering*, *142*(4), E4015011.

[66] Iqbal, A., Pampanin, S., Palermo, A., & Buchanan, A. H. (2015). Performance and design of LVL walls coupled with UFP dissipaters. *Journal of Earthquake Engineering*, *19*(3), 383-409.

[67] Ganey, R., J. Berman, T. Akbas, S. Loftus, J. Daniel Dolan, R. Sause, J. Ricles, S. Pei, J. V. D. Lindt, and H.-E. Blomgren. (2017). Experimental investigation of self-centering cross-laminated timber walls. *J. Struct. Eng*. *143* (10), 04017135. https://doi.org/10.1061/(ASCE)ST .1943-541X.0001877.

[68] Chen, Z., Popovski, M., & Iqbal, A. (2020). Structural performance of post-tensioned CLT shear walls with energy dissipators. *Journal of Structural Engineering*, *146*(4), 04020035.

[69] Hashemi, A., Zarnani, P., & Quenneville, P. (2020). Seismic assessment of rocking timber walls with energy dissipation devices. *Engineering Structures*, *221*, 111053.

[70] Padilla-Reyes, J., Maureira-Carsalade, N., San Martín, J., & Chávez, M. (2018). A self-centring semi-rigid connection with energy dissipation for wooden frames. In World Conference on Timber Engineering, WCTE 2018.

[71] Granello G., Palermo A., Pampanin S., Pei S., & van de Lindt J. (2020) Pres-Lam Buildings: State-of-the-Art. *Journal of Structural Engineering*, *146*(6): 04020085. DOI: 10.1061/(ASCE)ST.1943-541X.0002603

[72] Wanninger, F., & Frangi, A. (2016). Experimental and analytical analysis of a post-tensioned timber frame under horizontal loads. *Engineering Structures*, *113*, 16-25.

[73] Xiong, H., & Liu, Y. (2016). Experimental study of the lateral resistance of bolted glulam timber post and beam structural systems. *Journal of Structural Engineering*, *142*(4), E4014002.

[74] Pino, M. D., Pampanin, S., Carradine, D., Deam, B., & Buchanan, A. H. (2010). Dynamic response of a multi-storey post-tensioned timber building. In 11th World Conference on Timber Engineering (Vol. 8). Trentino, Italy: Riva del Garda.

[75] Pampanin, S., Ciurlanti, J., Bianchi, S., Perrone, D., Palmieri, M., Grant, D., ... & Candeias, P. X. (2020). Enhancing Seismic Safety and Reducing Seismic Losses: Overview and Preliminary Results of SERA Project-3D Shaking Table Tests on An Integrated Low-Damage Building System. 17WCEE 13-18 Sept., Sendai, Japan, *philosophy*, 1(2), 6.

[76] Faggiano B,. Iovane G, Salzillo D., Mazzolani F. M. & Landolfo R. (2020) Dissipative Bracing Systems for Seismic Upgrading of New and Existing Timber Structures, *International Journal of Architectural Heritage*, DOI: 10.1080/15583058.2020.1830451

[77] Holden, T., Devereux, C., Haydon, S., Buchanan, A., & Pampanin, S. (2016). NMIT Arts & Media Building—Innovative structural design of a three storey post-tensioned timber building. Case studies in structural engineering, 6, 76-83.

[78] Palermo, A., Sarti, F., Baird, A., Bonardi, D., Dekker, D., & Chung, S. (2012). From theory to practice: Design, analysis and construction of dissipative timber rocking post-tensioning wall system for Carterton Events Centre, New Zealand. In Proceedings of the 15th world conference on earthquake engineering, Lisbon, Portugal (pp. 24-28).

[79] Brown, A., J. Lester, S. Pampanin, and D. Pietra. (2012). Rebuilding timber navigation's offices using a damage-limiting seismic system. In Proc., World Conf. on Timber Engineering. Quebec City, Canada: World Conference on Timber Engineering

[80] Leyder, C., Wanninger, F., Frangi, A., & Chatzi, E. (2015). Dynamic response of an innovative hybrid structure in hardwood. Proceedings of the Institution of Civil Engineers-Construction Materials, 168(3), 132-143.

[81] http://www.pres-lam.com

[82] Loeding, S., Kowalsky, M. J., & Priestley, M. N. (1998). Direct displacement-based design of reinforced concrete building frames *Division of Structural Engineering*, *98* (8). University of California, San Diego.

[83] Varughese, J. A., Menon, D., & Prasad, A. M. (2012). Simplified Procedure for Displacement-based Design of Stepped Buildings. In *Proceedings of the 15th world conference on earthquake engineering (WCEE), Lisbon* (pp. 24-28).

[84] Sullivan, T. J., & Lago, A. (2012). Towards a simplified direct DBD procedure for the seismic design of moment resisting frames with viscous dampers. *Engineering Structures*, *35*, 140-148.

[85] Di Cesare, A., & Ponzo, F. C. (2017). Seismic retrofit of reinforced concrete frame buildings with hysteretic bracing systems: design procedure and behaviour factor. *Shock and Vibration*, *2017*. 2639361. doi: 10.1155/2017/2639361

[86] Mazza, F., Mazza, M., & Vulcano, A. (2015). Displacement-based seismic design of hysteretic damped braces for retrofitting in-elevation irregular rc framed structures. *Soil Dynamics and Earthquake Engineering*, *69*, 115-124.

[87] Mazza, F., & Pasceri, C. (2020). Seismic Retrofitting of Buildings with Damped Braces by Using a Computer-Aided Design Procedure. *In Proceedings of 1st International Conference on Structural Damage Modelling and Assessment* (pp. 121-134). Springer, Singapore.

[88] Mohsenian, V.; Mortezaei, A. (2018). New energy absorbing system for seismic retrofitting of frame structures with slender braces. *Bull. Earthq. Eng.*, 17, 2715–2739, doi:10.1007/s10518-018-00543-7.

[89] Nuzzo, I., Losanno, D., & Caterino, N. (2019). Seismic design and retrofit of frame structures with hysteretic dampers: a simplified displacement-based procedure. *Bulletin of Earthquake Engineering*, *17*(5), 2787-2819.

[90] Nuzzo, I., Caterino, N., & Pampanin, S. (2020). Seismic Design Framework Based on Loss-performance Matrix. *Journal of Earthquake Engineering*, 1-21.

[91] Quintana Gallo, P.; Carradine, D.M.; Bazaez, R. (2020). State of the art and practice of seismic-resistant hybrid timber structures. *Eur. J. Wood Prod.*, 1–24, doi:10.1007/s00107-020-01556-3.

[92] Nuzzo, I.; Ciliento, F.; Caterino, N. (2020). DIBRAST: A computer-aided seismic design procedure for frame structures equipped with hysteretic devices. *Front. Built Environ.*, *6*, 13, doi:10.3389/fbuil.2020.00013.

[93] Ponzo, F.C.; Di Cesare, A.; Lamarucciola, N.; Nigro, D. (2019). Seismic design and testing of post-tensioned timber buildings with dissipative bracing systems. *Front. Built Environ.*, *5*, 104, doi:10.3389/fbuil.2019.00104.

[94] Mazza, F.; Mazza, M. (2019). Seismic retrofitting of gravity-loads designed rc framed buildings combining CFRP and hysteretic damped braces. *Bull. Earthq. Eng.*, *17*(6), 3423–3445, doi:10.1007/s10518-019-00593-5.

[95] Foti, D.; Ruggiero, F.; Sabbà, M.F.; Lerna, M. (2020). A Dissipating Frames for Seismic Retrofitting and Building Energy-Efficiency. *Infrastructures*, *5*, 74, doi:10.3390/infrastructures5090074.

[96] Palermo, M.; Silvestri, S.; Gasparini, G.; Trombetti, T. (2015). Crescent shaped braces for the seismic design of building structures. Mater. Struct., 48, 1485–1502.

[97] Palermo, M.; Pieraccini, L.; Dib, A.; Silvestri, S.; Trombetti, T. (2017). Experimental tests on Crescent Shaped Braces hysteretic devices. *Eng. Struct., 144,* 185–200.

[98] Zahrai, S.M.; Froozanfar, M. (2019). Improving seismic behavior of MRFs by U-shaped hysteretic damper along diagonal brace. *Int. J. Steel Struct., 19*, 543–558.

[99] Yousef-beik, S.M.M.; Veismoradi, S.; Zarnani, P.; Hashemi, A.; Quenneville, P. (2020). Experimental Study on Cyclic Performance of a Damage-Free Brace with Self-Centering Connection. *J. Struct. Eng., 147*, 04020299, doi:10.1061/(asce)st.1943-541x.0002869.

[100] Varughese, K.; El-Hacha, R. (2020). Design and behavior of steel braced frame reinforced with NiTi SMA wires. *Eng. Struct., 212*, 110502, doi:10.1016/j.engstruct.2020.110502.

[101] Loss, C., Tannert, T., & Tesfamariam, S. (2018). State-of-the-art review of displacement-based seismic design of timber buildings. *Construction and Building Materials*, *191*, 481-497.

[102] Filiatrault, A., & Folz, B. (2002). Performance-based seismic design of wood framed buildings. *Journal of Structural Engineering*, *128*(1), 39-47.

[103] Pei, S., Popovski, M., van de Lindt, J. W. (2012). Performance based design and force modification factors for CLT structures, in Proceeding of the 45thMeeting, International Council for Research and Innovation in Building and Construction, Working CommissionW18 – Timber Structures, CIB-W18 (Växjö), 2012.

[104] Newcombe M.P., Marriott D., Kam W.Y., Pampanin S. and Buchanan A.H., (2011). Design of UFP-coupled Post-tensioned Timber Shear Walls. 9th Pacific Conference on Earthquake Engineering, Auckland, New Zealand.

[105] Newcombe,M. P., Pampanin, S., and Buchanan, A. H. (2010). Design, fabrication and assembly of a two-story post-tensioned timber building, in Proc. World Conference on Timber Engineering (Riva del Garda), 3092–3100.

[106] Priestley, M. J. N., Calvi, G. M., and Kowalsky, M. J. (2007). Displacement-Based Seismic Design of Structures. Pavia: IUSS Press, 670

[107] Chopra, Anil K. (1995). Dynamics of Structures: Theory and application to earthquake engineering Prentice Hall, USA

[108] M.P. Newcombe, (2011). Seismic design of post-tensioned timber frame and wall buildings PhD Thesis, University of Canterbury, Christchurch, New Zealand.

[109] Priestley, M. J. N., & Grant, D. N. (2005). Viscous damping in seismic design and analysis. *Journal of earthquake engineering*, *9*(spec02), 229-255

[110] Structural Timber Innovation Company Inc (2013). Post-Tensioned Timber Buildings - Design Guide, Structural Timber Innovation Company. Christchurch.

[111] Smith, T. (2014). Post-tensioned timber frames with supplemental damping devices. PhD Thesis, University of Canterbury, Christchurch, New Zealand.

[112] Di Cesare A, Ponzo FC, Nigro D, Pampanin S, Smith T. (2017). Shaking table testing of posttensioned timber frame building with passive energy dissipation systems. *Bull Earthq Eng*. https://doi.org/10.1007/s10518-017-0115-9.

[113] Di Cesare A., Ponzo F.C., Pampanin S., Smith T., Nigro D., Lamarucciola N. (2019) Displacement based design of post-tensioned timber framed buildings with dissipative rocking mechanism. *Soil Dynamics and Earthquake Engineering, 116*: 317-330

[114] Ponzo F.C., Smith T., Di Cesare A., Pampanin S., Carradine D., Nigro D. (2012) Shaking table test of a multistorey post- Tensioned glulam building: Design and construction. WCTE 2012, Auckland, New Zealand. 2: 44-52

[115] Krawinkler, H., andMoncarz, P. D. (1981). Theory and Application of Experimental Model Analysis in Earthquake Engineering. Standford, CA: NASA STI/Recon Technical Report N 82.

[116] Dolce M., Moroni C., Nigro D., Ponzo F.C., Santarsiero G., Di Croce M., De Canio G., Ranieri N., Caponero M., Berardis S., Goretti A., Spina D., Lamonaca B., Marnetto R. (2006) TREMA project experimental evaluation of the seismic performance of a R/C 1/4 scaled model upgraded with the DIS-CAM system. 2nd FIB Congress, Naples, Italy.

[117] Braga F., Laguardia R., Paolocci A., Gigliotti R. (2019) Experimental tests on dissipative device based on U-shaped plates for seismic isolation systems. XVIII Convegno di Ingegneria Sismica, Associazione Nazionale di Ingegneria Sismica, Ascoli Piceno, Italy, pp 56-63

[118] Wang, B., & Zhu, S. (2018). Superelastic SMA U-shaped dampers with self-centering functions. *Smart materials and structures*, *27*(5), 055003.

[119] Chen, Y., Palermo, A., & Mashal, M. (2020). Cyclic tests of an innovative seismic bracing member-multiple U-shaped flexural plates dissipater. NZSEE Conference, Wellington, New Zealand.

[120] Castigliano, A., (1879). Théorie de l'équilibre des systèmes élastiques et ses applications 1. AF Negro.

[121] Di Cesare A., Ponzo F.C., Nigro D., Simonetti M., Smith T., Pampanin S. (2013) Experimental testing and numerical analysis of steel angles as hysteretic energy dissipating systems. XV Convegno di Ingegneria Sismica, Associazione Nazionale di Ingegneria Sismica, Padova, Italy.

[122] Di Cesare, A., Ponzo, F. C., Lamarucciola, N., & Nigro, D. (2017). Experimental testing on U-shaped steel devices for the application of dissipative bracing systems for post-tensioned timber framed buildings, Atti del XVII Convegno ANIDIS L'ingegneria Sismica in Italia: Pistoia, 17-21 Settembre 2017, pp.178-188.

[123] Di Cesare, A., Ponzo, F. C., Lamarucciola, N., & Nigro, D., 2020. Experimental seismic response of a resilient 3-storey post-tensioned timber framed building with dissipative braces. Bulletin of Earthquake Engineering, 18, 6825–6848. https://doi.org/10.1007/s10518-020-00969-y

[124] CNR-DT 206 R1/2018-Istruzioni per la Progettazione, l'Esecuzione ed il Controllo delle Strutture di Legno

[125] UNI EN 15129: 2018. Anti-seismic devices, CEN, European Committee for Standardization, Brusseles.

[126] Housner GW. (1952). Spectrum intensity of strong motion earthquakes. Proceedings of the Symposium on Earthquakes and Blast Effects on Structures, Earthquake Engineering Research Institute, California: 20–36.

[127] Welch P. D. (1961) A direct digital method of power spectrum estimation. IBM *J. Res. and Dev*., *5*, 141- 56.

[128] Bouc, R. F. (1967). Forced vibration of mechanical system with hysteresis. In Proceedings of the 4th Conference on Nonlinear Oscillations, Prague, Czech Republic, 5-9 September, pp. 32–39.

[129] Wen, Y.K.; (1980). Equivalent linearization for hysteretic systems under random excitation. *J. Appl. Mech.*, *47*, 150–154, doi:10.1115/1.3153594.

[130] Priestley, M.J., Calvi, G.M. & Kowalsky, M.J., (2007). Displacement based seismic design of structures, IUSS, Pavia.

[131] Wanninger, F., Frangi, A., & Fragiacomo, M. (2015). Long-term behavior of post-tensioned timber connections. *Journal of Structural Engineering, 141*(6), 04014155.

[132] Granello, G., Palermo, A., Pampanin, S., Smith, T., & Sarti, F. (2018). The implications of post-tensioning losses on the seismic response of Pres-Lam frames. Bulletin of the New Zealand Society for Earthquake Engineering, 51(2), 57-69.

[133] Granello, G., Leyder, C., Frangi, A., Palermo, A., & Chatzi, E. (2019). Long-term performance assessment of an operative post-tensioned timber frame structure. *Journal of Structural Engineering, 145*(5), 04019034.

[134] Smith, T. (2014). Post-tensioned timber frames with supplemental damping devices. PhD Thesis, University of Canterbury, Christchurch, New Zealand.

[135] Smith, T., Ponzo, F.C., Di Cesare, A., Auletta, G., Pampanin, S., Carradine, D., Palermo, A. & Nigro, D., (20129. Testing of a post-tensioned glue laminated beam to column joint: experimental and numerical results. *12th World Conference on Timber Engineering*. July 16–19, Auckland, New Zealand.

[136] Kaldjian, M.J., (1967). Moment-curvature of beams as Ramberg-Osgood functions. *Journal of the Structural Division*, American Society of Civil Engineers, 93(ST5), pp. 53–65.

[137] Ponzo, F. C., Di Cesare, A., & Lamarucciola, N. (2018). Modelling of post-tensioned timber-framed buildings with seismic rocking mechanism at the column-foundation connections. *Timber structures and engineering*, *177*.

[138] Roh, H., & Reinhorn, A. M. (2009). Analytical modeling of rocking elements. *Engineering Structures*, *31*(5), 1179-1189.

[139] Computers and Structures Inc. 2014. SAP 2000 v. 16.1.0 [Software]. Computers and Structures, Inc.: Berkeley, CA.

[140] McKenna, F., Fenves, G.L., Scott, M.H., Jeremic, B. (2000) Open System for Earthquake Engineering Simulation (OpenSees) [Software]. Pacific Earthquake Engineering Research Center, University of California: Berkeley, CA.

[141] Di Cesare, A., Ponzo, F. C., Lamarucciola, N., and Nigro, D. (2019). Modelling of post-tensioned timber framed buildings with hysteretic bracing system: preliminary analysis. *In IOP Conference Series: Earth and Environmental Science 233* (2), p. 022026. IOP Publishing.

[142] Jacobsen, L. S. (1930). Steady forced vibrations as influenced by damping, *ASME Transactione*, *52*(1), 169–181.

[143] Jacobsen, L. S. (1960). Damping in composite structures. Proc., 2nd World Conf. on Earthquake Engineering, 2, Science Council of Japan, Tokyo, 1029–1044.

[144] Pino Merino, D. A. (2011). Dynamic response of post-tensioned timber frame buildings. PhD dissertation, New Zealand.

[145] Filiatrault, A., Isoda, H., & Folz, B. (2003). Hysteretic damping of wood framed buildings. *Engineering Structures*, *25*(4), 461-471.

[146] Rosenblueth, E., & Herrera, I. (1964). On a kind of hysteretic damping. *Journal of the Engineering Mechanics Division*, *90*(4), 37-48.

[147] Gulkan, P., and Sozen, M. (1974). Inelastic response of reinforced concrete structures to earthquake motion. *ACI J., 71*, 604–610.

[148] Iwan, W. D. (1980). Estimating inelastic response spectra from elastic spectra. *Earthquake Eng. Struct. Dyn*., *8*(4), 375–388.

[149] Dwairi, H. M., Kowalsky, M. J., and Nau, J. M. (2007). Equivalent damping in support of direct displacement-based design. *J. Earthquake Eng.*, 11(4), 512–530.

[150] Blandon, C. A., and Priestley, M. J. N. (2005). Equivalent viscous damping equations for direct displacement-based design. *J. Earthquake Eng.*, *9*(2), 257–278.

[151] Pennucci, D., Calvi, G. M., & Sullivan, T. J. (2009). Displacement-based design of precast walls with additional dampers. Journal of Earthquake Engineering, 13(S1), 40-65.

[152] Mazza, F., & Vulcano, A. (2014). Equivalent viscous damping for displacement-based seismic design of hysteretic damped braces for retrofitting framed buildings. *Bulletin of earthquake engineering*, *12*(6), 2797-2819.

[153] Bezabeh, M. A., Tesfamariam, S., & Stiemer, S. F. (2016). Equivalent viscous damping for steel moment-resisting frames with cross-laminated timber infill walls. *Journal of Structural Engineering*, *142*(1), 04015080.

[154] Meirovitch, L. (2010). Fundamentals of vibrations. Waveland Press. ISBN 10: 1-57766-691-7

[155] Morillas, L.; Escolano-Margarit, D. (2020). Estimation of Cyclic Demand in Metallic Yielding Dampers Installed on Frame Structures. *Appl. Sci., 10*, 4364, doi:10.3390/app10124364.

[156] Ponzo, F.C.; Di Cesare, A.; Lamarucciola, N.; Nigro, D. (2019). Testing requirements of hysteretic energy dissipating devices according to Italian seismic code. In Proceedings of the 7th ECCOMAS Thematic International Conference on Computational Methods in Structural Dynamics and Earthquake Engineering, Crete, Greece, 24–26 June 2019; Volume 2, pp. 3323–3332.

[157] Di Cesare, A.; Ponzo, F.C.; Lamarucciola, N.; Nigro, D. (2020) Dynamic Seismic Response of Nonlinear Displacement Dependent Devices Versus Testing Required by Codes: Experimental Case Studies. *Appl. Sci.*, *10*, 8857.

[158] AASHTO Guide Specification for Seismic Isolation Design; American Association of State Highway and Transportation Officials: Washington, DC, USA, 1991.

[159] FEMA 461. Interim Testing Protocols for Determining the Seismic Performance Characteristics of Structural and Nonstructural Components; Federal Emergency Management Agency: Washington, DC, USA, 2007.

Appendix A: Testing program and instrumentation

Testing configurations

ID Configurazione	Post-tensioning Longitudinal (kN)	Post-tensioning Transversal (kN)	Steel angles beam column joints	Steel angles column-foundation joints	Steel damper bracing-beam joint
Free rocking Frame (F)	100	50	-	-	
Dissipative rocking Frame (DF)	100	50	2 (ID5)	1 (ID8_A)	
Dissipative Braced Frame (BF)	100	50		1 (ID8_A)	UFP (C60)

Seismic inputs

ID Signal	ID Code	Location	Date	M	PGA (g)
RND	Random				
S1	1228x	Izmit, Turkey	17/08/1999	7.6	0.357
S2	196x	Montenegro, Serbia	15/04/1979	6.9	0.454
S3	535y	Erzican, Turkey	13/03/1992	6.6	0.769
S4	187x	Tabas, Iran	16/09/1978	7.3	0.926
S5	291y	Campano Lucano, IT	23/11/1980	6.9	0.264
S6	4673y	South Iceland	17/06/2000	6.5	0.716
S7	4677y	South Iceland	17/06/2000	6.5	0.227

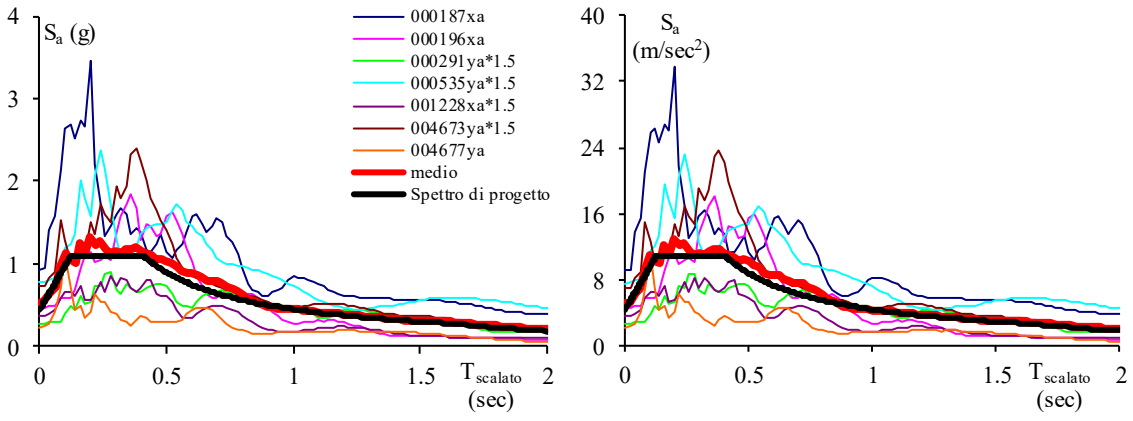

Scale factors

Intensity	*S1*	*S2*	*S3*	*S4*	*S5*	*S6*	*S7*
	1228	*196*	*535*	*187*	*291*	*4673*	*4677*
PGA (%)	***3.5009***	***4.453***	***7.5413***	***9.0835***	***2.5871***	***7.0163***	***2.2269***
0.1	0.35009	0.4453	0.75413	0.90835	0.25871	0.70163	0.22269
0.25	0.875225	1.11325	1.885325	2.270875	0.646775	1.754075	0.556725
0.5	1.75045	2.2265	3.77065	4.54175	1.29355	3.50815	1.11345
0.75	2.625675	3.33975	5.655975	6.812625	1.940325	5.262225	1.670175
1	3.5009	4.453	7.5413	9.0835	2.5871	7.0163	2.2269

Summary of previous testing configurations (F and DF)

F model

Intensity	Id. Din.	S1	S2	S3	S4	S5	S6	S7
PGA (%)	***Random***	***1228***	***196***	***535***	***187***	***291***	***4673***	***4677***
0.1	0	1	2	3				
0.25		4	5	6				
0.5		7	8	9	10	11	12	13
0.75		14	15	16				
1		17						

DF model

Intensity	Id. Din.	S1	S2	S3	S4	S5	S6	S7
PGA (%)	***Random***	***1228***	***196***	***535***	***187***	***291***	***4673***	***4677***
0.1	0	1	2	3				
0.25		4	5	6				
0.5		7	8	9				
0.75		10	11	12				
1		13	14	15	16	17	18	19

Testing of post-tensioned frame with dissipative bracing

BF model configuration

Intensity	Id. Din.	S1	S2	S3	S4	S5	S6	S7
PGA (%)	***Random***	***1228***	***196***	***535***	***187***	***291***	***4673***	***4677***
0.1	0	1	2	3				
0.25		4	5	6				
0.5		7	8	9	10	11	12	13
0.75		14	15	16				
1		17	18	19	20			

LEADAS Acquisitions					
Channel	*Description*	*Position*	*Type*	*ID channel*	*Notes*
1	Wall side – base Lev. - Dir.X	LAB-S	± 1g	181	
2	MTS side I Lev.- Dir.X	LA1- SW	± 2g	6606	
3	Schenck side – I° Liv. - Dir.X	LA1- SWb	± 2g	6607	Longitudinal beam
4	Wall side- I° Liv.- Dir.Y	TA1-SW	± 1g	185	
5	Doorway side – I Lev.- Dir.Y	TA1- NE	± 1g	183	
6	MTS side II Lev. - Dir.X	LA2- SW	± 4g	5504	
7	Schenck side – II Lev. - Dir.X	LA2- SWb	± 4g	5505	Longitudinal beam
8	Wall side - II Lev.- Dir.Y	TA2- SW	± 1g	332	
9	Doorway side – II Liv.- Dir.Y	TA2-NE	± 1g	327	
10	MTS side -III Lev.- Dir.X	LA3- SW	± 4g	5506	
11	Schenck side – III Lev. - Dir.X	LA3- SWb	± 4g	5507	Longitudinal beam
12	Wall side - III Lev.- Dir.Y	TA3- SW	± 1g	328	
13	Doorway side – III Lev.- Dir.Y	TA3-NE	± 1g	329	

14	Doorway side - I floor beam - Vert.	VA1-N	V ± 1g	186/V	
15	Doorway side -Trave III floor beam - Vert.	VA3-N	V ± 1g	187/V	
16	Doorway side -III lev (tower) - Dir. X	LA3T-N	± 1g	182	Tower

MTS Acquisitions						
Channel	*Description*	*Position*	*Type*	*ID channel*	*Run*	*Notes*
1	Col Rot (Base internal) – NW MTS	CbiNW1	± 50mm	T1	0-100	
2	Col Rot (Base external) – NW MTS	CbeNW1	± 50mm	T2	0-100	
3	Col Rot (Base internal) – SW	CbiSW1	± 50mm	T3	0-100	
4	Col Rot (Base external) – SW	CbeSW1	± 50mm	T4	0-100	
5	Gap (bottom) I Lev – SW	G1b	± 25mm	T7	0-50	
6	Gap (central) I Lev – SW	G1c	± 12.5mm	T8	0-25	
7	Gap (top) I Lev – SW	G1t	± 25mm	T9	0-50	
8	Gap (bottom) II Lev – SW	G2b	± 25mm	T12	0-50	
9	Gap (central) II Lev – SW	G2c	± 12.5mm	T13	0-25	
10	Gap (top) II Lev – SW	G2t	± 25mm	T14	0-50	
11	III lev- MTS side- UFP3 displ.		± 50mm	T15	0-50	
12	III lev- Shenck side - Spost. UFP3		± 50mm	T16	0-50	

13	Gap (bottom) III° Liv – SW	G3b	spo ± 25mm	T17	0-50	
14	Gap (central) III° Liv – SW	G3c	± 12.5mm	T18	0-25	
15	Gap (top) III Lev – SW	G3t	± 25mm	T19	0-50	
16	Base displ.	LDB -N	± 260mm	cel 2		
17	I Lev displ. – NW	LD1 – NW	± 250mm	cel 3		
18	I Lev displ. – NE	LD1 – NE	± 250mm	cel 4		
19	II Lev displ. – NW	LD2 – NW	± 250mm	cel 5		
20	II Lev displ. – NE	LD2 – NE	± 250mm	cel 6		
21	III Lev displ. - NW	LD3 – NW	± 514mm	cel 7		
22	III Lev displ. – NE	LD3 – NE	± 514mm	cel 8		
23	Cell PT3 – SW	PT3	± 300kN	C1		
24	Cell PT2 – SW	PT2	± 300kN	C2		
25	Cell PT1 – SW	PT1	± 300kN	C3		
26	Cell ST3 - SW	ST3	± 300kN	C4		
27	Cell ST2 – SW	ST2	± 300kN	C5		
28	Cella ST1 – SW	ST1	± 300kN	C6		
29	Shak. Table Acc. to Sincronyze	LAB-S	± 1g	181		From LEADAS - 181
30	3rd Floor Acc. to Sincronyze	LA3- SW	± 4g	5506		From LEADAS - 5506
31	2nd Floor Acc. to Sincronyze	LA2- SW	± 4g	5504		From LEADAS - 5504
32	1st Floor Acc. to Sincronyze	LA1- SW	± 2g	6606		From LEADAS - 6606

LIACQ GEN Acquisitions						
Channel	*Description*	*Position*	*Type*	*ID*	*Run*	*Notes*
1	I lev- MTS side - UFP1 Cell	Cel 7	for ± 50kN	C7		
2	I lev- Shenck side- UFP1 Cell	Cel 8	for ± 50kN	C8		
3	I lev- MTS side - UFP1 displ.		± 50mm	T5	0-50	
4	I lev- Shenck side - UFP1 displ.		± 50mm	T6	0-50	
5	II lev- MTS side - UFP2 Cell	Cel 9	± 50kN	C9		
6	II lev- Shenck side - Cell UFP2	Cel 10	± 50kN	C10		
7	II lev- MTS side - UFP2 displ.		± 50mm	T10	0-50	
8	II lev- Shenck side - UFP2 displ.		± 50mm	T11	0-50	
9	III lev- MTS side - UFP3 Cell	Cel 11	± 25kN	C11		
10	III lev- Shenck side - UFP3 Cell	Cel 12	± 25kN	C12		
11	III lev- MTS side -. UFP3 displ		± 50mm	T15	0-50	
12	III lev- Shenck side - UFP3 displ.		± 50mm	T16	0-50	
13	Shak. Table Acc.			181	± 1g	
14	Shake table displ.			cel 2	± 260mm	CELESCO
15	3rd Floor Acc			5506	± 4g	
16	Spost III° Liv - NW MTS side			cel 2	± 514mm	CELESCO